GEMS & GEMOLOGY

WINTER 2018
VOLUME LIV

THE QUARTERLY JOURNAL OF THE GEMOLOGICAL INSTITUTE OF AMERICA

Characterization of Natural-Color Pink Diamonds

The Allure of the Amber Room

Color Origin of Gem Diaspore

Diamond Inclusions Chart

GEMS & GEMOLOGY

Winter 2018
VOLUME 54, No. 4

pg. 358

pg. 389

pg. 419

pg. 432

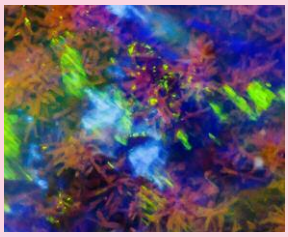

pg. 447

GEMS & GEMOLOGY

gia.edu/gems-gemology

Subscriptions
Copies of the current issue may be purchased for $29.95 plus shipping. Subscriptions are $79.99 for one year (4 issues) in the U.S. and $99.99 elsewhere. Canadian subscribers should add GST. Discounts are available for renewals, group subscriptions, GIA alumni, and current GIA students. To purchase print subscriptions, visit store.gia.edu or contact Customer Service. For institutional rates, contact Customer Service.

Database Coverage
Gems & Gemology's impact factor is 1.844, according to the 2017 Thomson Reuters Journal Citation Reports (issued July 2018). *G&G* is abstracted in Thomson Reuters products (Current Contents: Physical, Chemical & Earth Sciences and Science Citation Index—Expanded, including the Web of Knowledge) and other databases. For a complete list of sources abstracting *G&G*, go to gia.edu/gems-gemology, and click on "Publication Information."

Manuscript Submissions
Gems & Gemology, a peer-reviewed journal, welcomes the submission of articles on all aspects of the field. Please see the Author Guidelines at gia.edu/gems-gemology or contact the Managing Editor. Letters on articles published in *G&G* are also welcome. Please note that Field Reports, Lab Notes, Gem News International, Micro-World, and Charts are not peer-reviewed sections but do undergo technical and editorial review.

Gems & Gemology is published quarterly by the Gemological Institute of America, a nonprofit educational organization for the gem and jewelry industry.

Postmaster: Return undeliverable copies of *Gems & Gemology* to GIA, The Robert Mouawad Campus, 5345 Armada Drive, Carlsbad, CA 92008.

Our Canadian goods and service registration number is 126142892RT.

About the Cover

Natural-color pink diamonds are exceptional treasures. The lead article in this issue, based on GIA's database of more than 90,000 diamonds in the pink, orangy pink, purple, red, and brown color continuum, summarizes their gemological and spectroscopic characteristics. Shown on the cover is the 18.96 ct Winston Pink Legacy, a Fancy Vivid pink emerald-cut diamond that recently sold at auction for more than $50 million. Winston Pink Legacy courtesy of Harry Winston, Inc. © 2018 Christie's Images Limited.

Printing is by L+L Printers, Carlsbad, CA.
GIA World Headquarters The Robert Mouawad Campus 5345 Armada Drive Carlsbad, CA 92008 USA

ISSN 0016-626X

Pink Diamonds, Russia's Amber Room, and More...

The beauty and desirability of pink diamonds is exemplified by the Winston Pink Legacy, a stunning 18.96 ct Fancy Vivid pink diamond that realized US$50 million at auction in November 2018. Such sought-after diamonds are the subject of the third installment of our colored diamonds series. GIA researchers Sally Eaton-Magaña, Troy Ardon, Karen Smit, Christopher Breeding, and James Shigley summarize the current science on natural-color pink to red diamonds and detail the cause of their color. The authors provide an unprecedented gemological and spectroscopic characterization by presenting absorption and luminescence spectra drawn from a representative sample of 1,000 diamonds from GIA's database.

An unprecedented characterization of naturally colored pink to red diamonds...

Our second paper, by GIA's Russell Shor, surveys the history of the legendary Amber Room. Originally commissioned for Prussia's King Frederick I in the early 1700s and presented to Czar Peter I of Russia in 1716, the amber panels disappeared from St. Petersburg during the Second World War. In 1979, the Soviet Union initiated a painstaking reconstruction of this cultural treasure. Besides its rich history, the author provides firsthand accounts from those who participated in its recreation.

Next, Che Shen, a graduate student at the Gemmological Institute of China University of Geosciences in Wuhan, and Ren Lu investigate the color origin of gem-grade diaspore using LA-ICP-MS spectrometry.

A reaction rim or "corona" results from alteration of a crystal's exterior after its formation due to changes in geological conditions. In our fourth paper, researchers led by Nguyen Ngoc Khoi, from the Hanoi University of Science, provide a study on corundum with spinel corona from northern Vietnam. The authors explain the genesis of the corona by examining its reaction textures, chemical composition, and mineral inclusions and applying thermodynamic phase equilibria calculations.

Our fifth paper offers a gemological characterization of pipi pearls from the bivalve mollusk *Pinctada maculata*. Authors Nanthaporn Nilpetploy, Kwanreun Lawanwong, and Promlikit Kessrapong detail the internal structures and further investigate these small, sometimes strongly colored natural pearls using microradiography and UV-Vis, Raman, and photoluminescence spectroscopy.

Our final article is a brief summary of diamond inclusions by GIA's Nathan Renfro, John Koivula, Jonathan Muyal, Shane McClure, Kevin Schumacher, and James Shigley. A foldout wall chart with photomicrographs showcasing remarkable inclusions in natural, synthetic, and treated diamonds accompanies this article.

Besides our six articles and the chart, there's plenty to enjoy in our regular features: Lab Notes offers analysis of three freshwater blister pearls attached to their host shells, De Beers' Lightbox CVD-grown diamonds, and an exceptionally rare Montana ruby. Our new Diamonds from the Deep section provides an examination of how diamonds form in the deep earth. Micro-World serves up an array of internal features observed in gem materials, while Gem News International reports on sapphire treated with high pressure and high temperature, coated rough and faceted synthetic moissanite, and gemological conferences around the world.

Finally, don't forget to check our listing of the 2018 *G&G* Challenge winners, and please do remember to cast your vote for the Most Valuable Article of 2018 by mailing in the enclosed ballot card or by scanning the QR code to cast your vote online.

Duncan Pay | Editor-in-Chief | dpay@gia.edu

Natural-Color Pink, Purple, Red, and Brown Diamonds: Band of Many Colors

Sally Eaton-Magaña, Troy Ardon, Karen V. Smit, Christopher M. Breeding, and James E. Shigley

Among fancy-color diamonds, naturally pink to red stones are among the rarest and most valuable. The color origin for natural pink diamonds is due to either absorption from the as-yet-unidentified "550 nm" defect(s) that are correlated with shear stress and natural plastic deformation or, very rarely, the $NV^{0/-}$ centers (nitrogen combined with a vacancy). In this article we summarize prior research as well as the physical characteristics of more than 90,000 natural pink, orangy pink, red, purple, and brown diamonds from the internal GIA database. (Browns and purples are included here, as they coexist on a color continuum with pink diamonds.) We also present absorption and luminescence spectra on a representative subset of 1,000 diamonds to provide an unparalleled gemological and spectroscopic description of these rare gemstones. For pink diamonds, the gemological observations closely correlate with diamond type and the extent of nitrogen aggregation (i.e., type IaA<B, type IaA>B, and type IIa pinks show distinct characteristics). Since type IaA<B diamonds are predominantly sourced from the Argyle mine, which is scheduled to close in the next few years, we distinguish the properties of these pink diamonds from the others studied.

Diamond is one of Earth's most extraordinary materials. It represents the pinnacle for several material and physical properties. As a gem, however, it is the near-perfect examples—diamonds attaining the D-Flawless distinction—and those with imperfections resulting in a vibrant or surprising color that create the most enduring impressions. Fancy-color natural diamonds are among the most highly valued gemstones due to their attractiveness and great rarity. The 18.96 ct Winston Pink Legacy, with a color grade of Fancy Vivid pink, recently made history by selling at over $50 million, its $2.6 million per carat price an all-time high for a pink diamond (Christie's, 2018).

This article is the third in a series of studies on natural colored diamonds: Breeding et al. (2018) discussed the color origin of green diamonds, and Eaton-Magaña et al. (2018) dealt with blue/gray/violet diamonds. Here we summarize the color origin of orangy pink, purplish pink to pinkish purple, brownish pink to pinkish brown, pink, red, purple, and unmodified brown diamonds. Although this article covers a wide variety of color descriptions compared to, for example, the first article in the series, which was limited to natural diamonds with only green as the

In Brief

- Almost all pink/purple/red/orangy pink diamonds owe their color to the presence of an as-yet-unidentified 550 nm absorption band. Minor differences in band characteristics along with the presence of other defects (such as N3 and H3) lead to differences in hue and saturation.
- Among "pink" diamonds colored by the 550 nm band, distinctions in color distribution and observed strain can be correlated with their diamond type.
- A sizable percentage of the "pink" diamonds studied, particularly those with saturated colors, are consistent with material found at the Argyle mine, scheduled to close in 2020.

See end of article for About the Authors and Acknowledgments.
Gems & Gemology, Vol. 54, No. 4, pp. 352–377,
http://dx.doi.org/10.5741/GEMS.54.2.352

Figure 1. The 34.65 ct Princie (center, photo courtesy of Christie's) is a famous example of a pink diamond colored by $NV^{0/-}$ centers. It is flanked by an array of natural brown, brown-pink, orangy pink, purple-pink, and pink diamonds with the far more common cause of color—the 550 nm absorption band. These examples span the diverse color range of pinks submitted to GIA. The photos in this compilation are not imaged to scale.

dominant description, the color descriptions are joined here, as the vast majority of them (which will be quantified below) contain the 550 nm band as a prevalent absorption feature. For the sake of simplicity, this broad range of color descriptions (e.g., figures 1 and 2) will generally be shortened to "pink" in this article.

Previously, several aspects of gem-quality "pink" diamonds have been addressed, such as their gemological characteristics (e.g., King et al., 2002); their defects and associated spectroscopic features (e.g., Titkov et al., 2008; Deljanin et al., 2008; Fisher et al., 2009; Gaillou et al., 2010; Stepanov et al., 2011; Byrne et al., 2012a,b; Titkov et al., 2012; Gaillou et al., 2012; Howell et al., 2015); and reports on notable "pink" diamonds (Smith and Bosshart, 2002; King et al., 2014). Here we review the published literature and supplement it by compiling results obtained from 90,000+ natural diamonds recorded in the GIA internal database.

Our purpose is to provide a detailed account of the gemological and spectroscopic characteristics of natural "pink" diamonds, principally colored by an as-yet-unidentified "550 nm" absorption band, in order to help the trade better understand how these beautiful diamonds with extremely valuable colors originate.

CAUSES OF COLOR

All colored diamonds submitted to GIA are subject to a variety of spectroscopic analyses. The analytical techniques and specific details of the instrumentation and methods used are summarized in Breeding et al. (2018; see supplementary table S-1 at https://www.gia.edu/gems-gemology/spring-2018-natural-color-green-diamonds-beautiful-conundrum).

"Pink" color in diamonds spans a wide range in the GIA color description terminology (figure 2; King et al., 1994; King, 2006). In this article, we include all natural fancy-color diamonds with pink, purple, or red as the dominant hue (i.e., the final name in the color description) in addition to unmodified brown. Diamonds with yellow-brown or orange-brown color will be discussed in an upcoming article. In the full dataset of 90,000+ "pink" diamonds seen at GIA be-

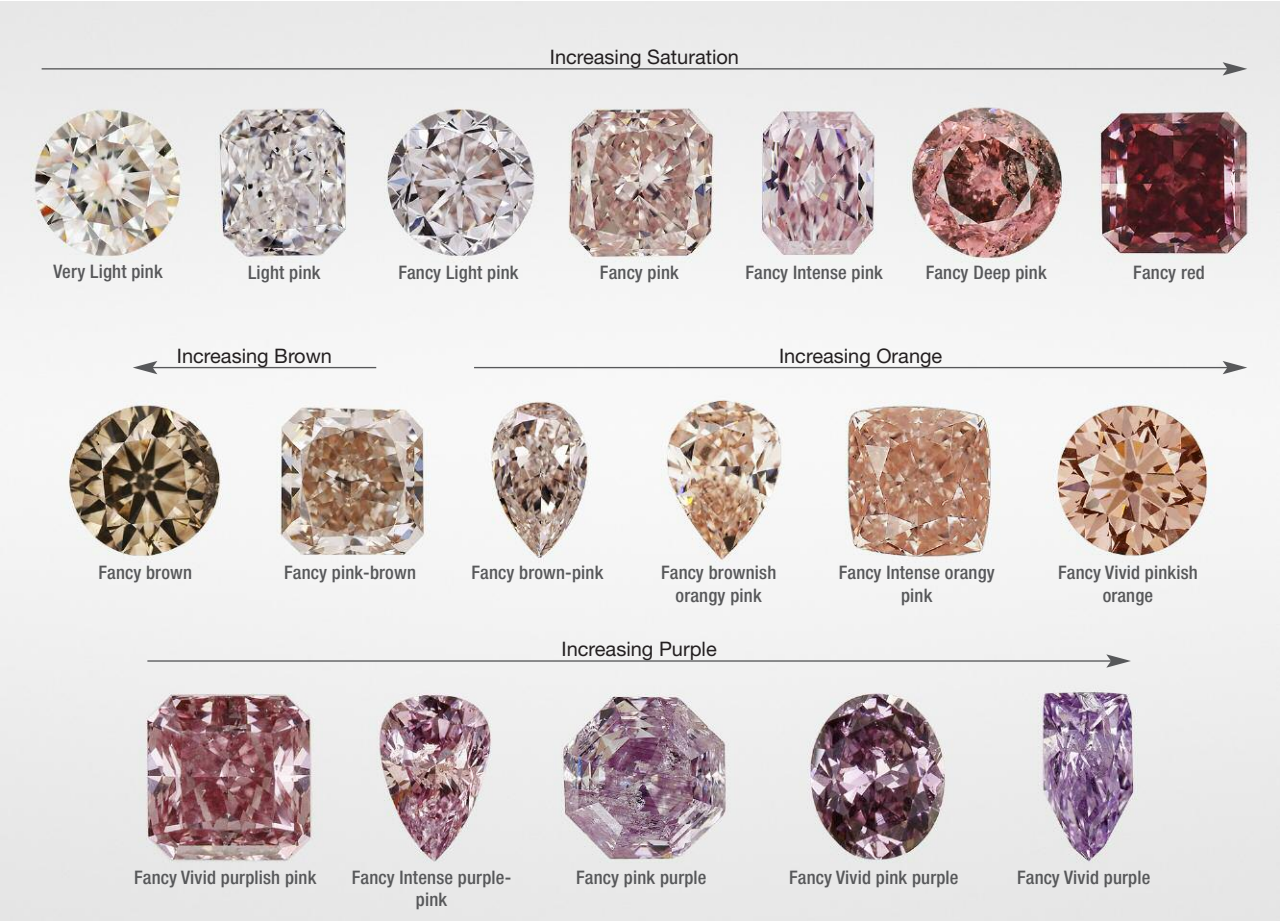

Figure 2. These examples of diamonds with varying hues and color saturations represent the "pink" color ranges. Photos by GIA staff. The photos in this compilation are not imaged to scale.

tween January 2008 and December 2016, the highest percentage were unmodified pink (40%), followed by pinkish purple to purplish pink (28%), brownish pink to pinkish brown (17%), and orangy pink (10%); see the color distribution in figure 3. The rarest colors were unmodified brown (3%); purple with brown or gray modifiers (1%); unmodified red (0.5%); red with brown, purple, or orange modifiers (0.4%); and, least of all, unmodified purple (0.05%).

In the description of color grades, it is more difficult for the eye to interpret subtle hue differences for very light-colored diamonds than it is for more saturated diamonds (King et al., 1994; King, 2006). For the lightest color grades, therefore, fewer hue names are used and the color description spans a wider portion of the hue wheel. Among unmodified pink diamonds, 54% were Faint, Very Light, or Light in color (figure 3, right).

Below we chronicle the main causes of color in the form of various structural defects, through which "pink" diamonds can be divided into different groups. Various colors and representative visible-near infrared spectra are shown in figures 2 and 4, respectively.

Colored Deformation Lamellae. In many brown, pink, and purple diamonds, the color is concentrated within parallel narrow bands (referred to as "brown graining," "pink graining," or glide planes, or alternatively as a more generalized term of colored lamellae). When manufactured as cut stones, these are typically oriented to minimize the face-up appearance of the lamellae, resulting in an apparent even color distribution through the table facet. Since the lamellae are along the {111} plane, these pink diamonds are generally oriented such that the table facet is {100} (J. Chapman, pers. comm., 2018). Microscopic observation of the lamellae is best accomplished looking through the pavilion facets of the diamond.

These colored lamellae are caused by shear stress and natural plastic deformation (figure 5, A and B). Deformation to form these lamellae only occurs dur-

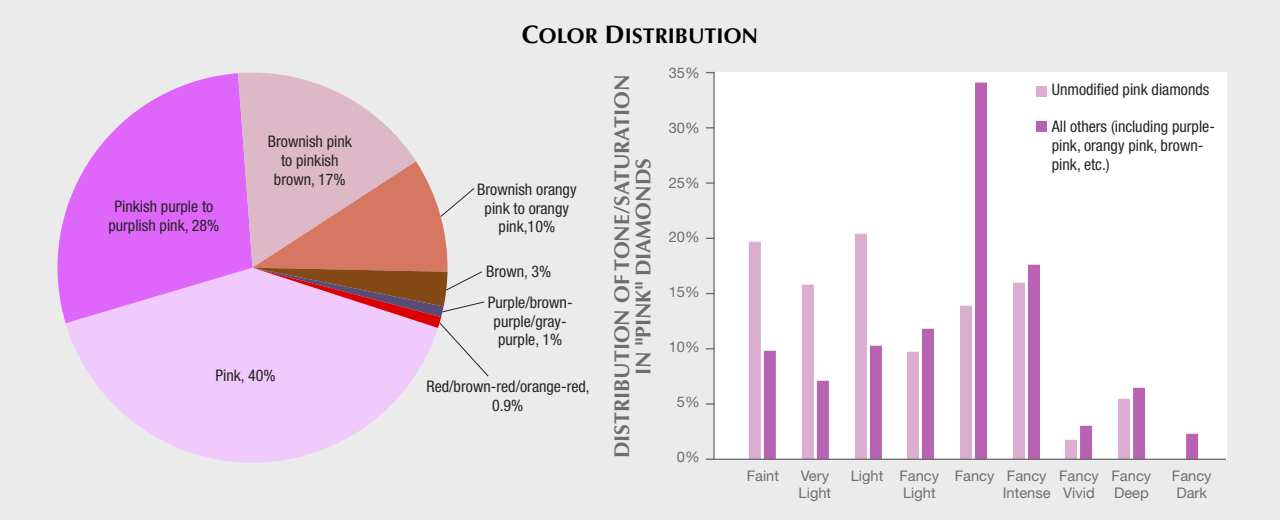

Figure 3. Color distribution of 90,000+ pink, purple, brown, orangy pink, and red diamonds graded at GIA between 2008 and 2016. Left: Unmodified pink and purplish pink diamonds dominated within this color range, while diamonds with a brown color description were submitted in lower quantities. Right: Saturation distribution of unmodified and modified pink diamonds. A majority of the unmodified pink samples (54%) are in the Faint to Light color range.

ing a diamond's extended residency at high temperature (>900°C; DeVries, 1975; Brookes and Daniel, 2001), either in the mantle or during kimberlite eruption to the earth's surface. These deformation lamellae have been attributed to slip/glide planes (dislocation movement) and to micro-twins (Mineeva et al., 2009: Gaillou et al., 2010; Titkov et al., 2012; Howell et al., 2015). In many diamonds these deformation lamellae are closely associated with brown, pink, or purple color; these colors can also appear evenly through the entire diamond or irregularly as distinct patchy areas (figure 5, C and D). The structural defects responsible for the different color contributions in pink, brown, and purple diamonds (i.e., the

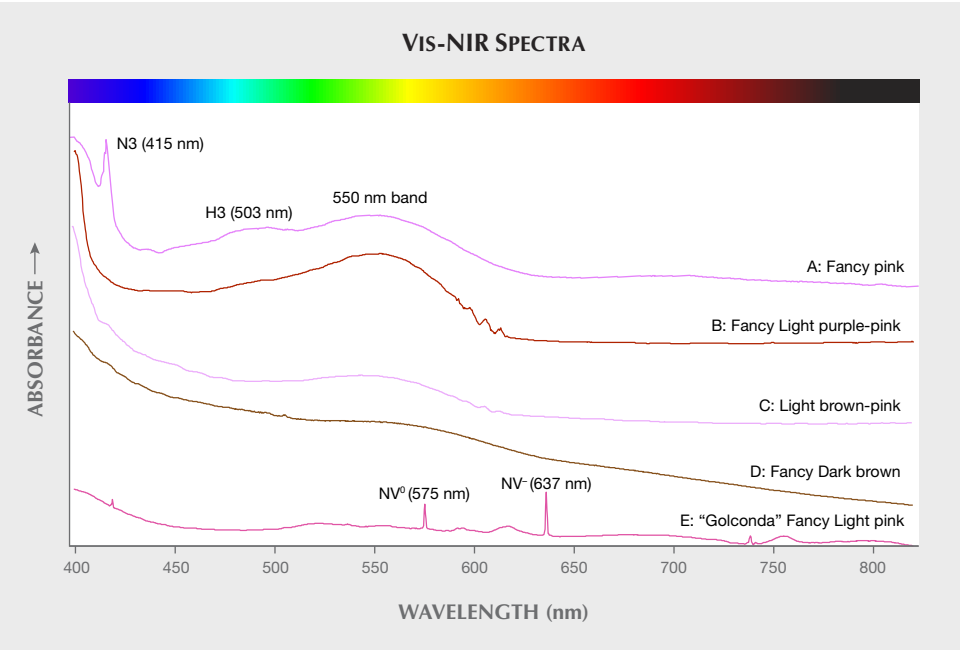

Figure 4. The vast majority of "pink" diamonds owe their color to the 550 nm absorption band (A–C). Spectrum A shows a diamond with the 550 nm band along with pronounced N3 and H3 centers. Spectrum D is for a brown diamond with a gradually increasing absorption toward lower wavelengths that creates the brown color; a very shallow 550 nm absorption band has little effect on the color. Spectrum E is for a "Golconda pink," which shows absorption by $NV^{0/-}$ centers. The spectra are offset vertically for clarity.

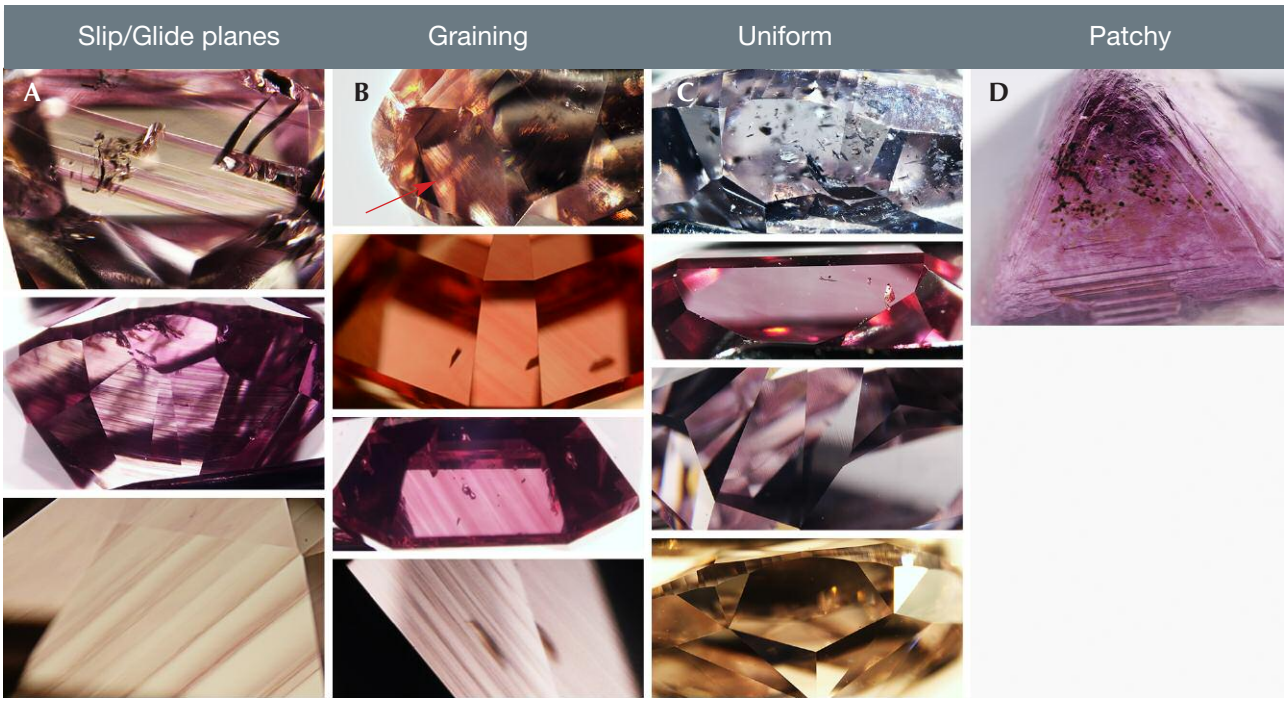

Figure 5. A: These pink type IaA>B diamonds show the color concentrated within pink lamellae (identified as "slip/glide planes" by GIA), while the remainder of the diamond is comparatively colorless. B: These type IaA<B pink diamonds show more subtle concentrations of color compared to A—the red arrow indicates the best example of this graining. C: These type IIa pink diamonds show uniformly distributed color. D: An unusual example of a rough pink diamond with radiation stains and irregular or "patchy" distribution of color.

"brown absorption continuum," the 550 nm absorption band, and $NV^{0/-}$ centers) are discussed in later sections.

Viewed with a microscope, the two types of lamellae appear distinct, and at GIA these are referred to as either slip/glide planes or graining. They also appear to correspond with the ratio of A centers (nitrogen pairs) and B centers (four nitrogen atoms around a vacancy) in the diamond (Gaillou et al., 2010). As diamonds reside in the mantle, or are exposed to higher temperatures, the A-aggregates decrease as they combine to form B-aggregates (Taylor et al., 1990). "Pink" diamonds where A-aggregates outnumber B-aggregates (i.e., type IaA>B, such as some Siberian diamonds; Titkov et al., 2008) show colored lamellae that appear distinctly different from "pink" diamonds where B-aggregates are greater than A-aggregates (i.e., type IaA<B, such as Argyle diamonds; Howell et al., 2015). In type IaA>B "pink" diamonds (designated below as Group 2), the colored lamellae appear distinct and straight along the {111} planes, and the pink color is restricted to these colored lamellae (Gaillou et al., 2010). Between these lamellae, the diamond is colorless (e.g., figure 5A). GIA often refers to these lamellae as "slip/glide planes" to distinguish them from the other type of colored lamellae. In type IaA<B "pink" diamonds (designated below as Group 1; figure 5B), the pink color is not restricted to the lamellae and does not appear as straight lines. GIA commonly refers to this as "graining," although these distinctions in terminology have not been defined within the gemological literature.

In faceted diamonds, the colored lamellae of type IaA<B "pink" diamonds can appear more subtle than the apparent contrast in color within type IaA>B "pink" diamonds (compare figure 5A with 5B). Recent research (see box B) shows that these classifications are not quite so distinct for diamonds that are low in nitrogen, and the visual distinction between colored "graining" and "slip/glide planes" becomes challenging.

In contrast, the majority of type IIa "pink" diamonds, and some pure type IaB diamonds, do not show visible evidence of colored lamellae (either as "graining" or "slip/glide planes"), and the "pink" color is uniformly distributed. However, type IIa "pink" diamonds do occasionally exhibit graining (appearing as colorless, brown, or pink) similar to that seen in type IaA<B diamonds.

Brown General Absorption. Brown color is quite common in natural diamonds, and a brownish tinge is reportedly observed in 98% of all as-mined diamonds, whether or not they are deemed gem-quality (Dobrinets et al., 2013). While brown diamonds are abundant, most are either not faceted or not submitted for grading reports unless there is another contributing color such as pink, orange, or yellow or if they can be faceted in such a way as to receive a grade on the D-to-Z scale (King et al., 2008). As mentioned previously, only 3% of the 90,000+ samples studied here had an unmodified brown color.

The vast majority of brown diamonds have their color ascribed to vacancy clusters (i.e., clusters of vacant carbon-atom positions; see Hounsome et al., 2006; Fisher et al., 2009) that are created through natural plastic deformation. These clusters are generally thought to contain approximately 40–60 vacancies, and the dissociation (generally through high-pressure, high-temperature HPHT annealing) of these vacancy clusters leads to the removal of brown color. These vacancy clusters create a so-called brown absorption continuum (Fisher et al., 2009; Dobrinets et al., 2013) that causes a gradually increasing absorption across the visible spectrum toward lower wavelengths (figure 4, spectrum D). This brown absorption continuum can coexist with other color centers (e.g., figure 4, spectrum C).

Brown coloration (by itself or in combination with other color centers) can also have other origins, including high concentrations of isolated substitutional nitrogen, CO_2, and micro-inclusions (Hainschwang et al., 2008; Dobrinets et al., 2013). However, these are not as commonly observed as those diamonds with the brown absorption continuum.

550 nm Visible Absorption Band. The most common cause of "pink" color is a broad absorption band centered at around 550 nm (Orlov, 1977; figure 4, spectrum B). The defect responsible for this visible absorption band has not yet been identified, but it has been correlated with plastic deformation (Gaillou et al., 2010; Howell et al., 2015). In conjunction with the 550 nm band is a smaller, narrower band within the UV range centered at ~390 nm (Fisher et al., 2009; Byrne et al., 2012a).

In "pink" type Ia diamonds, nitrogen often creates other visible absorption features that are detected in the visible absorption spectra and can affect the observed color. The N3 defect (zero phonon line, or ZPL, at 415.2 nm) and the H3 defect (ZPL at 503.2 nm) along with their vibronic structure (sidebands) create additional absorption at lower wavelengths (figure 4, spectrum A) that can alter the observed color.

Nitrogen-Vacancy Centers. "Pink" diamonds naturally colored by $NV^{0/-}$ centers are extremely rare; however, these centers are almost exclusively the cause of color in treated and synthetic "pink" diamonds. Absorption by the nitrogen-vacancy centers (the ZPL for the neutral NV center is at 575 nm, while the negative NV center is at 637 nm) along with their sidebands creates the absorption that produces the pale, uniform "pink" color in these very rare type IIa diamonds (figure 4, spectrum E). They are often referred to as "Golconda pink" diamonds (Fritsch, 1998). The 34.65 ct Fancy Intense pink Princie is a famous example of "Golconda pink," and it sold for more than $39 million at auction in 2013 (Christie's, 2013). While the Princie originates from the historical mining region of Golconda in India, today the term "Golconda" is generally associated with this cause of color and not with any geographical link to the ancient mining region.

OCCURRENCE AND FORMATION

The formation mechanism for "pink" diamonds in the earth varies significantly depending on the defects responsible for the color. Historical sources include India, Brazil, Indonesia (Borneo), and southern Africa. But before the Argyle mine in Australia opened in 1983, there was no stable supply of "pink" diamonds, and many of those currently available come from Argyle (figure 6; Hofer, 1985; Shigley et al., 2001; Shirey and Shigley, 2013). More recently, mines in the Siberian and Arkhangelsk regions of Russia have been documented as producing pink to purple-pink diamonds (Titkov et al., 2008; Smit and Shor, 2017). Finding new deposits with "pink" diamond production is important to the trade, since the final year of planned operation at the Argyle mine is 2020 (Shor, 2018).

"Pink" Diamonds with 550 nm Absorption Band. *Occurrence.* Nitrogen content and the extent of nitrogen aggregation in the atomic structure, and by inference the diamond's geographic origin, leads to very different observations of how "pink" color due to the 550 nm band is distributed within the diamond. Sources for Group 1 "pink" diamonds (type IaA<B, with wavy graining) include the Argyle mine in Australia and alluvial deposits in Venezuela. Group 2 "pink" diamonds (type IaA>B, slip/glide planes) are principally mined in southern Africa, Canada, and Russia (Howell et al., 2015).

Figure 6. The Argyle mine is well known as a source for pink diamonds, although these account for much less than 0.1% of the overall production. Photo © Rio Tinto.

An abundance of locality data is available on type Ia "pinks" but not for type IIa "pink" diamonds. There are several observations of type IIa "pinks" that coincide with Argyle "pinks" such as color range, the presence of wavy graining in some type IIa diamonds, and some photoluminescence peaks that appear in type IIa, IaB, and IaA<B "pinks." However, reports regarding the output of the Argyle mine largely exclude type IIa diamonds (J. Chapman, pers. comm., 2018). Type IIa pink-brown diamonds are known from localities that also yield so-called superdeep diamonds from >250 km in the earth's mantle (Smith et al., 2017). Pink-brown type IIa diamonds with superdeep mineral inclusions (i.e., minerals that are only stable, or could only form, under high-pressure conditions) have been documented in GIA's New York laboratory, but their geographic source location is unknown. One of the few superdeep IIa "pink" diamonds for which GIA does have locality information is a 23 ct rough pink type IIa diamond found at the Williamson mine (Tanzania) in November 2015 (Smith et al., 2017; Petra Diamonds, https://www.petradiamonds.com/about-us/our-heritage). Fisher et al. (2009) also cited the Williamson mine as a source of type IIa pinks, though production numbers are unknown. The Williamson mine has also been a source of high-nitrogen type Ia "pink" diamonds (Gaillou et al., 2012).

Although "pink" diamonds are known from several deposits around the world, they remain a very small percentage of the overall production from any particular deposit. The Argyle mine is well known as a source for "pink" diamonds, but these account for much less than 0.1% of the overall production, where 72% of the production is brown and 27% is colorless to yellow (Shigley et al., 2001; figure 6). At the Lomonosov deposit in northwestern Russia, only 0.04% of production is fancy-color diamonds (purple, pink, violet, green, yellow, and brown; Smit and Shor, 2017). Some parcels from the Mir deposit in Siberia contain 1–6% pink to purple diamonds, although no overall production data were available (Titkov et al., 2008 and references therein).

Formation. Pink-brown color is often associated with deformation lamellae in the diamond, and the geological process responsible for this deformation is often mountain building (Stachel et al., 2018). A geologically modern example of mountain building is the Himalayan range in Asia, which is increasing in elevation due to collision between the Eurasian and Indian tectonic plates. The remnants of mountain ranges that developed during collisional processes millions to billions of years ago, and have since been eroded away, are called "orogens." During continental collision, rocks become highly deformed with such severe mineral recrystallization that any diamonds and other minerals in the rock can take on a "flow" texture.

The Argyle mine, the most famous supplier of occasional pink and red diamonds, occurs in one such area that experienced ancient continental collision, the Proterozoic Halls Creek orogen (1.8 Ga; Tyler and Page, 1996). Argyle diamonds formed in close association with these collisional processes (Richardson et al., 1985), and after their formation resided near the base of the lithosphere (Stachel et al., 2018). It is in this high-temperature, high-deformation environ-

ment near the convecting mantle that the pink-brown-red color in these diamonds likely originated.

The Lomonosov mine, which produces pink-purple-brown diamonds, also lies within an area that experienced ancient subduction and continental collision—around 1.9 billion years ago—and is known as the Lapland-Kola orogen (Daly et al., 2006). Although the Lomonosov diamonds have not been dated, it is very possible that they formed in association with subduction, or experienced deformation related to the subduction-collision events, during their residence at depth in the lithospheric mantle (Smit and Shor, 2017).

Diamonds' presence within an orogenic belt does not necessarily imply high deformation that could result in pink-brown colors. The Ellendale mine is in the King Leopold orogen, a geologic region that experienced mountain building 545 million years ago along the southwest margin of the Kimberley craton in Australia. Although diamonds from this deposit are famous for their fancy colors, they are yellow (not the pink-brown colors typically associated with deformation) and the defects responsible for their yellow color are the very common "cape" absorption series (N3 and N2 defects). Additionally, cathodoluminescence images of the internal growth features in these diamonds are not dominated by deformation lamellae (Smit, 2008). Together, the bodycolor and lack of deformation features suggest that the 1.4 billion-year-old Ellendale diamonds survived in the lithospheric mantle through the Proterozoic orogenic event (until their eruption at 20 Ma) without being significantly deformed, implying that the King Leopold orogenic event was limited to the earth's crust.

Pink Diamonds with $NV^{0/-}$ Centers. *Occurrence.* Although pink diamonds colored by $NV^{0/-}$ centers (i.e., "Golconda pinks") are associated with the ancient diamond mining and trading center of Golconda in India (now Hyderabad), there are no known reliable modern sources in this region. Natural diamonds with sufficient concentrations of $NV^{0/-}$ absorption to contribute to the pink color are extremely rare. The "Golconda pink" diamonds examined in GIA laboratories (0.6% of 1,000 randomly selected "pink" diamonds; see the Absorption Spectroscopy section for further details) do not have any geographic source information.

Formation. The combination of geologic conditions necessary to create and preserve $NV^{0/-}$ centers in natural diamonds is exceedingly uncommon. $NV^{0/-}$ centers form when vacancies in the diamond lattice are trapped next to isolated substitutional nitrogen. Although these defects are rarely preserved in nature, they are relatively easy to create in a laboratory. Three rare conditions are needed to produce natural "Golconda pink" diamonds.

First, these diamonds need low nitrogen concentrations such that when any nitrogen present in the lattice combines with vacancies upon eventual annealing, no infrared-active nitrogen is detected. This would classify the diamond as rare type IIa, which according to a recent survey make up only 1.3% of diamonds submitted to GIA for grading (out of 3.5 million diamonds; Smith et al., 2017).

Secondly, vacancies need to be present in the diamond lattice. Vacancies in the lattice are created either through irradiation or deformation. Radiation exposure is rare in the mantle, and typically only occurs once the diamond is erupted to the earth's surface and has been in contact with crustal rocks or fluids that contain sufficient concentrations of elements such as uranium, thorium, or potassium (Breeding et al., 2018). Since high temperatures above 600°C are needed to combine vacancies with nitrogen, it is more likely that deformation processes in the mantle are responsible for vacancy creation. For example, brown coloration due to vacancy cluster formation often originates from deformation of diamond in the mantle (Fisher et al., 2009).

Thirdly, in order to preserve isolated nitrogen for annealing, and prevent any NV centers from annealing further to form A and B nitrogen centers, the diamonds must not have experienced high temperatures of greater than 900°C for more than a few million years (Smit et al., 2016, 2018).

The exact geological environment in the deep earth where all these conditions are met is not clear. It is possible that some "Golconda pink" diamonds are superdeep, since type IIa diamonds often have a sublithospheric origin (depths >300 km; Smith et al., 2016, 2017), and these superdeep diamonds often exhibit deformation features. For example, brittle fractures along the {110} crystallographic planes as well as polygonized dislocation networks have been observed in deformed superdeep diamonds (Smith et al., 2016, 2017). Deformation processes responsible for these features could be related to mantle convection or deep subduction processes. However, sublithospheric mantle temperatures are in excess of 1400°C, and it is not clear how isolated nitrogen and $NV^{0/-}$ would survive at these temperatures without being annealed to more aggregated nitrogen, which is common in superdeep nitrogen-bearing diamonds.

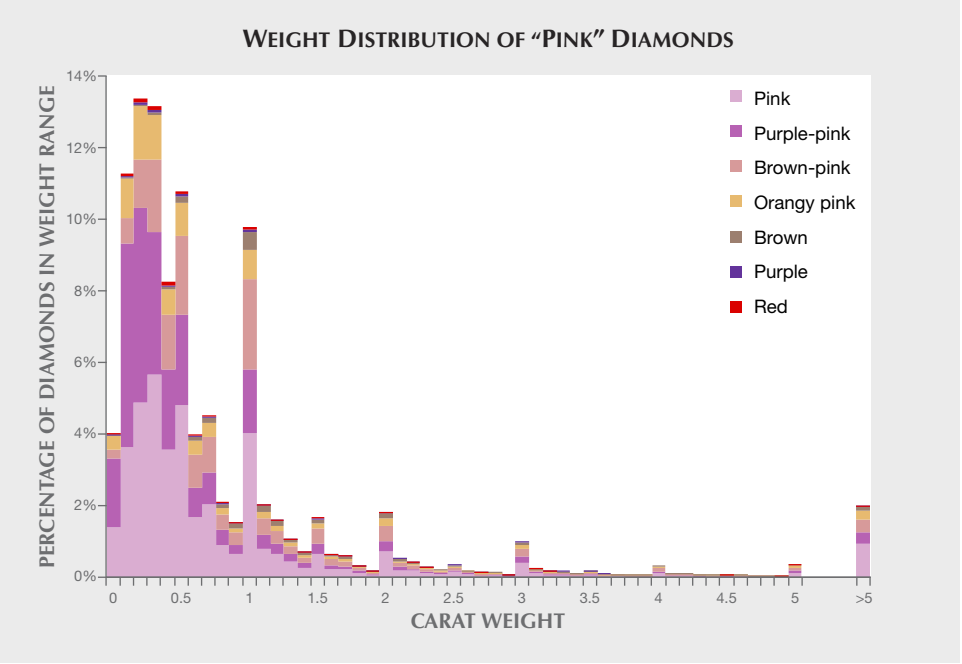

Figure 7. Histogram showing the weight distribution of the 90,000+ diamonds graded by GIA from 2008 to 2016 in the pink, purple, orangy pink, brown, and red color range. The histogram is divided into 0.1 carat increments between 0 and 5 carats. Also shown are the remaining 2% that weighed more than 5 carats.

LABORATORY GRADING

Stones weighing less than 1.0 ct comprised 83% of GIA intake of the 90,000+ natural "pink" diamonds in this study, and more than half (56%) weighed less than 0.5 ct (figure 7). This chart clearly shows that while the total number of "pink" diamonds appears to be quite large—compared to 15,000+ in the blue/gray/violet group (Eaton-Magaña et al., 2018) and 50,000+ in the green group (Breeding et al., 2018)—all colored diamonds submitted to GIA annually represent approximately 3% of overall intake. The vast majority are also quite small. Noticeable spikes in quantity are observed near important carat-weight thresholds (1.0, 1.5, 2.0, 3.0 ct, etc.), and many have a light color (figure 3, right).

This chart also serves to illustrate that while cutters make faceting and polishing decisions to maximize the face-up color and appearance, weight thresholds are often important considerations as well. Diamonds with purplish pink coloration are much more prevalent at weights below 1 carat, while those with brown coloration are much more prevalent above 1 carat (figure 7), likely because it is only worthwhile to submit brown diamonds in larger sizes.

Although colored diamonds are often fashioned as fancy shapes to enhance their face-up color, rounds represent a slight plurality (24%) of the 90,000+ "pink" diamonds (figure 8), followed by pears (20%), rectangles (16%), and cushions (13%) and others. While the fancy shapes are generally evenly distributed across the range of weights and color saturations, the rounds are predominantly seen among the smaller and lighter-color diamonds. Of all fancy-color "pink" rounds, 90% are less than one carat and 42% are Faint, Very Light, or Light.

ABSORPTION SPECTROSCOPY

To investigate the distribution of the major causes of color, we studied the visible absorption and IR ab-

Figure 8. The shape distribution of the 90,000+ "pink" diamonds graded by GIA from 2008 to 2016.

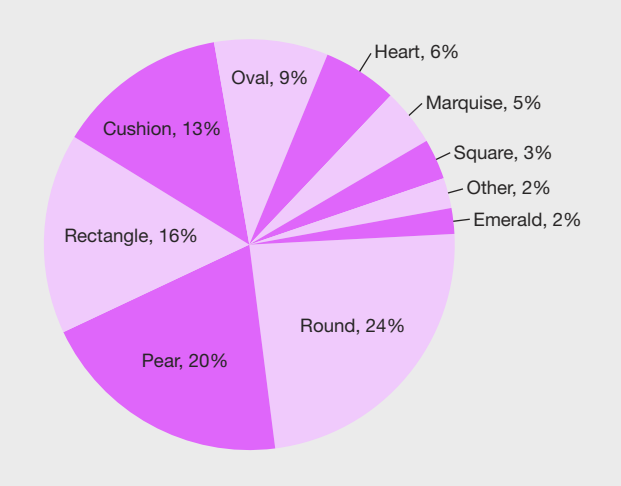

sorption spectra of 1,000 natural brown, pink, purple, and orangy pink diamonds. These were randomly selected as representative of the 90,000+ samples in our internal GIA database. This subset of data was used to generate the charts provided in figures 9–15.

Absorption spectroscopy measurements are nondestructive and indicate the major defects and impurities within a diamond by passing light through the stone and measuring the wavelengths (energies) absorbed by the impurities and defects present. Defects that cause absorption within the visible spectrum (between 400 and 700 nm) contribute to the bodycolor of the diamond. Other defects that are detected only through infrared (IR) absorption spectroscopy do not give information about the color-contributing defects but provide an indication of whether a diamond is natural, synthetic, or treated.

For this 1,000-diamond subset, we observed that 992 (99.2%) contained the 550 nm band. Six were colored by $NV^{0/-}$ defects (0.6%); this percentage indicates the extreme rarity of "Golconda pink" diamonds even among this restricted population of "pink" diamonds. The remaining two of the 1,000 diamonds in this subset were unmodified brown diamonds that did not show an observable 550 nm band, while the other brown diamonds showed a slight 550 nm band that did not cause sufficient absorption to affect the color (figure 4, spectrum D). The majority of this section will focus on the optical and infrared absorption spectra of diamonds colored by the 550 nm absorption band, and the diamonds containing $NV^{0/-}$ defects will be briefly discussed at the end.

Vis-NIR Absorption Spectroscopy of 550 nm "Pink" Diamonds. As the vast majority of these diamonds were principally colored by the 550 nm band, we looked for subtle distinctions between the Vis-NIR absorption spectra to chronicle their differences. As such, the Vis-NIR absorption spectra of most diamonds were distinguished by the presence or absence of the N3 and H3 centers, so we could gauge whether these had any effect on the resulting color grade. Figure 9 shows the effect of these various Vis-NIR absorption spectral features on the resulting hue and tone. Figure 9A indicates that the addition of N3 and H3 does not appear to correlate with the observed hue (that is, the proportion of diamonds with H3 and/or N3 does not significantly change between those with brown-pink, pink, and purple-pink designations). Unmodified purple and red diamonds deviate from this observation and are discussed in box A. Additionally, orange-pink diamonds showed a slightly higher percentage with H3/N3 centers; when these were present, the increased absorption of blue light shifted the perceived color to orange. However, the presence of N3 and H3 centers did have a dramatic effect on the tone of the color (figure 9B). In most cases, those diamonds with faint colors only have a detectable 550 nm band. For the majority of diamonds with a fancy or deeper tone, the 550 nm band is enhanced by the addition of the N3/H3 center (or the presence of both features).

The spectra of 50 "pink" diamonds with the 550 nm band were analyzed to determine the full width at half maximum (FWHM) of the band and the center wavelength, as minor variations in the peak width and position of this band can affect the color. The center wavelength of the absorption band is nominally at ~550 nm, but performing peak fitting using a mixed Gaussian/Lorentzian equation shows that the center wavelength can vary from 545 nm to 565 nm. Meanwhile, the width of the absorption band can vary from 60 nm to 100 nm. Fitting the 550 nm absorption bands from diamonds of various hues showed that the orangy pink to pink diamonds generally had a lower center wavelength (545–550 nm) and a narrower width (60–80 nm) than purple-pink diamonds (555–560 nm and 70–100 nm, respectively); for example, figure 9C compares the Vis-NIR absorption spectra of a purple and pinkish orange diamond. The slight shift of the 550 nm band away from the orange to red portion of the visible spectrum (for orangy pink diamonds) or away from the blue (for purple-pink to purple diamonds) can contribute to the transmission window that leads to the resulting bodycolor. A notable percentage of pink to purple-pink (~20%) also show a series of oscillations overlaid on the 550 nm band at ~600 nm (figure 4, spectra B and C; box B).

Fourier-Transform Infrared (FTIR) Absorption Spectroscopy of 550 nm "Pink" Diamonds. *Nitrogen Aggregation*. Within the 1,000-diamond subset, 992 contained the 550 nm band, as stated above. Of these, 243 (24%) were type IIa based on IR absorption spectra along with the six diamonds colored by $NV^{0/-}$ centers (i.e., "Golconda pinks"), for a total of 249 type IIa diamonds. The remaining 751 diamonds all contained aggregated nitrogen (figure 10A shows a variety of the IR spectra obtained for "pink" diamonds along with the corresponding A and B nitrogen aggregate concentrations, and figures 10B and 10C show the overall distribution of diamond type along with the origin of color and color description).

BOX A: PURPLE AND RED DIAMONDS

Purple Diamonds. Unmodified purple diamonds are among the rarest of all natural diamonds (figure A-1, inset). Due to their extreme rarity, none were randomly chosen for the 1,000-diamond subset. Nevertheless, we summarize here the properties of ~50 submitted purple diamonds. Among these purple diamonds, 69% were less than 1 carat, and 91% were less than 2 carats. Additionally, 42% had a color grade of Vivid or Intense purple.

Pinkish purple to purplish pink diamonds span across almost all diamond types, and about half contain sufficient quantities of H3 and/or N3 in their Vis-NIR absorption spectra to affect the color (figure 9A). In contrast, the vast majority (98%) of the approximately 50 unmodified purple diamonds did not show a significant H3 or N3 peak (figure A-1). In these samples, more blue light is then transmitted, giving rise to the purple tint. Additionally, as shown in figure 9C, the purple-pink to purple diamonds have the center of the ~550 nm band shifted slightly toward longer wavelengths, further increasing the blue light transmission. Additionally, the vast majority (96%) were either type IaA>B or IaA with total nitrogen greater than 150 ppm or showed a saturated type Ia spectrum, consistent with prior reports (Titkov et al., 2008). Among these, the color saturation (Very Light to Vivid) did not appear affected by nitrogen concentration. Instead, the color saturation appeared to be derived more from an increase in absorption of the 550 nm band.

The few samples deviating from the vast majority of purple diamonds were a Fancy purple low-nitrogen type IaA<B sample that had H3 and N3 centers, and a Light purple type IIa diamond. For the set of purple diamonds, 33% showed no fluorescence to long-wave UV, 33% showed blue fluorescence (most were very weak to weak), and 33% showed yellow fluorescence (most were very weak to weak).

Red Diamonds. Unmodified red diamonds are some of the most sought after gems (e.g., figure A-2, inset), and for decades it was uncertain whether any diamond would achieve this color description. To study these diamonds in more detail (as only five unmodified red and six with orange or purple modifiers were randomly selected for the 1,000-diamond subset), we looked at the spectra of 100 Fancy red diamonds colored by the 550 nm band. Unlike most hue groups, red diamonds do not show any distinction in tone—a "light red" diamond would be designated as pink instead. Among these 100 diamonds, 80 were less than 1 carat and all were less than 2 carats.

From examination of the Vis-NIR absorption spectra, *all* showed very similar spectra in that they were colored by the 550 nm band in combination with the H3 center and its sideband (figure A-2).

Almost all of the Fancy red diamonds were type IaA<B (96), with the balance including a saturated type Ia, IaA, IaA>B, and IaB. Of the type IaA<B diamonds, most had low to moderate amounts of nitrogen (20–100 ppm total nitrogen), with a few showing very low (<10 ppm) or comparatively high amounts of nitrogen (>150 ppm).

For these 100 Fancy red diamonds, all showed fluorescence to long-wave UV and most (95) showed blue fluorescence; the majority showed weak (30) or medium (53) intensity. Of these 100, the remaining five showed yellow fluorescence (weak to medium).

As the vast majority of Fancy red diamonds are type IaA<B, a diamond type principally sourced from the Argyle mine in Australia (e.g., Howell et al., 2015), this rare color will likely become even more so with the planned closing of the mine in a few years.

Figure A-1. These three Vis-NIR absorption spectra are from a 0.67 ct Light purple, a 0.83 ct Fancy purple, and a 0.81 ct Fancy Vivid purple. The diamond shown in the inset was identified as type IaA with 250 ppm of nitrogen (Darley et al., 2011).

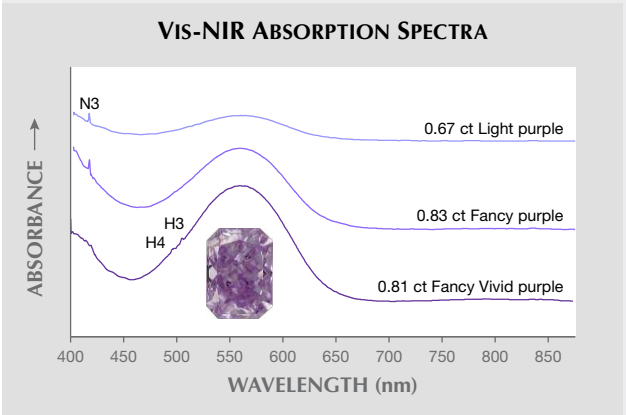

Figure A-2. The Vis-NIR absorption spectra are from three Fancy red diamonds (from top: 1.01 ct, 0.48 ct, and 0.67 ct) that show similar features.

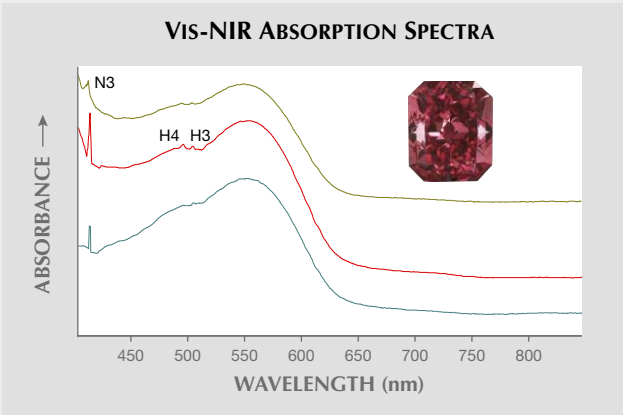

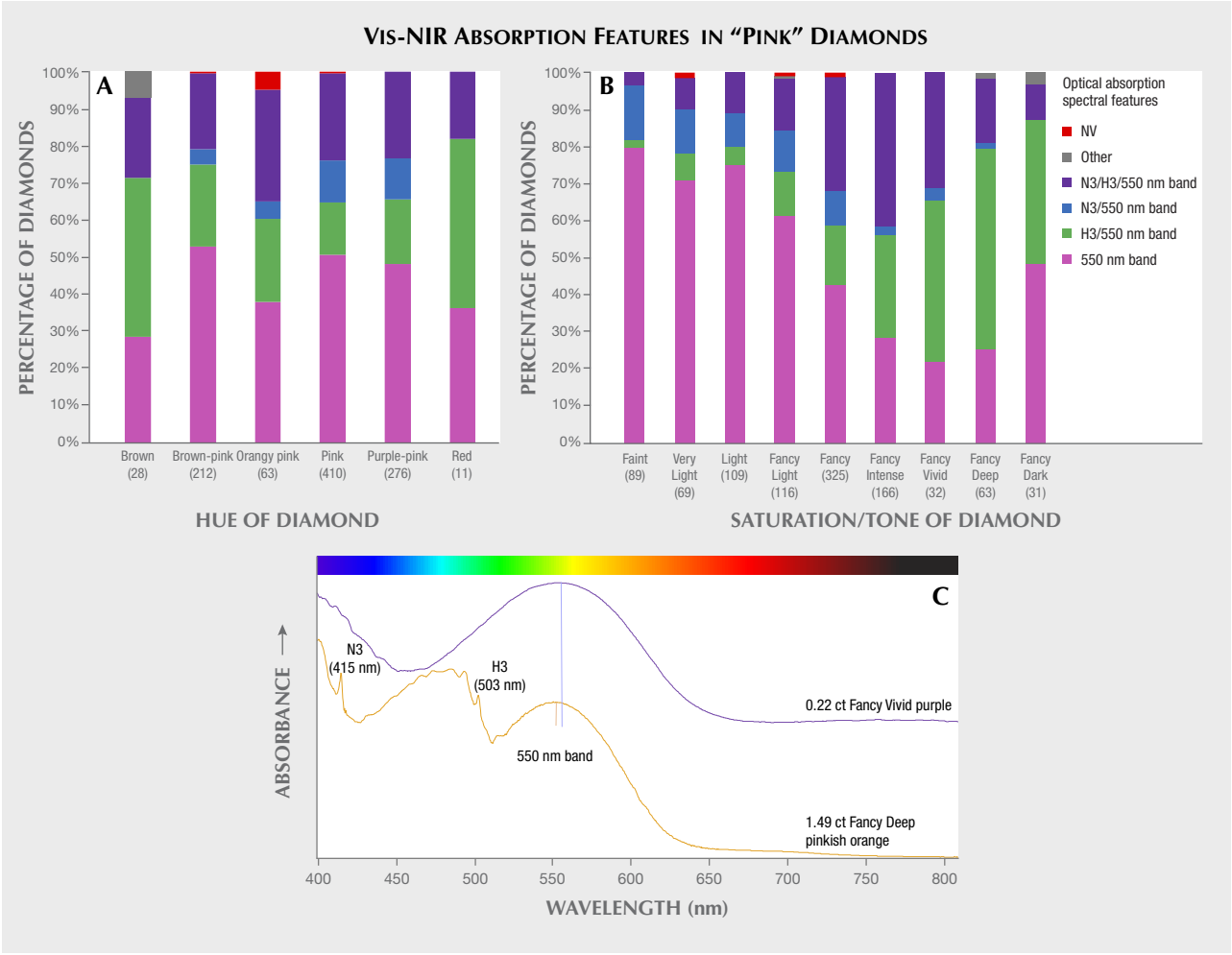

Figure 9. Natural "pink" diamonds submitted to GIA over the last decade are predominantly colored by the 550 nm band. A: When a subset of 1,000 diamonds are analyzed by hue, they show minor differences in the presence/absence of H3/N3 centers, indicating that intensity differences in peak characteristics, and not the presence/absence of these features, generally create the differences in hue. B: The addition of the N3 and/or H3 centers leads to an increase in overall absorption, creating more saturated colors. C: A comparison of the Vis-NIR absorption spectra between a 0.22 ct Fancy Vivid purple and a 1.49 ct Fancy Deep pinkish orange diamond. While both have a ~550 nm absorption band, differences in this band and the presence of other centers lead to vastly different colors. The pinkish orange diamond shows pronounced H3 and N3 centers that are lacking in the purple diamond. For the pinkish orange diamond, the 550 nm band is centered at 548 nm with a width of 62 nm. For the purple diamond, the center is located at 556 nm and the peak width is much wider, 105 nm. The vertical line indicates the center point for each of these bands.

Those 170 termed as type Ia (17%) had saturated nitrogen concentrations in their IR absorption spectra, and the specific A and B nitrogen aggregates were too great to be resolved with our instrumentation and thus could not be calculated. The remaining 581 diamonds had sufficiently low nitrogen to determine the aggregate concentrations (Boyd et al., 1994, 1995). Of those, 396 were type IaA<B (40%) followed by 125 type IaA>B (13%), 31 pure type IaA (3%), and 29 pure type IaB (3%).

Figure 10B shows that the type IIa "pink" diamonds were overwhelmingly colored by the 550 nm band alone and generally did not include the additional H3 and N3 centers. This is not surprising, as type IIa diamonds do not have sufficient nitrogen concentration to generate nitrogen-related defects that could be detected by visible absorption and affect the color.

Among the diamonds with nitrogen aggregates, many were colored by H3 and/or N3 that appeared

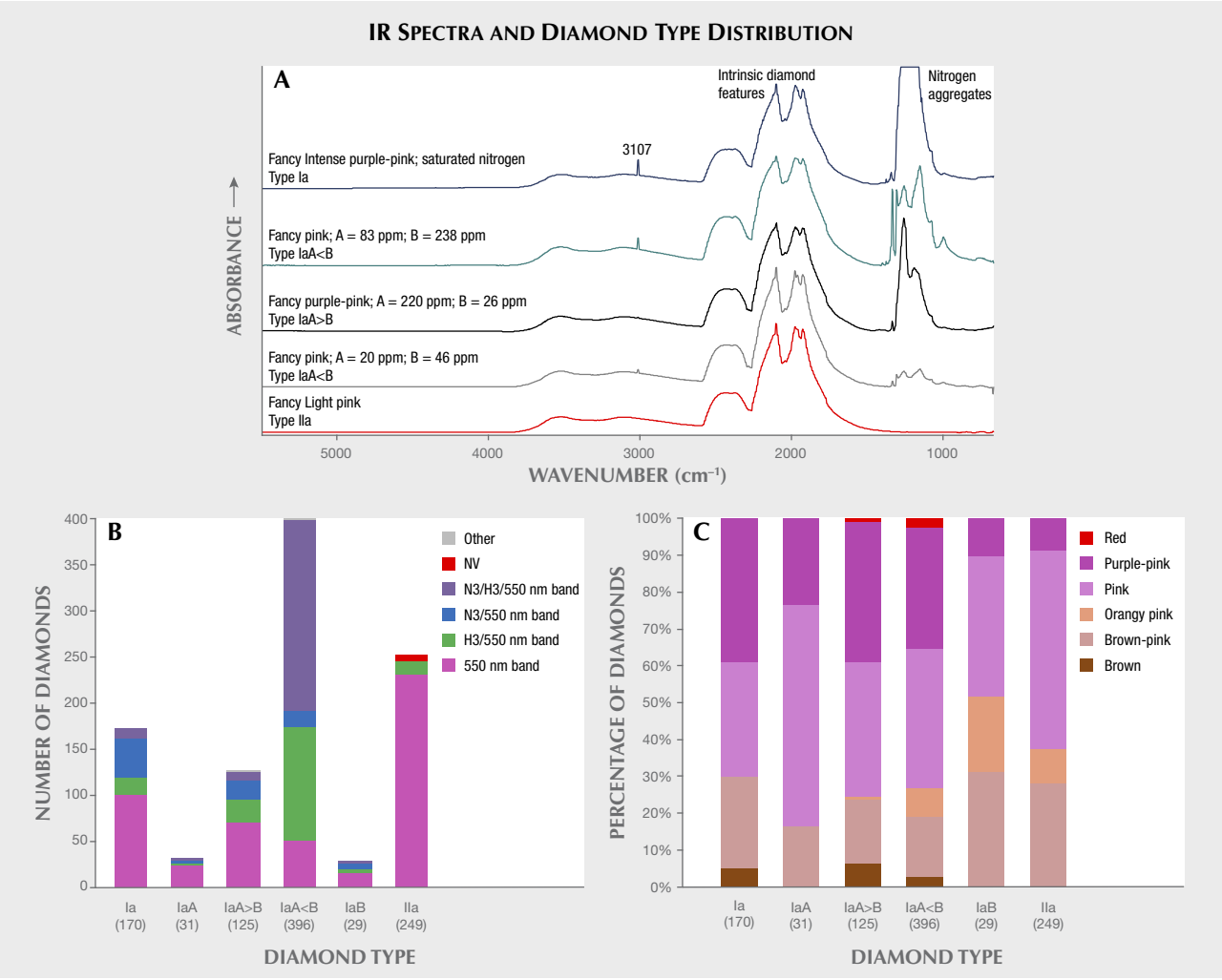

Figure 10. A: Five representative IR spectra of "pink" diamonds show the variety of possible nitrogen concentrations and ratios of A/B aggregates. B: The distribution of diamond type for these 1,000 "pink" diamonds is distinguished by features in their Vis-NIR absorption spectra. Type IIa and type IaA diamonds are almost always colored by the 550 nm band only. As more B centers develop, the percentage of diamonds with a contribution from H3 and/or N3 increases. Diamonds designated as type Ia have IR spectra with a saturated nitrogen region and very high nitrogen concentration; the A/B ratio of aggregates cannot be reliably determined in those cases. C: The distribution of the diamond type for these 1,000 "pink" diamonds and the color description.

to impact the color saturation more than the hue, as indicated by comparing figure 9A and 9B. Among type IaA diamonds, very few showed either H3 or N3 centers. In contrast, a majority of type IaA<B diamonds had both the N3 and the H3 in addition to the 550 nm band.

The observation that diamonds with higher amounts of B-aggregates also showed a higher incidence of H3 and N3 centers is not surprising given the evolution of these various defects within diamond. A very young diamond will show only isolated nitrogen. As time progresses, these nitrogen atoms combine to create more and more complex defects. The A-aggregates are composed of two nitrogen atoms; the H3 defect contains two nitrogen atoms plus a vacancy; the N3 defect includes three nitrogen atoms with a vacancy; and the B-aggregate includes four nitrogen atoms plus a vacancy. As the A-aggregate/B-aggregate ratio shifts toward higher amounts of B, other defects (such as H3 and N3) will be produced as well (Dobrinets et al., 2013).

Concentrations of A and B Nitrogen Aggregates. The ratio between A and B nitrogen aggregates can be used to assess the time and/or temperature of a diamond's residence deep within the earth (Leahy and

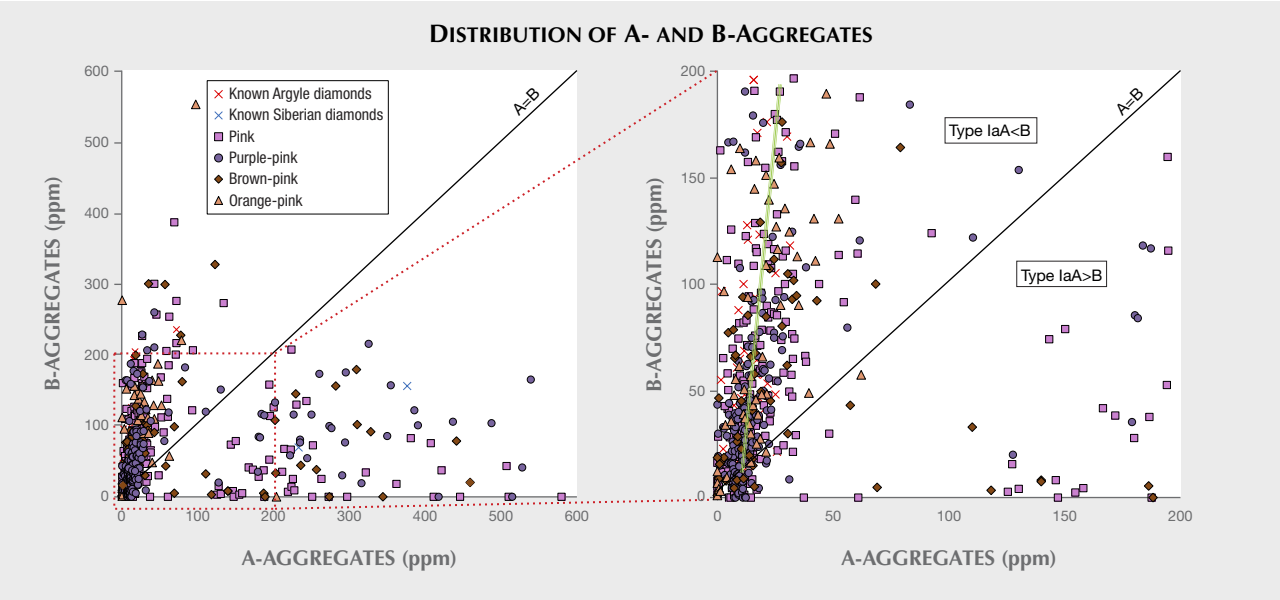

Figure 11. The A and B nitrogen aggregates for 581 type IaAB diamonds are plotted against each other along with A/B concentrations for 62 known Argyle diamonds and a pair of known Siberian diamonds (most IR spectra of the known Siberian samples had saturated spectra, thus reducing number of plottable datapoints). Also shown is a diagonal line designating where A- and B-aggregates are equal and a green slope line in the inset showing where the vast majority of data are clustered.

Taylor, 1997). Even if the total nitrogen concentration is different between diamonds, the transition from A-aggregates to B-aggregates increases at higher temperatures and longer timescales. If a population of diamonds has similar A-to-B ratios, they likely resided under similar time and temperature conditions, increasing the likelihood that they originated from the same source.

As mentioned previously, 581 of the "pink" diamonds from the 1,000-diamond subset had IR spectra from which the concentrations of A- and B-aggregates could be calculated (in atomic parts per million, or ppma; figure 11). These were calculated individually by baseline correcting each spectrum, and then calculating A- and B-aggregates using a spreadsheet provided by Dr. David Fisher (DTC Research Center, Maidenhead, UK) using absorption coefficients from Boyd et al. (1994, 1995). The majority of the 581 diamonds contained more aggregated nitrogen as B centers (type IaA<B; figure 11).

In the inset of figure 11, most of the datapoints are clustered near the green guide line (i.e., the calculated best-fit line for type IaA<B diamonds), indicating that A/B concentrations generally lie along that slope. Although the total nitrogen concentrations vary from a few ppm to a few hundred ppm, the conversion of A-aggregates to B-aggregates is roughly consistent for all values near the green slope line. This consistency strongly suggests that all of these diamonds experienced similar time/temperature conditions within the earth and potentially from the same mine. The sheer quantity of diamonds plotted here (compared with those scattered among the rest of the graph) imply that they come from the most abundant source—the Argyle mine—although they could also be from Namibia or Venezuela. Also plotted are the data of 67 diamonds, unrelated to this study, that are known to be sourced from the Argyle mine (unpublished GIA data, 2007). In contrast, pink to purple diamonds sourced from Siberia are predominantly type IaA>B, and two known Siberian samples with unsaturated IR spectra (Titkov et al., 2008) are also shown alongside the data from this study. This geographical distinction based on nitrogen aggregation has been documented before (Gaillou et al., 2010; Howell et al., 2015), and a good hypothesis of origin is possible, though not with any reliable certainty, as "pink" diamonds originate from very few sources.

Although this plot cannot include type IIa or saturated type Ia diamonds, it is consistent with prior reports (e.g., Howell et al., 2015) that "pink" diamonds clustered around the green slope line are mainly sourced from the Argyle mine, and these encompass a significant percentage of "pink" diamonds submitted to GIA. If we assume that the type IaB and IaA<B diamonds are generally from the Argyle mine

Box B: PL Features of Pink Type IIa to Type IaAB Diamonds

Photoluminescence Band Associated with 550 nm Absorption Band. As part of our identification procedure for pink diamonds, GIA routinely collects their PL spectra (e.g., using 514 nm excitation). One interesting and consistent feature in the PL spectra of these pink diamonds is a wide emission band extending from ~600 to 750 nm, with a series of smaller oscillations overlaid on the larger emission band (e.g., the black trace in figure B-1). This emission band is consistently seen in diamonds colored by the 550 nm absorption band; the absorption band often, but not always, shows similar oscillations at ~600 nm (e.g., the red trace in figure B-1; see also figure 4, B and C). The oscillations in the 550 nm absorption band are most often detected in saturated pink to purple-pink diamonds. While this feature is only rarely detected in light pink diamonds with a weak 550 nm absorption band, the 600–750 emission band may still be detected in their PL spectra. Although this emission band appears qualitatively similar to the PL band associated with the 480 nm band (figure 21C), the two are dissimilar in overall band width and the spacing between the oscillations.

Additional interesting observations about this 600–750 emission band include:

1. The spacing of the oscillations between the 550 nm absorption band and the emission band show a pronounced similarity.
2. After exposure to the high-energy UV of the DiamondView, the intensity of the emission band decreases and shows a bleaching behavior similar to that of the 550 nm absorption band. When the pink diamond returns to its stable color, so does the intensity of the emission band.
3. In diamonds with pink and brown graining, the intensity of the emission band is lower in the brown graining than in the pink graining.
4. This emission band is absent from diamonds that do not show a 550 nm absorption band.
5. This emission band is similar to one previously documented by Gaillou et al. (2010), appearing only within photoluminescence spectra obtained from pink lamellae and absent from colorless portions.

Photoluminescence Maps of Type IIa and Type IaAB Diamonds. We wished to study this emission band in more detail, and therefore 455 and 532 nm photoluminescence maps were analyzed to examine several features in pink diamonds. These included H3, H4, the 600–750 nm emission band, and several other common features seen in PL spectra (e.g., figure 14). These results will be discussed in an upcoming paper.

Gaillou et al. (2010) performed PL spectra line scans across a series of flat plates containing pink lamellae. In addition to finding this 600–750 nm emission band

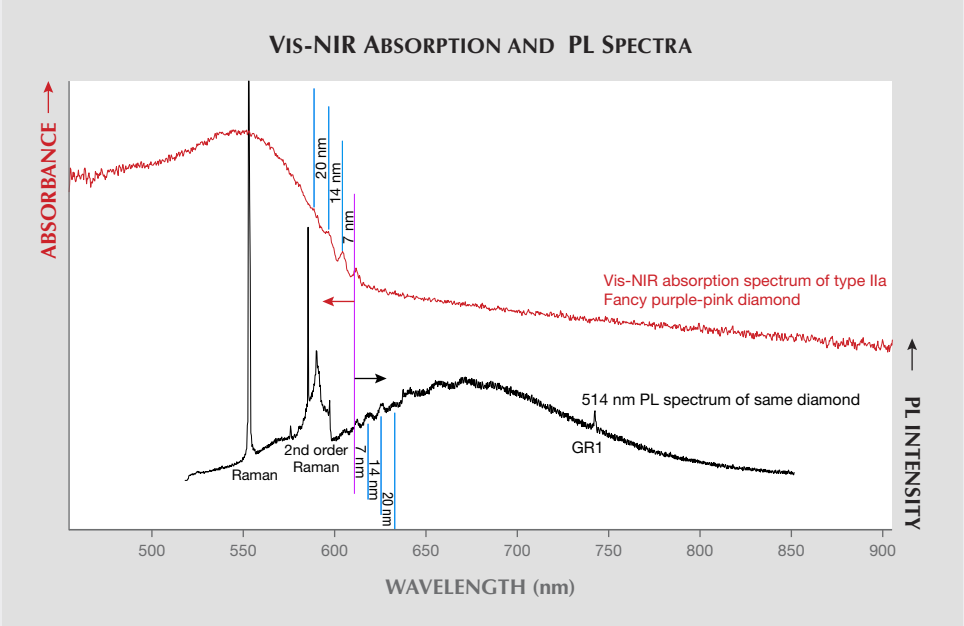

Figure B-1. The Vis-NIR absorption spectrum (red trace) for a purple-pink diamond is shown along with its 514 nm PL spectrum (black trace). Both spectra were collected at liquid nitrogen temperature and show an interesting symmetry in the oscillations observed within the 550 nm absorption band and the emission band.

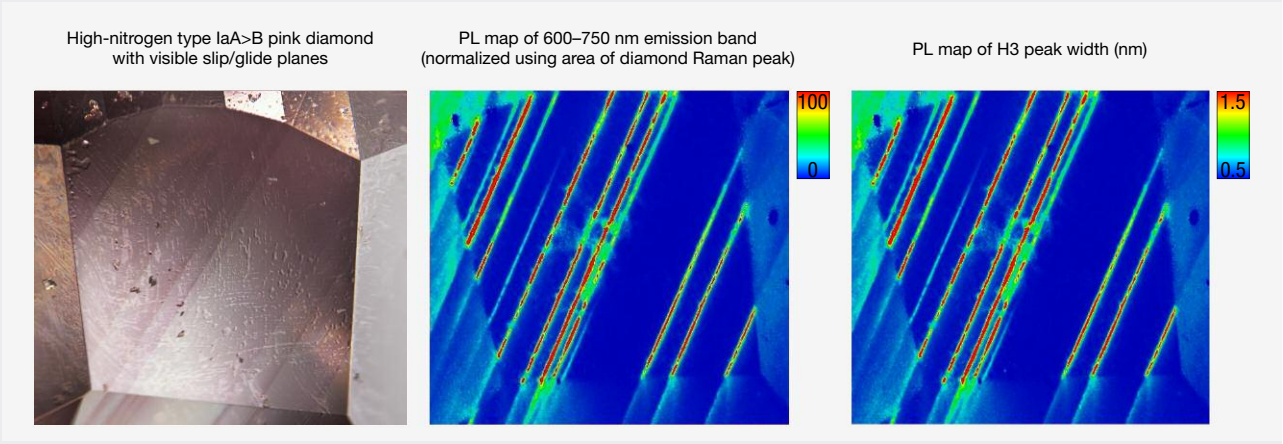

Figure B-2. Photoluminescence maps of the 600–750 nm emission band and H3 peak width show excellent agreement with the visual observation of pink color along deformation lamellae in this type IaA>B pink diamond. The intensity bars show the range of values.

solely within the pink lamellae, they observed that the Raman width noticeably increased as well. They were unable to produce the PL maps that are possible with today's technology, and they did not have type IIa pink diamonds available for comparison.

As PL is a very sensitive method capable of collecting information on defects at the parts-per-billion (ppb) level, it can detect subtle variations in diamond far better than the eye can distinguish pink color. Additionally, we are unable to perform visible absorption spatial mapping on these pink diamonds, so we cannot map the distribution of the 550 nm band in pink diamonds. We can collect PL spectral maps at liquid nitrogen temperature, however. Based on the observations of this 600–750 nm emission band, it is monitored as a proxy of the 550 nm absorption band.

Here we performed PL mapping on type IIa and type IaAB diamonds. In type IaAB pink diamonds, these data will show the spectral differences between the colored lamellae (either as graining or slip/glide planes), and also demonstrate that the PL spectra of type IIa diamonds are as spatially uniform as their pink color. We paid particular attention to low-nitrogen type Ia diamonds to examine the progression from the homogeneity of type IIa diamonds to the color segregations seen in type Ia diamonds.

For moderate-nitrogen type IaA<B diamonds (i.e., Group 1 pink diamonds; Gaillou et al., 2010), the distribution of the 600–750 nm emission band is consistent with its color distribution, with wavy-appearing concentrations of color that are slightly more saturated than the surrounding diamond. For higher-nitrogen type IaA>B diamonds (i.e., Group 2 pink diamonds) that have pronounced slip/glide planes, there is a distinct change in spectral properties within the pink slip/glide planes (figure B-2); these changes include a pronounced increased in the 600–750 nm emission band, along with other features such as H3 peak width. In contrast, the PL mapping of type IIa diamonds showed that the spatial distribution of the 600–750 nm emission is nearly uniformly distributed, as is the distribution of the pink color.

Low-nitrogen "pink" diamonds generally show a mixture of spectral features, with some exhibiting a combination of traits seen in the uniform color distribution of type IIa pinks, the irregular graining seen in type IaA<B pink diamonds (i.e., Group 1 diamonds; Gaillou et al., 2012), and the sharply defined, distinct, and parallel lamellae seen in type IaA>B (i.e., Group 2). Diamonds with low nitrogen concentrations generally show a combination of features seen in type IIa and Group 1 diamonds such as a uniform pink color distribution, though there are some instances of visible pink graining or a uniform distribution of the 600–750 nm emission band, as well as wavy graining when plotting the H3 peak width.

and the other types, including the saturated type Ia diamonds, are sourced from other mines, then 425 of the 992 diamonds with the 550 nm band, a total of at least 43%, originated from Argyle.

The nitrogen aggregation results for these diamonds, shown in figure 11, are also split according to the color description of the "pink" diamond. This indicates several interesting trends. Among the type IaA<B diamonds (i.e., the left side of the diagonal in figure 11), most purple-pink to pink-purple samples are congregated in the portion that indicates low nitrogen. Also, the orangy pink diamonds are almost exclusively contained among the type IaA<B population, while a single orangy pink type IaA sample is represented elsewhere on the plot (see also figure 10C).

Among type IaA>B diamonds (i.e., the right side of the diagonal in figure 11), the nitrogen concentrations are higher, with many showing A-aggregate concentrations of 300 ppm or more. Also, many of the unmodified pink diamonds are nearly pure type IaA, while the purple-pink diamonds have a greater concentration of B-aggregates, consistent with previous reports by Titkov et al. (2008).

Effect of Total Nitrogen Concentration. To visualize the effect that nitrogen concentration had on color hue, tone, and spectral features (figure 12), we grouped the A<B and A>B data of all 581 "pink" diamonds shown in figure 11 by the total aggregate concentration into five different ranges. The concentration range of each group was determined in order to create roughly equal groups.

With increasing nitrogen, we generally saw a decrease in purple-pink to pink-purple diamonds (figure 12A); this is likely due to a greater absorption of the H3 and N3 centers that reduced transmission of blue light. Additionally, among type IaA<B with increased nitrogen there was a greater proportion of unmodified brown diamonds. The other hues showed fluctuations with increasing nitrogen, but no clear trends. Again, orangy pink diamonds are essentially seen only among diamonds with A<B aggregates.

Across the range of total nitrogen, type IaA<B diamonds show more saturated colors (figure 12B) than type IaA>B that appears due to the higher incidence of the N3 and H3 centers (figure 12C and consistent with figure 9). For the highest range shown in figure 12C (>250 ppm total nitrogen), more than 80% of the type IaA<B diamonds show one or both of these centers. The additional absorption of the N3/H3 centers increases the overall absorption in these diamonds, leading to more saturated colors.

Other IR Features. Of the 1,000-diamond subset, half were randomly selected and surveyed for the presence in their spectra of the N_3VH defect (3107 cm^{-1} center), the platelet feature, and "amber" centers.

The 3107 cm^{-1} peak was designated for many years as a "hydrogen-related defect," and only recently was it ascribed to N_3VH by Goss et al. (2014). N_3VH was frequently observed in our sample suite, occurring in 74% of the "pink" diamonds surveyed. Of the diamonds without N_3VH visible in the infrared spectrum, 87% were type IIa. The saturated type Ia group contained 80% of the diamonds that were rated as having a strong 3107 cm^{-1} peak. The type IaA>B and IaA<B groups showed no significant difference in occurrence of the N_3VH defect or in the strength distribution.

The platelet feature is comprised of extended defects involving carbon interstitials (i.e., clusters of carbon atoms not in normal positions in the lattice) and nitrogen in thin layers thought to form as A-aggregates transition into B-aggregates (Humble, 1982; Speich et al., 2017). The position of the peak can vary from 1358 to 1380 cm^{-1} depending on the diameter of the platelet, where the lower wavenumber value corresponds to a higher platelet diameter (Speich et al., 2017). None of the type IIa and IaB stones in our dataset had a platelet peak present in the IR spectrum, which is to be expected due to their lack of A centers (Humble, 1982). The IaA, IaA>B, IaA<B, and Ia groups all showed a platelet peak occurrence more than 50% of the time, with the Ia group having an occurrence of 96%. The strength of the platelet peak correlated best with the concentration of B-aggregated nitrogen, consistent with previous studies (Woods, 1986; Speich et al., 2017). The type Ia diamonds had the highest average peak position (and therefore the smallest average platelet diameter) at 1369 cm^{-1}, and the IaA<B group had the lowest average peak position (and therefore the largest average platelet diameter) at 1362 cm^{-1}.

The "amber" centers are a series of broad bands related to diamonds with brown coloration and/or colored graining, occurring between 4000 to 4400 cm^{-1}. It has been suggested that the "amber" centers are defective A-aggregates formed along plastic deformation planes (Massi et al., 2005). Two specific bands were surveyed for this study: the "amber" centers at 4065 and 4165 cm^{-1}. The 4065 cm^{-1} "amber" center has been observed to be stable up to 1700°C,

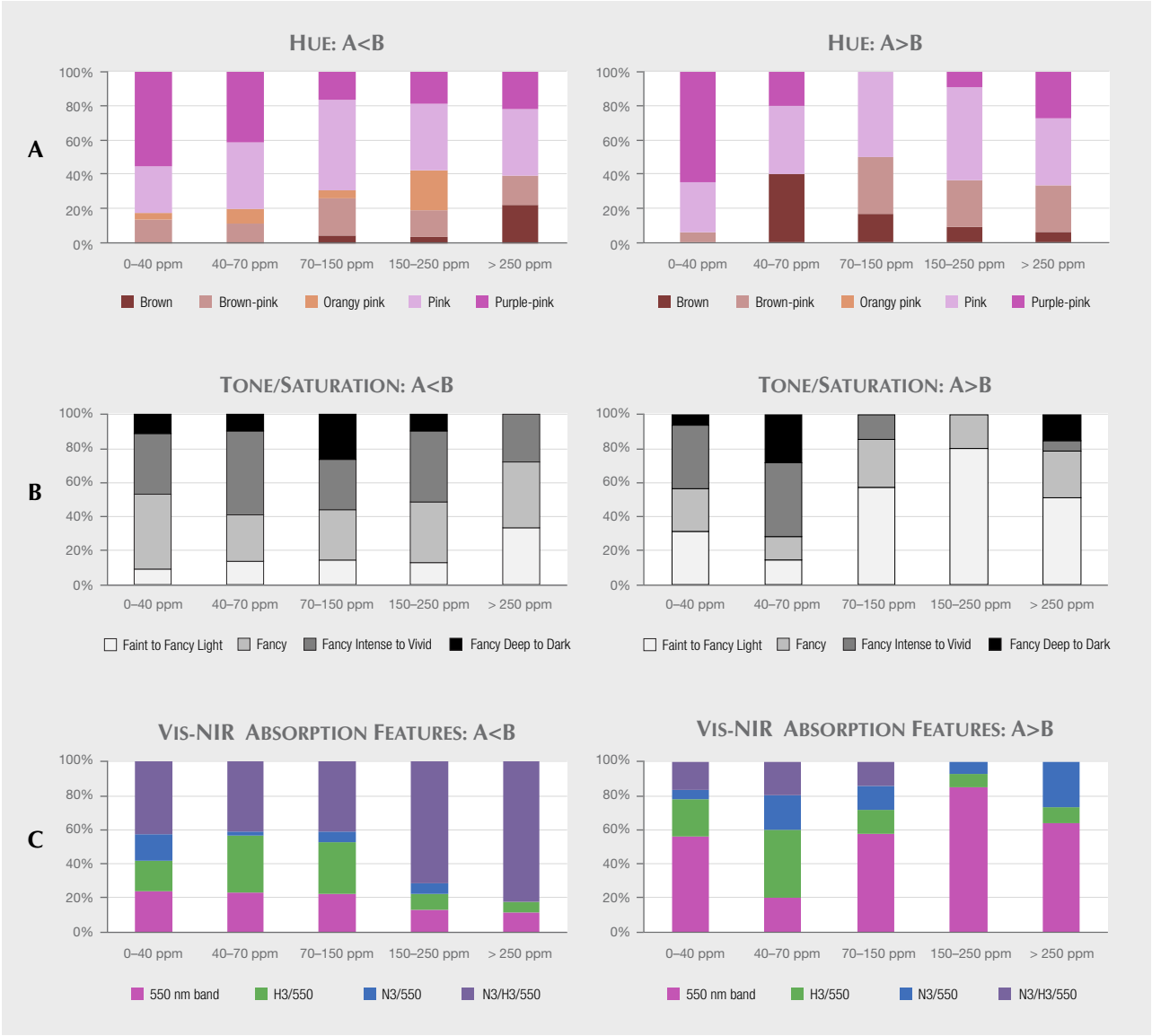

Figure 12. Type IaAB diamonds were split into two groups, IaA<B and IaA>B, and sorted based on total nitrogen concentration. A: The effect of total nitrogen concentration on hue. B: The effect of increasing nitrogen on the tone of the diamond. C: The effect of total nitrogen concentration on features present in Vis-NIR absorption spectra.

while the 4165 cm^{-1} "amber" center can survive heating until 1900°C (Eaton-Magaña et al., 2017). As these two features are stable to different temperatures, they are likely different centers. Previous reports have shown that the 4065 cm^{-1} "amber" center is more prevalent in diamonds of type IaA>B (Gaillou et al., 2010).

The IR spectra were categorized as having neither peak, one of these peaks, or both (figure 13). None of the type IaB stones and very few (14%) of the type IIa diamonds showed either the 4065 or the 4165 cm^{-1} peak, consistent with the model of the "amber" center being a defective A center (Massi et al., 2005). As the concentration of A-aggregates increased, the likelihood of one or both "amber" peaks increased as well; the type Ia diamonds showed a high percentage of "amber" centers, likely corresponding to the high concentration of A-aggregates within them (although the saturated spectra do not allow us to accurately make that determination).

Diamonds Colored by $NV^{0/-}$ Centers. Only six of the 1,000-diamond subset were colored by $NV^{0/-}$ centers, thus rendering a very small sample size and provide

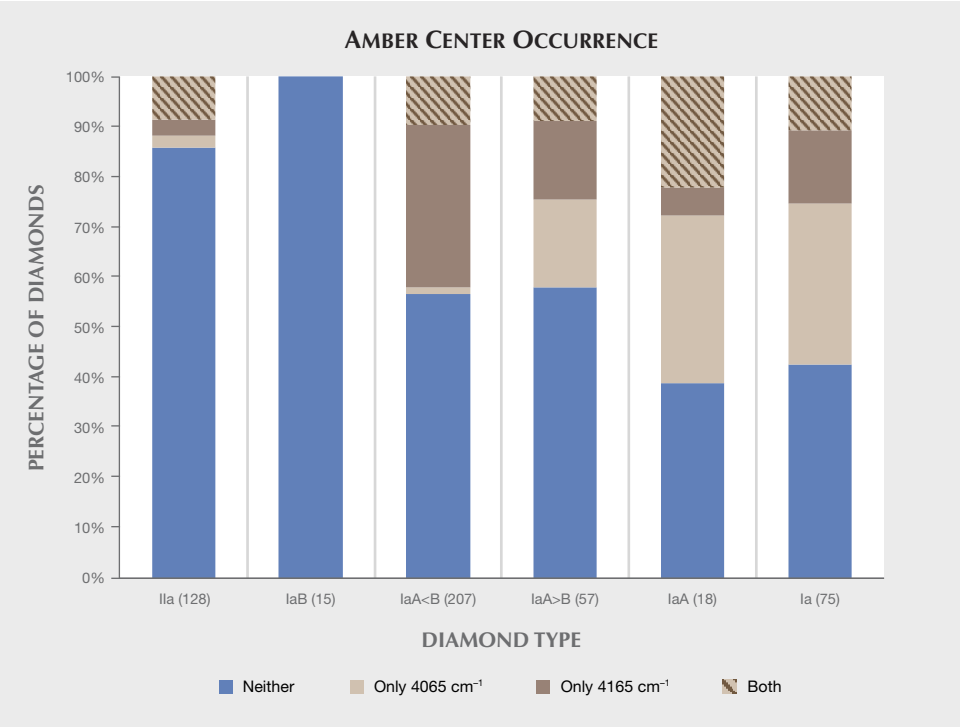

Figure 13. IR absorption peaks related to "amber" centers are plotted based on diamond type. The number of samples tested within each diamond type is shown in parentheses.

little more to illuminate beyond what has already been discussed in the Causes of Color section. As expected, all six showed type IIa IR absorption spectra that were featureless except for intrinsic diamond features. In the Vis-NIR absorption spectra, the six diamonds (three orangy pink, two pink, and one brownish pink) had $NV^{0/-}$ centers at 575 and 637 nm along with their accompanying sidebands, with the most prominent of those centered at ~520 and 620 nm (figure 4, spectrum E). Of these, four had detectable GR1 peaks and four showed the 595 nm center commonly seen in irradiated diamonds (Breeding et al., 2018). The presence or absence of these radiation-related peaks did not correspond with the graded color.

PHOTOLUMINESCENCE SPECTROSCOPY

Photoluminescence (PL) uses lasers of different wavelengths to produce emission spectra that reveal the optical defects present in a diamond. PL analysis is one of the most useful and sensitive techniques for defect characterization. Using PL spectroscopy, defects occurring at parts per billion (ppb) concentrations (and therefore not necessarily contributing to the diamond's bodycolor) can easily be detected (Eaton-Magaña and Breeding, 2016).

Diamonds Containing the 550 nm Absorption Band. The PL spectra of diamonds colored by the 550 nm absorption band often show features that either contain vacancies or correlate with plastic deformation. For example, the 566 nm triplet is seen in pink to brown diamonds of both type Ia and IIa (i.e., those with and without colored graining; GIA unpublished data).

Common vacancy-related peaks include the H3 (NVN^0 at 503.2 nm), H4 (NVN^- at 496 nm), GR1 (V^0 at 741.2 nm), and NV centers (NV^0 at 575 nm, NV^- at 637 nm; figure 14). The $NV^{0/-}$ centers are often present in diamonds containing the 550 nm band but not in sufficient concentrations to be detected in the Vis-NIR absorption spectra, and therefore they do not affect the color. Peaks at 657, 661, and 668 nm are often seen together in type IIa, IaA<B, and IaB "pink" diamonds; however, the defect structure of these peaks has not been identified. Box B further discusses the photoluminescence features within the graining and slip/glide planes that are observed in type IaAB diamonds.

The peak width of the diamond Raman line is affected by the local strain environment, and an increase in crystallographic strain leads to a broadening of the peak width (Grimsditch et al., 1978). The diamond Raman line has been shown to increase in width on pink grain lines in type Ia diamonds, demonstrating that the pink lamellae lie in planes of plastic deformation (Gaillou et al., 2010).

In contrast, type IIa "pink" diamonds rarely show colored lamellae and instead are evenly colored. In

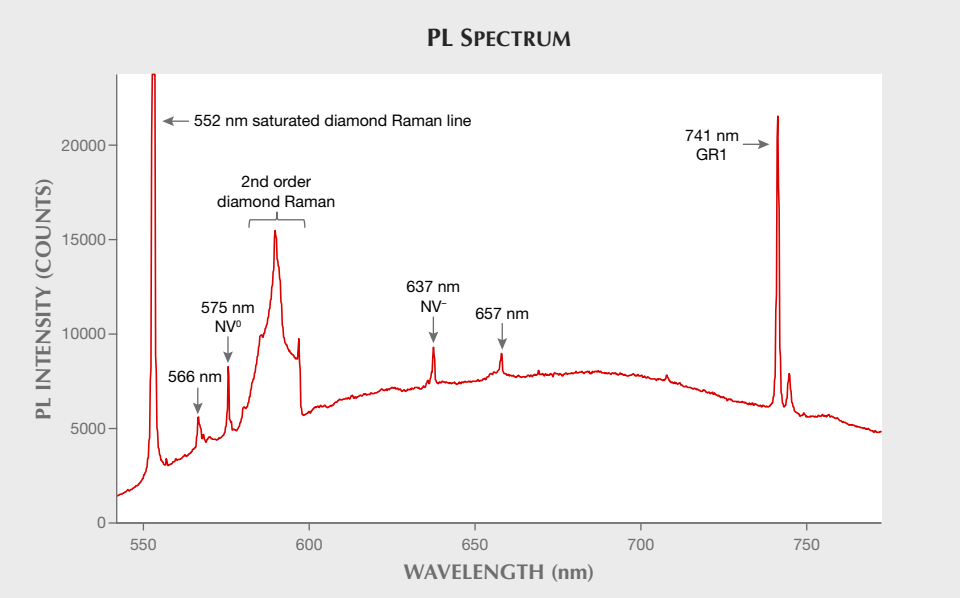

Figure 14. A typical 514 nm photoluminescence spectrum from a 550 band pink type IIa diamond. The 566 nm triplet, $NV^{0/-}$ centers, 657 nm peak, and GR1 are all shown. The diamond Raman line at 552 nm is saturated.

type IIa diamonds showing a uniform pink coloration, this relationship of strain versus pink color is not so easily visualized. Therefore, we plotted the GR1 width (i.e., increasing strain) of 239 type IIa "pink" diamonds from the 1,000-diamond subset against pink color intensity (figure 15). This plot shows that in type IIa diamonds, an increase in strain (represented by the peak width of the GR1 center) corresponds to an increase in pink color saturation in type IIa diamonds, despite the lack of easily distinguishable strained regions.

Figure 15. Among type IIa "pink" diamonds, the color is generally uniform rather than concentrated within graining. We see that among type IIa "pinks," an increase in GR1 full width at half maximum (functioning as a proxy for the strain measurement) corresponds with more saturated pink color. The individual points are shown along with the average values.

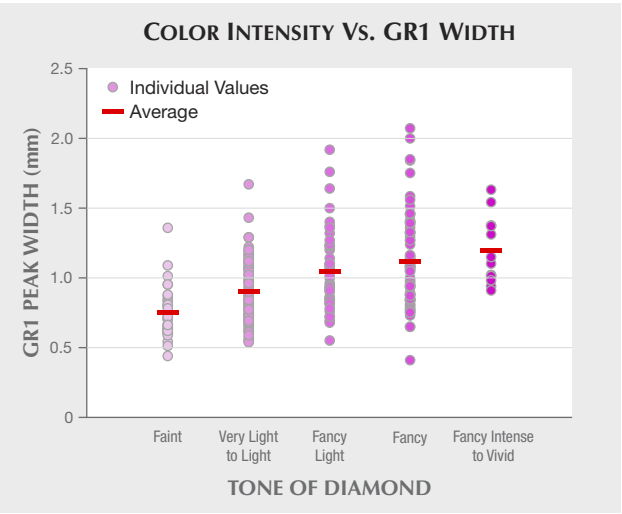

Diamonds Colored by $NV^{0/-}$ Centers. Diamonds colored by $NV^{0/-}$ centers (i.e., those with $NV^{0/-}$ centers in sufficient concentrations to be detected by Vis-NIR absorption spectroscopy) will have high-intensity $NV^{0/-}$ peaks in their PL spectra (figure 16). Due to this high intensity of the $NV^{0/-}$ centers and their associated vibronic structures, it can be difficult to detect other peaks that may be present at lower PL intensities. A peak at 561 nm is commonly seen, but

Figure 16. A typical 514 nm photoluminescence spectrum from a "Golconda pink" diamond. The $NV^{0/-}$ centers (and their vibronic structure/sidebands) and the diamond Raman line (R) are the only features detected.

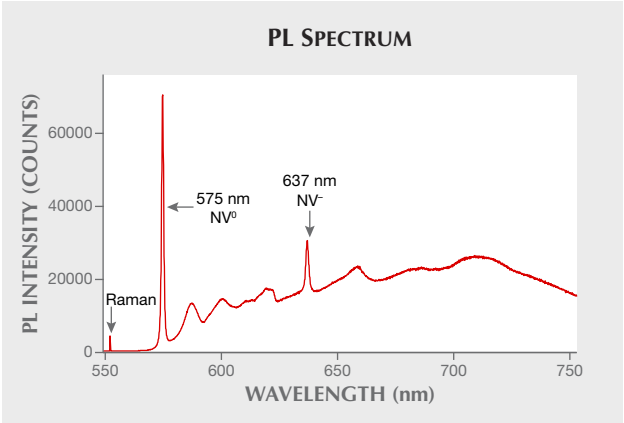

the structure of this defect is still unknown. Common vacancy-related defects seen in diamonds with $NV^{0/-}$ centers include H3 (NVN^0), H4 (4N-2V), and GR1 (V^0).

GEMOLOGICAL OBSERVATIONS

Physical Characteristics. Pink and brown color is often associated with plastic deformation lamellae ("graining" or "slip/glide planes"). These are often observed as visible lines on the polished surface of the diamond, known as surface graining, which result from differential polishing rates along the deformation lamellae relative to the surrounding diamond. This leaves visible lines on the surface; unlike polishing features, these can cross multiple facets (figure 18, right).

The graining usually has a hue similar to the diamond's bodycolor, though in some cases diamond can exhibit both pink and brown graining (figure 17A). Additionally, graining and slip/glide planes can appear more pronounced when the diamond is put between crossed polarizers to show the strain (i.e., anomalous birefringence; figure 17B). The disruption in the strain pattern apparent at a slip/glide plane provides further evidence that these planes are a disruption of the diamond lattice (figure 17C).

Trigons can be etched where deformation lamellae intersect the surface of a rough diamond (figure 18, left). Where two of these deformation lamellae intersect, it is common to see an etch channel or thin needle-like structure (Wang et al., 2006). Diamonds are etched by fluids during their mantle residency or during kimberlite ascent (Fedortchouk et al., 2005; Fedortchouk and Zhang, 2011), and these fluids first exploit preexisting weaknesses in a diamond. Hollow channels known as Rose channels can also occur along intersecting twin lamellae (Schoor et al., 2016; figure 18, right). First described by Gustav Rose in 1868, these are formed by the intersection of twin lamellae, where the twinning action can result in a straight, hollow channel with a prismatic opening (Rose, 1868).

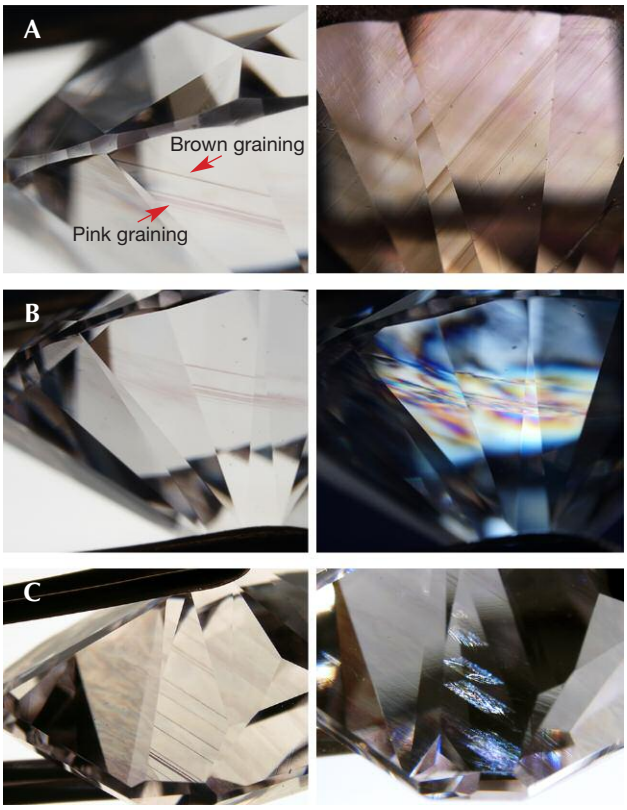

Figure 17. A: These two pink diamonds are rare examples exhibiting both pink and brown graining. B: This diamond shows slip/glide planes that are readily viewed through crossed polarizers (right), indicating that the lattice has been strongly distorted due to plastic deformation. C: This 5.09 ct Fancy pink-purple sample with obvious slip/glide planes (left) will show, when viewed at the proper angle and with proper illumination (right), that light is reflected from plastic deformation lamellae, indicating a physical discontinuity or a damaged zone of the diamond's lattice structure. Photomicrographs by GIA staff.

UV Fluorescence. *550 nm Band.* Of the 992 "pink" diamonds colored by the 550 nm band that were randomly selected for detailed spectroscopic analyses, 786 had observations of long-wave (365 nm excitation) and short-wave UV (254 nm excitation) reported in the database. Among those with fluorescence observations, 571 (73%) showed blue fluorescence to long-wave excitation; 89 (11%) exhibited yellow fluorescence and 113 (14%) no fluorescence. Those with reported blue fluorescence generally showed medium (53%) to strong (25%) intensity and had a diamond type of IaA<B (70%). Those with reported yellow fluorescence to long-wave UV generally had very weak to weak intensity (88%) and were either saturated type Ia (42%) or IaA>B (36%). Those with fluorescence reported as none generally were either saturated type Ia (67%) or IaA>B (29%).

$NV^{0/-}$ Centers. The rare "Golconda pink" diamonds (six out of the subset of 1,000 samples, or 0.6%) all showed yellow-orange-red fluorescence colors caused by $NV^{0/-}$ centers. Although all colored diamonds should be submitted to a laboratory to determine the

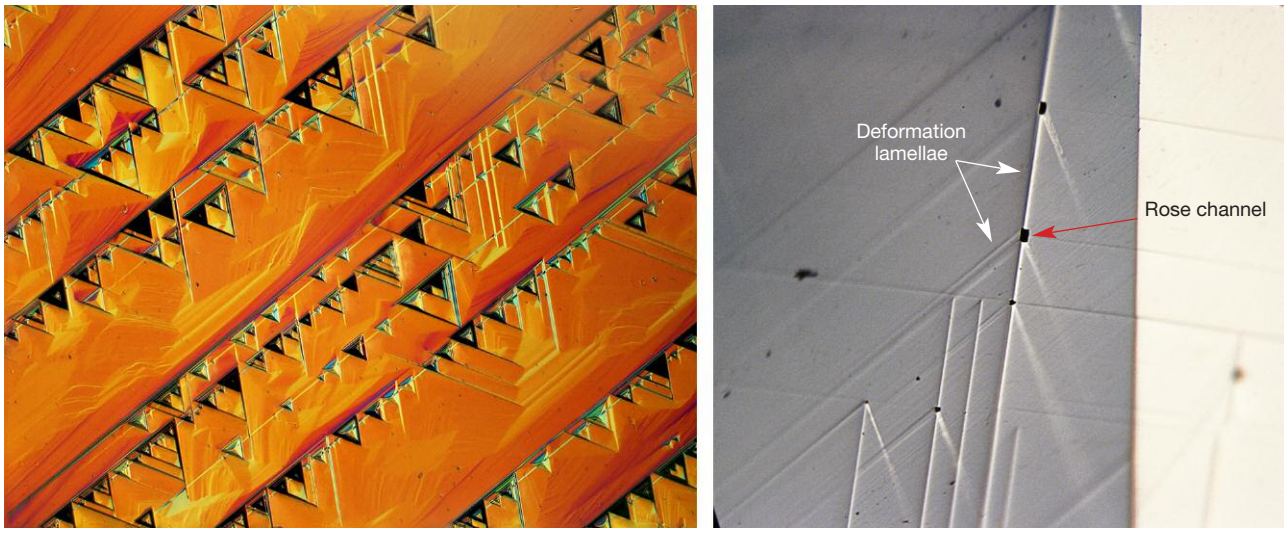

Figure 18. Left: Etching as trigons along plastic deformation lamellae in Light purplish pink type Ia diamonds, captured in differential interference contrast lighting to help improve image contrast. Photomicrograph by Nathan Renfro; field of view 1.24 mm. Right: Hollow channels (called Rose channels and indicated by the red arrow) have developed at the intersections of deformation lamellae in a 0.98 ct Fancy brownish pink diamond. Photomicrograph by Wuyi Wang; field of view 1.30 mm.

origin of their color, any "pink" diamond with yellow-orange-red fluorescence colors should be given special attention.

Bleaching. Many type IIa diamonds, including those colored by the 550 nm band and "Golconda pink" diamonds, change color after exposure to UV light. Although typically observed following exposure to the high-energy light of the DiamondView instrument (with wavelengths <225 nm), bleaching can be observed following exposure to longer-wave UV but the effect is lessened at lower-energy, higher wavelengths (Fisher et al., 2009; Byrne et al., 2012b, 2014). After exposure to UV, "pink" diamonds can change color to yellow, brown, or near-colorless, and these changes are due to several charge-transfer processes that have been associated with the vacancy clusters present in brown diamonds (Byrne et al., 2014). Bleaching has also been observed during polishing of pink diamonds (Chapman, 2014).

The diamond's color always reverts back to "pink," though this can take anywhere from several minutes to more than a day depending on the color and intensity of the light (Byrne et al., 2014). Exposure to bright light (such as placing the diamond in a microscope light well) accelerates the process. As a precaution, GIA gemologists generally do not collect DiamondView images on "pink" diamonds unless other data indicate potential treatment, and DiamondView images are always collected after color grading. Any "pink" diamonds that require DiamondView imaging are returned to their stable color before leaving the laboratory.

Figure 19 shows the photos and spectra of a type IIa Fancy Intense pink diamond that was exposed to

Figure 19. This 9.35 ct Fancy Intense pink type IIa diamond showed a dramatic color change to Fancy Intense brownish yellow following exposure to the high-energy UV of the DiamondView. The UV exposure caused a decrease in the ~390 and ~550 nm bands, and the original color was completely restored after 30 minutes of exposure to bright visible light.

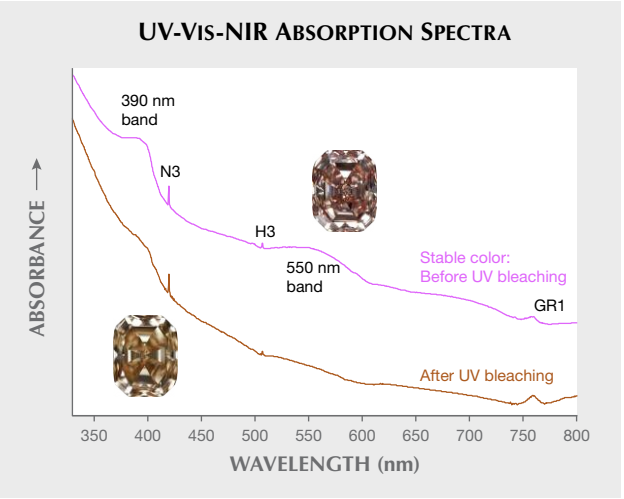

high-energy UV in the DiamondView. Its color dramatically and temporarily changed to Fancy Intense brownish yellow, which was accompanied by a decrease in the 390 nm and 550 nm absorption bands, while the intensities of the other centers (e.g., N3, H3, and GR1) remain unchanged.

IDENTIFICATION CONCERNS

Type Ia "Pinks." There is no known method of treatment to create the 550 nm absorption band in the laboratory. Except for the rare type IaB diamonds discussed below, the majority of type Ia diamonds cannot be treated to appear pink. Additionally, the colored graining common in type Ia "pinks" cannot be artificially created.

Type IIa and Type IaB "Pinks." As with the high-pressure, high-temperature (HPHT) decolorizing treatment, type IIa and type IaB pinkish brown diamonds can be HPHT-treated to remove the brown component (Hainschwang et al., 2003; Fisher et al., 2009). If the 550 nm band is present in these diamonds, the pink color will be accentuated by HPHT treatment, as the brown color is reduced. Diamonds that are HPHT-treated to pink are generally subjected to lower temperatures (1700–1800°C) than those that are HPHT-treated to colorless (2000–2300°C; Fisher et al., 2009; Dobrinets et al., 2013). As with colorless diamonds, these "pink" diamonds should be assessed by photoluminescence spectroscopy, which shows emission peaks that reliably distinguish between natural and treated diamonds. Additionally, a few "pink" CVD diamonds appear pink due to an absorption band at ~520 nm (Wang et al., 2007); therefore, careful assessment is needed to verify that the color-causing visible absorption band in type IIa "pink" diamonds is centered at ~550 nm. The cause of the ~520 nm band in CVDs is also unknown.

Type IIa "Golconda Pinks." Any diamond colored by $NV^{0/-}$ centers must be examined extremely carefully. Both treated naturals and treated synthetics are altered to a pink color by generating $NV^{0/-}$ centers. Eaton-Magaña and Shigley (2016) provide a comparison table contrasting the distinguishing characteristics of natural, treated, and synthetic "pink" diamonds that are colored by $NV^{0/-}$ centers. Natural "Golconda pink" diamonds typically have pale colors, while treated "pink" diamonds have much more saturated colors. Although the separation of synthetic diamonds is generally less complicated than the separation of treated diamonds, a full complement of absorption, luminescence (such as mapping the spatial distribution of defects; D'Haenens-Johansson et al., 2017), and gemological data should always be collected and carefully evaluated.

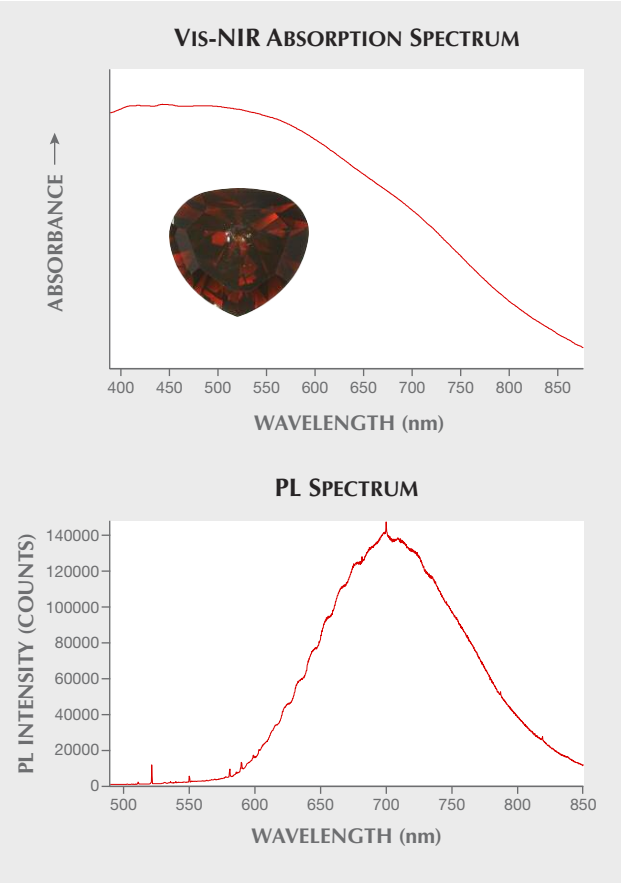

Figure 20. This 5.71 ct Fancy red-brown diamond derives its color from the 480 nm band, as shown by its Vis-NIR absorption spectrum (top). The presence of the sometimes subtle 480 nm band is unambiguously identified by a distinctive emission band determined by PL spectroscopy (bottom), such as this spectrum collected with 488 nm excitation.

UNUSUAL EXAMPLES

A small number of brown-red to red-brown diamonds owe their color to a combination of a slight 550 nm band with a 480 nm band (figure 20). The defect responsible for the ~480 nm absorption band also has a luminescence band centered at ~700 nm that is extremely broad with a unique wavy shape (figure 20, bottom). The combination of these two broad bands (the 480 and 550 nm absorption bands) leads to strong absorption from the orange to blue color regions. This combination of absorption features not only induced the common brown color but also cre-

Figure 21. These diamonds are from the 2016 Argyle Pink Tender in New York City. Left to right: 0.64 ct Fancy Deep pink oval, 0.75 ct Fancy Intense purplish pink trilliant, 0.91 ct Fancy Vivid purplish pink oval, 1.30 ct Fancy Intense pink heart, 1.35 ct Fancy Intense purplish pink cushion, 0.80 ct Fancy Vivid pink pear, and 0.45 ct Fancy Vivid purplish pink emerald cut. Photo by Robert Weldon; courtesy of Argyle Pink Diamonds.

ated a "transparent window" in the red region. The result is a red-brown coloration.

CONCLUSIONS

Most colored diamonds receive the ingredients for color deep within the earth as they are created—nitrogen, boron, nickel, and hydrogen impurities produce yellow, yellowish green, violet, and blue colors, while abundant micro-inclusions can create white and black colors. After reaching the earth's surface, diamonds can be exposed to radiation to create blue to green colors. However, the vast majority of natural "pink" diamonds colored by the 550 nm absorption band are produced through deformation processes deep within the earth.

Many source locality reports have been written about type Ia "pink" diamonds from Australia and Russia (Iakoubovskii and Adriaenssens, 2002; Titkov et al., 2008, 2012; Gaillou et al., 2010, 2012; Howell et al., 2015), yet very little has been written about type IIa "pinks," and we could find no studies of a mine that regularly produces type IIa "pinks." Therefore, one enduring question is the source locality of the type IIa "pink" diamonds colored by the 550 nm absorption band. Of the 992 diamonds colored by the 550 nm band that were randomly selected and studied in detail, almost one-fourth (243) were type IIa. Although this is a comparatively high percentage, little has been written about their source localities (e.g., Fisher et al., 2009; Smith et al., 2017).

Today, the Argyle mine produces a sizeable percentage of the world's "pink" diamonds (e.g., figure 21), although pink to purple diamonds also come from countries such as Brazil, South Africa, and Russia. Since the Argyle mine is set to close within the next few years, the supply of "pink" diamonds, particularly those with saturated colors or those with red color descriptions, will decline unless the supply from other producers becomes more substantial.

ABOUT THE AUTHORS

Dr. Eaton-Magaña and Dr. Breeding are senior research scientists, Mr. Ardon is a research associate, and Dr. Shigley is a distinguished research fellow, at GIA in Carlsbad, California. Dr. Smit is a research scientist at GIA in New York.

ACKNOWLEDGMENTS

Discussions with GIA's Dr. Evan Smith and John King contributed to some ideas presented here. John Chapman (Gemetrix, Perth, Australia) and Sergey Titkov provided helpful insight.

REFERENCES

Boyd S.R., Kiflawi I., Woods G.S. (1994) The relationship between infrared absorption and the A defect concentration in diamond. *Philosophical Magazine B*, Vol. 69, No. 6, pp. 1149–1153, http://dx.doi.org/10.1080/01418639408240185

——— (1995) Infrared absorption by the B nitrogen aggregation in diamond. *Philosophical Magazine B*, Vol. 72, No. 3, pp. 351–361.

Breeding C.M., Eaton-Magaña S.C., Shigley J.E. (2018) Natural color green diamonds: A beautiful conundrum. *G&G*, Vol. 54, No. 1, pp. 2–27, http://dx.doi.org/10.5741/GEMS.54.1.2

Brookes E.J., Daniel R.D. (2001) Influence of nitrogen content on the mechanical properties of diamond. In M.H. Nazaré and A.J. Neves, Eds., *Properties, Growth and Applications of Diamond*, Vol. 26, pp. 142–148.

Byrne K.S., Anstie J.D., Luiten A.N. (2012a) Infrared microspectroscopy of natural Argyle pink diamond. *Diamond and Related Materials*, Vol. 23, pp. 125–129, http://dx.doi.org/10.1016/j.diamond.2012.01.032

Byrne K.S., Anstie J.D., Chapman J.G., Luiten A.N. (2012b) Optically reversible photochromism in natural pink diamond. *Diamond and Related Materials*, Vol. 30, pp. 31–36, http://dx.doi.org/10.1016/j.diamond.2012.09.005

Byrne K.S., Chapman J.G., Luiten A.N. (2014) Photochromic charge transfer processes in natural pink and brown diamonds. *Journal of Physics: Condensed Matter*, Vol. 26, No. 3, pp. 035501-1–035501-6, http://dx.doi.org/10.1088/0953-8984/26/3/035501

Chapman J. (2014) Chromism in pink diamonds. *Australian Gemmologist*, Vol. 25, No. 8, pp. 268–271.

Christie's (2013) https://www.christies.com/lotfinder/Lot/the-princie-diamond-5672735-details.aspx [Accessed June 2, 2018]

——— (2018) 'As good as it gets' — The Pink Legacy diamond. Nov. 14, https://www.christies.com/features/The-Pink-Legacy-diamond-9398-3.aspx

Daly J.S., Balagansky V.V., Timmerman M.J., Whitehouse M.J. (2006) The Lapland-Kola orogen: Palaeoproterozoic collision and accretion of the northern Fennoscandian lithosphere. *Geological Society, London, Memoirs*, Vol. 32, No. 1, pp. 579–598, http://dx.doi.org/10.1144/GSL.MEM.2006.032.01.35

Darley J., Johnson P., King J. (2011) Lab Notes: A rare fancy vivid purple diamond. *G&G*, Vol. 47, No. 4, p. 308.

Deljanin B., Simic D., Zaitsev A., Chapman J., Dobrinets I., Widemann A., Del Re N., Middleton T., Deljanin E., De Stefano A. (2008) Characterization of pink diamonds of different origin: Natural (Argyle, non-Argyle), irradiated and annealed, treated with multi-process, coated and synthetic. *Diamond and Related Materials*, Vol. 17, No. 7/10, pp. 1169–1178, http://dx.doi.org/10.1016/j.diamond.2008.03.014

DeVries R.C. (1975) Plastic deformation and "work-hardening" of diamond. *Materials Research Bulletin*, Vol. 10, No. 11, pp. 1193–1199, http://dx.doi.org/10.1016/0025-5408(75)90026-4

D'Haenens-Johansson U.F.S., Loudin L., Myagkaya E., Persaud S. (2017) Photoluminescence defect mapping of impurity centers in "Golconda" pink and colorless type IIa natural diamonds and CVD synthetics. *Diamond Conference*, University of Warwick, July 10–13 (unpublished abstract).

Dobrinets I.A., Vins V.G., Zaitsev A.M. (2013) *HPHT-Treated Diamonds: Diamonds Forever*. Springer, Heidelberg.

Eaton-Magaña S.C., Breeding C.M. (2016) An introduction to photoluminescence spectroscopy for diamond and its applications in gemology. *G&G*, Vol. 52, No. 1, pp. 2–17, http://dx.doi.org/10.5741/GEMS.52.1.2

Eaton-Magaña S.C., Shigley J.E. (2016) Observations on CVD-grown synthetic diamonds: A review. *G&G*, Vol. 52, No. 3, pp. 222–245, http://dx.doi.org/10.5741/GEMS.52.3.222

Eaton-Magaña S.C., Ardon T., Zaitsev A.M. (2017) LPHT annealing of brown-to-yellow type Ia diamonds. *Diamond and Related Materials*, Vol. 77, pp. 159–170, http://dx.doi.org/10.1016/j.diamond.2017.06.008

Eaton-Magaña S.C., Breeding C.M., Shigley J.E. (2018) Natural-color blue, gray, and violet diamonds: Allure of the deep. *G&G*, Vol. 54, No. 2, pp. 112–131, http://dx.doi.org/10.5741/GEMS.54.2.112

Fedortchouk Y., Zhang Z. (2011) Diamond resorption: link to metasomatic events in the mantle or record of magmatic fluid in kimberlitic magma? *The Canadian Mineralogist*, Vol. 49, No. 3, pp. 707–719, http://dx.doi.org/10.3749/canmin.49.3.707

Fedortchouk Y., Canil D., Carlson J.A. (2005) Dissolution forms in the Lac de Gras diamonds and their relationship to the temperature and redox state of kimberlite magma. *Contributions to Mineralogy and Petrology*, Vol. 150, No. 1, pp. 54–69, http://dx.doi.org/10.1007/s00410-005-0003-1

Fisher D., Sibley S.J., Kelly C.J. (2009) Brown colour in natural diamond and interaction between the brown related and other colour-inducing defects. *Journal of Physics: Condensed Matter*, Vol. 21, No. 36, Article 364213, 10 pp., http://dx.doi.org/10.1088/0953-8984/21/36/364213

Fritsch E. (1998) The nature of color in diamonds. In G. Harlow, Ed., *The Nature of Diamonds*. Cambridge University Press, Cambridge, UK, pp. 23–47.

Gaillou E., Post J.E., Bassim N.D., Zaitsev A.M., Rose T., Fries M.D., Stroud R.M., Steele A., Butler J.E. (2010) Spectroscopic and microscopic characterizations of color lamellae in natural pink diamonds. *Diamond and Related Materials*, Vol. 19, No. 10, pp. 1207–1220, http://dx.doi.org/10.1016/j.diamond.2010.06.015

Gaillou E., Post J.E., Rose T., Butler J.E. (2012) Cathodoluminescence of natural, plastically deformed pink diamonds. *Microscopy and Microanalysis*, Vol. 18, No. 6, pp. 1292–1302, http://dx.doi.org/10.1017/S1431927612013542

Goss J.P., Briddon P.R., Hill V., Jones R., Rayson M.J. (2014) Identification of the structure of the 3107 cm^{-1} H-related defect in diamond. *Journal of Physics: Condensed Matter*, Vol. 26, No. 14, pp. 1–6, http://dx.doi.org/10.1088/0953-8984/26/14/145801

Grimsditch M.H., Anastassakis E., Cardona M. (1978) Effect of uniaxial stress on the zone-center optical phonon of diamond. *Physical Review B*, Vol. 18, pp. 901–904, http://dx.doi.org/10.1103/PhysRevB.18.901

Hainschwang T., Katrusha A., Vollstaedt H. (2003) HPHT treatment of different classes of type I brown diamonds. *Journal of Gemmology*, Vol. 28, No. 5/6, pp. 261–273, http://dx.doi.org/10.15506/JoG.2005.29.5.261

Hainschwang T., Notari F., Fritsch E., Massi L., Rondeau B., Breeding C.M., Vollstaedt H. (2008) HPHT treatment of CO_2 containing and CO_2-related brown diamonds. *Diamond and Related Materials*, Vol. 17, No. 3, pp. 340–351, http://dx.doi.org/10.1016/j.diamond.2008.01.022

Hofer S.C. (1985) Pink diamonds from Australia. *G&G*, Vol. 21, No. 3, pp. 147–155, http://dx.doi.org/10.5741/GEMS.21.3.147

Hounsome L.S., Jones R., Martineau P.M., Fisher D., Shaw M.J., Briddon P.R., Oberg S. (2006) Origin of brown coloration in diamond. *Physical Review B*, Vol. 73, No. 12, article 125203, http://dx.doi.org/10.1103/PhysRevB.73.125203

Howell D., Fisher D., Piazolo S., Griffin W.L., Sibley S.J. (2015) Pink color in type I diamonds: Is deformation twinning the cause? *American Mineralogist*, Vol. 100, No. 7, pp. 1518–1527, http://dx.doi.org/10.2138/am-2015-5044

Humble P. (1982) The structure and mechanism of formation of platelets in natural type Ia diamond. *Proceedings of the Royal Society of London A*, Vol. 381, No. 1780, pp. 65–81, http://dx.doi.org/10.1098/rspa.1982.0059

Iakoubovskii K., Adriaenssens G.J. (2002) Optical characterization of natural Argyle diamonds. *Diamond and Related Materials*, Vol. 11, No. 1, pp. 125–131, http://dx.doi.org/10.1016/S0925-9635(01)00533-7

King J.M. (2006) *GIA Colored Diamonds Color Reference Charts*. Gemological Institute of America, Carlsbad, California.
King J.M., Moses T.M., Shigley J.E., Liu Y. (1994) Color grading of colored diamonds in the GIA Gem Trade Laboratory. *G&G*, Vol. 30, No. 4, pp. 220–242, http://dx.doi.org/10.5741/GEMS.30.4.220
King J.M., Shigley J.E., Guhin S.S., Gelb T.H., Hall M. (2002) Characterization and grading of natural-color pink diamonds. *G&G*, Vol. 38, No. 2, pp. 128–147, http://dx.doi.org/10.5741/GEMS.38.2.128
King J.M., Geurts R.H., Gilbertson A.M., Shigley J.E. (2008) Color grading "D-to-Z" diamonds at the GIA laboratory. *G&G*, Vol. 44, No. 4, pp. 296–321, http://dx.doi.org/10.5741/GEMS.44.4.296
King J.M., Shigley J.E., Jannucci C. (2014) Exceptional pink to red diamonds: A celebration of the 30th Argyle diamond tender. *G&G*, Vol. 50, No. 4, pp. 268–279, http://dx.doi.org/10.5741/GEMS.50.4.268
Leahy K., Taylor W.R. (1997) The influence of the Glennie domain deep structure on the diamonds in Saskatchewan kimberlites. *Geologiya i Geofizika*, Vol. 38, No. 2, pp. 451–460.
Massi L., Fritsch E., Collins A.T., Hainschwang T., Notari F. (2005) The "amber centres" and their relation to the brown colour. *Diamond and Related Materials*, Vol. 14, No. 10, pp. 1623–1629, http://dx.doi.org/10.1016/j.diamond.2005.05.003
Mineeva R.M., Titkov S.V., Speransky A.V. (2009) Structural defects in natural plastically deformed diamonds: evidence from EPR spectroscopy. *Geology of Ore Deposits*, Vol. 51, No. 3, pp. 233–242, http://dx.doi.org/10.1134/S1075701509030052
Orlov I.L. (1977) *The Mineralogy of the Diamond*. John Wiley & Sons, New York.
Rose G. (1868) Über Die Im Kalkspath Vorkommenden Hohlen Canäle. *Abhandlungen der Königlichen Akademie der Wissenschaften*, Berlin, pp. 55–70.
Schoor M., Boulliard J.C., Gaillou E., Hardouin Duparc O., Esteve I., Baptiste B., Rondeau B., Fritsch E. (2016) Plastic deformation in natural diamonds: Rose channels associated to mechanical twinning. *Diamond and Related Materials*, Vol. 66, pp. 102–106, http://dx.doi.org/10.1016/j.diamond.2016.04.004
Shigley J.E., Chapman J., Ellison R.K. (2001) Discovery and mining of the Argyle diamond deposit, Australia. *G&G*, Vol. 37, No. 1, pp. 26–41, http://dx.doi.org/10.5741/GEMS.37.1.26
Shirey S.B., Shigley J.E. (2013) Recent advances in understanding the geology of diamonds. *G&G*, Vol. 49, No. 4, pp. 188–222, http://dx.doi.org/10.5741/GEMS.49.4.188
Shor R. (2018) Is the swan song for Argyle pink diamonds close at hand? https://www.gia.edu/gia-news-research-swan-song-argyle-pink-diamonds-close-hand [Accessed June 7, 2018]
Smit K.V. (2008) Diamond formation in craton margin settings: Mesoproterozoic age of Ellendale peridotitic diamonds (Western Australia). Master's thesis, University of Cape Town, South Africa.
Smit K.V., Shor R. (2017) Geology and development of the Lomonosov diamond deposit, northwestern Russia. *G&G*, Vol. 53, No. 2, pp. 144–167, http://dx.doi.org/10.5741/GEMS.53.2.144
Smit K.V., Shirey S.B., Wang W. (2016) Type Ib diamond formation and preservation in the West African lithospheric mantle: Re–Os age constraints from sulphide inclusions in Zimmi diamonds. *Precambrian Research*, Vol. 286, pp. 152–166, http://dx.doi.org/10.1016/j.precamres.2016.09.022
Smit K.V., D'Haenens-Johansson U.F.S., Howell D., Loudin L.C., Wang W. (2018) Deformation-related spectroscopic features in natural type Ib-IaA diamonds from Zimmi (West African craton). *Mineralogy and Petrology*, https://doi.org/10.1007/s00710-018-0587-6.
Smith C.P., Bosshart G. (2002) Star of the South: A historic 128 ct diamond. *G&G*, Vol. 38, No. 1, pp. 54–64, http://dx.doi.org/10.5741/GEMS.38.1.54
Smith E.M., Shirey S.B., Nestola F., Bullock E.S., Wang J., Richardson S.H., Wang W. (2016) Large gem diamonds from metallic liquid in Earth's deep mantle. *Science*, Vol. 354, No. 6318, pp. 1403–1405, http://dx.doi.org/10.1126/science.aal1303
Smith E.M., Shirey S.B., Wang W. (2017) The very deep origin of the world's biggest diamonds. *G&G*, Vol. 53, No. 4, pp. 388–403, http://dx.doi.org/10.5741/GEMS.53.4.388
Speich L., Kohn S.C., Wirth R., Smith C.B. (2017) The relationship between platelet size and the B′ infrared peak of natural diamonds revisited. *Lithos*, Vols. 278-281, pp. 419–426, http://dx.doi.org/10.1016/j.lithos.2017.02.010
Stachel T., Harris J.W., Hunt L., Muehlenbachs K., Kobussen A., EIMF (2018) Argyle diamonds – how subduction along the Kimberley Craton edge generated the world's biggest diamond deposit. Society of Economic Geologists, Inc. Special Publication 20, pp. 145–167.
Stepanov A.S., Korsakov A.V., Yuryeva O.P., Nadolinniy V.A., Perraki M., De Gussem K., Vandenabeele P. (2011) Brown diamonds from an eclogite xenolith from Udachnaya kimberlite, Yakutia, Russia. *Spectrochimica Acta Part A*, Vol. 80, No. 1, pp. 41–48, http://dx.doi.org/10.1016/j.saa.2011.01.006
Taylor W.R., Jaques A.L., Ridd M. (1990) Nitrogen-defect aggregation characteristics of some Australasian diamonds: Time-temperature constraints on the source regions of pipe and alluvial diamonds. *American Mineralogist*, Vol. 75, pp. 1290–1310.
Titkov S.V., Shigley J.E., Breeding C.M., Mineeva R.M., Zudin N.J., Sergeev A.M. (2008) Natural-color purple diamonds from Siberia. *G&G*, Vol. 44, No. 1, pp. 56–64, http://dx.doi.org/10.5741/GEMS.44.1.56
Titkov S.V., Krivovichev S.V., Organova N.I. (2012) Plastic deformation of natural diamonds by twinning: evidence from X-ray diffraction studies. *Mineralogical Magazine*, Vol. 76, No. 1, pp. 143–149, http://dx.doi.org/10.1180/minmag.2012.076.1.143
Tyler I.M., Page R.W. (1996) Palaeoproterozoic deformation, metamorphism and igneous intrusion in the central zone of the Lamboo Complex, Halls Creek Orogen. In *Geological Society of Australia Abstracts*, Vol. 41, p. 450.
Wang W., Cracco V., Moses T.M. (2006) Lab Notes: Pink diamond with etch channels at the intersection of glide planes. *G&G*, Vol. 42, No. 1, p. 56.
Wang W., Hall M.S., Moe K.S., Tower J., Moses T.M. (2007) Latest-generation CVD-grown synthetic diamonds from Apollo Diamond Inc. *G&G*, Vol. 43, No. 4, pp. 294–312, http://dx.doi.org/10.5741/GEMS.43.4.294
Woods G.S. (1986) Platelets and the infrared-absorption of type-Ia diamonds. *Proceedings of the Royal Society of London Series A*, Vol. 407, No. 1832, pp. 219–238, http://dx.doi.org/10.1098/rspa.1986.0094

The History and Reconstruction of The Amber Room

Russell Shor

The Amber Room was constructed for King Frederick I of Prussia in Danzig (modern-day Gdansk, Poland) between 1701 and 1714. The amber panels making up the room were presented to Czar Peter I of Russia in 1716 and eventually installed in the Catherine Palace near St. Petersburg. They remained there until the outbreak of World War II, when a German army unit looted the room. The Soviet government, which deemed the room a cultural treasure, mandated its reconstruction in 1979, beginning a 24-year process that culminated with its reopening in 2003. This article offers a history of the original room drawn from the published writings of historians, accounts of the looting and subsequent disappearance of the amber panels, and detailed firsthand accounts of the reconstruction from those who participated in its planning, design, and execution.

The Amber Room (figure 1), located in the Catherine Palace in the Russian town of Pushkin (previously Tsarskoye Selo), is considered by many historians the pinnacle of amber craftsmanship. The chamber is a reconstruction of the first Amber Room, which was begun in 1701 by order of Frederick I of Prussia and was actually a series of large panels designed to be mounted onto walls within Berlin's Charlottenburg Palace. The original project took 13 years to complete. Once it was finished, Frederick's son, William I, presented the amber panels to Peter the Great of Russia to commemorate a treaty between the two rulers against Charles XII of Sweden. The panels were installed in the Winter Palace in St. Petersburg and in 1755 moved to the Catherine Palace, where they remained for nearly 200 years.

In 1941, Nazi Germany invaded Russia. After surrounding St. Petersburg (called Leningrad between 1924 and 1991), they occupied Pushkin. Just before the invaders reached the palace, its caretakers removed the smaller amber objects from the Amber Room and attempted to hide the panels behind wallpaper. The invading German officers, however, knew of the room and confiscated the panels before destroying most of the palace. After the war, the panels were never seen again.

In 1979, Russian craftsmen began the long process of recreating the Amber Room. This was extremely challenging because there was little documentation of the original room. Many of the amber working skills of the eighteenth-century craftsmen had been lost, and the materials used in adhesives and dyes were no longer known. With the work less than half completed, political changes nearly forced the project's end. From initial research to the reopening of the room before heads of state in 2003, the reconstruction took 24 years to complete.

In Brief

- The original Amber Room panels were constructed in Prussia from 1701 to 1714, presented to Peter the Great of Russia, and installed in the Catherine Palace.
- The panels were looted by the advancing German army in 1941 and are presumed lost.
- Reconstruction began in 1979, but there was scant photographic evidence of the original room and little documentation of the materials and techniques used.
- After 24 years of work, the craftsmen in the amber studio achieved an accurate reconstruction of the room.

BALTIC AMBER

Baltic amber, or succinate, is fossilized resin from *Pinus succinifera*. This tree grew in abundance

See end of article for About the Author and Acknowledgments.
Gems & Gemology, Vol. 54, No. 2, pp. 378–393,
http://dx.doi.org/10.5741/GEMS.54.4.393

Figure 1. Detail showing the upper portions of the reconstructed room, including the gilded sculptures and the imitation amber painting above the cornice. Photo courtesy of Amberif.

throughout Scandinavia and northern Europe more than 20 million years ago (Kosmowska-Ceranowicz, 2009). The vast Baltic area deposits were formed when resin-bearing sediments flowed from Scandinavia to the Sambia Peninsula (figure 2), transforming those resins over millions of years into amber. Streams and rivers and glaciers carried large amounts of amber throughout northern Europe as secondary deposits (Gaigalas and Salas, 2009). The primary deposits of the southern Baltic region—particularly the Sambia Peninsula, where Kaliningrad, Russia, is situated—are the world's most prolific sources of amber and among the oldest gem deposits still in production, dating back to before recorded history. While there are no ancient accounts of amber mining, most of the material was probably collected on beaches following storms—a method still used today by amateur collectors. Amber objects and carvings dating back to prehistoric times have been found in Great Britain (9000 BCE) and in the southern Baltic region (6000 BCE) (Langenheim, 1990).

THE AMBER ROADS

Collection and trade of amber in the Baltic region for ornamental uses is believed to have begun some 6,000 years ago, during the Neolithic period. Amber was regarded as a valuable trading commodity for its decorative qualities and for its use as fuel for fires. Amber trade routes extended from the Baltic through the continent to southern Europe and the Arabian Peninsula; some routes dating back to the Neolithic have been documented (Butrimas and Jovaiša, 2013). Among the best documented were the amber trade routes extending from the Baltic Sea to the Mediterranean. These were established around 3000 BCE, based on archeological finds of beads and carvings in various locations in Eastern Europe (Mazurowski, 2011). In addition, a trove of 850 amber ornaments, estimated to have been created about 3000 BCE, were found in present-day Lithuania, and evidence of an amber carving enterprise was discovered in what is now Latvia (Grimaldi, 1996; Czebreszuk and Szmyt, 2013).

Figure 2. The southern Baltic region and Sambia Peninsula are the source of a vast amber deposit that has been producing since before recorded history. The most prolific area of the deposit is located near Kaliningrad. The city of Danzig (now Gdansk) on the western portion of the map has been a center of amber craftsmanship for more than 1,000 years and was the home of the designers and builders of the original Amber Room.

Amber's origins were known by the first century CE. Pliny the Elder, a contemporary of Roman Emperor Nero (37–68 CE), wrote in *Natural History* that the material "is formed from the liquid that exudes from a type of pine tree" but noted it was generally useless except as an adornment for women (Clark, 2010). The Roman historian Tacitus described the trading of Baltic amber with Germanic tribes that collected and bartered the material (Clark, 2010). Pliny noted the high value Romans placed on amber and wrote that Nero's chief gladiator, Julian, dispatched a mission to the north to bring back large quantities of it. Upon their return, the Romans used the amber to decorate the arena for gladiator games. Because it was believed to have protective qualities, the material was sewn into the nets separating the spectators from the wild animals in the area.

Trade routes originated at the southern Baltic coast near the site where Danzig (now Gdansk, Poland) was founded. The best-known route was down the Vistula River and over land to the Danube, to the Roman port of Aquileia on the Adriatic Sea. This was generally known as the Amber Road. However, archaeological evidence indicates many so-called Amber Roads that wound through Europe, all leading from Danzig or Königsberg (now Kaliningrad), about 120 km (75 miles) east from Danzig, to Aquileia, or ports on the Mediterranean as far west as Massalia (now Marseille; Clark, 2010).

One of the most important amber trading centers was the Viking village of Truso, located near the modern-day city of Elblag in Poland. Excavations conducted over the past 120 years have found remains of amber workshops and objects from Viking and Celtic civilizations (Mazurowski, 2011). By the time Danzig, about approximately 60 km (37 miles) from Truso, was founded around 980, amber working

Figure 3. Amber has been collected and traded throughout Europe and as far as the Middle East for at least 6,000 years. Archaeological finds show a number of early trade routes from the Baltic to the Adriatic and Mediterranean Seas; these roads were highly developed by the time of ancient Greece and Rome.

was a recognized skill among its inhabitants (City of Gdansk, 2017; see figure 3).

Up to this point, most amber had been collected by Baltic tribes inhabiting the southern coastal areas and the Sambia Peninsula. After the religious order known as the Teutonic Knights returned from the Crusades in 1211, the Duke of Masovia (which encompassed modern-day Warsaw) enlisted their help in conquering the tribes. The Knights completed their conquest of the Balts in 1283 and in 1312 assumed a monopoly over the amber trade, even forbidding its collection on the beaches. Despite the restrictions, amber remained a widely traded commodity in the southern Baltic region in the Prussian states, especially between Danzig and other cities that were members of the Hanseatic League, a Baltic-centered trading alliance (Grimaldi, 1996). Because of the Knights' iron rule over trade in the region, craft guilds specializing in amber formed in cities outside their jurisdiction, even as far away as Bruges, Belgium, where craftsmen carved the material into rosaries (Grimaldi, 1996).

By the end of the fifteenth century, the Knights' centuries-long grip over amber mining and trade had weakened. In 1533, the Duke of Prussia granted control over much of the raw amber supply to a syndicate of traders led by Paul Koehn von Jaski. This syndicate established workshops in Livorno, Italy, Vienna, Berlin, Paris, and Persia, and their monopoly endured until 1642 (Netzer, 1993). As supply increased and trade became freer, amber workers formed guilds. The first was in Danzig in 1477, followed by Stolp (now Słupsk) and Kolberg (now Kołobrzeg), both in 1480 (Netzer, 1993). The Danzig guild produced mainly religious items such as altars, shrines, and images of saints. The others created an array of amber goods: small furniture pieces, game boards, mythological figures, lidded tankards, and decorative objects (Grimaldi, 1996). The Königsberg guild was founded much later (1641), when the elector of Brandenburg permitted it to set up in his residence (Netzer, 1993).

Through the guilds, amber craftsmanship evolved to a high art in Prussia over the following two centuries. Workshops developed techniques beyond carving to create large furniture pieces, sculptures, and other commissions from the Brandenburg Court, which ruled the region from 1618 to 1701. By the end of the seventeenth century, many prominent amber craftsmen had assembled in Danzig and Königsberg because the Brandenburg Court had begun commissioning major amber works as gifts to foreign rulers to seal diplomatic pacts (Netzer, 1993). One of the most renowned workshops in Danzig, where many such works were made, was operated by the head of the guild, Gottfried Turau, and his partner, Ernst Schacht. These men would figure prominently in the construction of the Amber Room (Grimaldi, 1996).

THE ORIGINAL AMBER ROOM

The idea of the Amber Room was first raised by Frederick III, elector of Brandenburg, then a principality within the Holy Roman Empire and today a province that surrounds Berlin. Frederick III (later Frederick I of Prussia) inherited the title of elector in 1688 at the same time he was named Duke of

Figure 4. The Amber Room was designed for a chamber in the Charlottenburg Palace in Berlin but was never housed there. Courtesy of Tsarskoye Selo Amber Workshop.

Prussia, which encompassed the southern Baltic coast and the Sambia Peninsula. During this period, Frederick commissioned three large mirror frames made from natural-color and dyed amber with ivory accents. The mirrors measured 142 × 120 cm, 156 × 116 cm, and 156 × 116 cm at their outer dimensions, and each frame was 13 cm wide (Gierlowski, 2006a). These mirror frames would be incorporated into the Amber Room during its construction some 20 years later.

Upon his elevation to King of Prussia in 1701, Frederick decided to commemorate his rule by creating a room fully lined with amber in the Charlottenburg Palace in Berlin (figure 4). That room, he believed, would surpass the opulence of Louis XIV's palace at Versailles (Gierlowski, 2006a).

At that time, large stocks of uncut amber, including many very large pieces, had accumulated in warehouses in Danzig, about 480 km (300 miles) east of Berlin. The excess supplies were a result of increased mining activities in the Sambia Peninsula and the Curonian Spit, a sand barrier separating Königsberg from the Baltic Sea (Grimaldi, 1996).

To design the room, the monarch appointed Andreas Schlüter, director of royal construction in Danzig and one of the architects of the City Palace in Berlin. He selected a cabinet room meant for Frederick I's private audiences, located in a corner of the palace. The room measured more than 74.25 square meters and stood about 5 meters high from floor to ceiling (Gierlowski, 2006a).

The plan was to create the appearance of amber walls through a series of large wood-backed mosaic panels, on which were glued amber slices of varied hues. The design called for 12 main panels measuring over 3.5 meters high, with most nearly 56 cm wide. Several narrower panels, each approximately 25 cm wide, were fitted near the corners and windows. Each panel was separated by mirrored pilasters decorated with candelabras and gilded wood carvings. Below the main panels were wainscot panels of equal width, approximately three feet high and separated from the main pieces by a chair rail, also made from assembled amber pieces, and supported by a plinth all the way around. The design called for the craftsmen to add bas-relief decorative elements such as frames, wreaths, and garlands to the amber mosaic panels. The completed panels would then be mounted on the walls. Other decorative elements carved from amber, including garlands, fruit clusters, and sculptured figures carved from wood and gilded with gold foil, would then be mounted on top of the panels. Mounted on the cornice around the room, just below the ceiling, was a series of carved amber pieces with rose, tulip, and other motifs, approximately 20 to 25 cm high. The design called for the completed amber works to cover 80% of the wall surface (Gierlowski, 2006a; Owen, 2009).

In addition, there were to be large mirrors on each of the four walls surrounded by the amber frames manufactured in Dresden 25 years earlier. These mirrors would be replaced by stone mosaics after the panels were relocated to the Catherine Palace.

The task of executing the design fell to Gottfried Wolfram, who had worked in the Danish court as a master amber and ivory carver and was renowned for

his skill in executing intricate, artistic designs. In 1701, Frederick IV of Denmark recommended Wolfram to Frederick I of Prussia to supervise the work (Hein, 1991). In constructing the panels, Wolfram first lined the oak panels with bronze foil, having discovered when making amber-covered furniture that the subtle expansion and contraction of wood due to temperature and humidity caused the amber to crack, fall off, or separate (Gierlowski, 2006a). The slightly reflective bronze backing also enhanced the color of the translucent amber. Wolfram's workmen laid the large oak panels flat and fastened bronze foil to them using iron clasps. They prepared the pieces of amber by sawing them into strips, approximately 5 mm thick, to be mounted in a mosaic onto the bronze foil (Gierlowski, 2006a).

The adhesive was a mixture of pine resin and beeswax with a low melting point so craftsmen could easily remove or replace broken or ill-fitting slices. The amber carvings were assembled by mortise-and-tenon joints (similar to tongue and groove) and fixed to the panel by ivory pegs. The design elements on the main wall panels, cartouches, and cameos and the Dresden frames for the four mirrors were also made of amber and attached by either method. The frames also served as a structural element to strengthen the panels.

After six years, Wolfram's shop had completed one-fourth of the panels, frames, and carvings. In 1707, however, Schlüter fell out of favor with the court and was abruptly dismissed from his post, with the captain of the guards, Eosander von Goethe, appointed in his place. In turn, Goethe dismissed Wolfram over a payment dispute and ordered the guards to remove the amber panels and carvings from his workshops—barring Wolfram in the process—and transport everything to Charlottenburg. Wolfram spent a number of years trying to recover his workshop and payment, but he eventually fled to Copenhagen after being threatened with arrest (Hein, 1991; Gierlowski, 2006a).

Schlüter also left Prussia for Saxony and eventually moved to St. Petersburg at the invitation of Peter the Great. Goethe did not modify Schlüter's original design and eventually hired Gottfried Turau and Ernst Schacht to complete the project. An inventory taken six years later, in 1713, indicated that the two craftsmen had completed a majority of the carvings, four of the 12 pilasters, and most of the panels that would cover about 95% of the walls in the room (Gierlowski, 2006a).

The death of Frederick I in 1713 brought his successor to the Prussian throne. Frederick William I disdained the extravagance the Amber Room represented and promptly ordered all work on it to stop, with the materials packed up and deposited in the Berlin armory. The new monarch also halted payments to Turau and Schacht (Gierlowski, 2006a). The panels and carvings remained hidden in the Berlin armory until 1716, after a visit to the Prussian court by Czar Peter I. Frederick William I took the occasion to present the still-unfinished panels to the Russian monarch in exchange for a company of 40 grenadiers, on November 17, 1716. The exchange sealed a valuable alliance of the two states to end Swedish occupation of large sections of Russia's Baltic coast.

The presentation of the amber panels to Peter I was not an impulsive decision. Prussian royalty had regarded amber as their national treasure for at least a century and had established a tradition of sealing diplomatic agreements with objects such as furniture pieces, chandeliers, and large mirror frames fashioned from the material. The panels for the Amber Room were the largest such gifts (Netzer, 1993). On January 13, 1717, workmen packed the pieces into eight large crates and dispatched them to St. Petersburg. The journey proceeded by road through Königsberg and Klaipeda (in modern-day Lithuania) and took nearly six months. A report from Alexander Menshikov, St. Petersburg's first governor general, noted that "there was practically no damage to the amber cabinet" (Gierlowski, 2006a).

After the shipment's arrival in St. Petersburg, it was discovered that the amber panels, which had been designed for a specific cabinet room in the Charlottenburg Palace, did not conform to any rooms in the Russian palace. Several panels remained unfinished, as did the mirrored pilasters, and no local craftsmen had the skills to complete them and mount the elements to the walls. Neither Peter I, who died in 1725, nor his wife Catherine (r. 1725–7) or grandson Peter II (r. 1727–30) made any decision about where to install the amber panels.

After the death of Peter I, his daughter, Elizabeth, in 1730 ordered the large panels to be displayed in the St. Petersburg Summer Palace, where they remained propped against the walls in various function rooms for 13 years. In 1743, Elizabeth, who had taken the throne two years earlier, ordered her staff to transport the amber elements to the much larger third Winter Palace. She appointed Italian craftsman Alexander Martelli to oversee the mounting of the amber panels in a suitable room. Martelli, who served the Russian court as a monument conservator, also had some skill

in amber working and the techniques employed by the original Danzig craftsmen (Gierlowski, 2006a). Francesco Bartolomeo Rastrelli, senior court architect, was appointed to redesign the amber elements to fit the new room, which was a much larger ceremonial hall. Other problems presented themselves. When Martelli's workers could not replicate the intricate amber engravings and bas-relief on the remaining eight pilasters, Rastrelli replaced the amber elements with mirrors mounted in gilded frames to fill the remaining space. This solution created another problem. Russia had no glassmaker capable of making one-piece mirrors more than 3.65 meters in height. This delayed the project for nearly three years, until a French company delivered the mirrors in oak frames at the end of 1745. Martelli also replaced the mirrors in the Dresden frames with oil paintings by Dutch artist Johan van Groot (Gierlowski, 2006a). The Winter Palace room also required an additional amber window frame, so Martelli had to commission an amber workshop in Königsberg to create one. When the window frame arrived, two months before the mirrors, it was discovered that the makers had measured it incorrectly. It took another six weeks to correct the problem (Gierlowski, 2006a).

The Amber Room was completed in late 1745 but was moved again and reassembled in other rooms within the Winter Palace several times before August 1755, when Empress Elizabeth I ordered the entire room to be dismantled a final time and moved about 24 km (15 miles) out of the city to Tsarskoye Selo, a royal preserve that held the newly constructed palace (also designed by Rastrelli) named for Elizabeth's mother, Catherine I.

The Catherine Palace was one of the largest in Europe. The square chamber selected for the Amber Room was even more spacious than the Winter Palace site and nearly three times the size of the original Prussian cabinet room, despite the fact that one wall consisted mainly of three very large arched windows. The 12 amber panels covered 68.5 square meters and the other elements an additional 5.57 square meters. The wall space of the square room in the Catherine Palace, whose ceiling stood nearly twice as high as the original room, was approximately 216 square meters. And no amber craftspeople who resided in the region possessed the skills to create additional panels.

Rastrelli's goal was to convey the impression that the three walls were composed almost entirely of amber. To occupy the additional space, Rastrelli added 18 mirrored pilasters to separate the amber panels. To account for the ceiling height, he raised the amber panels onto a stone base and placed an elaborate gilded cornice above them. The decorations on the cornice were wreath patterns carved in relief, all coated with gold foil. Above the cornice, Rastrelli commissioned artist Ivan Belsky to paint a simulated amber mosaic on a 30 × 2.68 meter canvas. The canvas was mounted over the three non-windowed walls to fill the space between the top of the cornice and the ceiling, creating the illusion that this upper portion was also lined with amber. He painted imitation amber panels to fit in the narrow strips between the double pilasters. Rastrelli also mounted gilded figures, carved reliefs, and gilded bronze candelabras on top of the painting, further obscuring the facade. The wooden panels over the double doors were painted white and covered by gilded reliefs (Gierlowski, 2006a).

To replace the van Groot oil paintings from the Winter Palace amber panels, Rastrelli commissioned Florentine artist and printer Giuseppe Zocchi to create four mosaics depicting the five human senses (sight, hearing, touch, smell, and taste) that would be mounted in the same amber frames as the oil paintings. Craftsmen also created a parquet floor containing 15 different varieties of wood, each a different shade, set in circular motifs (Gierlowski, 2006a).

The basic design was completed in 1756, and Empress Elizabeth began using the room for official functions. However, the many moves had damaged some of the original amber pieces, and she wanted to add amber furnishings to complement the room. Much work was needed before the panels would be completed to her satisfaction.

In 1758 the empress appointed Friedrich Roggenbucke, a noted amber craftsman in Königsberg, to serve as the room's curator and to create amber-covered tables, chests, and bureaus for it. Roggenbucke established an on-site workshop and brought in amber workers from his native city to train local workers, who were mostly recruited from nearby villages. These craftsmen added an amber section over the middle door, replacing a wooden section, and set amber mosaic strips in the narrow sections between the mirrored pilasters and in other small spaces throughout the room (Owen, 2009).

Contemporary reports said that the staff worked long hours (for 12 rubles yearly) because continual repairs were necessary. The palace was not occupied and not heated during the cold Russian winters. When it was occupied, the heat from the 550 wall-mounted candles could make the room very warm.

Figure 5. The only known color photograph of the original Amber Room, taken in Tsarskoye Selo in 1937. This photograph helped researchers establish the design and color scheme of the reconstructed Amber Room. Photo courtesy of Amberif.

The extreme changes of temperature and humidity created problems. The temperature-sensitive glue and the wood base expanded or contracted with the changes, causing some of the amber pieces to crack or fall off (Gierlowski, 2006a; Owen, 2009; figure 5).

Besides making continual repairs, the staff constructed a number of amber furniture pieces and small *objets* to furnish the room. While there was no formal opening ceremony, researchers and historians agree that the main design and construction, other than conservation and repair, was completed in 1780, some 73 years after the project was begun (Gierlowski, 2006a).

THE LOOTING OF THE ROOM

The Amber Room remained in the Catherine Palace relatively unchanged, except for restorations in 1833, 1865, and 1890. After the Russian Revolution of 1917, the palace was turned into a museum. The room remained intact, though not on public display. Conservation efforts were minimal. In 1937, the Soviet government renamed the town that surrounded the Tsarskoye Selo preserve to Pushkin.

With the invasion by three million German troops in the summer of 1941, Soviet officials began evacuating palace treasures east toward Siberia. As the Germans advanced toward St. Petersburg, the curators of the Amber Room attempted to dissemble and evacuate the panels for safekeeping. But the years had made the amber very brittle, and the pieces crumbled easily, forcing the curators to abandon the effort. Instead, they covered the room with wallpaper veneer in an attempt to disguise the amber (Krylov, 1999).

By September 1941, the German army had advanced to the outskirts of Leningrad and occupied Pushkin and the Catherine Palace. The Amber Room was a priority for removal because it had been included in the Kummel Report, a list of German-made artworks to be "repatriated" to German soil (Owen, 2009). The German army dismantled the room panels and decorations within 36 hours, packing it in 27 crates, and shipped it by rail to Königsberg, where it was reassembled and displayed in the city's castle (Krylov, 1999). Two years later, museum director Dr. Alfred Rohde was ordered to dismantle the room again and crate it in the event that British or U.S.

bombers attacked the city. The room panels were last seen January 12, 1945, when Dr. Rohde wrote that the amber panels were being crated. "As soon as it is done, I shall evacuate the panels to Wechselberg near Rochlitz in Saxon" (Owen, 2009). By then the Allied air raids on Königsberg had already begun, though the castle had remained intact. The air raids eventually destroyed most of Königsberg Castle, leaving the outer walls and some battlements. In the spring of 1945, Soviet troops advanced into the city and leveled the remainder of the castle.

Immediately following the war, the Soviet government made finding the Amber Room a priority. It seized the territory of East Prussia as a Russian province (including Königsberg, renamed Kaliningrad in 1946), and soon afterward dispatched a group of investigators to search the ruins of the castle. They located several items of furniture from the Catherine Palace in an intact tower and, the following year, discovered the ruins of three of Giuseppe Zocchi's Florentine mosaics from the room (Owen, 2009; figure 6).

While there have been numerous theories about the fate of the Amber Room, the only certainty is that it disappeared between the time of the German invasion in 1941 and the arrival of the Soviet troops in Königsberg in 1945. Erich Koch, the SS commander who had ordered the removal of the amber panels from the city, reportedly led a group of Russian officials on a search during the 1950s but failed to find them. He died in 1986 without ever providing additional information (Grimaldi, 1996; Blumberg, 2007). In 1967, the Soviet government formed a commission to systematically search known art repositories in the USSR and Germany for the Amber Room panels. The commission continued the search until 1984, five years after the decision was made to recreate the room (Owen, 2009).

Most historians believe that the Amber Room was destroyed by Allied bombing raids on the castle after January 1945 or the subsequent Russian invasion and shelling of the city. One museum conservator, an amber expert, noted that the panels, if ever discovered, would be too deteriorated to be of any use today (Varoli, 2000). Since the war's end, numerous parties have appeared from time to time claiming, without substantiation, to have found the missing amber panels. Most recently, in October 2017, a group of treasure hunters claimed to have located them behind the doors of a Polish bunker (Wight, 2016; "Amber Room: Priceless Russian treasure…", 2017).

While the room panels have never been found, some pieces of the original have surfaced over the years, most importantly one of the Zocchi mosaics, "Touch and Smell." The ruins of the other three mosaics were found in the destroyed Königsberg Castle in 1945, and this piece had been considered lost until then. It was offered for sale by Meinhardt Kaiser to an antiques dealer in Bremen, Germany, in 1997. The dealer alerted police, and Kaiser led them to a man named Rudi Wurst, whose father had been part of the SS unit that escorted the train carrying the Amber Room components from the Catherine Palace to Königsberg in 1941. Police believe that this piece had been long separated from the rest of the room's treasures. Locating it helped the restorers achieve much greater historical accuracy in their recreation (National Geographic, 2004; Owen, 2009; A. Krylov, pers. comm., 2017).

Figure 6. This photo, purportedly taken by a German soldier, shows the destruction of the Catherine Palace during the German siege of St. Petersburg in World War II. The panels from the Amber Room were seized by the German army at the beginning of the siege and transported to a castle in Königsberg for display. They were never recovered after the war. Photo courtesy of REX/Shutterstock.com.

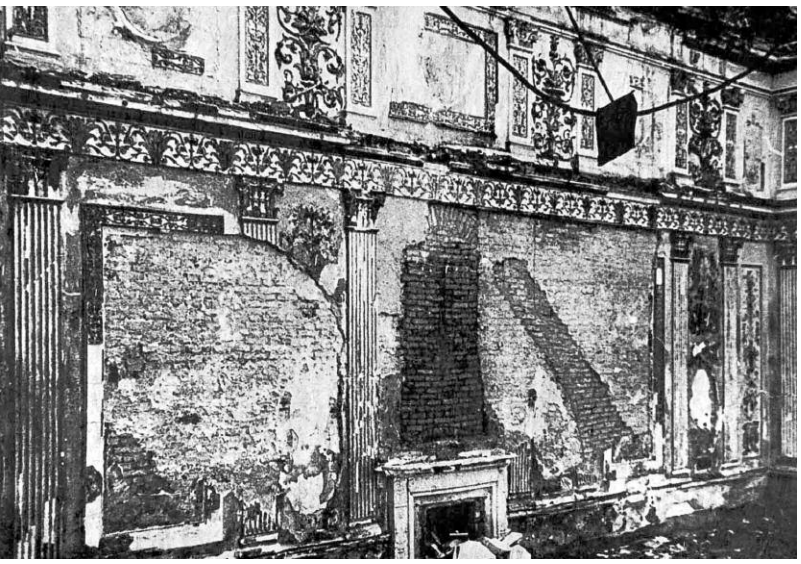

THE RECONSTRUCTION

The end of World War II left the entire Catherine Palace in ruins. An exhibit of wartime photographs (Tsarskoye Selo State Museum, 2013) shows part of the palace ablaze and some interior images of the ruined structure. A photograph purported to be of the

Amber Room shows the walls completely stripped to bare brick, except for fragments of the paintings above the cornice. The roof is collapsed, leaving the room exposed to the elements.

In the 1950s, the Soviet government embarked on a project to restore this and other historical sites destroyed and damaged during the war. Reconstruction took 25 years, and the Catherine Palace was reopened to the public in the summer of 1980. The Amber Room, however, had only been minimally renovated. The imitation amber mosaic painting over the cornices had been redone, and the parquet floors, decorated ceilings, and mirrored pilasters were all restored as closely as possible to the original designs. The walls, however, remained unadorned (Zhuravlov, 2006). The empty walls were temporary; in April of the previous year, the Federal Council of Ministers had issued an order to begin reconstruction of the panels for the Amber Room (Gierlowski, 2006a). The mandate was to recreate the room as closely as possible to the design completed in the eighteenth century. The challenge was formidable since very little documentation of the original room existed. Available resources included:

- Eighty-six black-and-white photographs of the room, taken in the late 1930s for a planned restoration.
- A single color slide of one section of the room, from 1937. The slide showed the southwest corner and included two of the mosaics, their frames, six mirrored pilasters, the statues, candelabras, and the gilding around the cornice. The slide provided some information on how various colored pieces of amber were assembled on the walls in irregular but aesthetically pleasing patterns.
- Seventy-six amber fragments found in the destroyed room. Some were pieces of wall decorations and chips from amber carvings. These gave researchers information on the thickness and hues of the amber pieces used on the walls.
- A miniature chest assembled with amber, dating from the time of the Amber Room construction, which survived in the Catherine Palace collection but was in very poor condition (Krylov, 2006). While working on its restoration, the team found the signature of Gottfried Turau. Thus, the team had an opportunity to study firsthand the techniques of one of the room's creators (Gierlowski, 2006b).
- The curator of the Amber Room from 1916 to 1941, Anatoly Kuchumov, who was still alive and able to help plan the reconstruction.

Other than the amber itself and the oak frames and base, no one knew the composition of the other materials employed in the frames and adhesives (M. Trutanova, pers. comm., 2017).

With so little to guide them, several years of research were necessary before the reconstruction could begin (M. Trutanova, pers. comm., 2017). The research team, assembled two years before the decision to begin the reconstruction, was composed of Alexander Krylov, Alexander Zhuravlov, and three other graduates of the Mukhina Academy of Arts and Design at Leningrad State University (now St. Petersburg State University). They began by studying other amber objects that had been removed from the Catherine Palace well before the German invasion, examining the few amber objects that had been removed from the palace and hidden in a Siberian bunker just prior to the invasion. In addition, the research team assembled all the documents on seventeenth- and eighteenth-century amber craft they could locate, including an original drawing by Andreas Schlüter from 1701 (Krylov, 1999). They enlarged and enhanced the grainy 1930s photographs to reveal shadings and grayscales that would offer clues to color patterns of the amber mosaics and details in the carvings (Owen, 2009).

Each piece was cleaned thoroughly and photographed on a white background. They were matched against similar pieces located in the photographs, which allowed the team to match the actual color in the reconstructed elements (Krylov, 2006).

The researchers tested what they had learned from restoring and reconstructing other amber objects such as furniture and sculptures that resided in the Hermitage Museum and Pavlovsk Palace, both in St. Petersburg, and the Oruzheynaya Palace in Moscow. Between 1979 and 1984, the team, which included Zhuravlov and Krylov, recreated a number of historical pieces. Among these were a chessboard with 32 carved figures, the original of which was made in Germany in the eighteenth century and housed at the Hermitage; a casket bearing a figure of the Greek goddess Dione, also from the Hermitage, that was made in Danzig in the seventeenth century; a large cameo with a likeness of Empress Elizabeth from the Amber Room; and six amber obelisks from Pavlovsk (Zhuravlov, 2006). To test their techniques, they created a model panel of the Amber Room from simulated amber (Owen, 2009).

It took three years from the official approval before the room reconstruction could begin in earnest. The Restavrator, the team that would perform all of the reconstruction work, was formed in 1982. Headed by Boris Igdalov and including Marina Trutanova, they commenced work in a studio in St. Petersburg (Zhuravlov, 2006). The distance between St. Petersburg and Pushkin would allow the work to be kept secret (Owen, 2009).

Much research remained, however. First, the teams investigated the wood to use for the baseboards and the adhesives to hold the amber pieces in place. For the baseboards, the restoration team decided to use pressure-treated pine rather than the oak used in the original, because it would be less likely to absorb moisture or expand and contract with changes in temperature and humidity. The foil backing chosen for the amber was brass instead of bronze (M. Trutanova, pers. comm., 2017).

To determine the makeup of the adhesive, the research team submitted several of the surviving pieces of amber to the Leningrad Institute of Criminal Investigation. Through spectroscopic analysis, the Institute found that the adhesive consisted of 40% beeswax and 60% dammar resin, a gum from the Dipterocarpaceae family of trees in India and East Asia that was used for ship caulking at the time the original room was constructed (Zhuravlov, 2006). Determining the correct adhesive was more than a matter of historical accuracy. Permanent adhesives were not suitable because they would have prevented the replacement of amber pieces broken during the reconstruction process or in future repairs or restorations. In addition, permanent adhesives would likely crack over time (M. Trutanova, pers. comm., 2017).

Using the crime lab's findings as a guide, the reconstruction team developed an adhesive from beeswax and a type of pine resin that melted at about 140°F (60°C). This combination allowed workers to use a commercial hair dryer to apply or remove amber pieces. The research team tested this and other adhesives, subjecting them to heat (three hours at 40ºC), cold (2.5 hours at –15ºC), ultraviolet light (2.5 hours), and a high-moisture environment (14 hours) (M. Trutanova, pers. comm., 2017; A. Zhuravlov-Nikiforova, pers. comm., 2017). Next was acquiring the amber. The research team estimated that the reconstruction would require 6,000 kg of "best-quality" amber. The wall areas measured 86.12 square meters. The decorative objects and motifs would require an additional 122 square meters of material. The average thickness of each piece of amber was planned at 5 mm, similar to the original (Zhuravlov, 2006).

With the approval of the Soviet government, the reconstruction team was given access to the amber deposits in the Sambia Peninsula, which were then under state control. While the amount of amber required for the reconstruction was substantial (6,000 kg or 3 metric tons), production in the Samland region was much higher, ranging between 595 and 744 metric tons yearly from 1979 to 1988 (Kosmowska-Ceranowicz, 2006).

With supplies assured by the Soviet government, the workshop team began researching dyes and treatments that would have been used in the eighteenth century to recreate the yellow to reddish orange patterns on the original walls. No one knew what materials were used for the original dyes, so a team from the Leningrad Institute of Technology developed dyes that would not fade, change color, or fully absorb into the amber (Gierlowski, 2006b). While the ingredients used in the dyes are proprietary, the process involves immersing the amber into boiling water for 10 minutes, with the appropriate dyes added afterward (M. Trutanova, pers. comm., 2017). However, a division developed among researchers between those who wanted to employ natural-color amber and those who wanted to dye the material to the darker shades it had assumed by the time the 1937 color slide was taken. Ultimately, the latter group prevailed (Gierlowski, 2006a).

Before dyeing, the amber to be mounted on the wall in mosaic patterns was sliced to 3 mm thick instead of the planned 5 mm—presumably a cost reduction—and then fitted onto the wood panel without adhesive. The reconstruction team then numbered each piece and dyed them the appropriate colors (M. Trutanova, pers. comm., 2017). Not all of the reconstruction followed eighteenth-century techniques. Some of the amber was treated at high pressure and temperature to improve its translucency and match the colors from the original room. The material was placed in pressure chambers filled with nitrogen or argon, and then heated to 300°C. In other cases, pressed amber—material left over from carvings or cuttings, ground into powder, and pressed into the appropriate shapes before dyeing—was used in the reconstruction (Gierlowski, 2006b). In all, 4.2 square meters of pressed amber was used in the wall panels.

The amber mosaics lining the wall panels were only the beginning of the reconstruction. The ornate decorative motifs such as scrolls, wreaths, laurels

Figure 7. A corner section and end table showing the detail of the multi-hued recreated amber mosaics, the bas-relief employing darker shades of amber, and the table itself, which is also coated with amber. Photo courtesy of Amberif.

(which used the darkest-colored pieces), floral bas-reliefs, and objects such as grotesques and other sculptures were all made from carved amber. While the carving and assembly skills required were transferable from jewelry and sculpting crafts, they proved extremely time-consuming (Krylov, 2006; figure 7). Working from the black-and-white photos, the workshop recreated the destroyed Zocchi mosaics of the senses using jasper, malachite, quartz, chalcedony, and nephrite.

The comparison with the recently discovered Zocchi mosaic in Bremen validated their reconstructive work, which was nearly identical to the original. The only exception was in the materials—the original contained various colored marble slices instead of the decorative stones used by the studio (Krylov, 2006). The original mosaic is kept in storage at the palace but put on display for significant occasions (M. Trutanova, pers. comm., 2017; see figures 8–10).

After the collapse of the Soviet Union in 1991, the Russian government could no longer fund the project, and work was nearly suspended with fewer than 40% of the panels completed (Varoni, 2000). The Restavrator studio, which numbered about 50 artisans, was liquidated, though some work continued. Up to that point, the government had spent the equivalent of US$7.85 million on the reconstruction—largely on salaries since the amber had been provided as a state

Figure 8. A craftsman in the Tsarskoye Selo Amber Workshop completing a carving for the mosaic "Touch and Smell" from slices of jasper, malachite, quartz, chalcedony, and nephrite. Photo courtesy of Tsarskoye Selo Amber Workshop.

Figure 9. Detail of the original "Touch and Smell" mosaic panel made from colored marble pieces. The panel was apparently stolen by a German officer as the contents of the Amber Room were being evacuated from Königsberg Castle in 1941. It was discovered in Bremen, Germany, in 1997. Photo courtesy of Tsarskoye Selo Amber Workshop.

resource (A. Zhuravlov-Nikiforova, pers. comm., 2017). The new market economy meant that instead of relying upon the Russian government for funding, the company had to raise funds from private sources (Gierlowski, 2006b).

Figure 10. Detail showing the Florentine mosaic "Sight," one of four such recreated mosaics in the room. The frames are fashioned from carved and sliced pieces of amber of various hues. Photo courtesy of Amberif.

Through the intercession of Dr. Burkhart Gores, the director of the Prussian Palaces and Gardens Foundation, funding was obtained in 1999 from the German energy company Ruhrgas, which had extensive dealings in Russia (Owen, 2009). Ruhrgas agreed to provide an additional US$3.5 million to complete the reconstruction and ordered its completion by April 2003. Ruhrgas chairman Friedrich Spath told the *New York Times*, "The Amber Room has enormous emotional significance for both Germany and Russia. And it is a leading symbol of a time when close German and Russian relations were a model for the world." At that time, Ruhrgas was receiving one-third of its natural gas supplies from Russia (Varoli, 2000).

With new funding, the Restavrator reorganized into a corporation named the Tsarskoye Selo Amber Workshop to resume its work full time and complete it by the contracted deadline. The new company also began earning income by manufacturing and selling amber carvings, miniature chests, and chess sets that resembled historical pieces, and taking commissions to restore or reconstruct other amber pieces in museums. This, along with the use of synthetics, raised objections from some members of the research team who felt they were acting against the Venice Charter of 1964, which forbids the use of contemporary techniques and materials and "conjecture" in reconstructing historical monuments (Gierlowski, 2006b; Owen, 2009).

Figure 11. Two sections of the reconstructed Amber Room wall showing the mirrored pilasters that separate the panels, the Florentine mosaics, and the intricate amber wreaths and clusters on and atop the cornice. Photo by Sergey Bogomyako/Shutterstock.com.

The completed room used some 100,000 pieces of amber encompassing more than 150 square meters of wall space. While the design was as faithful as possible, some who remembered the original Amber Room believed the reconstructed room was brighter, though others countered that the varnishes used on the amber surfaces in previous repair and restoration efforts had darkened over the years (Owen, 2009; see figures 11 and 12).

In May 2003, as the city of St. Petersburg celebrated its 300th anniversary, a summit of world leaders—including Russian President Vladimir Putin, German Chancellor Gerhard Schroeder, U.S. President George W. Bush, French President Jacques Chirac, British Prime Minister Tony Blair, Italian Prime Minister Silvio Berlusconi, and Japanese Prime Minister Junichiro Koizumi—formally opened the reconstructed Amber Room to the public. According to saint-petersburg.com, the tourist attraction receives about 7,000 daily visitors during the peak summer months.

The Tsarskoye Selo Amber Workshop remains on site for ongoing maintenance because the temperature-sensitive adhesives require constant attention. Amber itself is called a "living stone" that can react to relatively small changes in temperature and humidity. Inspectors check the room weekly (*After the Amber Room*, 2013). Other rooms in the Tsarskoye Selo complex are also undergoing reconstruction, including the church, the Agate Room, and the Catherine Palace Museum, as well as restoring amber artifacts in other Russian museums. In addition, the

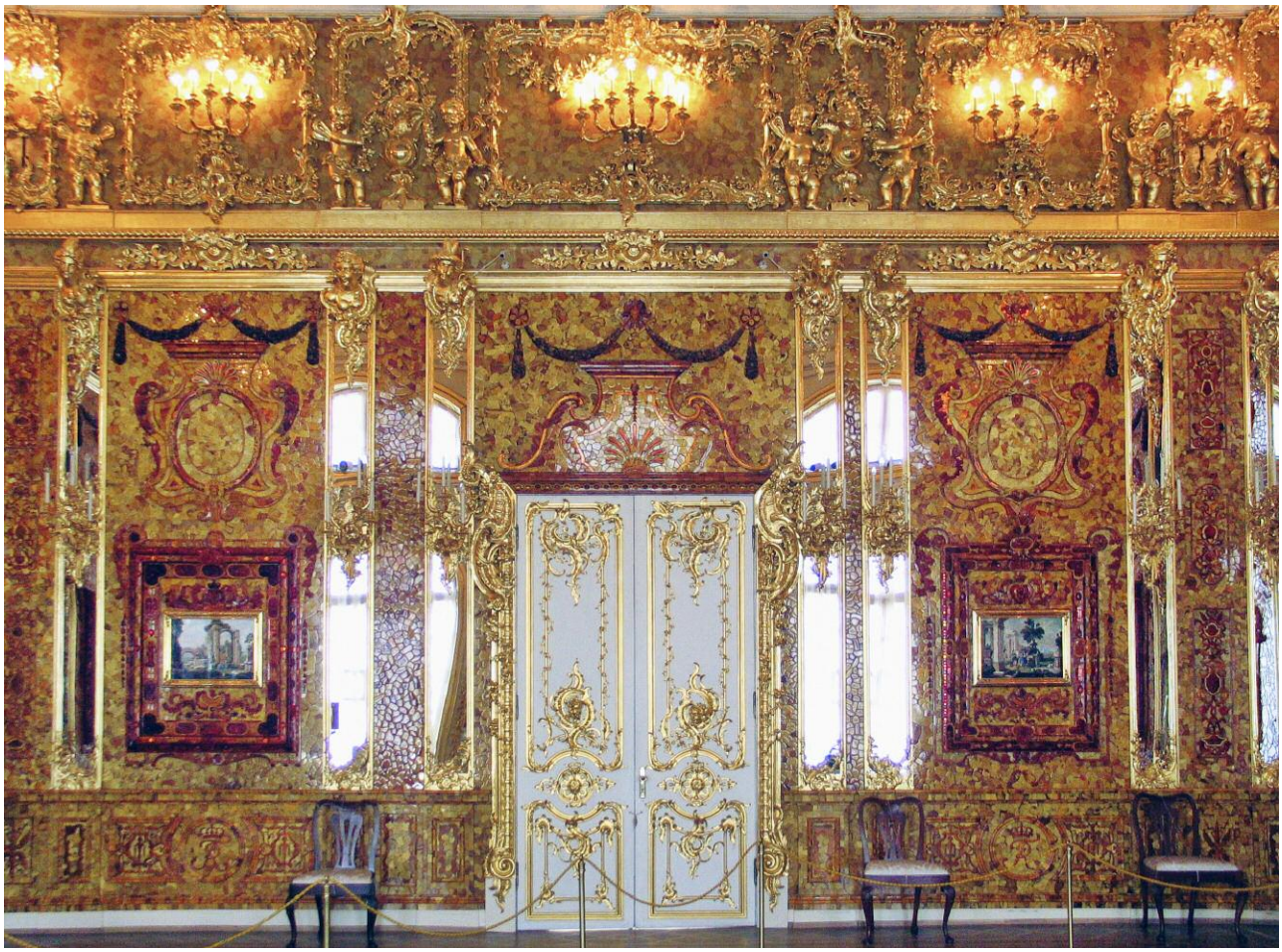

Figure 12. A section of the wall of the reconstructed Amber Room. Photo courtesy of Amberif.

studio continues to produce amber objects for sale to help offset the high costs of maintaining the Amber Room.

CONCLUSIONS

Although many articles have been written about the original Amber Room, few have documented its reconstruction, and fewer still have offered detailed accounts of both the original and reconstructed rooms. Its reconstruction was fraught with a number of challenges, but the result is regarded as being faithful to the version of the Amber Room that was housed in the Catherine Palace from 1780 to 1941. Firsthand accounts from the principal researchers, designers, and builders of the reconstructed room describe a combination of eighteenth-century techniques, many of which had to be relearned or adapted to modern materials, offering insight into the significant challenges encountered to reconstruct this cultural landmark.

ABOUT THE AUTHOR

Mr. Shor is a senior industry analyst at GIA in Carlsbad, California.

ACKNOWLEDGMENTS

The author would like to thank Ewa Rachon, project director at Amberif and Amber Mart (Gdansk, Poland), who provided introductions and offered valuable insights for the manuscript; Alexander Krylov, an amber craftsman who helped design the reconstruction; and Anastasia Zhuravlev-Nikiforova, who provided some of her father's, Alexander Zhuravlov's, papers on the reconstruction of the room. Boris Igdalov and Marina Trutanova of the Amber Workshop (Tsarskoye Selo) are thanked for sharing their research and invaluable expertise.

REFERENCES

After the Amber Room: History of the Tsarskoselskaya Workshop (2013) Avrora-Design, St. Petersburg.

Amber Room: Priceless Russian treasure stolen by Nazis "discovered" by German researchers (2017) www.independent.co.uk/news/world/europe/amber-room-nazis-russian-catherine-palace-st-petersburg-tsar-second-world-war-stolen-treasure-a8008526.html

Blumberg J. (2007) A brief history of the Amber Room. Smithsonian.com, https://www.smithsonianmag.com/history/a-brief-history-of-the-amber-room-160940121/

Butrimas A., Jovaiša E. (2013) The Balt's amber route to classical civilization. Paper presented at International Amber Researcher Symposium, March 20–23.

City of Gdansk (2017) Gdansk treasures – amber. www.gdansk.pl/en/about-gdansk/Gdansk-treasures-Amber,a,3019

Clark N.L.D (2010) *Amber: Tears of the Gods*. Dunedin Academic Press, Edinburgh, pp. 23–28.

Czebreszuk J., Szmyt M. (2013) Amber in Europe 3000 Years BCE. Paper presented at International Amber Researcher Symposium, March 20–23.

Gaigalas A., Halas S. (2009) Stable isotopes (H,C,S) and the origin of Baltic amber. *Geochronometria*, Vol. 33, No. 1, pp. 33–36, http://dx.doi.org/10.2478/v10003-009-0001-9

Gierlowski W. (2006a) Amber Room – the founders and creators. In B. Kosmowska-Ceranowicz and W. Gierlowski, Eds., *Amber: Views, Opinions. Scientific Seminars: AMBERIF—1994–2005*. International Amber Association, Gdansk, Poland, pp. 147–155.

——— (2006b) Reconstruction of the Amber Room as an impulse for the creation of copies and reconstructions of lost historical artifacts. In B. Kosmowska-Ceranowicz and W. Gierlowski, Eds., *Amber: Views, Opinions. Scientific Seminars: AMBERIF—1994–2005*. International Amber Association, Gdansk, Poland, pp. 165–172.

Grimaldi D.A. (1996) *Amber: Window to the Past*. Harry N. Abrams Inc. in association with the American Museum of Natural History, New York, pp. 147–191.

Hein J. (1991) Ivories by Gottfried Wolfram. *Scandinavian Journal of Design History*, Vol. 1. pp. 7–34.

Kosmowska-Ceranowicz B. (2006) Finds, deposits and mines of amber and other fossil resins. In B. Kosmowska-Ceranowicz and W. Gierlowski, Eds., *Amber: Views, Opinions. Scientific Seminars: AMBERIF—1994–2005*. International Amber Association, Gdansk, Poland, pp. 9–13.

——— (2009) Baltic amber deposits. *InColor*. Fall/Winter, pp. 22–24.

Krylov A. (1999) Reconstructing the amber masterpiece. Paper presented at International Amber Research Symposium, March 23–24.

——— (2006) Reconstructing the Amber Room. Selected problems. In B. Kosmowska-Ceranowicz and W. Gierlowski, Eds., *Amber: Views, Opinions. Scientific Seminars: AMBERIF—1994–2005*. International Amber Association, Gdansk, Poland, pp. 160–162.

Langenheim J.H. (1990) Plant resins. *American Scientist*, Vol. 78, No. 1., pp. 16–24.

Mazurowski R. (2011) From the research on the Late Neolithic amber art in the Neidzwiedziowka microregion near Nowy Dwor Gdanski (3100–2400 BCE) Session of the World Amber Council, May 27–28. http://prusaspira.org/pogezana/Bursztyn.pdf

National Geographic (2004) The mystery of the Amber Room. https://video.nationalgeographic.com/video/treasure-wars/amber-room-tw

Netzer S. (1993) Bernsteingeschenke in der Preussischen Diplomatie des 17 Jahrhunderts. *Yearbook of the Berlin State Museum, Berlin*, pp. 227–246.

Owen J. (2009) Forever amber: The impact of the Amber Room on Russia's cultural stature then, now and in the future. Master's thesis, Georgetown University, Apr. 27, https://repository.library.georgetown.edu/bitstream/handle/10822/552838/owenJennifer.pdf

Tsarskoye Selo State Museum (2013) The loss of the palaces: Tsarskoye Selo in 1941–1944. http://eng.tzar.ru/shows/show/archive/?id=3142

Varoli J. (2000) Amber Room, lost to war, is recreated. *New York Times*, Jan. 23, https://www.nytimes.com/2000/01/23/arts/art-architecture-amber-room-lost-to-war-is-recreated.html

Wight E. (2016) Is 60-year hunt for the missing $400million Amber Room finally over? Daily Mail, Apr. 22, http://www.dailymail.co.uk/news/article-3552241/Is-60-year-hunt-missing-250million-Amber-Room-FINALLY-New-images-Nazi-looted-treasure-hidden-sealed-wall-secret-room-underground-bunker-Poland.html

Zhuravlov A. (2006) Amber Room - Beginning the reconstruction. In B. Kosmowska-Ceranowicz and W. Gierlowski, Eds., *Amber: Views, Opinions. Scientific Seminars: AMBERIF—1994–2005*. International Amber Association, Gdansk, Poland, pp. 155–162.

The Color Origin of Gem Diaspore: Correlation to Corundum

Che Shen and Ren Lu

Color-change diaspore, known commercially as Zultanite, is sought by designers and consumers for its special optical characteristics, namely its color and color change. Understanding the color origin of gem-grade diaspore could provide a scientific basis to guide its gemological testing, cutting, and valuation. This study uses ultraviolet-visible (UV-Vis) spectra and laser ablation–inductively coupled plasma–mass spectrometry (LA-ICP-MS) to examine the color origin of color-change diaspore and to compare it with corundum. As Raman spectra vibration intensities are closely related to crystal direction for diaspore, crystal orientation was determined through Raman spectroscopy. The color correlation between color-change diaspore and corundum confirmed the identity of each chromophore. In addition, the effectiveness of different chromophores such as Cr^{3+}, Fe^{3+}, Fe^{2+}-Ti^{4+} pairs, and V^{3+} between gem-quality diaspore and corundum is compared quantitatively.

Gem-quality diaspore occupies an important position in the gem market due to its rarity, striking pleochroism, and color-change phenomenon (figure 1). The material's value depends on these factors. A clear understanding of color origin offers considerable benefits for gemological testing, cutting, and even valuation of gem diaspore.

By replacing the major elements in definite structural units through isomorphous substitution, trace elements play an important role in the color of gemstones. The AlO_6 octahedra is a significant structural unit that produces color when different trace elements substitute for Al. For example, Cr^{3+} substitutes for Al^{3+} in the AlO_6 octahedra in jadeite and spinel, causing green and red color (Lu, 2012; Malsy, 2012), while the substitution of Fe^{3+} for Al^{3+} in sapphire produces yellow color (Emmett et al., 2003).

Diaspore and corundum have a similar chemical composition and crystal structure (see figure 2). Diaspore, with the chemical formula AlO(OH), belongs to the orthorhombic space group 2/m 2/m 2/m (Hill, 1979); corundum, with the chemical formula Al_2O_3, belongs to the trigonal space group $\overline{3}$ 2/m (Lewis et al., 1982). The crystal structure of diaspore consists of $AlO_4(OH)_2$ octahedra, whereas the corundum crystal structure consists of AlO_6 octahedra (Hill, 1979; Lewis et al., 1982). Both types of crystals are composed solely of octahedral units. In addition, the diaspore structure is able to convert to corundum structure through dehydration (Iwai et al., 1973). Due to their closely related crystallographic structure and chemical composition, we may speculate that there is also a close color correlation. There are two other reasons for this hypothesis:

1. Compared to other gemstones containing the AlO_6 octahedral structural unit, diaspore and corundum share the closest similarity in average Al-O bond length, octahedral volume, and degree of distortion of octahedral sites (quantified by determining the octahedral quadratic elongation). For specific data, refer to table 1.

In Brief

- Gem-quality diaspore with an attractive color and remarkable color-change phenomenon is rare and often highly valued.
- The AlO_6 octahedral structural unit, a very important structural unit related to gemstone color, is very similar between diaspore and corundum.
- The structural similarity between diaspore and corundum helps us confirm the color origin of diaspore quantitatively.

See end of article for About the Authors and Acknowledgments.
Gems & Gemology, Vol. 54, No. 4, pp. 394–403,
http://dx.doi.org/10.5741/GEMS.54.2.394

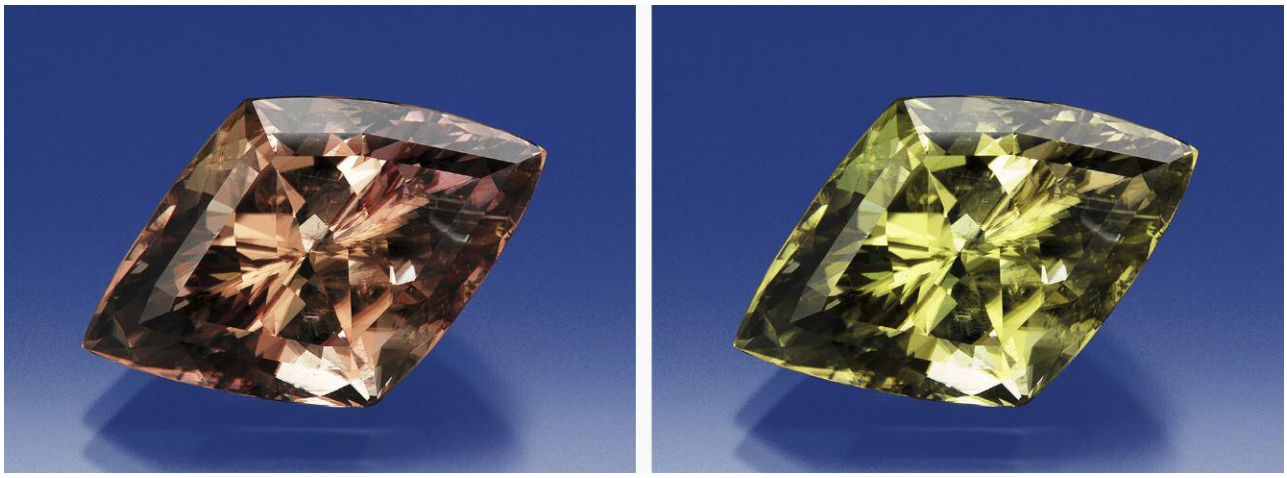

Figure 1. This 24.60 ct color-change diaspore is shown under D65 illumination (left) and A illumination (right). Photos by Robert Weldon, courtesy of Zultanite Gems LLC.

2. The structural similarity between corundum and diaspore was first referred to by Deflandre (1932). Both diaspore and corundum are connected by octahedral units, and both contain edge-shared octahedra. However, there are face-shared octahedra along the c-axis that only exist in corundum, and this is the main difference between the two. Other related studies involving X-ray powder photography (Francombe and Rooksby, 1959), single-crystal X-ray techniques, scanning electron microscopy (SEM), and high-temperature optical microscopy (Iwai et al., 1973) have confirmed a structural similarity between the two gem materials.

This intensely close relationship between corundum and diaspore with respect to the octahedral Al site and their overall structural similarity indicates that chromophores substituted into the Al site of both materials are expected to present similar UV-visible absorption features. Consequently, this study adopts an analogy to address the color origin of diaspore by quantitatively analyzing the trace-element chemistry in diaspore from two geographic origins—Myanmar (formerly Burma) and Turkey—and comparing them with high-quality natural and synthetic corundum. The research aims to use the color correlation between diaspore and corundum to confirm the color origin of gem diaspore.

MATERIALS AND METHODS

Samples. Nine diaspore samples from Turkey were purchased from a gem dealer at the Beijing International Jewelry Show in November 2016. Forty slices of diaspore were collected in the field from Mogok, Myanmar, by author RL. All samples were prepared as wafers. These wafers are perpendicular to the a-axis, b-axis, and c-axis, respectively. Photos of samples are shown in table 2.

Raman and Photoluminescence (PL) Spectroscopy. Raman and PL spectra were collected from the samples with a Renishaw inVia Raman microscope system at the Gemstone Center of Hebei GEO University in China. Raman spectra were collected from 100 to 1400 cm^{-1} using Nd-YAG laser excitation, producing highly polarized light at 532 nm

TABLE 1. Crystallographic parameters of corundum, diaspore, and spinel.

Gemstone	Average distance of Al-O (Å)	Octahedral volume ($Å^3$)	Octahedral quadratic elongation	Deviation of average Al-O distance (% difference from corundum)	Deviation of octahedral volume (% difference from corundum)	Deviation of quadratic elongation (% difference from corundum)
Corundum	1.9133	9.0754	1.0202	0	0	0
Diaspore	1.9154	9.1042	1.0203	0.10976	0.31734	9.8020×10^{-3}
Spinel	1.9327	9.4955	1.0092	1.0140	4.6290	1.0782

Note: The crystallographic parameters are from Lewis et al. (1982), Hill (1979), and Peterson et al. (1991).

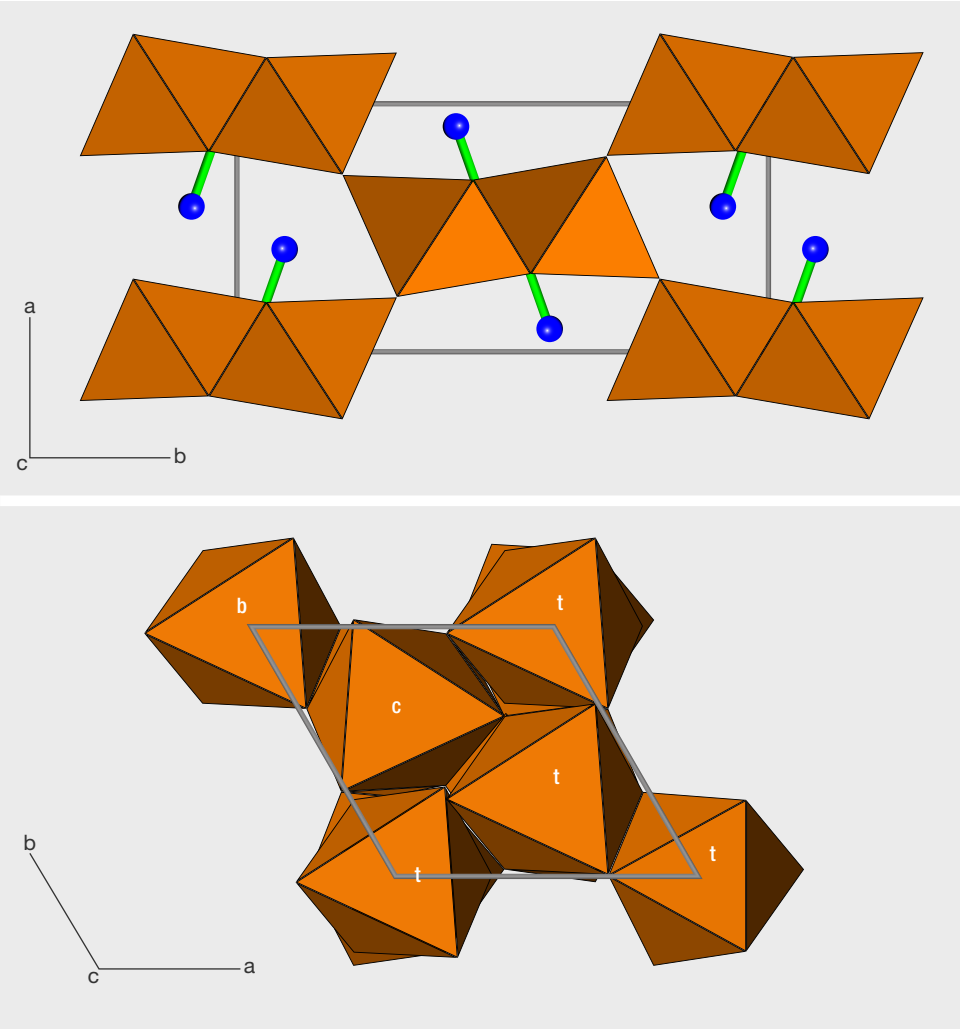

Figure 2. These views of the crystal structure of diaspore (top) and corundum (bottom) illustrate the basic building blocks, $AlO_4(OH)_2$ and AlO_6 octahedra, and their geometric relationships. The crystallographic orientation is shown in the upper left corner projected down the c-axis. The blue spheres in the diaspore's crystal structure represent the hydrogen atoms. The structure is characterized by edge-shared octahedral double-chains, which are extended along the a-axis. The corner-linked octahedral layers are connected along the a-axis. In addition, the OH-vector is approximately parallel to the a-axis. In the crystal structure of corundum, each octahedron is edge-shared, with three octahedra in the a-b plane. All octahedra are face-shared, with one octahedron along the c-axis. The letters b, c, *and* t *represent the different layers in corundum (bottom, center, and top). Based on Hill (1979) for diaspore and Lewis et al. (1982) for corundum.*

(1800 lines/mm grating, 10 s). The orientation of all samples was carefully controlled. The polarization direction of the injected laser was parallel to the a-axis, b-axis, and c-axis. The 600–800 nm spectral ranges for Raman photoluminescence analysis (under liquid nitrogen conditions) were excited by an Nd-YAG laser at 532 nm (1800 lines/mm grating, 10 s).

LA-ICP-MS Analysis. For trace-element analysis, we used an Agilent 7900a ICP-MS coupled with a deep-UV laser at 193 nm excitation at the State Key Laboratory of Geological Processes and Mineral Resources, China University of Geosciences in Wuhan. NIST glass standard SRM 610 and USGS glass standards BHVO-2G, BIR-1G, and BCR-2G were used for external calibration. Ablation was achieved using a 44 µm diameter laser spot size, a fluence of around 5 J/cm^2, and a 6 Hz repetition rate. The diaspore was initially standardized internally with ^{27}Al using a fixed internal standard method. We selected three spots on each sample for general chemical composition.

UV-Vis Spectroscopy. Five diaspore samples (Dia-006-a, Dia-006-b, Dia-006-c, Dia-Bur-001, and Dia-Bur-002) were prepared as well-polished, oriented wafers with various thicknesses. UV-Vis spectra were collected with a Perkin-Elmer Lambda 650 UV-Vis spectrophotometer equipped with mercury and tungsten light sources and photomultiplier tube (PMT) detectors installed in an integrating sphere. The spectra were collected at the Gemological Institute, China University of Geosciences in Wuhan. Polarized spectra were collected in the 300–800 nm range with 1 nm spectral resolution at a scan speed of 267 nm/min. The spectral baseline was corrected by subtracting spectral offsets at or beyond 800 nm, where the chromophores' features were insignificant or nonexistent.

TABLE 2. Trace-element composition of diaspore by LA-ICP-MS (in ppma), with standard deviation in parentheses.

	Dia-006	Dia-008	Dia-Bur-001	Dia-Bur-002
Trace element, with detection limit				
Ti—9	110 (3)	185 (0.9)	220 (13)	418 (5)
V—0.1	6 (0.2)	4 (1)	44 (2)	359 (2)
Cr—1	36 (0.7)	32 (2)	2166 (58)	2081 (29)
Fe—20	1169 (12)	548 (53)	4 (bdl)	1 (bdl)

bdl = below detection limit

RESULTS AND DISCUSSION

Chemical Analysis. Table 2 shows the chemical composition (expressed in ppma) of two diaspore samples from Turkey (Dia-006, Dia-008) and two from Myanmar (Dia-Bur-001, Dia-Bur-002). We concluded that the Burmese samples contained more Cr, while the Turkish diaspore had a higher Fe content. However, the V content of the Burmese samples was higher than that of the Turkish samples, especially in Dia-Bur-002 (358 ppma).

Raman Spectroscopy. Unlike Turkish diaspore, Burmese material often occurs as thin crystals that are difficult to orient by crystal growth characteristics. However, Raman vibration is closely related to crystal direction (see http://rruff.info/diaspore/display=default/R060287). By comparing the Raman spectra of the diaspore from Myanmar with the oriented sample from Turkey, the Burmese diaspore could be oriented properly. Raman spectra of both the Burmese and Turkish diaspore were collected in the 100–1400 cm^{-1} range.

According to previous research by Ruan et al. (2001) and San Juan-Farfán et al. (2011), the band at 154 cm^{-1} is assigned by the rotation of two edge-shared AlO_6 octahedra around the c-axis. The most intense peak, at 447 cm^{-1}, is related to Al-O symmetric stretching modes, which means the different polarization direction of the laser has little impact on this peak. Therefore, we normalized the peak intensity at 447 cm^{-1} and compared the intensity at 154 cm^{-1}. When the polarization direction of the injected laser is parallel to the c-axis, the intensity of the 154 cm^{-1} peak is much stronger than those that run parallel to the b-axis and a-axis (see note on figure 3). Based on figure 4, we can accurately diagnose the

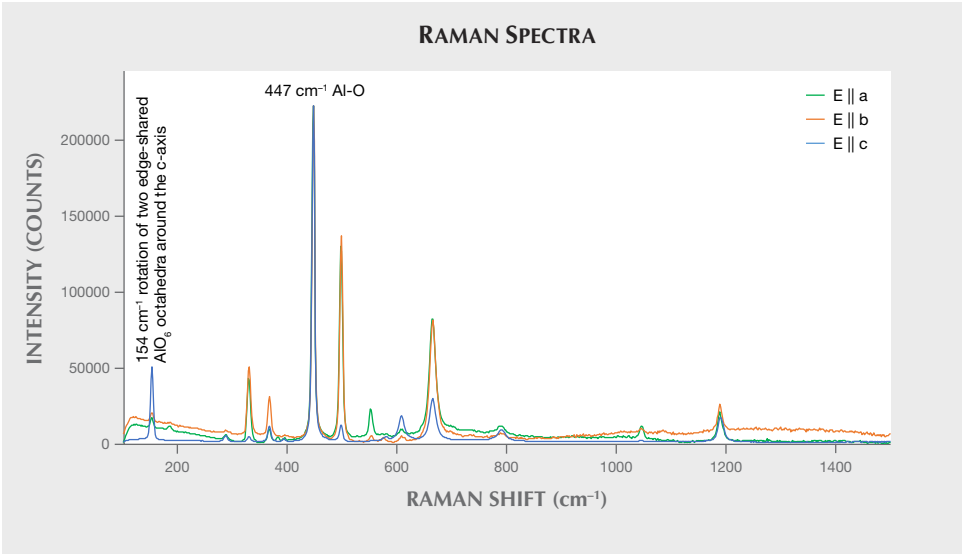

Figure 3. The Raman spectra of the Turkish diaspore, with the polarization direction of the injected laser parallel to the c-axis (blue trace), the b-axis (orange trace), and the a-axis (green trace).

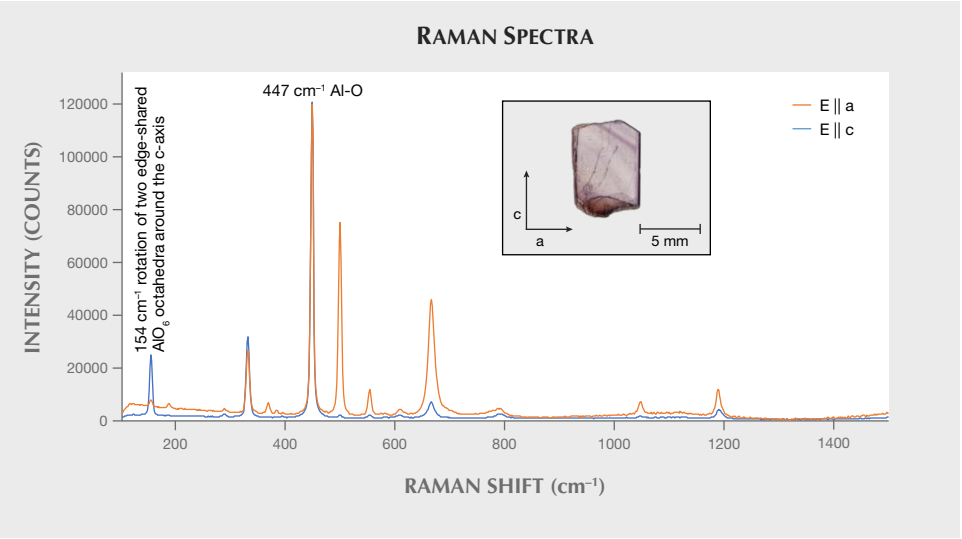

Figure 4. The Raman spectra of Burmese diaspore with the polarization direction of the injected laser parallel to the short side, or a-axis (orange trace), and the c-axis (blue trace).

crystal orientation by Raman vibration (154 cm^{-1}). The Burmese diaspore wafers were manufactured perpendicular to the b-axis based on perfect cleavage along the {010} direction. Hence, we can consider the long side of the wafer parallel to the c-axis, and the short side parallel to the a-axis.

UV-Vis and PL Spectroscopy of Cr^{3+}. Corundum, a uniaxial crystal, shows dichroism. Its UV-Vis spectra are often collected from two orthogonal orientations with polarized light (o-ray and e-ray). As a biaxial crystal, diaspore shows trichroism; its UV-Vis spectra are collected from three orthogonal orientations with polarized light (E ∥ a, E ∥ b, and E ∥ c). In gem cutting, the table of a ruby or sapphire is generally perpendicular to the c-axis. When the polarization direction (E vector) is parallel to the a-axis, diaspore shows UV-visible absorption features similar to those of corundum (see figure 5). Our corundum samples included three synthetic sapphires—a Cr-bearing synthetic ruby, a Fe-Ti bearing synthetic blue sapphire, a V-bearing color-change sapphire—and one natural yellow Fe-bearing sapphire from Garba Tula, Kenya.

In order to make our initial comparisons between chromophores in corundum and diaspore, we have chosen to compare the spectra of corundum collected from the o-ray (R. Lu, previously unpublished data) with those of diaspore collected from the orientation of polarized light parallel to the a-axis. From LA-ICP-MS data, we know that the Cr content is significantly higher in Burmese samples than in Turkish samples. However, as the Fe content is near

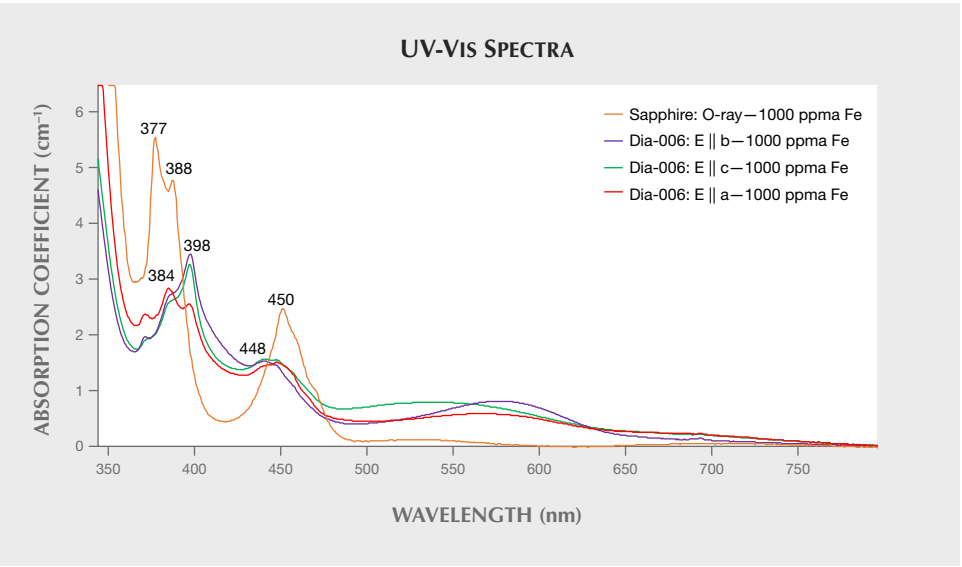

Figure 5. The three polarizations of diaspore (E ∥ a, E ∥ b, E ∥ c) were collected to compare with the spectra of sapphire (o-ray). Peaks at 377 and 388 nm in sapphire and at 384 and 398 nm in diaspore are attributed to Fe^{3+}. The height of sapphire's 377 and 388 nm peaks (384 and 398 nm in diaspore) is closely related to directionality. In diaspore, the best match with the spectrum of corundum (o-ray) is shown when the polarization direction is parallel to the a-axis (E ∥ a).

BOX A: SPECTRAL FITTING BASED ON THE BEER-LAMBERT LAW

There are additive properties that exist in a UV-Vis spectrum. A simple mathematical step will lead to the following equation:

$$A = A_1 + A_2 + \ldots + A_n$$

where:

- A is total absorbance of all absorbers
- A_1, A_2, … , and A_n are the absorbance of each absorber n

Figure A-1 illustrates how this is accomplished.

According to the Beer-Lambert law, the absorption is proportional to the concentration of absorbers (chromophores) through which light passes. It can be expressed simply by the following mathematical expression:

$$A = 1 \sum_{i=1}^{n} \varepsilon_i c_i$$

where:

- A is absorbance
- l is the path length of the light beam through the material sample
- ε_i is the molar attenuation coefficient or absorptivity of the attenuating species i in the material sample
- c_i is the concentration (in ppma) of the attenuating species i in the material sample

Based on this law, if we have collected the absorption spectrum of a chromophore at a certain thickness, we can simulate absorption spectra of different concentrations and thicknesses within a certain range. Figure 6 shows two spectra of Burmese diaspore. By subtracting the two spectra, we will essentially obtain only the V absorption since the Cr concentrations are almost the same. Since we have the pure V^{3+} spectrum, it is easy to obtain the pure Cr^{3+} spectrum by subtracting the pure V^{3+} spectrum from the spectrum of Burmese diaspore.

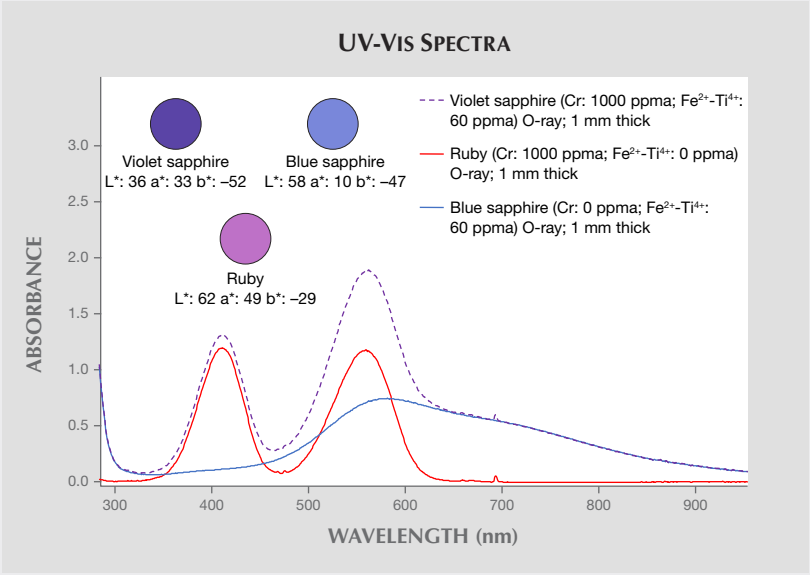

Figure A-1. The absorption of violet sapphire (violet dotted line) shown here represents the sum of the other two spectra: ruby (red line) and blue sapphire (blue line). The color circles calculated under D55 illumination are demonstrated for all of the spectra. We may conclude that violet is a combination of Cr^{3+} red with Fe^{2+}-Ti^{4+} blue. As described above for the additive properties, the absorption of violet sapphire (A) is calculated from two known sets: A_1 (the absorption of ruby) and A_2 (the absorption of blue sapphire). However, we could also use the difference (A–A_1) of any two spectra to show the remaining absorption (A_2).

zero in the Burmese samples, we disregarded the absorption of Fe in the UV-Vis spectra of that material. The spectra of Dia-Bur-001 and Dia-Bur-002 are shown in figure 6. Although the Cr content of the two samples is almost the same (2166 and 2081 ppma, respectively), there is a large difference in the absorption intensity. This difference is related to the absorption of vanadium. By subtracting the two spectra, we essentially obtain only V absorption, which can be subtracted from the other spectra to obtain the pure Cr spectrum (see box A). Based on the author's color analysis, chromium will cause a slight color-change phenomenon in diaspore (figure 7). Additionally, we used the PL spectra (figure 8) to confirm that gem diaspore and ruby show comparable fluorescence spectra (694/693 nm for ruby and 690/693 nm for diaspore).

UV-Visible Spectroscopy of Fe^{3+} in Diaspore and Sapphire. The UV-Vis spectrum of Turkish diaspore (figure 9) shows features corresponding with those of Fe^{3+}-bearing yellowish sapphire from Garba Tula,

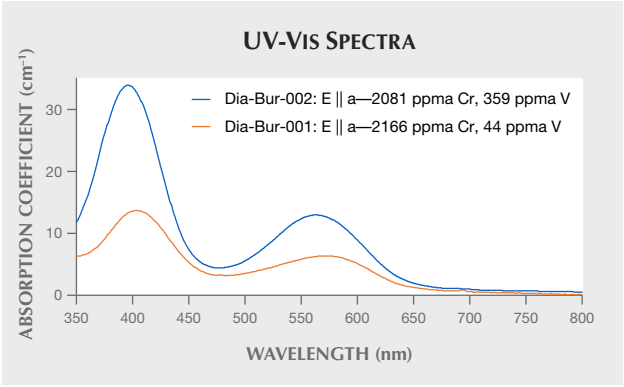

Figure 6. The UV-visible spectra of the Burmese diaspore samples show a large difference in absorption intensity.

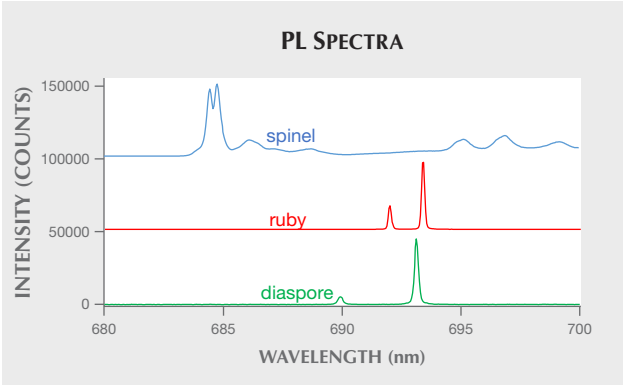

Figure 8. The PL spectra of natural ruby and one of the Burmese diaspore samples show very similar characteristics based on table 1. The crystallographic parameters of diaspore are very close to those of ruby, but quite different from those of spinel. The PL spectra of spinel (data provided by Dr. Chengsi Wang) are considerably different from those of ruby and diaspore. Therefore, we can also use PL spectra to demonstrate that the structural units of diaspore and ruby are very closely related.

Kenya. In those sapphires, the peak at 388 nm is attributed to Fe^{3+}, while the peaks at 377 and 450 nm are attributed to Fe^{3+}-Fe^{3+} pairs (Ferguson and Fielding, 1971, 1972; Krebs and Maisch, 1971). The spectra of diaspore show features very similar to those of Fe^{3+}-bearing sapphire. Hence, the peaks at 384 and 448 nm are attributed to Fe^{3+}-Fe^{3+} pairs, and the peak at 398 nm is attributed to Fe^{3+}.

UV-Visible Spectroscopy of Fe^{2+}-Ti^{4+} Pairing in Diaspore and Sapphire. The UV-Vis spectra of the Turkish diaspore show an obvious absorption band at around 570 nm. Based on the LA-ICP-MS data, chromium and vanadium are very low in Turkish diaspore. In blue sapphire, the absorption at around 580 nm is attributed

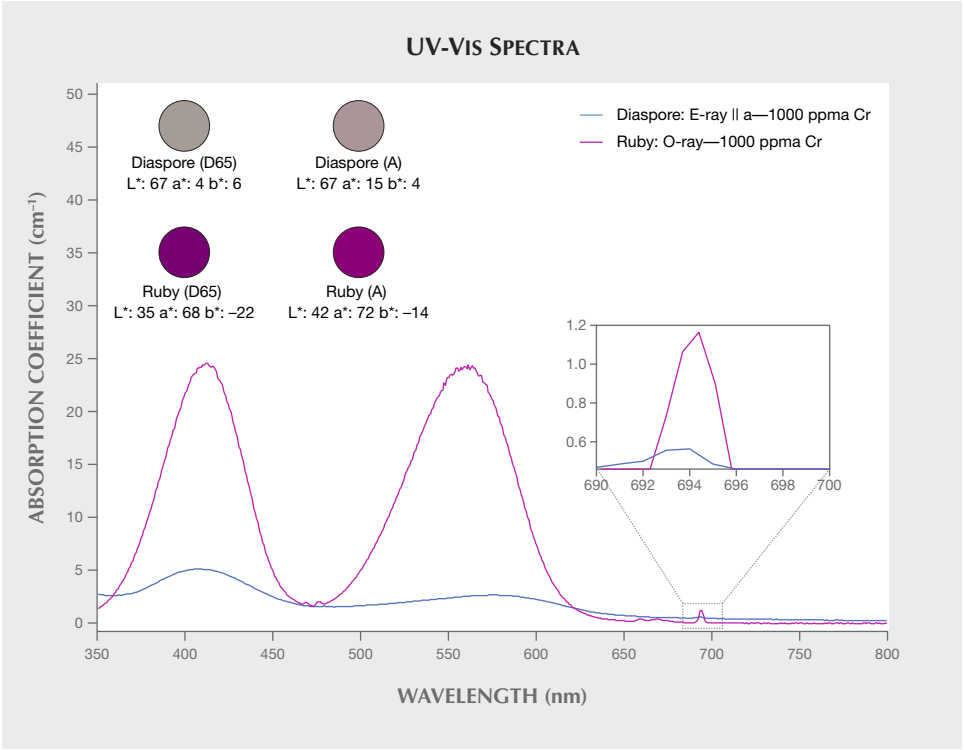

Figure 7. The calculated UV-visible spectra of diaspore and synthetic ruby—both only containing Cr—have similar absorption regions but show much different intensities. The color circles above the spectra, calculated under D65 and A illumination, demonstrate coloration for diaspore and ruby with 1000 ppma Cr concentrations for a 5 mm path length. (The spectra of 1000 ppma and 5 mm path length are calculated rather than taken directly from the sample. A similar method is used in the analysis of the other chromophores.) According to the author's calculation, the chromophore effectiveness of Cr^{3+} in ruby is about 5–10 times higher (peak intensity) than in diaspore.

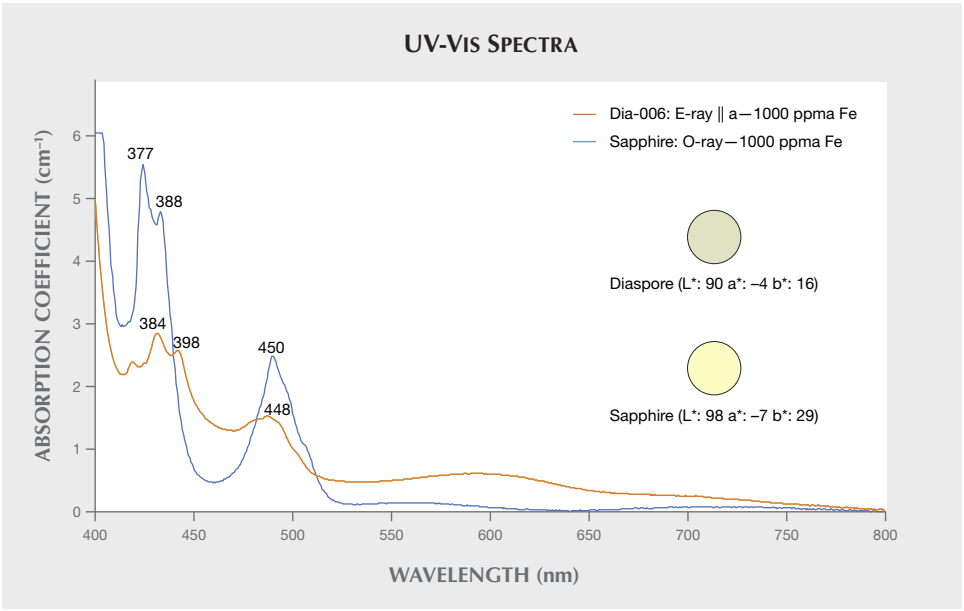

Figure 9. The UV-visible spectra of Turkish diaspore and yellowish sapphire from Garba Tula, Kenya, exhibit closely matched absorption features, especially when polarized light is parallel to the a-axis. The color circles are calculated under D55 illumination, demonstrating the coloration for diaspore and sapphire with 1000 ppma Fe concentrations for a 5 mm path length. According to the author's calculation, the chromophore effectiveness of Fe^{3+} in sapphire is about 1.6 times higher (peak intensity) than in diaspore.

to an Fe^{2+}-Ti^{4+} pairing (Emmett et al., 2003). It is possible that the absorption at around 570 nm in diaspore is related to Fe^{2+}-Ti^{4+} (see figure 10). In blue sapphire, the absorption of the Fe^{2+}-Ti^{4+} pair does not cause the color-change effect because the absorption band extends to the near-infrared region, so the transmission rate of red areas and green areas is not relatively equal. But in diaspore, these transmission areas are fairly equal. The value of a* has changed from –3 to 1, which means the color will change from green to red.

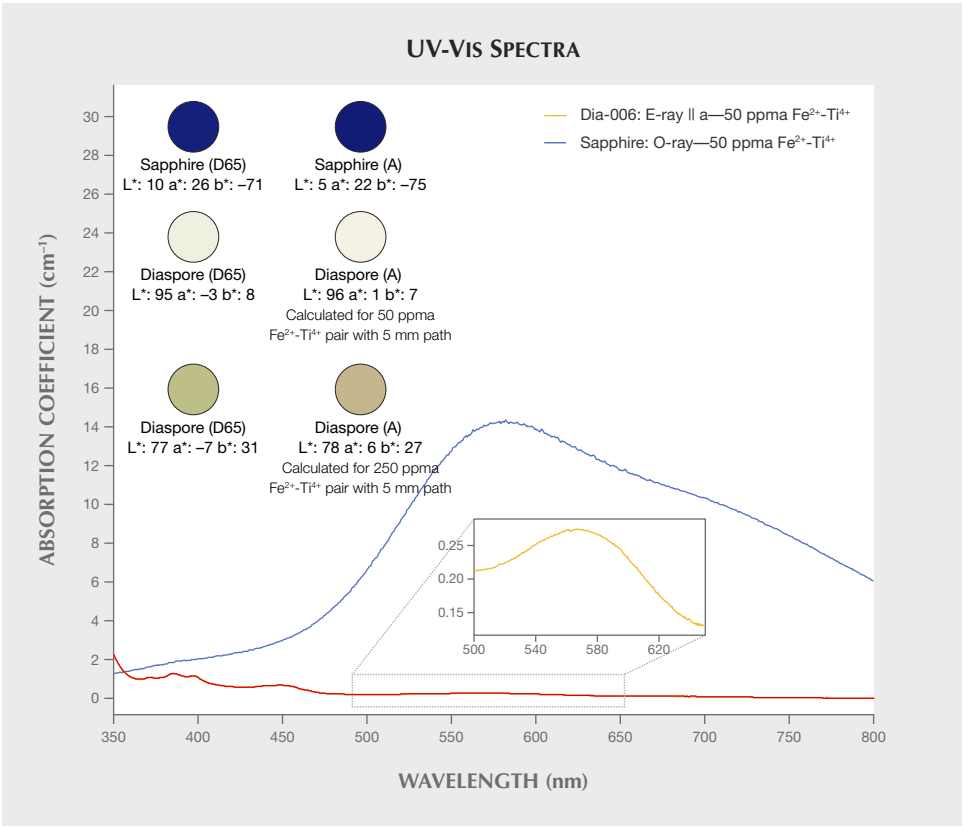

Figure 10. The UV-visible spectra of Turkish diaspore and blue synthetic sapphire (containing Fe^{2+}-Ti^{4+} only). The two spectra have similar absorption regions but show much different absorption intensities. The color circles, calculated under D65 and A illumination, demonstrate the coloration for sapphire and diaspore with 50 ppma Fe^{2+}-Ti^{4+} pair concentrations for a 5 mm path length. Since the color swatches of diaspore calculated using 50 ppma concentration of Fe^{2+}-Ti^{4+} pairs do not show a clear color change, we must calculate the colors, which are shown in the spectra, at a higher concentration of Fe^{2+}-Ti^{4+} pairs (250 ppma) for a 5 mm path length. The chromophore effectiveness of the Fe^{2+}-Ti^{4+} pair is about 50 times higher (peak intensity) in sapphire.

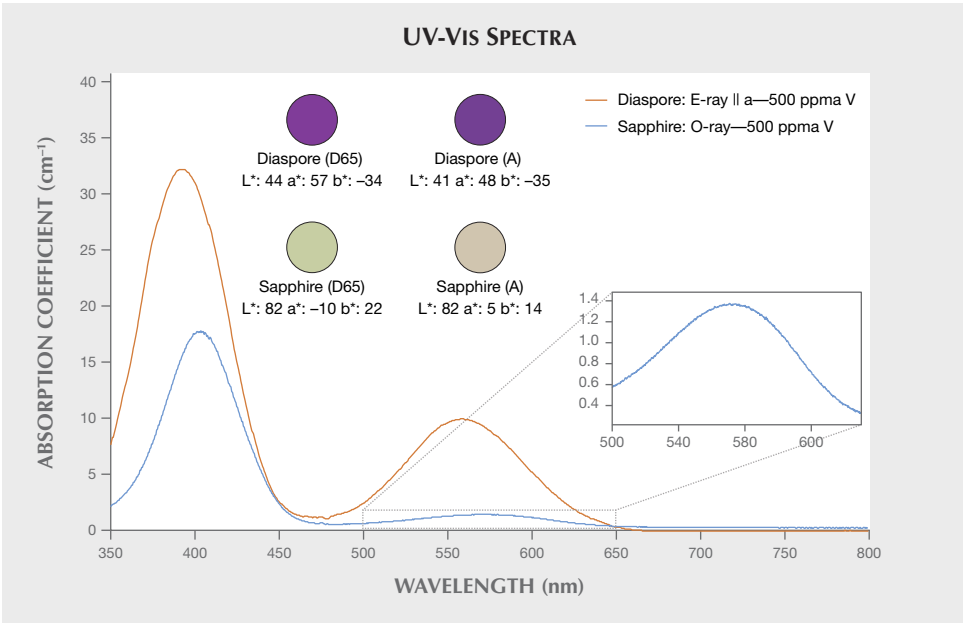

Figure 11. The UV-visible spectra of diaspore (after calculation) and synthetic sapphire (containing V only). The two spectra show similar absorption regions but different absorption intensities. The color circles are calculated under D65 and A illumination and demonstrate coloration for sapphire and diaspore with 500 ppma V concentrations for a 5 mm path length. According to the author's calculation, the chromophore effectiveness of V^{3+} in diaspore is about 2–7 times higher (peak intensity) than in sapphire.

Emmett et al. (2017) proposed that Si plays a role in the color chemistry of corundum. If corundum contains Ti, Si, Mg, and Fe, the Fe will pair with Si before Ti. If diaspore is similar to corundum, Fe will charge-compensate Si before Ti. However, the instruments used for LA-ICP-MS show significant interferences for the three silicon isotopes (Shen, 2010), and as a result the Si content is higher than the value shown. The author does not take Si into consideration because of this instrumental error, and assumes that all of the Ti pairs with Fe. Therefore, the actual content of the Fe^{2+}-Ti^{4+} pair may be lower than the content determined through analysis.

UV-Visible Spectroscopy of V in Diaspore and Sapphire. In natural corundum, vanadium content is generally very low. Synthetic sapphire, which has been manufactured with V, will show an obvious color-change effect. This type of synthetic sapphire is similar to natural alexandrite. However, there is some V in natural diaspore from Myanmar, which plays an important role in color origin and color change.

We compared the spectra of diaspore (containing V only; see box A) to pure vanadium-bearing synthetic sapphire. They also show similar absorption characteristics in their UV-Vis spectra, as both peaks are at around 400 nm and 560 nm in diaspore and sapphire (see also figure 11).

CONCLUSIONS

In color-change diaspore, Cr^{3+}, V^{3+}, and Fe^{2+}-Ti^{4+} pairs are the chromophores, and all of these contain an absorption area at around 560–580 nm. These chromophores may all play a role in causing the color-change effect. Raman spectroscopy proved to be a powerful tool for determining the crystal orientation of the Burmese diaspore wafer; it is also useful to measure and compare the directional UV-Vis spectra of diaspore and corundum. Because of their structural similarity, we can confirm the color correlation between corundum and diaspore and compare the effectiveness of the chromophores. According to the calculation, the chromophore effectiveness of Cr^{3+}, Fe^{3+}, and Fe^{2+}-Ti^{4+} in corundum is about 5–10, 1.6, and 50 times higher, respectively, than in diaspore. However, the chromophore effectiveness of V^{3+} in diaspore is approximately 2–7 times higher than in corundum.

ABOUT THE AUTHORS

Mr. Shen is a graduate student at the Gemmological Institute, China University of Geosciences in Wuhan. In 2018, he was a research intern at the Gemological Institute of America in Carlsbad, California. Dr. Lu is a professor at the Gemmological Institute, China University of Geosciences in Wuhan.

ACKNOWLEDGMENTS

The authors would like to thank Mr. Yungui Liu at HGTC (Gemstone Center of Hebei GEO University) provided Raman and PL testing. Dr. Aaron Palke (GIA, Carlsbad) and anonymous peer reviewers provided many helpful comments and suggestions.

REFERENCES

Deflandre M. (1932) La structure cristalline du diaspore. *Bulletin de la Société Française de Minéraologie et de Cristallographie*, Vol. 55, pp. 140–165.

Emmett J.L., Scarratt K., McClure S.F., Moses T., Douthit T.R., Hughes R., Novak S., Shigley J.E., Wang W., Bordelon O., Kane R.E. (2003) Beryllium diffusion of ruby and sapphire. *G&G*, Vol. 39, No. 2, pp. 84–135, http://dx.doi.org/10.5741/GEMS.39.2.84

Emmett J.L., Stone-Sundberg J., Guan Y., Sun Z. (2017) The role of silicon in the color of gem corundum. *G&G*, Vol. 53, No. 1, pp. 42–47, http://dx.doi.org/10.5741/GEMS.53.1.42

Ferguson J., Fielding P.E. (1971) The origins of the colours of yellow, green and blue sapphires. *Chemical Physics Letters*, Vol. 10, No. 3, pp. 262–265.

Ferguson J., Fielding P.E. (1972) The origins of the colours of natural yellow, blue, and green sapphires. *Australian Journal of Chemistry*, Vol. 25, No. 7, pp. 1371–1385.

Francombe M.H., Rooksby H.P. (1959) Structure transformations effected by the dehydration of diaspore, goethite and delta ferric oxide. *Clay Minerals*, Vol. 4, pp. 1–14, http://dx.doi.org/10.1180/claymin.1959.004.21.01

Hill R.J. (1979) Crystal structure refinement and electron density distribution in diaspore. *Physics and Chemistry of Minerals*, Vol. 5, No. 2, pp. 179–200, http://dx.doi.org/10.1007/BF00307552

Iwai S.I., Yamamoto H., Morikawa H., Isobe M. (1973) Topotactic thermal-transformation of diaspore to corundum. *Mineralogical Journal*, Vol. 7, No. 2, pp. 137–158, http://dx.doi.org/10.2465/minerj1953.7.137

Krebs J.J., Maisch W.G. (1971) Exchange effects in the optical-absorption spectrum of Fe^{3+} in Al_2O_3. *Physical Review B*, Vol. 4, No. 3, p. 757.

Lewis J., Schwarzenbach D., Flack H.D. (1982) Electric field gradient and charge density in corundum, α–Al_2O_3. *Acta Crystallographica*, Vol. 38, No. 5, pp.733–739, http://dx.doi.org/10.1107/S0567739482001478

Lu R. (2012) Color origin of lavender jadeite: An alternative approach. *G&G*, Vol. 48, No. 4, pp. 273–283, http://dx.doi.org/10.5741/GEMS.48.4.273

Malsy A.K. (2012) Orangey-red to orangey-pink gem spinels from a new deposit at Lang Chap (Tan Huong-Truc Lau), Vietnam. *Journal of Gemmology*, Vol. 3, No. 1, pp. 19–27, http://dx.doi.org/10.15506/JoG.2012.33.1.19

Peterson R.C., Lager G.A., Hitterman R.L. (1991) A time-of-flight neutron powder diffraction study of $MgAl_2O_4$ at temperatures up to 1273 K. *American Mineralogist*, Vol. 76, No. 9-10, pp. 1455–1458.

Ruan H.D., Frost R.L., Kloprogge J.T. (2001) Comparison of Raman spectra in characterizing gibbsite, bayerite, diaspore and boehmite. *Journal of Raman Spectroscopy*, Vol. 32, No. 9, pp. 745–750, http://dx.doi.org/10.1002/jrs.736

San Juan-Farfán R.E., Bayarjargal L., Winkler B., Haussühl E., Avalos-Borja M., Refson K., Milman V. (2011) Pressure dependence of the lattice dynamics of diaspore, α-AlO (OH), from Raman spectroscopy and density functional perturbation theory. *Physics and Chemistry of Minerals*, Vol. 38, No. 9, pp. 693–700, http://dx.doi.org/10.1007/s00269-011-0442-3

Shen A.H. (2010) Silicon in sapphires—its role and detectability by LA-ICP-QMS. *Goldschmidt Conference Abstracts 2010*, p. A945.

THANK YOU, REVIEWERS

GEMS & GEMOLOGY requires each manuscript submitted for publication to undergo a rigorous peer review process, in which each paper is evaluated by at least three experts in the field prior to acceptance. This is essential to the accuracy, integrity, and readability of *G&G* content. In addition to our dedicated Editorial Review Board, we extend many thanks to the following individuals who devoted their valuable time to reviewing manuscripts in 2018.

Non-Editorial Board Reviewers

Laurent Cartier • John Chapman • Sally Eaton-Magaña • Ronnie Geurts • Al Gilbertson • George Harlow • Peter Heaney • Darrell Henry • Artitaya Homkrajae • Richard Hughes • John King • Rachel King • Yan Liu • Cigdem Lule • Laura Otter • Dieter Quast • Ewa Rachón • Ilene Reinitz • Sudarat Saeseaw • Russell Shor • Jana Smith • Monica Solorzano-Kraemer • Jeffrey Spier • Ziyin Sun • John Valley • Alexander Zaitsev • Chunhui Zhou

Corundum with Spinel Corona from the Tan Huong–Truc Lau Area in Northern Vietnam

Nguyen Ngoc Khoi, Christoph A. Hauzenberger, Chakkaphan Sutthirat, Duong Anh Tuan, Tobias Häger, and Nguyen Van Nam

Corundum deposits in the Tan Huong–Truc Lau area of Vietnam are hosted mainly in gneiss and partly in feldspathic pegmatoid and marble. Encountered here in both primary and secondary placer deposits is a considerable quantity of stones with a well-developed spinel corona following the morphology of the corundum core. The genesis of the observed spinel corona can be explained by their reaction textures, chemical composition, and mineral inclusions as well as by applying thermodynamic phase equilibria calculations. The following reactions were found to be responsible for the formation of the spinel corona around corundum in gneiss:

biotite + corundum → spinel + K-feldspar + fluid, or
garnet + corundum → spinel + sillimanite

For corundum-spinel associations in metacarbonate rocks, the relevant reaction is:

dolomite + corundum → spinel + calcite + carbon dioxide

Mineralogical and chemical studies have shown that the gem quality of ruby and sapphire grains from Tan Huong–Truc Lau deteriorated substantially after their formation due to this corona texture.

Corundum occurrences in northern Vietnam are hosted not only in marble but also in partly migmatized gneiss. Gneiss-hosted corundum deposits are located mainly in the Tan Huong–Truc Lau area of the Day Nui Con Voi range in the Red River shear zone (RRSZ, figure 1). Here the partly migmatized gneiss contains gray, grayish white to bluish, and yellowish gray sapphires, while dark red to pinkish ruby occurs in the marble lenses intercalated with gneiss and in the weathered feldspathic pegmatoid rocks (Khoi et al., 2011, 2016). The gemological properties of corundum from the Tan Huong–Truc Lau area and the mineralogy, petrology, pressure-temperature *(P-T)* formation conditions, and genetic model of these gneiss-hosted deposits were reported by Khoi et al. (2011, 2016).

One of the remarkable phenomena of these deposits is that in some secondary (alluvial and diluvial) and primary deposits, the corundum is frequently surrounded by a well-developed spinel corona. This corona mainly follows the morphology of the corundum crystal. These encrusted stones have an unattractive yellowish gray or brownish gray to almost black appearance until the spinel corona is removed to occasionally uncover a gem-quality corundum core (figure 2).

Several questions related to this mineral assemblage arise. Why did the spinel corona form around the corundum core, and what reaction(s) occurred during the corundum → spinel transformation? What were the characteristics of the corundum before this transformation, and how was its quality affected afterward? What was the original host rock? These questions are of scientific and also economic importance. According to the information from DOJI's Truc Lau mine (Khoi et al., 2011), approximately 30% of the corundum recovered from this type of deposit has a spinel corona, which sometimes hides the gem-quality corundum core almost entirely. To an-

See end of article for About the Authors and Acknowledgments.
Gems & Gemology, Vol. 54, No. 4, pp. 404–417,
http://dx.doi.org/10.5741/GEMS.54.4.404

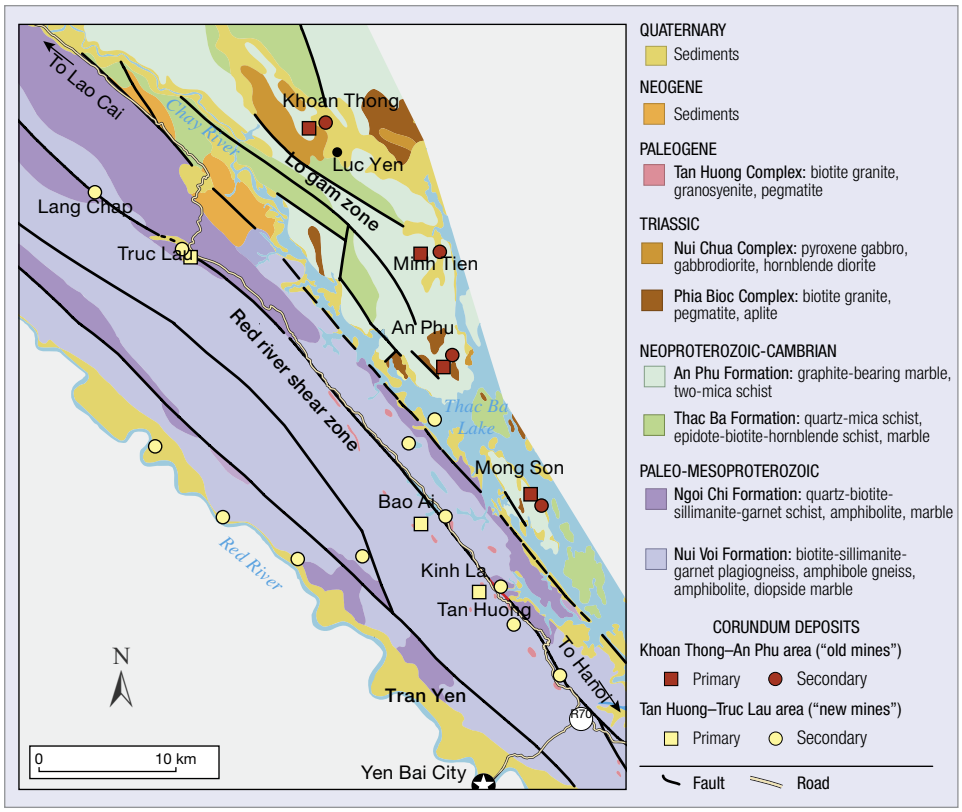

Figure 1. Simplified geologic map showing the locations and rock formations of the gneiss-hosted corundum occurrences in the Day Nui Con Voi range and marble-hosted occurrences in the adjacent Lo Gam structural zone (modified after Xuyen, 2000 and Vinh, 2005).

swer these questions, we have conducted a petrographic (macro- and microscopic) and chemical study of corundum with an associated spinel corona. This data set, together with available published *P-T* conditions of the host rocks (Khoi et al., 2016) and thermodynamic phase equilibria calculations as well as inclusions in mineral phases, was used to explain the genesis of the spinel corona.

GEOLOGICAL SETTINGS

Corundum occurrences and deposits in northern Vietnam's Yen Bai Province are located in marble and in partly migmatized gneiss of the Red River shear zone. The more than 1,000 km NW-SE trending RRSZ fault zone is one of Southeast Asia's most distinct geological discontinuities with a left-lateral shear sense. Along the shear zone, several suites of high-grade metamor-

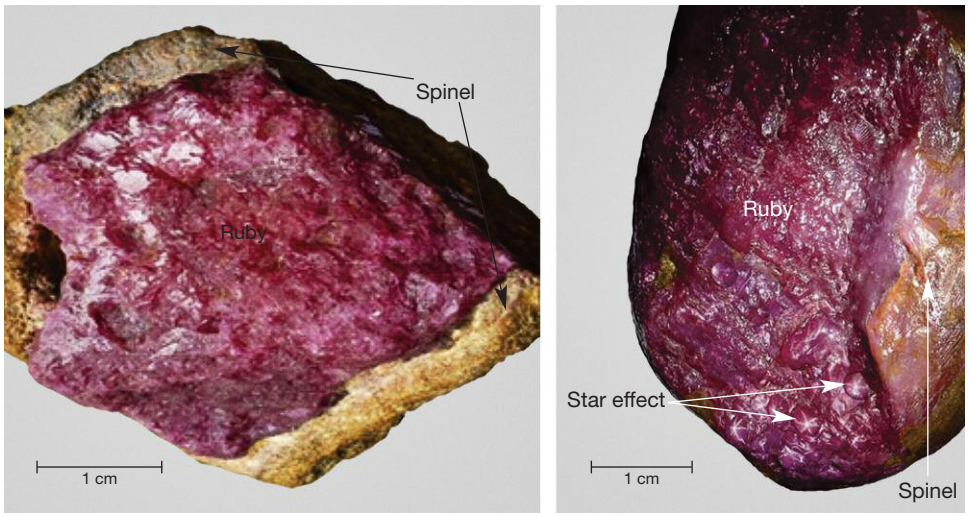

Figure 2. Some encrusted stones have an unsightly yellowish gray or brownish gray appearance until the spinel corona is cut away to reveal a gem-quality corundum core with an appealing color and possibly a star effect (right). Photos by N.N. Binh, DOJI Gold & Gems Group.

phic rocks were exhumed (see figure 1) between 35 and 17 million years ago (Leloup et al., 1995, 2001).

The gneiss-hosted corundum deposits in Tan Huong–Truc Lau are located entirely within the Day Nui Con Voi range, which is composed of high-grade metamorphic rocks with sillimanite-biotite-garnet gneiss, mica schist, and amphibolite, all locally intercalated with marble lenses. These rocks appear to have been intruded by granite, syenite, and pegmatite of the Tan Huong magmatic complex (again, see figure 1). In contrast, the marble-hosted corundum deposits in the nearby Lo Gam zone occur in a thick metasedimentary sequence, composed of marble and overlying sillimanite-biotite-garnet schist (Long et al., 2004). These units, bounded by left-lateral faults, are intruded by granitic rocks and related pegmatite of Triassic age (Trinh and Vinh, 1997).

$^{40}Ar/^{39}Ar$ dating of biotite and phlogopite syngenetic with corundum has yielded an Oligocene minimum age for the deposits in the Lo Gam tectonic zone and a Miocene minimum age for those in the Day Nui Con Voi range (Leloup et al., 2001; Garnier et al., 2002, 2008; Khoi et al., 2016). In the Tan Huong–Truc Lau area, corundum-hosting lithologies can have one of four variations:

- *Gneiss to partly migmatized gneiss* containing gray, grayish white to bluish, and yellowish gray sapphire (figure 3, left). Examples include the Co Man outcrop at the Truc Lau valley and the Kinh La occurrence (Long et al., 2004; Thuyet, 2008; Nam, 2012; Khoi et al., 2016).
- *Weathered feldspathic (pegmatoid) rocks* usually found within gneiss, hosting dark red to pinkish ruby crystals. Occurrences include Slope 700 (figure 3, right) and kilometer markers 13, 15, and 23 along National Road 70 (Nam, 2012; Khoi et al., 2016).
- *Marble in lenses and boudins* intercalated within gneiss, mica schist, and amphibolite, containing ruby and sapphire—for example, the Slope 700 outcrop (Bao Ai occurrence), the Tan Huong drill core (Long et al., 2004), and the Truc Lau mine.
- *Amphibolite* transformed by metasomatism into biotite schist, bearing gray to dark gray sapphire—for example, the Km 15 occurrence (Long et al., 2004).

The corundum-bearing host rocks in the Tan Huong–Truc Lau area appear to have originated from the metamorphism of fine-grained sediments of variable composition (Katz, 1972, 1986; Simandl and Paradis, 1999; Khoi et al., 2010, 2011, 2016). For example, gneiss from the Co Man outcrop and the Kinh La occurrence has a wide compositional range: 50–90% feldspar, up to 40% biotite, and up to 20% sillimanite. In addition, ruby-bearing feldspathic rocks (e.g., the Slope 700 outcrop) typically consist of K-feldspar and biotite (or vermiculite; again, see figure 3, right). Temperatures of 650–760°C and pressures of 5–7.6 kbar have been calculated for the metamorphism and corundum formation, which corresponds to upper amphibolite to lower granulite facies (Khoi et al., 2016).

The primary deposits and host rocks are usually deeply weathered, forming numerous secondary deposits. The secondary (eluvial, diluvial, and alluvial) corundum deposits generally contain dark red ruby, pink sapphire, and red and brown spinel, as well as some garnet, trapiche-like bluish gray sapphire, sillimanite, and quartz. Corundum samples with spinel corona have been found in different primary and secondary deposits and occurrences in the Tan Huong–Truc Lau area. For this study, specimens were taken from the Kinh La primary occurrence and the Truc Lau secondary (alluvial) deposit.

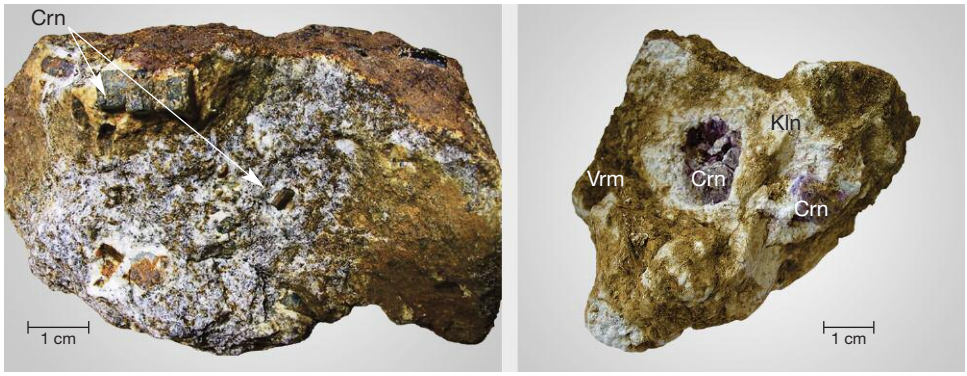

Figure 3. Left: This sample of corundum-bearing gneiss from the Co Man outcrop contains mainly feldspar, biotite, sillimanite, and sapphire crystals up to 3 cm long. Right: Weathered feldspathic rock from the Slope 700 outcrop typically consists of kaolinite (Kln), vermiculite (Vrm), and ruby (Crn). Photos by N.V. Nam.

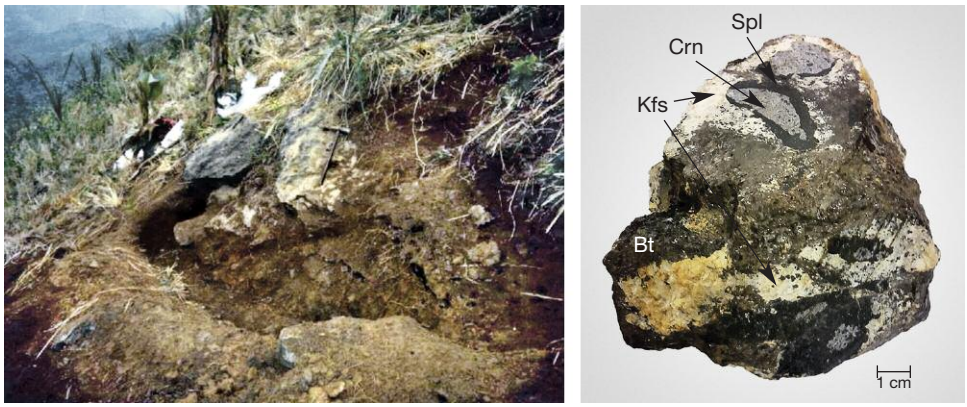

Figure 4. In this outcrop at the Kinh La occurrence, several samples of primary corundum with spinel corona were collected for this study. Bt = biotite, Kfs = K-feldspar, Crn = corundum, Spl = spinel. Photos by N.N. Khoi.

The Kinh La (Km 13) occurrence is located 2 km southwest of the Tan Huong mine, at 21°48′55″N, 104°52′12″E (again, see figure 1). The gem-bearing body is 0.1 to 1 m thick and 100 m long. The corundum ranges in color from black to bluish gray and from 0.1 to 5 cm in size (figure 4).

The Truc Lau deposit, located at 22°02′05″N, 104°40′46″E, occupies a large valley, about 5 km long, that contains eluvial and alluvial sediments (Khoi et al., 2011). The eluvium consists of three layers: topsoil (averaging 1 m thick); a gem-bearing layer (0.8–1 m thick) containing corundum and spinel that is composed of pebble, gravel, and sand; and a deeply weathered gneiss layer (3 m thick) that typically contains ruby and sapphire. Compared to the eluvium, the alluvial deposits at Truc Lau are thicker (approximately 10 m thick). Ruby, sapphire, and spinel are found within a gravel paleoplacer (1.2–5.0 m thick) that lies on bedrock and is buried below 0.5–3.5 m of Quaternary sediments and 0.5–1.5 m of topsoil (Khoi et al., 2011).

Gem corundum here usually shows a tabular crystal form with deformed polysynthetic twinning along rhombohedral faces, and growth zones are typically sharp. Colors range from pink to pinkish red, and color irregularities such as zoning and spots or patches are rare. Many stones, particularly the sapphire, have low transparency due to abundant fracturing and inclusions. Mineral inclusions such as ilmenite, magnetite, plagioclase, muscovite, biotite, apatite, zircon, and chlorite are found in corundum from the primary deposits. Among these, dark inclusions (e.g., biotite, ilmenite, and magnetite) are most common. Primary and secondary gas-liquid inclusions also occur frequently in this corundum. Common mineral inclusions in corundum from the secondary deposits are rutile, ilmenite, zircon, apatite, plagioclase, calcite, boehmite, and mica (margarite and muscovite), nearly identical to those in corundum from the primary deposits (Khoi et al., 2011, 2013, 2016).

MATERIALS AND METHODS

For this study, we analyzed 53 samples of corundum with spinel corona: 18 from the Kinh La primary occurrence and 35 from the Truc Lau placer deposits (figures 5–7). These samples were initially investigated using optical microscopy (gemological and petrological) and scanning electron microscopy (SEM). Mineral inclusions were identified with the help of Raman spectroscopy, SEM, and optical microscopy. A quantitatively equipped SEM microscope was subsequently used to analyze mineral chemistry of both the corundum host and the spinel corona in several specimens. Laser ablation–inductively coupled plasma–mass spectrometry (LA-ICP-MS) was applied for trace-element analysis of these samples as well as other alluvial gem corundum from Truc

Figure 5. Gray corundum coated by a black spinel (hercynite) layer, from the Kinh La primary occurrence. Photo by N.V. Nam.

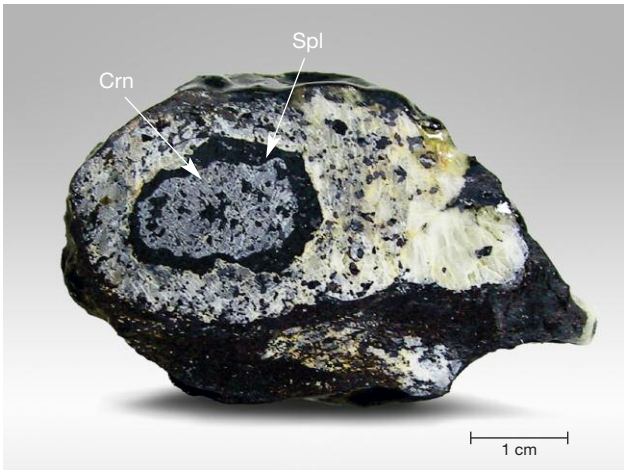

Figure 6. Left: Rough stones from the Truc Lau secondary deposit, some of which contain a spinel corona. Right: Twelve pieces of corundum with spinel corona were selected from the lot and used for this study. Photos by N.N. Khoi.

Lau for comparison and further discussion. Some of the chemistry data used in this study—such as trace-element composition of the corundum core and microprobe analyses of the spinel corona and other coexisting minerals from the Kinh La primary occurrence—were published previously (Khoi et al., 2013, 2016).

Major elements were determined by SEM analysis, using a JEOL 6310 unit equipped with a Link ISIS energy-dispersive X-ray (EDX) spectrometer and a Microspec wavelength-dispersive X-ray (WDX) spectrometer at the NAWI Graz Geocenter, Department of Petrology and Geochemistry, Karl Franzens University in Graz, Austria. Accelerating voltage was set to 15 kV and sample current to 6 nA on a probe current detector (PCD). The elements Al, Mg, and Zn were determined by EDX; Ti, Cr, and Fe were quantified by WDX. Detection limits were around 0.1 wt.% for EDX and about 0.03 wt.% for WDX. For additional analyses we used a JEOL JXA-8100 electron probe microanalyzer (EPMA) at the Department of Geology, Chulalongkorn University in Bangkok.

Trace elements were determined by LA-ICP-MS using an ESI NWR193 laser ablation unit coupled to an Agilent 7500 ICP-quadrupole MS at the NAWI Graz Central Lab for Water, Minerals and Rocks, University of Graz and Graz University of Technology. Material was ablated using a 193 nm laser pulsed at 9 Hz and a 75 µm spot size corresponding to an energy of ~7 J/cm^2. Helium was used as a carrier gas at ~0.8 L/min flow, and data was acquired in time-resolved mode. NIST 610 and 612 glasses were routinely analyzed for standardization and drift correction. The glass standard BCR-2 was analyzed as an unknown and could be reproduced to within a 10% relative error. Aluminum was used as an internal standard. Mineral abbreviations presented here follow Whitney and Evans (2010).

MACROSCOPIC AND MICROSCOPIC STUDY

Corundum with Spinel Corona from Primary Deposits. At Kinh La, corundum occurs in a sillimanite + biotite + plagioclase + K-feldspar + ilmenite ± garnet ± hercynite ± magnetite migmatitic gneiss. The corundum crystals are often coated by hercynite-rich spinel (figures 5 and 8), with or without signs of corrosion. The corundum core in the samples is gray to dark gray, while the spinel rim is dark gray to black. The size of the corundum core frequently ranges from 10 to 30 mm, while the spinel corona has a thickness of a few millimeters to several centimeters. As can be seen in figure 8, the thickness of the spinel corona increases at the expense of the corundum core.

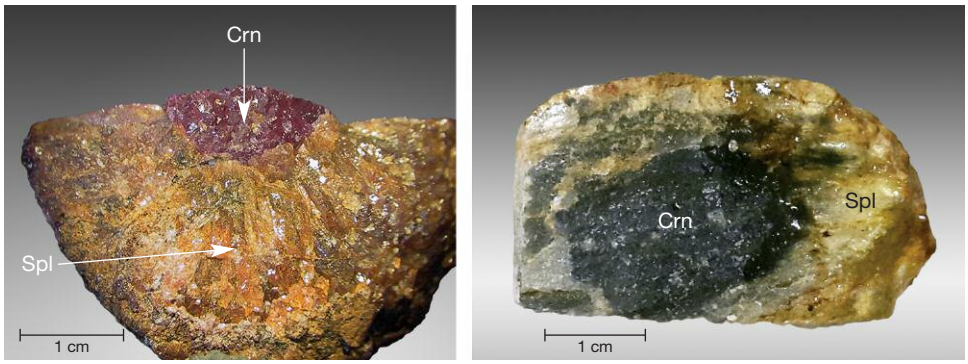

Figure 7. Spinel-coated ruby (left) and sapphire (right) crystals from the Truc Lau deposit. Photos by N.N. Khoi.

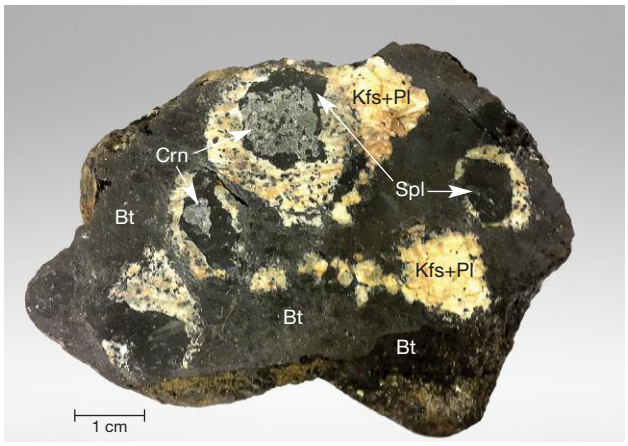

Figure 8. Gray corundum coated by a dark spinel corona in sillimanite + biotite + plagioclase + K-feldspar + ilmenite ± garnet ± hercynite ± magnetite migmatitic gneiss. Sample H7005 from the Kinh La occurrence. Photo by N.N. Khoi.

Under transmitted light, coarse twin lamellae and fractures are prominent in the corundum core. Frequently encountered in the corundum are ilmenite and magnetite inclusions (figure 9), as well as some zircon and apatite.

Under transmitted light, the spinel corona is green to deep green in color (figure 10) and translucent. It occurs as coarse xenoblastic crystals that formed during metamorphic overprint and took their outlines from neighboring crystals. Common inclusions in the spinel are biotite and K-feldspar. K-feldspar and plagioclase (figure 10) usually account for 20–70% of the ground mass, occurring as aggregates of tabular subhedral to anhedral crystals together with corundum, biotite, and hercynite. Biotite, accounting for 10–90% of the samples, occurs as aggregates of brown millimeter-sized flakes or alternating with K-feldspar, plagioclase, spinel, and corundum.

Petrographic study of the samples also revealed other minerals, such as sillimanite, garnet, and quartz. The sillimanite usually has a long prismatic, needle-like shape. The garnet is subhedral to anhedral, strongly fractured, and millimeter- to centimeter-sized (figure 11).

Corundum with Spinel Corona from Secondary Deposits. Figure 12 shows hand specimens of corundum with spinel corona collected from the Truc Lau secondary deposit. The color of the corundum core shows much more variety than samples from primary deposits, ranging from white to gray to pink, pinkish red, and dark red. The shape of the internal corundum is mostly irregular to subrounded, and the boundary of the surrounding spinel corona is marked by a sharp change in color. Signs of corrosion are apparent in some samples. Almost all of the internal corundum grains are fractured to some extent and range in size up to tens of millimeters, and in rarer cases up to hun-

In Brief

- Corundum deposits in northern Vietnam are hosted mainly in marble and gneiss.
- An interesting phenomenon that occurs in some corundum found in the gneiss-hosted deposits is a rim or "corona" of spinel.
- This spinel corona, which formed through metamorphic reactions, causes a substantial deterioration of the gem quality of the ruby and sapphire.

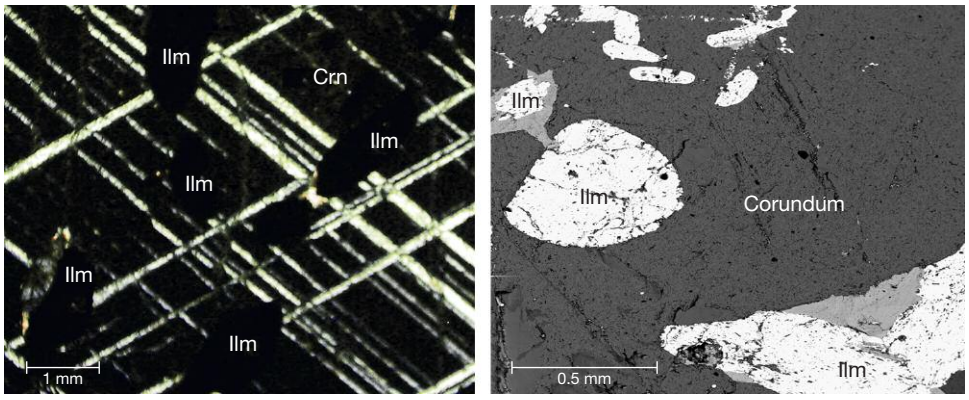

Figure 9. Ilmenite inclusions in corundum core from the Kinh La occurrence, shown in cross-polarized light on the left and as a backscattered electron (BSE) image on the right. Photomicrographs by C.A. Hauzenberger.

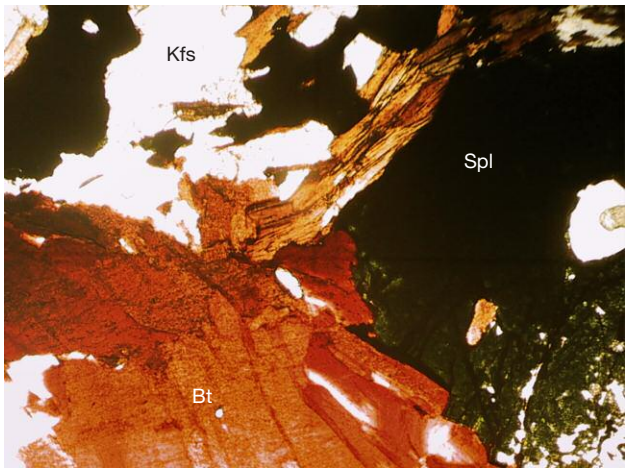

Figure 10. Spinel (hercynite), biotite, and K-feldspar in sample H7005, migmatized corundum-bearing gneiss from the Kinh La occurrence, shown in parallel-polarized light. Photomicrograph by N.V. Nam; field of view 1.2 mm.

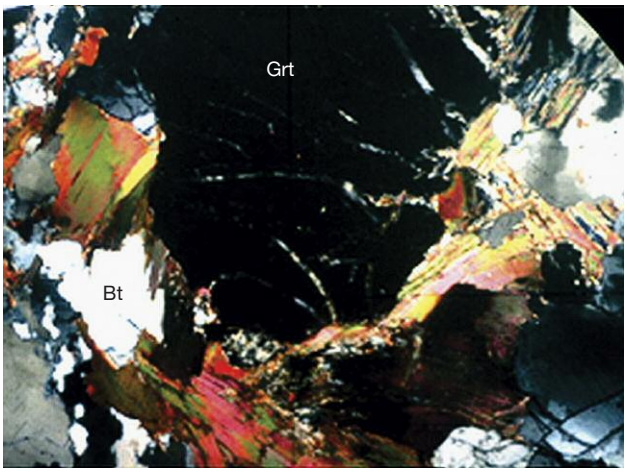

Figure 11. Biotite and garnet in sample H7005 from the Kinh La occurrence, shown in cross-polarized light. Photomicrograph by N.V. Nam; field of view 1.2 mm.

dreds of millimeters. Some corundum grains show a distinct corona texture due to the presence of a spinel rim. The spinel corona has gray, dark gray to yellow, brown, and sometimes pink to grayish red color with a thickness ranging up to tens of millimeters. Grains have either comb-like (palisade) or xenoblastic texture.

In general, four different types of corundum samples with spinel corona from secondary deposits can be recognized (again, see figure 12):

Type I: A nearly inclusion-free ruby crystal surrounded by a dense, nearly inclusion-free Mg-spinel (figure 12A)

Type II: A sapphire crystal surrounded by a thin, palisade-type Mg-spinel rim (figure 12B)

Type III: A pink sapphire/ruby surrounded by a dark Mg-Fe-Al spinel phase (figure 12C)

Type IV: A sapphire surrounded by a hercynite-rich spinel (figure 12D)

Inclusions were generally rare in all four types. In each type, corundum typically contains Al-hydroxide and subordinate rutile inclusions (figure 13A). In the type I sample, calcite and dolomite were found in the spinel rim (figure 13B) while a Ba-rich feldspar and plagioclase were found in the corundum. The spinel rim in type II samples was partially developed as a series of elongated grains growing perpendicular to the sapphire surface and was either completely free of inclusions or showed only a few small calcite and dolomite

Figure 12. Samples of corundum with spinel corona from the Truc Lau secondary deposit. Photos by C.A. Hauzenberger.

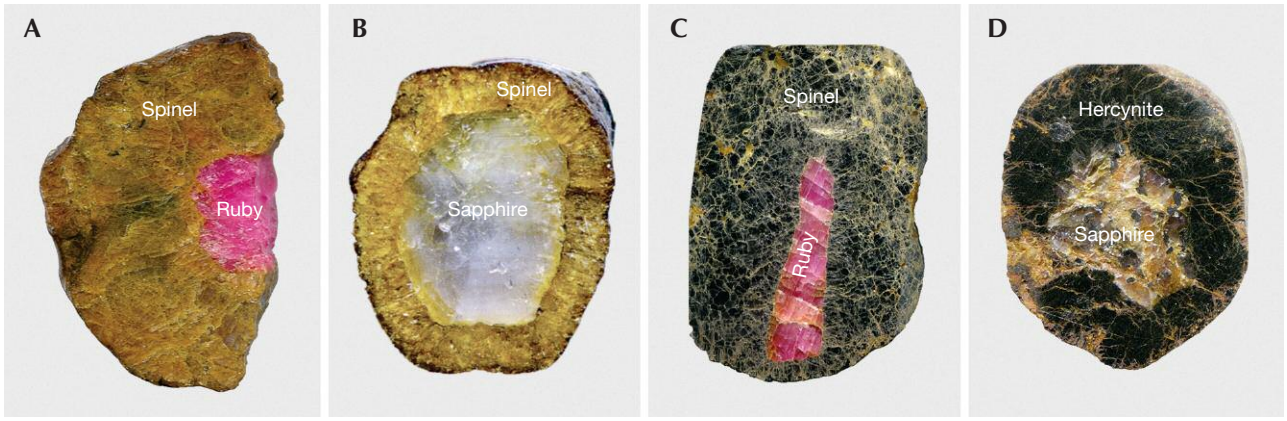

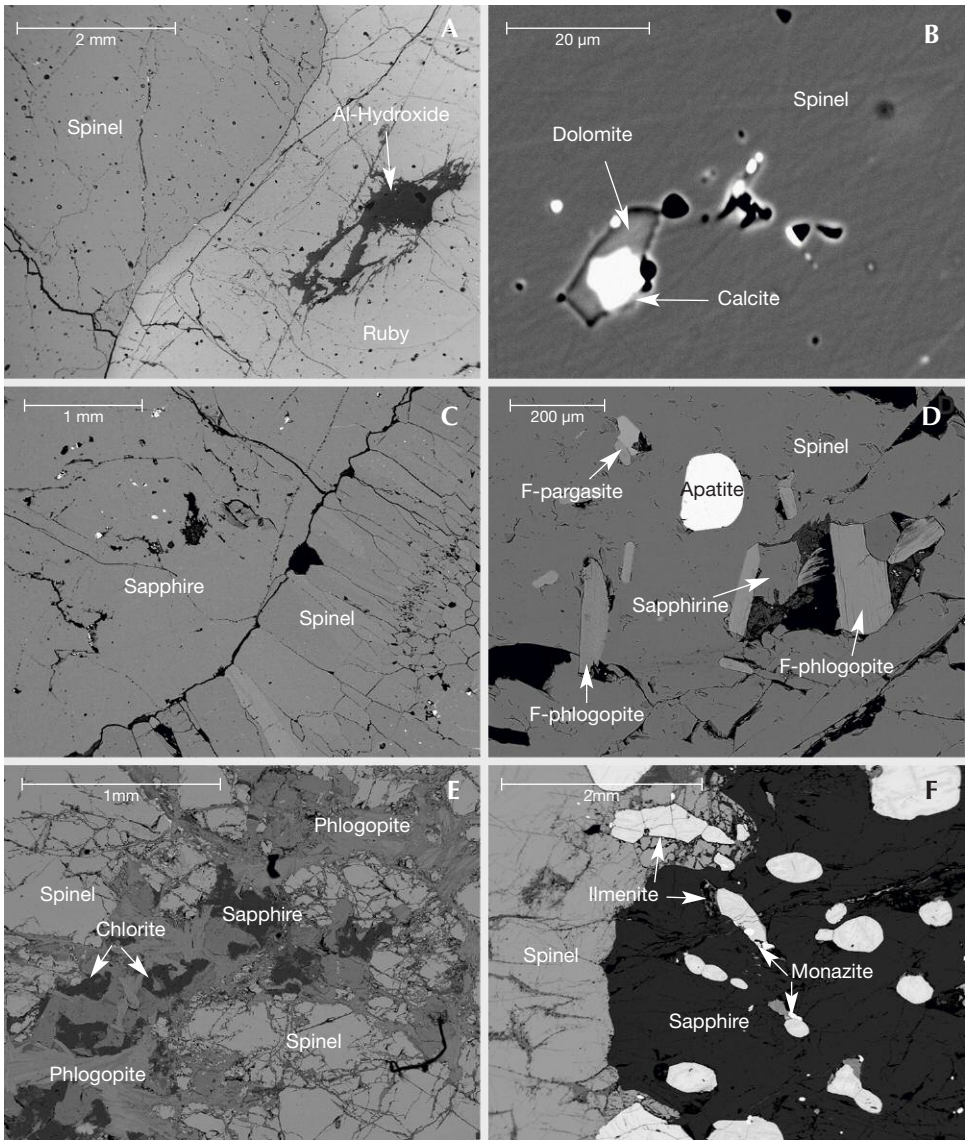

Figure 13. BSE images of inclusions in corundum cores and spinel corona. A: Al-hydroxide in corundum. The spinel is an inclusion-free type I. B: Dolomite and calcite inclusions in type I spinel. C: Apatite, sapphirine, F-phlogopite, and F-pargasite in the spinel corona of the type II sample. D: Palisade spinel rim around a sapphire (type II sample). E: Phlogopite, chlorite, and sapphire within the spinel corona (type III sample). F: Sapphire surrounded by a hercynite-rich spinel containing inclusions of ilmenite and monazite (type IV sample). Images by C.A. Hauzenberger.

inclusions (figure 13C). In one type II sample, sapphirine, fluorian pargasite, and fluorian phlogopite were identified in the spinel corona (figure 13D). Type III samples contain phlogopite and chlorite within the spinel corona (figure 13E). Type IV contains numerous ilmenite inclusions and a smaller number of apatite, monazite, and zircon inclusions (figure 13F).

CHEMICAL COMPOSITION

Corundum with Spinel Corona from Primary Deposits. The major element compositions of the corundum cores in samples from the Kinh La primary occurrence are shown in table 1, while trace-element contents by LA-ICP-MS analysis are from table 2.a in Khoi et al. (2016). In general, the corundum core showed high Fe content (5119 to 5717 ppm) and low Ti and Cr content (16 to 81 and 55 to 62 ppm, respectively). Other elements such as Ga, Mg, and V were found in all samples, but with low content.

TABLE 1. Major element composition[a] (wt.%) of 12 samples of corundum core from the Kinh La primary deposit.

Oxide	Content
Al_2O_3	99.15–99.36 (99.25)
TiO_2	0.12–0.21 (0.22)
Cr_2O_3	0.00–0.09 (0.05)
FeO	0.45–0.97 (0.25)
Total	**99.80–100.54 (100.10)**

[a]*Analyzed by EPMA. Values are averaged from three to five analyses. Average oxide contents are shown in parentheses.*

TABLE 2. Major element composition[a] (wt.%) of corundum cores from the Truc Lau secondary deposit.

Sample	TLM2	TLM3	TLM5	TLM6	TLM7	TLL5
Al_2O_3	99.88	99.86	99.15	99.97	99.43	99.60
TiO_2	0.035	0.040	<0.03	<0.03	0.067	0.033
Cr_2O_3	0.238	0.162	0.233	0.160	<0.03	0.090
FeO	<0.03	0.053	0.054	0.075	0.501	<0.03
Total	**100.15**	**100.11**	**99.44**	**100.21**	**100.00**	**99.73**

[a]*Values are averaged from three to five analyses.*

Representative analyses of the spinel rim and other minerals encountered with corundum from the Kinh La primary occurrence were also presented in tables 3.a through 3.d of Khoi et al. (2016). Generally, minerals of the samples from Kinh La are extremely iron-rich. The spinel is nearly pure hercynite with very low V and no Cr and Zn content. Garnet was observed in only one sample, with ~80 mol.% almandine content, grossular and pyrope contents of ~10 mol.% each, and spessartine below 5 mol.%. The biotite is nearly pure annite with some Tschermak substitution and up to 5 wt.% TiO_2. The feldspathic matrix usually consists of plagioclase with X_{Ab} of ~0.75 and K-feldspar with albite content of about 25 to 30 mol.%. Magnetite and ilmenite are frequently encountered, either as inclusions in corundum, spinel, and garnet or as single phases in the matrix.

Corundum with Spinel Corona from Secondary Deposits. Tables 2 and 3 present the analyses of the corundum core. Ruby has relatively low Cr_2O_3 values. The TiO_2 concentrations are below the detection limit and the FeO values slightly above. The sapphire sample contained about 0.5 wt.% Fe_2O_3 and very low Cr_2O_3 and TiO_2 values.

Spinel corona compositions are shown in table 4. The composition is of a nearly pure Al-Mg spinel (*sensu stricto*), with only minor amounts of FeO (<0.7 wt.%, except the spinel corona around sapphire in one sample, with FeO = 1.27 wt.%), Cr_2O_3, and ZnO.

TABLE 3. Trace-element composition[a] of corundum cores from the Truc Lau secondary deposit (ppma).

Sample	^{9}Be	^{24}Mg	^{49}Ti	^{51}V	^{53}Cr	^{56}Fe	^{71}Ga	^{118}Sn
TLM2	<0.05	68.1	142	196	940	15.4	61.0	6.20
TLM3	<0.05	67.6	108	23.1	926	30.2	31.1	0.21
TLM5	<0.05	39.4	46.6	288	1304	11.1	53.3	0.18
TLM6	<0.05	57.6	82.3	349	1338	60.4	107	0.54
TLM7	<0.05	131	363	6.59	<1	2572.1	74.5	1.12
TLL5	<0.05	82.6	126	248	674	8.37	44.2	0.20

[a]*Values are averaged from three to five analyses.*

GENESIS OF SPINEL CORONA AROUND CORUNDUM

Corundum with Spinel Corona from Primary Deposits. In many unaltered corundum-bearing rocks from primary deposits, the corundum crystals were enclosed by a spinel corona (figures 5 and 8). Petrographic investigation and, to some extent, the chemical composition of corundum grains with spinel corona from primary occurrences can be used to explain the genesis of the spinel corona. The Mg-Fe-Al-rich spinel and the hercynite-rich spinel corona samples were formed in migmatitic SiO_2-undersaturated and Fe-rich gneiss. The mineral assemblage is typically corundum surrounded by a hercynitic spinel–magnetite phase, Fe-rich biotite, plagioclase, K-

Figure 14. Corundum + spinel + biotite + garnet mineral assemblage from the Kinh La occurrence, shown in parallel-polarized light. Photomicrograph by N.V. Nam; field of view 1.2 mm.

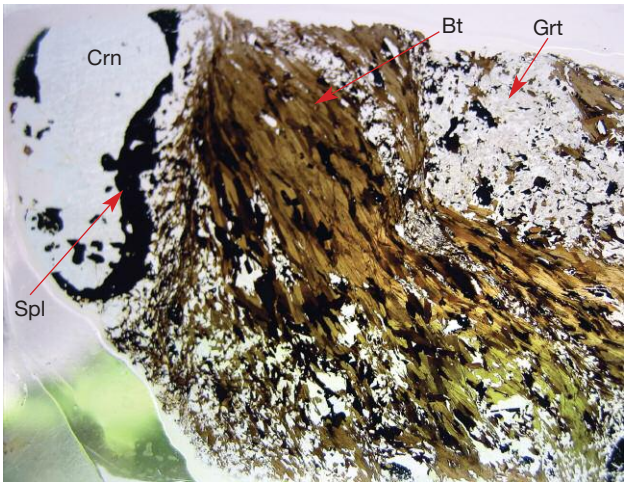

TABLE 4. Major element composition[a] (wt.%) of spinel rims on corundum from the Truc Lau secondary deposit.

Sample	TLM2	TLM3	TLM5	TLM6	TLM7	TLL5
Al_2O_3	69.47	70.59	70.09	70.46	69.58	70.00
TiO_2	<0.03	<0.03	<0.03	<0.03	<0.03	<0.03
Cr_2O_3	0.208	0.114	0.266	0.130	<0.03	0.326
FeO	0.353	0.654	0.050	0.667	1.272	0.255
MgO	28.52	28.90	28.86	28.89	28.51	28.97
ZnO	0.74	0.11	<0.1	<0.1	0.16	<0.1
Total	**99.29**	**100.37**	**99.26**	**100.14**	**99.52**	**99.55**

[a]*Values are averaged from three to five analyses.*

feldspar (figures 10, 15, and 17). In some samples the corundum and spinel are surrounded by garnet (almandine + pyrope + grossular or almandine-rich garnet; figures 14 and 16) and sillimanite (figure 16).

The significant amounts of Fe and Mg contained in the spinel grains, along with textural observations, suggest that the spinel might have been formed by the reaction of corundum and Mg-Fe containing silicate mineral, biotite, and/or garnet.

In the same calc-silicate rock were some portions with abundant biotite mica and some where it had been exhausted. Generally, corundum-bearing rocks were subjected to regional upper amphibolite to lower granulite facies metamorphism (about 650–760°C and 5.0–7.6 kbar; Khoi et al., 2016). In spite of these conditions, the corundum could have been stable during metamorphism. During prograde metamorphism, however, the corundum-bearing assemblages reacted with biotite to form spinel. This reaction is dependent not only on pressure and temperature, but also on the composition of the fluid phase (ratio of H_2O to CO_2), and thus it may occur in one locality but not in another due to different fluid compositions. Observations revealed that the outer edge of the corundum was eroded to varying degrees and became less hexagonal, and the corundum core became thinner and thinner, while the spinel corona around the corundum crystal became thicker depending on the different stages of reaction (see figure 17, stages 1 to 4). Therefore, it is assumed that a reaction between corundum and biotite mica formed spinel as the major product along with K-feldspar:

(1) Biotite + Corundum → Spinel + K-feldspar + Fluid

$$K(Mg, Fe)_3[AlSi_3O_{10}](OH)_2 + 3Al_2O_3 \rightarrow 3(Mg, Fe)Al_2O_4 + KAlSi_3O_8 + H_2O$$

Figure 15. Corundum with hercynite-rich spinel corona in a sample from the Kinh La primary occurrence, shown in cross-polarized light. Photomicrograph by N.V. Nam; field of view 1.2 mm.

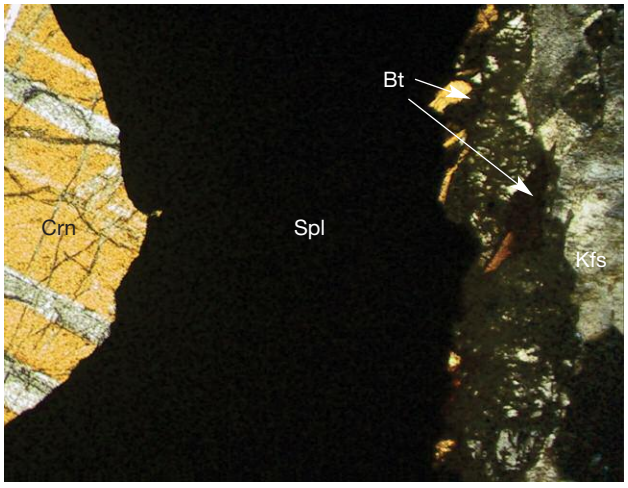

Figure 16. Corundum + spinel + garnet + sillimanite assemblage in a sample from the Kinh La primary occurrence (parallel-polarized light). Photomicrograph by N.V. Nam; field of view 1.2 mm.

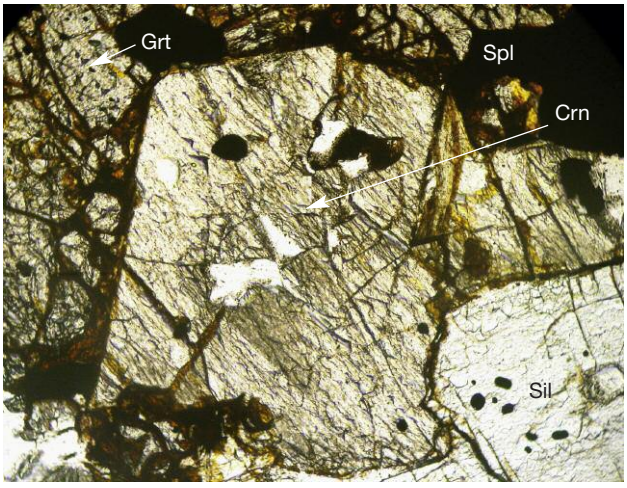

Figure 17. Observed stages of spinel corona formation around corundum grains. As can be seen, from stage 1 to stage 4 the spinel rim around the corundum crystal became progressively thicker, while the corundum core became thinner (until exhausted) and less perfectly hexagonal. Photo by N.N. Khoi.

This reaction could have been continuous until all the mica was exhausted or the corundum grains were completely transformed into spinel (see figure 17, stage 4). The reaction suggested on the basis of investigations of a hand specimen (figure 17) and a thin section (see figure 15) is illustrated in figure 18.

The corundum-spinel reaction would have continued until all the adjoining biotite was exhausted. This type of reaction is fluid dependent, and the chemical potential gradient in Al_2O_3 is the main driving force. As a result of this type of reaction, the quality of corundum was significantly reduced for almost all of the samples in the study.

If garnet and sillimanite are present in the samples, the following reaction can be proposed:

(2) Garnet + Corundum → Spinel + Sillimanite

$$(Fe, Mg)_3Al_2[SiO_4]_3 + 5Al_2O_3 \rightarrow 3(Mg, Fe)Al_2O_4 + 3AlO[AlSiO_4]$$

The above reactions, alone or in combination, are responsible for the observed corundum-spinel textural features.

Corundum with Spinel Corona from Secondary Deposits. Since samples recovered from secondary deposits are not enclosed in their original host rock, mineral compositions and inclusions must be used to determine the source and possible mineral reaction that led to the observed spinel-corundum texture. The spinels in types I and II are pure Al-Mg spinels (see table 4) with calcite and dolomite inclusions (see figure 13B). The chemical composition points toward an Fe-poor host rock, either (a) ultramafic rock (containing some Fe) or (b) metacarbonate (marble). Based on the scarcity of ultrabasic rocks and the nearly Fe-free spinel composition, we conclude that this type of corundum with spinel corona most likely developed in a metacarbonate rock. Additionally, the calcite and dolomite inclusions in the spinel corona clearly point toward this host rock source. Corundum typically forms in metacarbonate rocks during prograde metamorphism from an originally sedimentary deposited Al-hydroxide phase such as diaspore and/or boehmite. With increasing temperature, corundum could transform to spinel if dolomite is present by the following reaction (Hauzenberger et al., 2010, 2012; Häger et al., 2010):

(3) Dolomite + Corundum → Spinel + Calcite + Carbon dioxide

$$3MgCa(CO_3)_2 + 3Al_2O_3 \rightarrow 3MgAl_2O_4 + 3CaCO_3 + 3CO_2$$

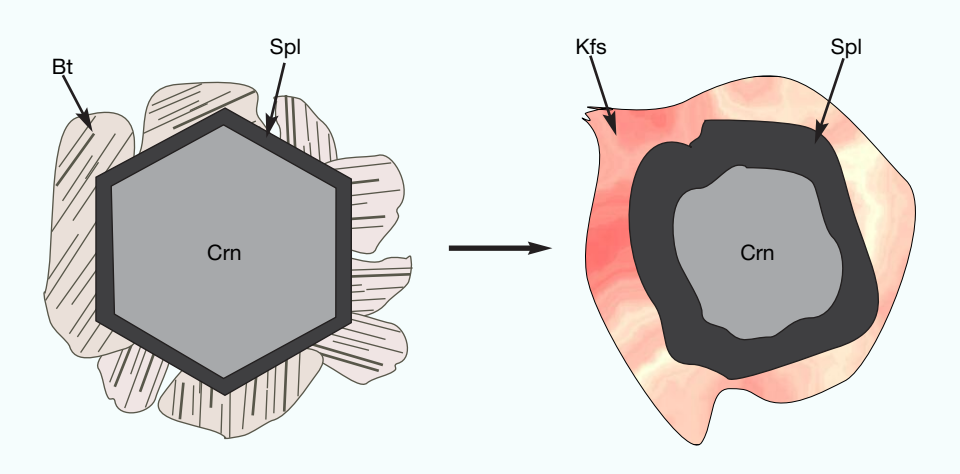

Figure 18. Schematic illustration of the non-uniform enlargement of spinel corona due to the reaction of corundum and biotite.

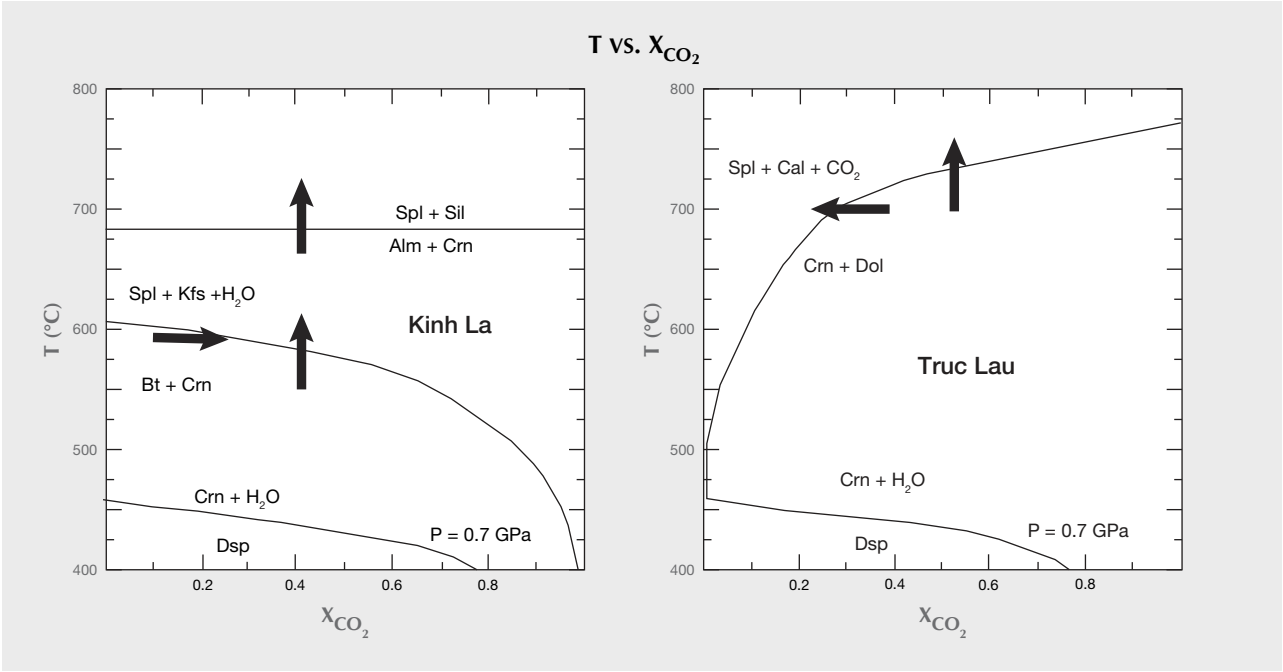

Figure 19. T vs. X_{CO_2} diagram showing the phase relations and mineral reactions that formed the spinel corona. The arrows indicate the possible direction to overstep the reactions (T increase or change in fluid composition). Spl = spinel, Kfs = K-feldspar, Sil = sillimanite, Bt = biotite, Crn = corundum, Dsp = diaspore, Cal = calcite, and Dol = dolomite.

Similar to the samples from primary sources, the outer edges of the corundum core were also eroded to different extents, suggesting a disequilibrium between the two phases. As a result, the spinel rim around the corundum crystal became thicker and the corundum core became less perfectly hexagonal, depending on the stage of this corundum-consuming reaction (see figure 12). The difference between the spinels of different stages clearly indicates the role of the above hypothesized reaction, which led to the increase in the amount of spinel and thickening of the corona, with a simultaneous reduction in the amount of corundum.

The spinel composition in types III and IV is a hercynite-rich spinel to hercynite with phlogopite inclusions (see again, figure 13E). In this case the above-mentioned reaction (1) could also be hypothesized for corundum → spinel transformation.

The three equations above describing reactions of corundum → spinel transformation were calculated in a T vs. X_{CO_2} diagram (figure 19). A T vs. X_{CO_2} diagram is used instead of a *P-T* diagram to demonstrate the importance of fluid composition for the stability of mineral assemblages and hence possible mineral reactions, especially in metacarbonate. The observed spinel corona textures are evidence that a reaction must have proceeded quickly. While changes in P and especially T are usually relatively slow, a change in fluid composition can be accomplished very quickly and thus is the likely mechanism to produce the observed spinel corona. The spinel-forming reactions are strongly dependent on the mole fraction of CO_2 in the fluid phase (X_{CO_2}). A drop in X_{CO_2} below ~0.2 destabilizes corundum and dolomite, and spinel and calcite form at a temperature of about 600–700°C. A final late-stage H_2O-rich fluid infiltration is recorded in diaspore veins (confirmed by Raman spectroscopy) crosscutting the corundum core as well as the spinel corona, as shown in figure 13A. As seen in figure 19, this event must have occurred below 450°C.

Reaction textures in corundum and spinel have been studied to some extent elsewhere: by Schmetzer et al. (1996) and Sunagawa et al. (1999) in trapiche ruby, by Das et al. (2014) in Indian ruby from alluvial deposits, and by Francis et al. (2002, 2004) in Sri Lankan ruby and sapphire from marble. Samples of sapphire with spinel corona were also found rarely in pegmatite and nepheline syenite rocks at Mogok, Myanmar (Themelis, 2008). The hypothesized reaction (1) is essentially similar to the one proposed by Francis et al. (2002, 2004) for the corundum-spinel texture found in marble from Sri Lanka (Katz, 1986):

(4) Phlogopite — Corundum — Spinel — K-feldspar — Water

$$KMg_3[AlSi_3O_{10}](OH)_2 + 3Al_2O_3 \rightarrow 3MgAl_2O_4 + KAlSi_3O_8 + H_2O$$

Figure 20. Cutting away the spinel coating revealed a high-quality internal ruby core. Photo by N.N. Khoi.

Here, the Mg biotite end member phlogopite reacted with corundum to form pure Mg spinel.

As shown above, corundum occurrences and deposits in northern Vietnam are hosted not only in marble of the Lo Gam structural zone, but also in partly migmatized gneiss of the Day Nui Con Voi range in the Red River shear zone (see again, figure 1). It is interesting to note that until now corundum crystals with spinel corona were found only in the so-called gneiss-hosted deposits, both primary and secondary, in the Tan Huong–Truc Lau area (Khoi et al., 2011, 2016).

Local gem dealers call the spinel-encrusted corundum "gamble merchandise" (*hàng mở bát*) or "coated merchandise" (*hàng bọc*), indicating the uncertainty of dealing with these goods. Cutting away the spinel crust sometimes reveals gem-quality ruby inside (figure 20).

CONCLUSIONS

Corundum with a spinel corona is a noteworthy characteristic of both primary and secondary deposits of the Tan Huong–Truc Lau area in the Red River shear zone of northern Vietnam. Typically, corundum formed during regional prograde, upper amphibolite to lower granulite facies metamorphism (650–760°C and 5.0–7.6 kbar) from an originally sedimentary deposited Al-hydroxide phase such as diaspore and/or boehmite (bauxitic layers).

During high-grade metamorphism, corundum reacts with biotite, garnet, or dolomite at a certain stage to form spinel, producing the typical spinel corona. This transformation process can be explained by the following reactions:

(a) biotite + corundum → spinel + K-feldspar + fluid (H_2O)
(b) corundum + garnet → spinel + sillimanite for calc-silicate gneissic rocks
(c) corundum + dolomite → spinel + calcite + carbon dioxide for metacarbonate rocks

These reactions, either singularly or in combination, might have given rise to the observed corundum-spinel textural features. The macroscopic reaction textures associated with corundum are important in the sense that they reveal how it was affected after formation. Because of volume change during the transformation of corundum to spinel, fracturing occurred in the involved phases, and these fractures were often filled with retrograde reaction products such as diaspore. Hence, the gem quality deteriorated substantially after the formation of the corona.

ABOUT THE AUTHORS

Dr. Khoi (khoinn@vnu.edu.vn) is an associate professor of geology at the Hanoi University of Science and director of the DOJI Institute and Laboratory for Gemology and Jewelry. Dr. Hauzenberger is a professor of petrology and geochemistry at the University of Graz, Austria. Dr. Sutthirat is an associate professor of geology in the Faculty of Science and director of Environmental Research Institute at Chulalongkorn University in Bangkok. Mr. Tuan is vice general director of DOJI Gold & Gems Group in Hanoi. Dr. Häger is senior scientist at the Centre for Gemstone Research at Johannes Gutenberg University and lecturer in gemstone and jewelry design at the University for Applied Sciences in Idar-Oberstein, Germany. Dr. Nam is senior researcher of the Vietnam Institute of Geosciences and Mineral Resources in Hanoi.

ACKNOWLEDGMENTS

This research is funded by the Vietnam National Foundation for Science and Technology Development (NAFOSTED) under grant number 105.02-2012.08. We would like to thank ASEA-UNINET for financial support. We also thank DOJI Gold & Gems Group and its technical staff for their assistance with this work. Research facilities were provided by the Institute of Earth Sciences (Mineralogy and Petrology) at Karl-Franzens-University of Graz (Austria), the Institute of Geosciences (Gemstone Research Center) at Johannes Gutenberg University (Mainz, Germany), the Hanoi University of Science (Vietnam National University), Chulalongkorn University (Bangkok), and the Vietnam Institute of Geosciences and Mineral Resources.

REFERENCES

Das S.K., Mohanty J.K. (2014) Characterisation of eluvial corundum (ruby) from Kermunda, Kalahandi district, Odisha, India. *Journal of Geology & Geophysics*, Vol. 3, No. 6, p. 180, http://dx.doi.org/10.4172/2329-6755.1000180

Francis M.D.P.L., Dharmaratne P.G.R. (2002) Corundum/spinel reaction textures in carbonate-origin rocks, Sri Lanka—Preliminary observations. *The Australian Gemmologist*, Vol. 21, No. 5, pp. 211–214.

Francis M.D.P.L., Matsueda H. (2004) Study of macroscopic and microscopic reaction textures associated with corundum of Balangoda region, Sri Lanka. *Proceedings of International Symposium on "Dawn of a New Natural History—Integration of Geoscience and Biodiversity Studies,"* Sapporo, March 5–6, pp. 129–136.

Garnier V., Giuliani G., Maluski H., Ohnenstetter D., Trinh P.T., Vinh H.Q., Long P.V., Tich V.V., Schwarz D. (2002) Ar–Ar ages in phlogopites from marble-hosted ruby deposits in northern Vietnam: evidence for Cenozoic ruby formation. *Chemical Geology*, Vol. 188, No. 1-2, pp. 33–49, http://dx.doi.org/10.1016/S0009-2541(02)00063-3

Garnier V., Giuliani G., Ohnenstetter D., Fallick A.E., Dubessy J., Banks D., Hoàng Q.V., Lhomme T., Maluski H., Pecher A., Bakhsh K.A., Pham V.L, Trinh P.T., Schwarz D. (2008) Marble-hosted ruby deposits from Central and Southeast Asia: Towards a new genetic model. *Ore Geology Reviews*, Vol. 34, No. 1-2, pp. 169–191, http://dx.doi.org/10.1016/j.oregeorev.2008.03.003

Häger T., Khoi N.N., Tuan D.A., Huong L.T.T., Hofmeister W. (2010) Ruby and sapphire rimmed by spinel from the Luc Yen–Yen Bai gem mining area, Vietnam. *20th General Meeting of the International Mineralogical Association: Abstracts*, Budapest, August 21-27, p. 27.

Hauzenberger C.A., Häger T., Wathanakul P., Khoi N.N., Nantasin P., Goessler W. (2010) Petrology and geochemical characteristics of ruby with associated spinel corona from Truc Lau, N. Vietnam. *Proceedings of the 5th International Conference on the Provenance and Properties of Gems and Geo-Materials*, Hanoi, October 17–24, pp. 23–28.

Hauzenberger C.A., Khoi N.N., Sutthirat C., Häger T., Wathanakul P., Tuan D.A. (2012) Ruby with associated spinel corona from Truc Lau and Kinh La, North Vietnam. *Proceedings of the 3rd International Gem & Jewelry Conference (GIT 2012)*, Bangkok and Chanthaburi, December 12–16, pp. 123–126.

Katz M.B. (1972) On the origin of the Ratnapura-type gem deposit of Ceylon. *Economic Geology*, Vol. 67, No. 1, pp. 113–115, http://doi.org/10.2113/gsecongeo.67.1.113

Katz M.B. (1986) Review of the geology of the gemstones of Sri Lanka. *Australian Gemmologist*, Vol. 16, No. 2, pp. 52–56.

Khoi N.N., Sutthirat C., Tuan D.A., Nam N.V., Thuyet N.T.M., Nhung N.T. (2010) Comparative study of rubies and fancy sapphires from two different deposit types in Yen Bai Province, Vietnam. *Proceedings of the 5th International Workshop on Provenance and Properties of Gems and Geo-Materials*, Hanoi, October 17–24, pp. 212–223.

Khoi N.N., Sutthirat C., Tuan D.A., Nam N.V., Thuyet N.T.M., Nhung N.T. (2011) Ruby and sapphire from the Tan Huong–Truc Lau Area, Yen Bai Province, northern Vietnam. *G&G*, Vol. 47, No. 3, pp. 182–195, http://dx.doi.org/10.5741/GEMS.47.3.182

Khoi N.N., Hauzenberger C.A., Sutthirat C., Tuan D.A., Thuyet N.T.M., Duong N.T., Nam N.V., Lam C.V. (2013) The characteristics of gneiss-hosted corundum deposits of Tan Huong-Truc Lau area, northern Vietnam. *Proceedings of the 33rd International Gemmological Conference (IGC33)*, Hanoi, October 13–17, pp. 25–28.

Khoi N.N., Hauzenberger C.A., Tuan D.A., Häger T., Nam N.V., Duong N.T. (2016) Mineralogy and petrology of gneiss hosted corundum deposits from the Day Nui Con Voi metamorphic range, Ailao Shan–Red River shear zone (North Vietnam). *Journal of Mineralogy and Geochemistry*, Vol. 193, No. 2, pp. 161–181, http://dx.doi.org/10.1127/njma/2016/0300

Leloup P.H., Lacassin R., Tapponnier P., Schärer U., Zhong D., Liu X., Zhang L., Ji S., Trinh P.T. (1995) The Ailao Shan-Red River shear zone (Yunnan, China), Tertiary transform boundary of Indochina. *Tectonophysics*, Vol. 251, No. 1-4, pp. 3–84, http://dx.doi.org/10.1016/0040-1951(95)00070-4

Leloup P.H., Arnaud N., Lacassin R., Kienast J.R., Harrison T.M., Trong T.T.P., Replumaz A., Tapponnier P. (2001) New constraints on the structure, thermochronology, and timing of the Ailao Shan-Red River shear zone, SE Asia. *Journal of Geophysical Research*, Vol. 106, No. B4, pp. 6683–6732, http://dx.doi.org/10.1029/2000JB900322

Long P.V., Vinh H.Q., Garnier V., Giuliani G., Ohnenstetter D., Lhomme T., Schwarz D., Fallick A., Dubessy J., Trinh P.T. (2004) Gem corundum deposits in Vietnam. *Journal of Gemmology*, Vol. 29, No. 3, pp. 129–147.

Nam N.V. (2012) Mineralogical and chemical composition and formation conditions of rubies and sapphires in metamorphic rocks of Tan Huong-Truc Lau area (Red River zone). PhD Thesis, Vietnam Institute of Geosciences and Mineral Resources, 181 pp. [in Vietnamese].

Schmetzer K., Hänni H.A., Bernhardt H.J., Schwarz D. (1996) Trapiche rubies. *G&G*, Vol. 32, No. 4, pp. 242–250, http://dx.doi.org/10.5741/GEMS.32.4.242

Simandl G.J., Paradis S. (1999) Corundum in alumina-rich metasediments. In G.J. Simandl, Z.D. Hora, and D.V. Lefebure, Eds., *Selected British Columbia Mineral Deposit Profiles*, Vol. 3, Industrial Minerals and Gemstones. British Columbia Ministry of Energy and Mines, Open File 1999-10, pp. 105–108.

Sunagawa I., Bernhardt H.-J., Schmetzer K. (1999) Texture formation and element partitioning in trapiche ruby. *Journal of Crystal Growth*, Vol. 206, No. 4, pp. 322–330, http://dx.doi.org/10.1016/S0022-0248(99)00331-0

Themelis T. (2008) *Gems & Mines of Mogok: The Forbidden Gem Land*. Published by the author, Bangkok.

Thuyet N.T.M. (2008) Study on typomorphic and gemological characteristics of corundum from some genetic types of deposits in Yen Bai and Dak Nong Provinces of Vietnam. PhD thesis, Hanoi University of Science, 133 pp. [in Vietnamese].

Trinh P.T., Vinh H.Q. (1997) Sketch tectonic map of Luc Yen area, Scale 1:200,000. Institute of Geological Sciences, Hanoi [in Vietnamese].

Vinh N., Ed. (2005) Geology and Mineral Resources of Vietnam, Yen Bai Sheet, Scale 1:200,000 (F 48 XXI). Department of Geology and Minerals of Vietnam, Hanoi.

Whitney D.L, Evans B.W. (2010) Abbreviations for names of rock-forming minerals. *American Mineralogist*, Vol. 95, No. 1, pp. 185–187, http://dx.doi.org/10.2138/am.2010.3371

Xuyen T., Ed. (2000) Geology and Mineral Resources Map of Vietnam, Bac Quang Sheet, Scale 1:200,000 (F 48 XV). Department of Geology and Minerals of Vietnam, Hanoi.

The Gemological Characteristics of Pipi Pearls Reportedly from *Pinctada maculata*

Nanthaporn Nilpetploy, Kwanreun Lawanwong, and Promlikit Kessrapong

Pipi pearls originating from the bivalve mollusk *Pinctada maculata* are usually small natural pearls with a desirable and variable range of moderate to strong colors. This study details their characteristic features, including their internal structures and the spectroscopic data that may aid in their identification. The samples were examined by microradiography to reveal the range of internal structures found within these natural pearls. Spectroscopic studies were also employed using conventional gemological methods such as ultraviolet-visible (UV-Vis) reflectance, Raman, and photoluminescence (PL) spectroscopy. The spectroscopic results showed some characteristic patterns such as a distinct absorption feature around 495 nm in the UV-Vis spectra and peaks at 1380 and 1540 cm^{-1} in the Raman spectra. The spectral features show some similarities to other mollusk species within the same family but may still assist gemologists in separating, to some degree, *Pinctada maculata* species from their relatives.

In the Polynesian language, *pipi* means "small" or "tiny" and is used to refer to the small, predominantly yellow or "golden" pearls that originate from the bivalve mollusk *Pinctada maculata* (Gould, 1846). As the smallest mollusk species in the *Pinctada* genus, *Pinctada maculata* rarely exceeds 5 cm when measured in the anterioposterior or dorsoventral positions. The mollusk lives in the Indo-Pacific Ocean, mostly around French Polynesia and the Cook Islands, where they are often found in association with the *Pinctada margaritifera* mollusk species (Strack, 2006). Pearls from *Pinctada maculata* often form in round to near-round shapes. As the name implies, the small shells produce small pearls that rarely exceed 8 mm in diameter (Krzemnicki, 2014). Based on GIA's experience, 6 mm or under is more typical of the species.

Pipi pearls are known to occur as natural pearls rather than cultured and, compared with other *Pinctada* species, are deemed rare. One report recorded only one gem-quality pearl found from a total of 355 mollusks (Passfield, 1997). In 1950, several cultured pearl experiments using *Pinctada maculata* reportedly took place but were unsuccessful (Segura et al., 2014). In the late 1990s, a few *Pinctada maculata* cultured blister pearls resulted from experiments in the waters off Penrhyn, an island in the northern atoll of the Cook Islands (Kessrapong et al., 2017). The nacre covering the bead nuclei did not fully overgrow the nuclei, however, and this attempt was not very successful. Some reports suggest that the *Pinctada maculata* mollusk is not abundant enough for commercial exploitation. Local regulations also protect them from being harvested by foreigners, further limiting the chances of cultured pearl production (Buscher, 1999). Given the limited documentation of *Pinctada maculata* cultured pearls, it is almost certain that all pearls currently fished from the species are natural pearls.

In Brief

- Pearls originating from the *Pinctada maculata* mollusk are rare and no known commercial cultured pearl production has been reported.
- Previous studies on pipi pearls were less comprehensive than this work and the results provide some information on the characteristics that may assist in the identification of pearls produced by the *Pinctada maculata* mollusk.
- The combination of the nature of a pearl's internal structure via microradiography and its spectroscopic results (ultraviolet visible (UV-Vis) reflectance, Raman, and photoluminescence (PL) spectroscopy) help indicate whether a pearl formed in a *Pinctada maculata* mollusk or another species.

See end of article for About the Authors and Acknowledgments.
Gems & Gemology, Vol. 54, No. 4, pp. 418–427,
http://dx.doi.org/10.5741/GEMS.54.4.418

Figure 1. Pinctada maculata *pearls alongside a* Pinctada maculata *mollusk valve with an attached blister pearl. The pearls range from 2.20 mm to 6.49 × 4.83 × 4.49 mm, and the shell measures approximately 28.54 × 26.50 mm. Photo by Nuttapol Kitdee.*

The spectroscopic data of *Pinctada maculata* shells and pearls appear to show some characteristic features that would help with their identification. While some previous work on the spectra of *Pinctada maculata* pearls has been undertaken (Segura et al., 2014), the results were inconclusive and could not specify the mollusk. The authors decided to pursue this study to record the characteristic features of reported *Pinctada maculata* pearls in order to share the data with the wider gemological community.

MATERIALS AND METHODS

GIA's Bangkok laboratory received 31 pearl samples that were claimed to be natural Pipi pearls originating from *Pinctada maculata* mollusks. One shell sample included an attached blister or blister pearl (figure 1). The pearls varied widely in color and exhibited a range of different tones. Colors within the group included white, cream, yellow—some of strong saturation, referred to as "golden" in the trade (*GIA Pearl Grading Color Reference Charts*, 2000)—and yellow-orange to dark brown. Their sizes ranged from 2.22 × 2.20 mm to 6.49 × 4.83 × 4.49 mm, and their weights ranged from 0.06 to 1.00 ct. The shell measured approximately 28.54 × 26.50 mm and weighed 5.04 grams. As indicated by the measurements, some of the samples fell within the size range known in the trade as "seed pearls." This term is usually applied to very small natural pearls between two and three millimeters when sieved (CIBJO, 2016).

Real-time microradiography (RTX) analysis was performed on the samples in three orientations using a Pacific Industries (PXI) GenX 90 X-ray system with 4 micron microfocus, 90 kV voltage, and 0.18 mA current X-ray source with an exposure time of 200–

350 milliseconds per frame, and a PerkinElmer 1512 4"/2" dual-view flat panel detector with maximum 128 frames average and 74.8 micropixel pitch with 1944 × 1536 pixel resolution. Ultraviolet-visible (UV-Vis) spectra were obtained using an Agilent Cary 60 spectrophotometer with a custom-made GIA integrated sphere diffuse reflectance accessory (DRA) incorporating an 80 Hz xenon flash lamp source. Spectra were recorded in the 200–800 nm range with a data interval set at 1.0 nm and a 1.5 nm fixed spectral bandwidth and scan rate of 184.62 nm/min over a 3.5 mm^2 area. Raman and photoluminescence (PL) spectra were collected using a Renishaw inVia Reflex micro-Raman spectrometer system with a 50× magnification Leica objective lens and a 514 nm argon-ion laser. A laser power of 50 mW was used directly on the samples, and the system was calibrated using the standard internal silicon 520 cm^{-1} method. The Rayleigh radiation was blocked using edge filters. The laser was set at 100% power with three accumulations and an exposure time of 10 seconds with a grating of 1800 grooves/mm. PL spectra were collected with the laser power set at 50% with one accumulation and an exposure time of 15 seconds with a grating of 1200 grooves/mm. The fluorescence reactions of the pearls were observed under UV radiation using a GIA-designed long-wave UV unit with a 4-watt UV lamp emitting 365 nm radiation. A GIA binocular gemological microscope was used to observe surface structures, determine the nature of the color (namely natural or artificial deposition), and assist with the detection of any other potential treatments.

RESULTS

Internal Structures. Pearls are composed of $CaCO_3$ in the form of aragonite or calcite, conchiolin (an organic component), and water, as well as other residual substances (Southgate and Lucas, 2008). The radiopacity of the main $CaCO_3$ component and the

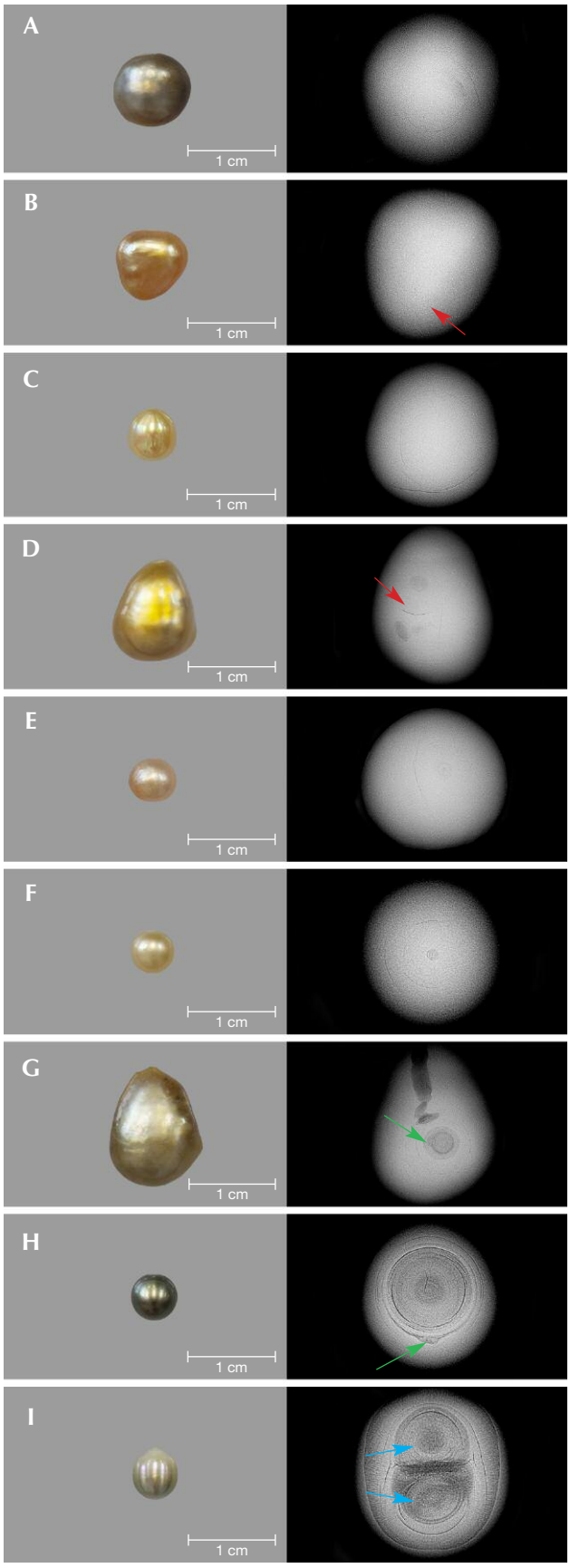

Figure 2. Macro images of nine pearls (A–I, left column) weighing 0.11–0.97 ct. Photos by Sasithorn Engniwat. The RTX results for six pearls (A–F, right column) revealed natural internal structures, typical of many nacreous pearls, while the structures of the other three pearls (G–I, right column) showed some features that might raise suspicion, such as seed-like features (G–H, green arrows) and off-round cores. Radial structure is evident in the organic-rich area of pearl I, and the blue arrows indicate the twin cores, one of which is ovoid. Spectroscopic analysis was also carried out on pearls B, D, and G (labeled P593, P587, and P588, respectively).

other components differ—the former is denser, while the latter are more transparent—allowing the internal structures to be viewed on the resulting images (Farn, 1986; Webster, 1994).

Microradiography was carried out on all the *Pinctada maculata* pearl samples and revealed clear natural pearl structures (Alexander, 1941; Farn, 1986; Taburiaux, 1986) in the majority. Growth arcs from the center toward the surface of the pearl, akin to the ring structure seen in onions or cross-sections of trees, together with faint organic-rich shadows positioned on the curves of some arcs, all typical of many natural pearls (figure 2, A–C), were present in most of the samples, although it is the authors' experience that some, such as pearl B, show a very faint structure (figure 2B, red arrow), which is also typical of natural pearls. Another commonly encountered structural feature of many natural pearls—a small dark radio-translucent, rounded organic-rich core—was also evident in the RTX results of many samples (figure 2, D–F). Another common feature in the way of a growth boundary was visible in the RTX results of pearl D (figure 2D, red arrow). Two organic-rich cores, one on each side of the boundary, were also visible. "Twins," or pearls formed of aggregates of pearls, are not uncommon in natural pearls from a number of species (Krzemnicki et al., 2010).

The last three pearls (figure 2, G–I) revealed internal structures with similarities to those that have been noted in pearls from *Pinctada maxima* and *Pinctada radiata* (Krzemnicki et al., 2010; Sturman et al., 2015) but differed from most of the other natural samples in the group we examined. Only these three pearls from the group exhibited such organic-rich core structures. While the structures are likely natural, the minute whitish core in the center with some associated gaps between the concentric rings and the additional odd irregular white feature at the outer concentric rings or near the core of two of the pearls (figure 2, G–H, green arrows) raised some minor concerns about their identity (Sturman et al., 2016). The remaining pearl showed a twin structure (figure 2I, blue arrows) consisting of concentric organic-rich features with radial structures and a near-oval core in one part. While it is entirely possible for natural pearls such as this one to possess an unusually shaped core, it is the authors' experience that elliptical, drop, or other elongated core features are more often associated with non-bead-cultured pearls.

Among the group selected for examination was one blister/blister pearl[1] attached to the valve of a *Pinctada maculata* shell (figure 3A). In keeping with many blisters/blister pearls, the preliminary observations of the RTX results showed the internal structure of the pearl "superimposed" with the growth features and imperfections of its host shell (figure 3B). The imperfections, found in the shells of most mollusk species, were present as veins or channels created by a living organism boring its way through the shell throughout its life. While it was unclear from initial observation whether this would be classified as a blister or a blister pearl, more detailed RTX analysis soon revealed that it was solid and possessed clear concentric rings more characteristic of a blister pearl than a blister (figure 3C).

Fluorescence Reactions. All the samples were examined under long-wave ultraviolet (LWUV) radiation. Their reactions varied in relation to their color saturation. Most of the darker samples were inert, while the lighter-color pearls and lighter-color areas on some of the more saturated pearls showed a moderate to strong chalky bluish green reaction. These fluorescence reactions are not diagnostic in any way and may be observed in pearls of similar saturations from other *Pinctada* species (Elen, 2001; Nilpetploy et al., 2018). Their reactions are also in keeping with naturally colored pearls and do not indicate the presence of any color treatment (Elen, 2001; Zhou et al., 2012).

Spectroscopic Results. Some of the *Pinctada maculata* pearl samples showing the most homogenous coloration were also selected for UV-Vis, Raman, and PL spectroscopic examination. Many were too small (approximately 3 mm or less) to examine with the external DRA of the UV-Vis and would have produced noisy spectra while potentially damaging the DRA's integrated sphere. Owing to the instrument's limitations and the generally smaller size of *Pinctada maculata* pearls, it was only possible to examine six samples with enough variation in their coloration with the UV-Vis spectrophotometer to show the results of the Raman and PL analyses. The spectral results directly corresponded with the color saturation and tone of the samples. The lighter samples showed higher reflectance values while the darker and more saturated ones exhibited less reflectance in the UV-Vis spectra.

[1]A *blister* is a structure that forms on the inside surface of a mollusk's shell and has the appearance of a pearl but is not a pearl by definition. A *blister pearl* forms in the body of a mollusk but for some reason moves to a position near the inside surface of a mollusk's shell. Layers of nacre are subsequently secreted over the pearl so that it becomes attached to the shell.

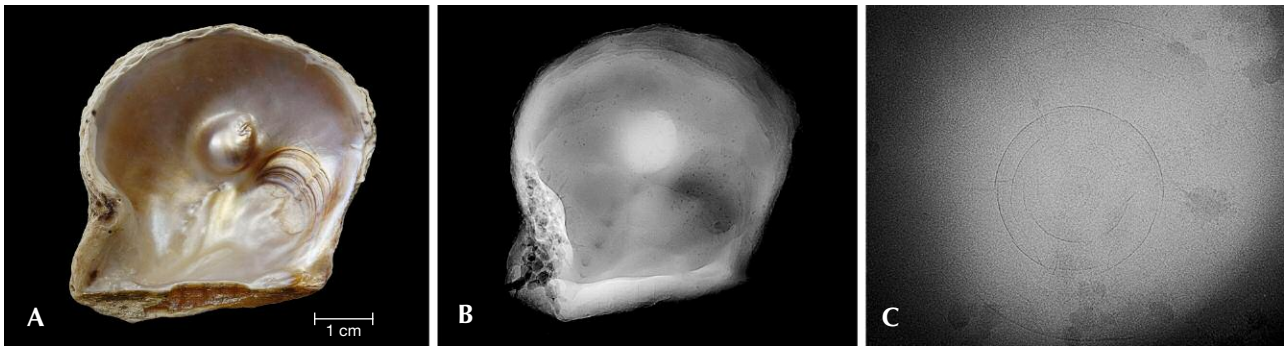

Figure 3. A blister pearl attached to its shell (A), measuring approximately 28.54 × 26.50 mm. Photo by Sasithorn Engniwat. RTX analysis revealed the shell with its blister/blister pearl (B), and when examined in more detail the blister pearl's internal structure (C).

The UV-Vis spectra of the six pearls displayed a diffuse reflectance decrease between 330 and 460 nm (figure 4, blue shaded area), and four showed a clear feature at 495 nm (figure 4, indicated by a red dotted line) and a reflectance maximum between 550 and 720 nm (figure 4, green shaded area). Samples P590 and P593 did not show the 495 nm feature but did reveal a spectrum that differed from those of the other samples. In addition, a weaker feature around 445–455 nm was observed in P586 and P589. Other lightly colored pearl samples (white and light gray) were also examined. As expected, they did not exhibit any helpful features, so their spectra are excluded.

Raman spectra were collected for the same pearls (figure 5) in the same area tested when recording the UV-Vis spectra, and as expected all showed the doublet peaks at 701, 704 cm^{-1} attributed to the ν_4 (in-plane bending), a prominent peak at 1086 cm^{-1} attributed to the ν_1 (symmetric stretching), and weak features at 1464 and 1574 cm^{-1} attributed to the ν_3 (in-plane asymmetric stretching) of aragonite; the latter peak was recorded by previous authors (Urmos et al., 1991; Buzgar and Apopei, 2009). Furthermore, the spectra exhibited two small features at 1380 and 1540 cm^{-1} (figure 5, indicated by red dotted lines) most likely associated with pigments responsible for coloring the pearls. Samples P590 and P593 did not show any helpful features in their UV-Vis spectra (figure 4); however, two weak features were observed in the Raman spectra (figure 5). Other lightly colored

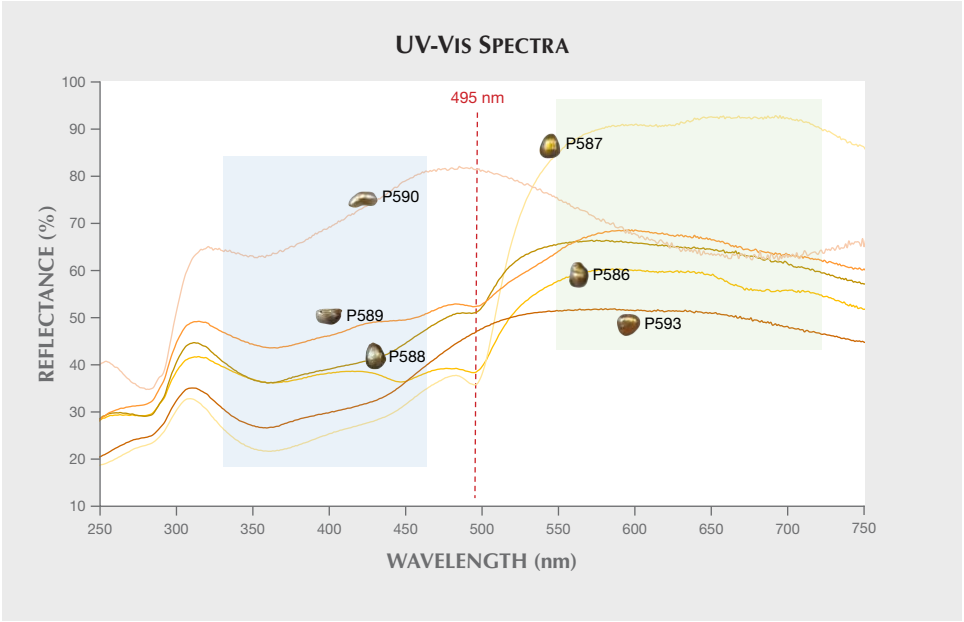

Figure 4. UV-Vis spectra of six Pinctada maculata *samples. Four of the samples display a clear 495 nm feature (red dotted line). A diffuse reflectance decrease is also visible between 330 and 460 nm (blue shaded area), as well as a broad reflectance band around 550–720 nm (green shaded area).*

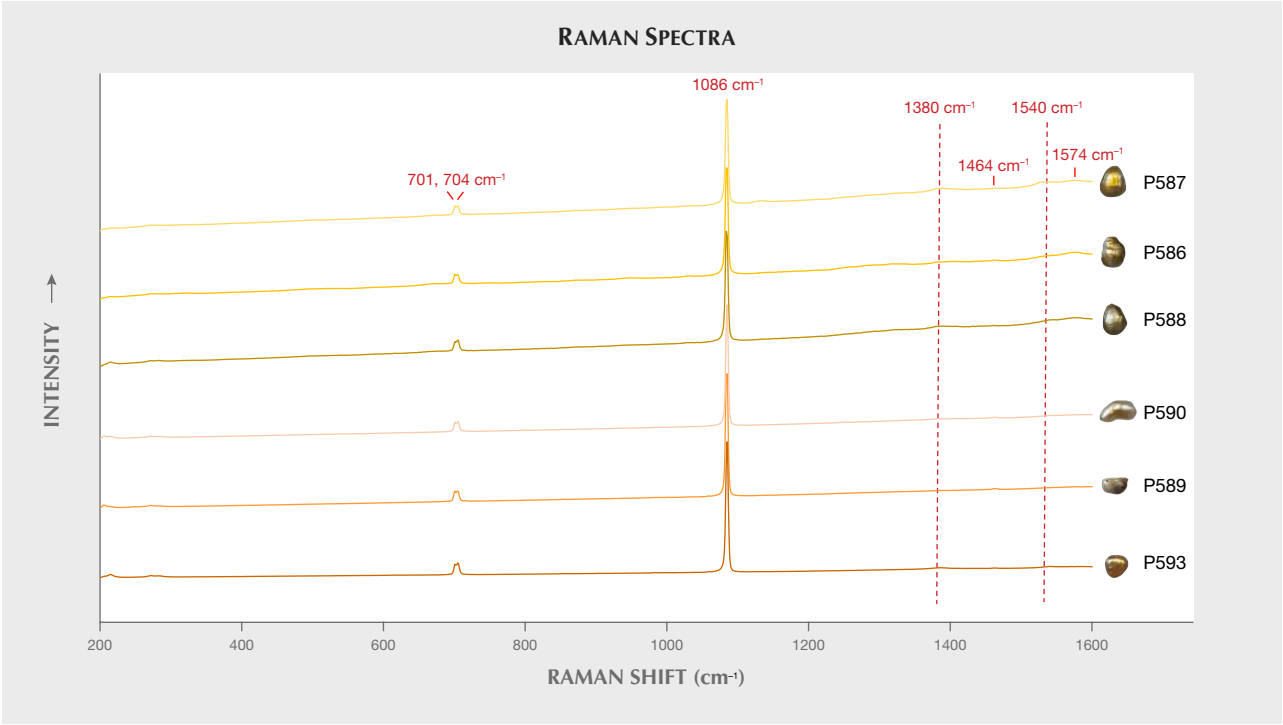

Figure 5. Raman spectra of six Pinctada maculata *samples showing the aragonite-related peaks at 701, 704, 1086, 1464, and 1574 cm^{-1}, with two additional features at 1380 and 1540 cm^{-1} (red dotted lines). The spectra were normalized and offset for clarity, each shifted upward by 30%.*

samples (white and light gray) were also tested, but as with the UV-Vis work, they did not show any helpful features either and therefore their spectra are excluded.

The PL spectra of four samples exhibited three broad peaks at approximately 620, 650, and 680 nm (figure 6, indicated by red dotted lines). Additional peaks of varying intensity, most likely corresponding

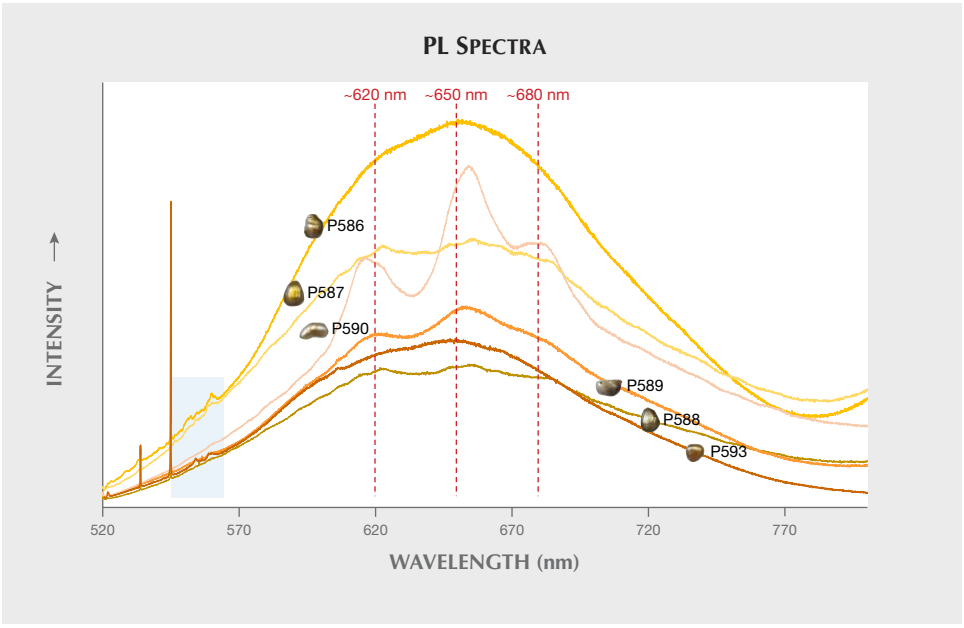

Figure 6. PL spectra of six Pinctada maculata *samples showing the three broad peaks at approximately 620, 650, and 680 nm (red dotted lines), as well as a series of peaks between 545 and 565 nm (blue shaded area). The latter correspond to Raman peaks observed between 1106 and 1756 cm^{-1}.*

TABLE 1. Comparison of features used in the separation of *Pinctada maculata* pearls from other mollusks.

Mollusk	Characteristic features			References
	UV-Vis spectra (nm)	Raman spectra (cm^{-1})	PL spectra (nm)	
Pinctada maculata	330–460, 495	1380, 1540	~620, 650, 680	This study
Pinctada margaritifera	330–460 (only in yellow), 405, 495, 700	Bands between 1100 and 1800	~620, 650, 680	Miyoshi et al. (1987); Iwahashi and Akamatsu (1994); Elen (2002); Karampelas et al. (2011); Homkrajae (2016); Nilpetploy et al. (2018)
Pinctada mazatlanica	330–460 (only in yellow), 405, 700	1380, 1540 (only in yellow)	~620, 650, 680	Homkrajae (2016)
Pteria penguin and *Pteria sterna*	405, 495	Bands between 1100 and 1800	~620, 650, 680	Miyoshi et al. (1987); Iwahashi and Akamatsu (1994); Kiefert et al. (2004)
Pinctada maxima (moderate to dark colors)	495	—	~620, 650, weak 680	Karampelas (2012)
Pinctada maxima (yellow color range)	330–460	1380, 1540	—	Elen (2001); Cartier and Krzemnicki (2016); GIA reference pearls collected from Jewelmer farms

to Raman peaks between 1106 and 1756 cm^{-1}, were also observed between 545 and 565 nm (figure 6, blue shaded area) in all the spectra. Even though the body-color of sample P590 was lighter than the others, it still exhibited three obvious features in the PL spectra, but the UV-Vis spectra obtained from it were not helpful. The three bands in samples P586 and P593 were less prominent than noted in the other four pearls. As with the UV-Vis and Raman spectra collected from the white and light gray pearls, their lack of diagnostic features precluded their spectra from being included in this report.

The representative spectra from all the spectral methods, together with observation through a gemological microscope, did not reveal anything to indicate that the pearls were treated (i.e., color concentrations, veining, and patchiness via transmitted lighting), thus proving the natural color origin of the samples examined (Elen, 2001; Zhou et al., 2012).

DISCUSSION

The majority of pearl samples revealed natural structures, including three (figure 2, G–I) that exhibited more pronounced structures than the others. The concentric rings within the organic-rich core structures were very distinct and are similar to those of other natural pearls from *Pinctada* species examined in the laboratory. Such structures have, for example, been observed in both natural and non-bead-cultured *Pinctada maxima* pearls, with sufficient differences between the two to separate them in most cases (Sturman et al., 2015). However, since the samples in this study reportedly formed in a different mollusk species and their other gemological features (appearance and spectra) differ, it is more likely that these pearls too are natural and are not the challenging non-bead-cultured pearls that have been misrepresented as natural. Nevertheless, since the samples were not found by the authors *in situ* within a specific mollusk, other gemologists could disagree with the result based on their interpretation of the structures. On the other hand, the natural blister pearl attached to the valve of a *Pinctada maculata* specimen was from the same source as the other samples, providing a degree of assurance that their claimed origin is the same. The authors failed to find any published record of non-bead-cultured pearls from *Pinctada maculata* mollusks. Therefore, the data we obtained indicates that the samples in this study likely formed within *Pinctada maculata* mollusks.

The spectroscopic work revealed features consistent with those observed for naturally colored pearls from various *Pinctada* species mollusks, including *Pinctada maculata* (table 1). The UV-Vis reflectance spectra results provide the most helpful features to indicate that the pearls possibly originated from *Pinctada maculata*, including a clear 495 nm feature in most of the samples. However, this feature has also been recorded in some naturally colored pearls from other mollusks such as *Pinctada margaritifera*

(Elen, 2002; Karampelas et al., 2011), *Pteria penguin* (Miyoshi et al., 1987; Iwahashi and Akamatsu, 1994), and *Pteria sterna* (Kiefert et al., 2004), often in association with a feature at 405 nm that is reportedly related to uroporphyrin protein (Iwahashi and Akamatsu, 1994). Moreover, previous research also reports that the 495 nm feature is present in moderate to dark *Pinctada maxima* cultured pearls covering a range of colors (Karampelas, 2012).

While most *Pinctada maculata* samples display the 495 nm feature, they do not show other features at 405 and 700 nm. This could provide a way to separate them from pearls that form in *Pinctada margaritifera*, *Pinctada mazatlanica*, *Pteria penguin*, and *Pteria sterna* mollusks.

Furthermore, the diffuse reflectance decrease around 330–460 nm in most samples is similar to that seen in naturally colored yellow pearls from *Pinctada maxima* (Elen, 2001), *Pinctada margaritifera* (Elen, 2002), and *Pinctada mazatlanica* (Homkrajae, 2016). When comparing the UV-Vis spectra of yellow *Pinctada maculata* with *Pinctada maxima*, *Pinctada margaritifera*, and *Pinctada mazatlanica* pearls (figure 7), some similarities are evident between some samples, yet differences that may allow separation also exist. The 495 nm feature (figure 7, indicated by a red dotted line) usually appears to be fairly pronounced in *Pinctada maculata* pearl. It is not present in *Pinctada maxima* or *Pinctada mazatlanica* samples, while *Pinctada margaritifera* pearl shows the feature to varying degrees depending on its color, tone, and saturation. Unlike the other mollusks, nearly all *Pinctada margaritifera* and *Pinctada mazatlanica* pearls show the 700 nm feature, which helps differentiate them from the other *Pinctada* species.

The majority of *Pinctada maculata* samples show two features at 1380 and 1540 cm^{-1} in their Raman spectra. Similar features have also have been recorded in naturally colored yellow *Pinctada maxima* pearls (Cartier and Krzemnicki, 2016). Moreover, based on prior experience when compared with known naturally colored "golden" *Pinctada maxima* pearls sourced directly from Jewelmer's pearl farms (internal GIA research, unpublished results), these features are typically present in pearls of both species, and in those of *Pinctada mazatlanica* with a yellow component, but they are not recorded in pearls of a yellow hue range from other mollusk species. The specific cause of these features is unknown, and their positions do not exactly match with other known color pigments recorded (Karampelas et al., 2009; Bergamonti et al., 2011; Zhou and Dzikowski, 2015; Cartier and Krzemnicki, 2016). While the features around 1540 cm^{-1} show some similarity to the Raman peak recorded in freshwater pearls attributed to polyenic proteins (Soldati et al., 2008), the pearls from this study are saltwater, and therefore the features' relevance is questionable since the positions do not match exactly.

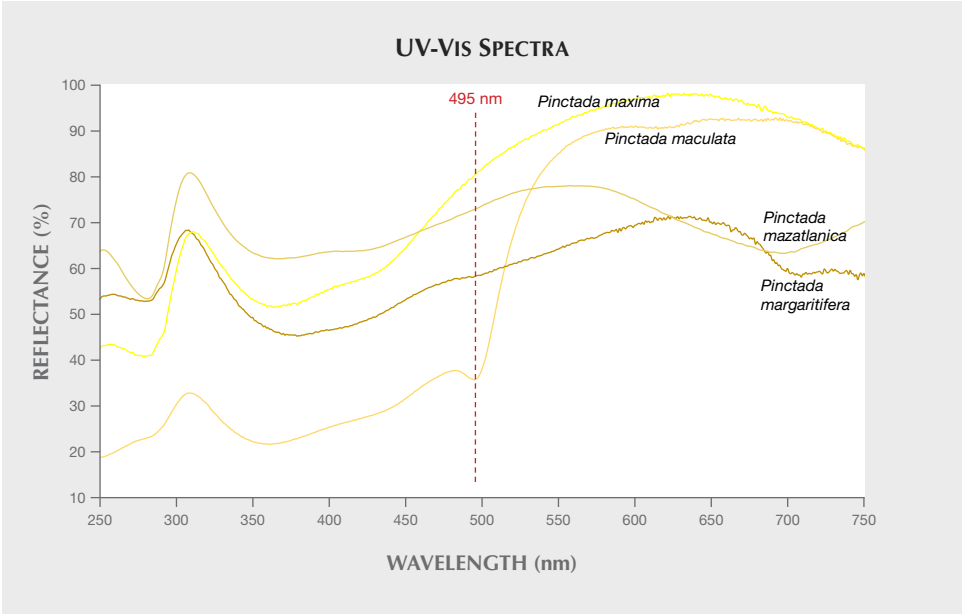

Figure 7. Comparative UV-Vis spectra of four yellow Pinctada maxima, Pinctada maculata, Pinctada mazatlanica, *and* Pinctada margaritifera *pearls showing some spectral features that help distinguish them from one another.*

The three PL spectral features at approximately 620, 650, and 680 nm have been recorded in naturally colored pearls, usually with moderate to darker tones and saturations, from *Pinctada maxima* (Karampelas, 2012), *Pinctada margaritifera* (Nilpetploy et al., 2018), *Pinctada mazatlanica* (Homkrajae, 2016), *Pteria penguin* (Miyoshi et al., 1987; Iwahashi and Akamatsu, 1994), and *Pteria sterna* (Kiefert et al., 2004). The peak around 620 nm is reportedly associated with the uroporphyrin protein (Iwahashi and Akamatsu, 1994). A *Pinctada maculata* blister pearl sample (again, see figure 3) was also subjected to spectroscopic analysis. The PL spectrum of the blister pearl showed the same three features referred to above, indicating a natural coloration. The Raman results were not so helpful, probably because of the sample's light color, while a useful UV-Vis spectrum could not be obtained owing to the limitation of the specimen's shape.

CONCLUSIONS

Pipi pearls found in *Pinctada maculata* mollusks are almost always natural since successful cultivation using this mollusk has never been documented, and the authors are aware of no such commercial products in the market. Even though *Pinctada maculata* pearls are small, owing to the mollusk being the smallest member of the *Pinctada* genus, their color range is desirable enough to warrant interest, and it is not inconceivable that future technology might permit commercial quantities of cultured pearls to be produced one day. Unfortunately, the mollusk's population is limited in comparison to economic species such as *Pinctada maxima* or *Pinctada margaritifera* mollusks. *Pinctada maculata*'s small size and limited geographical habitat may make investment in any culturing venture unlikely.

The internal structures found in this study did not reveal evidence of any culturing, and virtually every sample showed structures routinely observed within natural pearls from a wide variety of mollusks. It would not be possible to conclude that a pearl formed within a *Pinctada maculata* mollusk based only on its structure, but there could be strong indications that a pearl originated from the mollusk if its internal structure, external appearance, and spectral characteristics were all taken into account and met the relevant criteria. For example, pearl P587 (figure 2D) shows a distinct uneven yellow color that may be observed for either *Pinctada maculata* or *Pinctada maxima* pearls; however, there are some brownish yellow areas and its size is also small, under 6 mm, which is more toward *Pinctada maculata* pearls. Moreover, its UV-Vis spectra (the presence of the 495 nm feature in particular), PL spectrum (a weak three-peak pattern), and small dark organic core (albeit a twin-core pearl with a boundary) all strongly suggest that it was recovered from a *Pinctada maculata* mollusk. Samples P606 and P609 (figure 2, E–F) also show small organic cores more typical of yellow to orange pearls that form in *Pinctada maculata* mollusks, but they were too small to obtain UV-Vis spectra. However, their PL spectra did show the three bands seen in other *Pinctada maculata* pearls of similar colors and not the pattern seen in comparable *Pinctada maxima* pearls. Most natural *Pinctada maculata* pearls are colored and smaller than natural or non-bead-cultured *Pinctada maxima* pearls, and this may assist to some extent in separating them.

Although the spectroscopic results of some of the *Pinctada maculata* samples revealed characteristic features that help in some respects with their mollusk identification (e.g., sample P587), they also shared other features in common with other mollusk species such as *Pinctada maxima*, *Pinctada margaritifera*, *Pteria penguin*, and *Pteria sterna*. Therefore, no definitive information can be gleaned from the spectra of *Pinctada maculata* pearls that will guarantee their separation from other mollusk species, so other factors such as external appearance and internal structures must also be considered. Since mollusks of the *Pinctada* genus and *Pteria* genus are members of the Pteriidae family, it is not surprising that they share some common traits with respect to composition, appearance, and spectral characteristics. While some of these traits may not be precise matches, they still provide useful criteria with which to make a well-reasoned conclusion on the identity of the mollusk that produced a specific pearl.

Further study of known *Pinctada maculata* pearls and their mollusks, ideally sourced directly from the ocean, would be the best option to enforce the findings provided by samples we believed to be from the same mollusk. In order to make the findings even more comprehensive, the full structural and spectroscopic details of natural pearls from other known mollusks (e.g., *Pinctada* and *Pteria* species) ideally should be studied and compared.

ABOUT THE AUTHORS
Ms. Nilpetploy (née Somsa-ard) is a staff gemologist, and Ms. Lawanwong and Mr. Kessrapong are analytics technicians, in pearl services at GIA in Bangkok.

ACKNOWLEDGMENTS
The authors would like to thank GIA colleagues in Bangkok, New York, and Carlsbad for their valuable assistance. Suggestions from two anonymous peer reviewers and Elisabeth Strack, the third peer reviewer, to improve the content are also greatly appreciated.

REFERENCES

Alexander A.E. (1941) Natural and cultured pearl differentiation. *G&G*, Vol. 3, No. 12, pp. 184–187.

Bergamonti L., Bersani D., Csermely D., Lottici P.P. (2011) The nature of the pigments in corals and pearls: A contribution from Raman spectroscopy. *Spectroscopy Letters*, Vol. 44, No. 7-8, pp. 453–458, http://dx.doi.org/10.1080/00387010.2011.610399

Buscher E. (1999) Gem News: Natural pearls from the northern Cook Islands. *G&G*, Vol. 35, No. 2, pp. 147–148.

Buzgar N., Apopei A. (2009) The Raman study of certain carbonates. *Geologie*. Tomul LV, No. 2, pp. 97–112.

Cartier L.E., Krzemnicki M.S. (2016) Golden South Sea cultured pearls: cultivation steps & gemological investigations. *The Journal of the Gemmological Association of Hong Kong*, Vol. 37, pp. 16–21.

CIBJO International Jewellery Confederation (2016) *The Pearl Book*. CIBJO Pearl Commission, p. 41.

Elen S. (2001) Spectral reflectance and fluorescence characteristic of natural-color and heat-treated "golden" South Sea cultured pearls. *G&G*, Vol. 37, No. 2, pp. 114–197, http://dx.doi.org/10.5741/GEMS.37.2.114

Elen S. (2002) Identification of yellow cultured pearls from the black-lipped oyster *Pinctada margaritifera*. *G&G*, Vol. 38, No. 1, pp. 66–72, http://dx.doi.org/10.5741/GEMS.38.1.66

Farn A.E. (1986) *Pearls: Natural, Cultured and Imitation*. Butterworths Gem Books, United Kingdom.

GIA Pearl Grading Color Reference Charts (2000) Gemological Institute of America, Carlsbad, CA.

Gould A.A. (1846) On the shells collected by the United States Exploring Expedition under the command of Charles Wiles. *Proceedings of the Boston Society of Natural History*, Vol. 2, pp. 141–145.

Homkrajae A. (2016) Gem News International: Spectral characteristics of *Pinctada mazatlanica* and *Pinctada margaritifera* oyster species. *G&G*, Vol. 52, No. 2, pp. 207–208.

Iwahashi Y., Akamatsu S. (1994) Porphyrin pigment in black-lip pearls and its application to pearl identification. *Fisheries Science*, Vol. 60, No. 1, pp. 69–71, http://dx.doi.org/10.2331/fishsci.60.69

Karampelas S. (2012) Spectral characteristics of natural-color saltwater cultured pearls from *Pinctada maxima*. *G&G*, Vol. 48, No. 3, pp. 193–197, http://dx.doi.org/10.5741/GEMS.48.3.193

Karampelas S., Fritsch E., Mevellec J.-Y., Sklavounos S., Soldatos T. (2009) Role of polyenes in the coloration of cultured freshwater pearls. *European Journal of Mineralogy*, Vol. 21, No. 1, pp. 85–97, http://dx.doi.org/10.1127/0935-1221/2009/0021-1897

Karampelas S., Fritsch E., Gauthier J.-P., Hainschwang T. (2011) UV-Vis-NIR reflectance spectroscopy of natural-color saltwater cultured pearls from *Pinctada margaritifera*. *G&G*, Vol. 47, No. 1, pp. 31–35, http://dx.doi.org/10.5741/GEMS.47.1.31

Kessrapong P., Lawanwong K., Sturman N. (2017) *Pinctada maculata* (Pipi) bead-cultured blister pearls attached to their shells. Research News, https://www.gia.edu/gia-news-research/pinctada-maculata-bead-cultured-blister-pearls-shells.

Kiefert L., Moreno D.M., Arizmendi E., Hänni H., Elen S. (2004) Cultured pearls from the Gulf of California, Mexico. *G&G*, Vol. 40, No. 1, pp. 26–38, http://dx.doi.org/10.5741/GEMS.40.1.26

Krzemnicki M. (2014) Pipi pearls from the Pacific. *Facette*, No. 21, p. 20.

Krzemnicki M., Friess S.D., Chalus P., Hänni H.A., Karampelas S. (2010) X-ray computed microtomography: Distinguishing natural pearls from beaded and non-beaded cultured pearls. *G&G*, Vol. 46, No. 2, pp. 128–134, http://dx.doi.org/10.5741/GEMS.46.2.128

Miyoshi T., Matsuda Y., Komatsu H. (1987) Fluorescence from pearls and shells of black lip oyster, *Pinctada margaritifera*, and its contribution to the distinction of mother oysters used in pearl culture. *Japanese Journal of Applied Physics*, Vol. 26, No. 7, pp. 1069–1072, http://dx.doi.org/10.1143/JJAP.26.1069

Nilpetploy N., Lawanwong K., Kessrapong P. (2018) Non-bead-cultured pearls from *Pinctada margaritifera*. Research News, https://www.gia.edu/gia-news-research/non-bead-cultured-pearls-from-pinctada-margaritifera.

Passfield K. (1997) Notes on 'pipi' pearl oyster, *Pinctada maculata*, fishing in Tongareva, Cook Islands, 1995. *SPC Pearl Oyster Information Bulletin #10*, August 1997, pp. 21.

Segura O., Fritsch E., Touati D. (2014) Gem News International: Natural pipi pearls from Tahiti. *G&G*, Vol. 50, No. 1, pp. 89–90.

Soldati A.L., Jacob D.E., Wehrmeister U., Häger T., Hofmeister W. (2008) Micro-Raman spectroscopy of pigments contained in different calcium carbonate polymorphs from freshwater cultured pearls. *Journal of Raman Spectroscopy*, Vol. 39, No. 4, pp. 525–536, http://dx.doi.org/10.1002/jrs.1873

Southgate P.C., Lucas J.S. (2008) *The Pearl Oyster*. Elsevier, Oxford, United Kingdom, p. 279.

Strack E. (2006) *Pearls*. Rühle-Diebener-Verlag, Stuttgart, Germany.

Sturman N., Homkrajae A., Manustrong A., Somsa-ard N. (2015) X-ray computed microtomography (μ-CT) structures of known natural and non-bead cultured *Pinctada maxima* pearls. *Proceedings of the 34th International Gemmological Conference IGC*, Vilnius, Lithuania, pp. 121–124.

Sturman N., Manustrong A., Pardieu V. (2016) The cultured pearls of Mergui with an emphasis on their internal structures. *Proceedings: The 5th GIT International Gem and Jewelry Conference*, Pattaya, Thailand, pp. 143–144.

Taburiaux J. (1986) *Pearls: Their Origin, Treatment and Identification*. Chilton Book Co., Radnor, PA.

Urmos J., Sharma S.K., Mackenzie F.T. (1991) Characterization of some biogenic carbonates with Raman spectroscopy. *American Mineralogist*, Vol. 76, pp. 641–646.

Webster R. (1994) *Gems: Their Sources, Descriptions and Identification*. 5th ed., rev. by P.G. Read, Butterworth-Heinemann, Oxford, United Kingdom.

Zhou C., Homkrajae A., Ho J.W.Y., Hyatt A., Sturman N. (2012) Update on the identification of dye treatment in yellow or "golden" cultured pearls. *G&G*, Vol. 48, No. 4, pp. 284–291, http://dx.doi.org/10.5741/GEMS.48.4.284

Zhou W., Dzikowski T. (2015) Species identification and treatment detection in dark coloured pearls. *Swiss Geoscience Meeting 2015*, Basel, Switzerland, pp. 134–135.

CHARTS

Inclusions in Natural, Synthetic, and Treated Diamond

Nathan D. Renfro, John I. Koivula, Jonathan Muyal, Shane F. McClure, Kevin Schumacher, and James E. Shigley

Figure 1. Diamonds such as this 1.15 ct round brilliant are some of the most highly sought-after gem materials and may contain inclusions that give the gemologist clues about their origin or treatment status. Photo by Robert Weldon.

Diamonds (figure 1) are the subject of the latest chart in our series on the micro-features of gemstones. One of the most highly-sought gem materials, diamond—like emerald, sapphire, and ruby—may be treated or grown in laboratory conditions. While many diamonds contain inclusions that are indicative of their origin or treatment status, many gem-quality diamonds are free of such diagnostic characteristics and will require advanced gemological testing to determine whether they are mined, laboratory grown, or treated. For example, chromian garnet inclusions can indicate the diamond formed in a peridotitic environment, while omphacite and kyanite would suggest an eclogitic environment. Other features that are notably diagnostic to the gemologist are so-called "flash-effect" colors that decorate lead glass–filled fractures and tapering tubes that indicate laser drilling.

Gem-quality synthetic diamonds have been commercially available since 1986; however, recent im-

See end of article for About the Authors.
Gems & Gemology, Vol. 54, No. 4, pp. 428–429,
http://dx.doi.org/10.5741/GEMS.54.4.428

provements in growth methods are responsible for increases in both the size of finished stones and the quantity produced. Chemical vapor deposition (CVD) and high-pressure, high-temperature (HPHT) processes have had increasing impact in the diamond trade, with CVD stones reaching finished sizes of more than five carats (Eaton-Magaña and Shigley, 2016) and a 15 ct HPHT-grown specimen recently reported (Ardon and Eaton-Magaña, 2018). Melee-size material is also becoming widely available. As a result, GIA offers a melee screening service and has developed a consumer diamond screening device, the iD100, to separate natural and synthetic specimens.

Treatments intended to improve a diamond's clarity have been around since the late 1970s and include laser drilling and the filling of cracks with a lead glass; this glass reduces the impact of a crack's appearance on the stone (Koivula et al., 1989). Other treatments may improve or modify the bodycolor of a diamond. Irradiation and HPHT treatment can accomplish this but often leave no microscopic evidence of the process.

While the accompanying chart is not meant to be comprehensive, it aims to remind the gemologist of the microscopic evidence that one may encounter and what that evidence indicates regarding a diamond's natural, treated, or synthetic origin.

ABOUT THE AUTHORS

Mr. Renfro is manager of colored stones identification, and John Koivula is analytical microscopist at GIA in Carlsbad, California. Mr. Muyal is a staff gemologist, Mr. McClure is global director of colored stone services, Mr. Schumacher is a photo and video producer for Gems & Gemology, *and Dr. Shigley is distinguished research fellow at GIA in Carlsbad.*

REFERENCES

Ardon T., Eaton-Magaña S. (2018) Lab Notes: 15 carat HPHT synthetic diamond. *G&G*, Vol. 54, No. 2, pp. 217–218.

Eaton-Magaña S., Shigley J.E. (2016) Observations on CVD-grown synthetic diamonds: A review. *G&G*, Vol. 52, No. 3, pp. 222–245, http://dx.doi.org/10.5741/GEMS.52.3.222

Koivula J.I., Kammerling R.C., Fritsch E., Fryer C.W., Hargett D., Kane R.E. (1989) The characteristics and identification of filled diamonds. *G&G*, Vol. 25, No. 2, pp. 68–83, http://dx.doi.org/10.5741/GEMS.25.2.68

Additional Reading

For a list of references pertaining to inclusions in natural, synthetic, and treated diamond, go to www.gia.edu/gems-gemology/winter-2018-suggested-reading-diamond-chart or scan the QR code on the right.

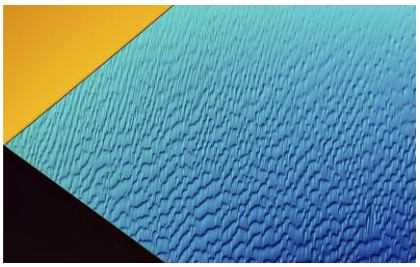

Natural DIAMOND Mistaken as HPHT Synthetic

When a declared synthetic diamond is submitted to a GIA laboratory, it is not often that the diamond turns out to be natural. But this was the case recently when a D-color 2.23 ct round brilliant was submitted to the Carlsbad laboratory for a synthetic diamond grading report (figure 1). Its infrared absorption spectrum established it as type IaA>B, with nitrogen aggregates around 80 ppm, confirming a natural color origin. Since it was stated as synthetic, further analysis was performed.

There are very few gemological indicators of lab-grown diamonds (S. Eaton-Magaña and C.M. Breeding, "Features of synthetic diamonds," Summer 2018 *G&G*, pp. 202–204). Yet one of the most reliable and easily seen observations is the lack of birefringence (or strain) patterns in HPHT synthetics when viewed between crossed polarizers. To our knowledge, visible strain in HPHT-grown synthetic diamonds has only been documented in one rare case (Winter 2016 Lab Notes, pp. 417–418).

Although strain observations are rarely used by many in the trade, this natural diamond was perhaps presumed to be synthetic due to its apparent lack of observable strain. When viewed under crossed polarizers, the strain was very difficult to discern (figure 2, left), and this apparent absence was consistent with our observations of HPHT synthetics. With extensive searching and careful positioning, the strain was visible in a few scattered areas of the diamond. The observed strain was linear in appearance, consistent with type Ia natural diamonds (figure 2, right).

Figure 1. This D-color 2.23 ct natural diamond was originally submitted as a synthetic.

With further investigation using a variety of techniques such as photoluminescence spectroscopy and DiamondView imaging, all tests confirmed a natural origin. Additionally, microscopic observation revealed unidentified dark natural crystal inclusions (figure 3), which might have been mistaken for metallic flux.

Subsequently the client indicated that this stone was believed to be synthetic after examination by another party in the trade. However, several gemological and spectroscopic tests confirmed its natural origin.

This diamond demonstrates why stones of uncertain origin should be submitted to a gemological laboratory for further testing. It also provides confirmation that occasional excep-

Figure 2. An apparent lack of strain was observed throughout most of the stone, with strain visible only around inclusions (left). Such observations are common in HPHT synthetics and not generally seen in natural or CVD synthetic diamonds. With extensive searching and careful positioning, linear strain was visible within small areas of the stone (right). Field of view 7.19 mm.

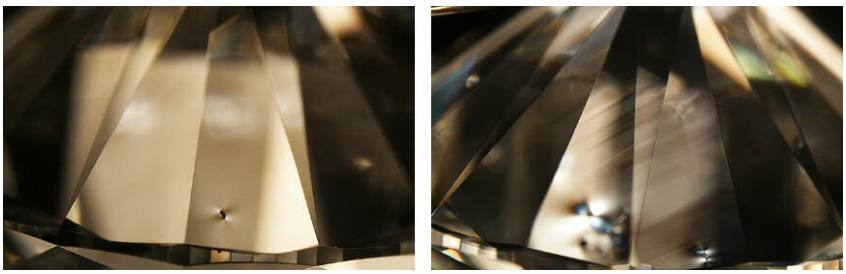

Editors' note: All items were written by staff members of GIA laboratories.

GEMS & GEMOLOGY, Vol. 54, No. 4, pp. 430–439.

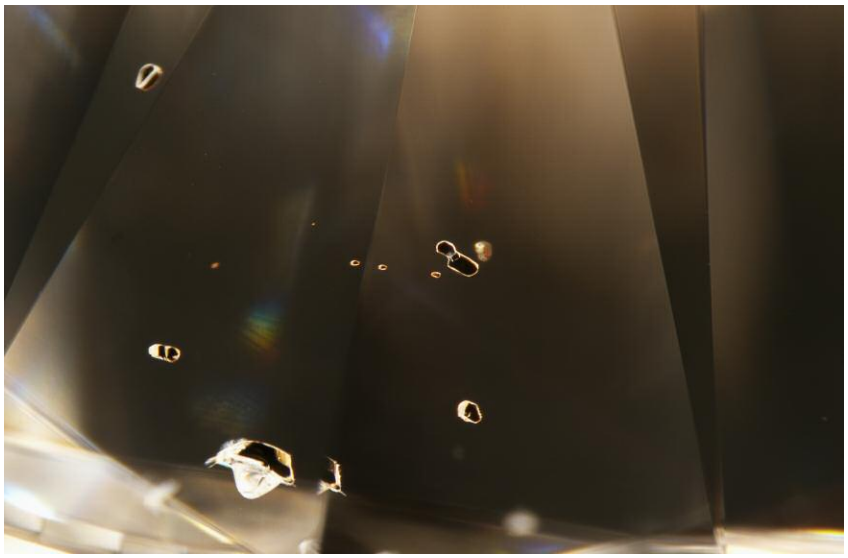

Figure 3. Microscopic examination shows discernible dark mineral inclusions that occur naturally in diamonds and could have been mistaken for metallic flux inclusions. Field of view 3.57 mm.

tions exist for the general guidelines that help distinguish natural from lab-grown diamonds. In this case, the correction worked to the client's advantage.

Garrett McElhenny and Sally Eaton-Magaña

Manufactured GOLD-IN-QUARTZ Jewelry

Due to its desirability, gold is often imitated with minerals such as pyrite or with gold plating. Gold occurs in small quantities in many kinds of rocks throughout the world. It is typically found in epithermal deposits where hydrothermal fluids deposit gold, along with pyrite and other sulfides, into cracks and faults of rocks—commonly quartz-bearing rocks (J.W. Anthony et al., *Handbook of Mineralogy, Vol. 1: Elements, Sulfides, Sulfosalts*, Mineral Data Publishing, Tucson, Arizona, 1990). Due to the aggregate structure of this material, the gold contained in natural gold-in-quartz is deposited irregularly, showing a more natural-looking sporadic veining system in the host quartz (figure 4).

The Carlsbad lab was recently sent three jewelry pieces—two bracelets and a ring—for identification reports (figure 5). The ring and one of the bracelets were set with numerous white stones cross-cut with yellow metallic veins. One bracelet had black stones cross-cut with similar yellow metallic veining. Standard gemological testing of both the white and black stones revealed properties consistent with quartz; these results were confirmed with Raman spectroscopy. The Raman analysis of the black stones indicated the presence of amorphous carbon, which drew some suspicion.

These jewelry pieces initially seemed to contain natural gold-in-quartz. Upon further inspection, the yellow metallic veining system appeared inorganic in the host quartz due to its very consistent appearance in all the stones. In the three pieces, the metallic veins had a spiderweb-like structure, and a colorless polymer was also present alongside the metallic veins (figure 6, left). The colorless polymer areas also showed undercutting, and the metallic veining had areas of incomplete filling (figure 6, center and right). These features were consistent with the manufactured gold-in-quartz products that were first introduced to the market at the 2005 Tucson shows (B. Laurs, "Manufactured gold/silver-in-quartz," Spring 2005 *G&G*, pp. 63–64). This material was composed of polymer, quartz, and metallic veining similar to what was observed in the stones we examined. Even with the slight difference in the face-up appearance of the natural and manufactured gold-in-quartz, the manufacturer claims that the only way to clearly distinguish this imitation material is with chemical analysis of the metal alloy.

Figure 4. The gold veins in natural gold-in-quartz are irregular and show a natural nugget structure below the surface. Field of view 4.79 mm.

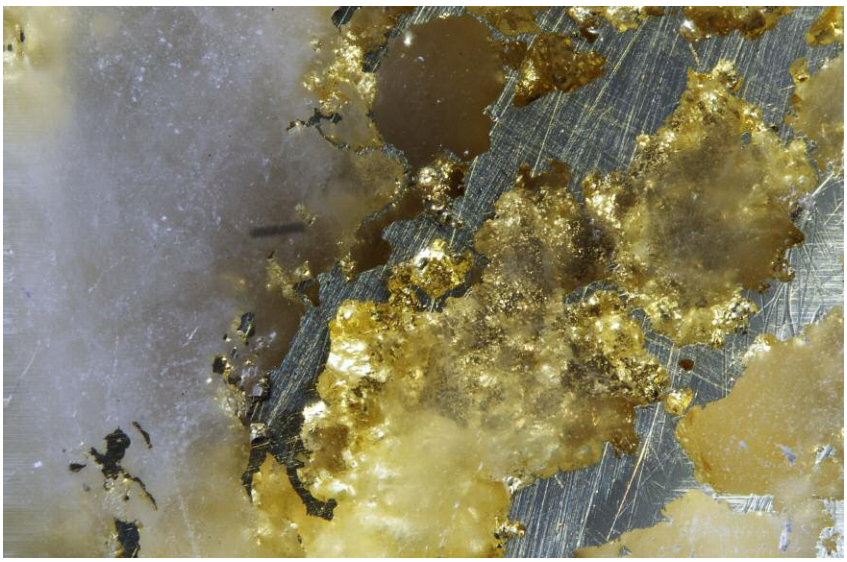

Figure 5. Manufactured gold-in-quartz, set in two bracelets and a ring that were submitted for identification reports.

Laser ablation–inductively coupled plasma–mass spectrometry (LA-ICP-MS) analyses were performed on the yellow metallic veins in the white and black stones of each bracelet to further separate them from natural gold-in-quartz. Each ablation spot was drilled twice into the veins. The chemistry of the first spot was very similar for the stones in both bracelets. The vein was mainly composed of gold (Au) and silver (Ag) with traces of nickel (0.90–2.67 parts per million weight, ppmw) and copper (23.58–30.02 ppmw). The gold to silver weight ratio (Au_{ppmw}/Ag_{ppmw}) was between 2.71 and 3.33. The chemistry of the second spot on the same position showed little gold or silver and a significant amount of silica, which indicated that the laser had passed through the yellow metallic layer and into the host quartz below.

One natural gold-in-quartz cabochon obtained from the GIA Museum was analyzed for comparison. The veins found in the natural sample (again, see figure 4) were composed mainly of yellow metallic materials, with additional gray metallic minerals. The same experimental procedures were applied to both the yellow and gray areas. The chemistry of the gray metallic areas identified them as an iron sulfide mineral. The chemistry of the first spot on a yellow metallic area showed a large amount of gold and silver with traces of copper (215–257 ppmw). The gold and silver weight ratio (Au_{ppmw}/Ag_{ppmw}) was between 7.84 and 8.04. It was evident that the concentration of gold in the yellow metallic veins in the natural gold-in-quartz was much higher than that of the yellow metallic veins in the white and black panels of the two bracelets. In addition, the natural veins had a higher copper concentration than the two bracelets.

The manufactured gold-in-quartz materials first reported in 2005 are still circulating in the market today. Consumers should be aware of this when purchasing pieces reported to contain gold-in-quartz. The telling indicator of manufactured gold-in-quartz is the consistent texture of its yellow metallic veins. The gold in the natural version is much more sporadic and appears as chunky conglomerated nuggets.

Nicole Ahline and Ziyin Sun

Freshwater PEARLS, Blister and Loose, with Their Host Shells

GIA occasionally receives blister pearls attached to their host shells for identification (Winter 2015 Lab Notes, pp. 432–434; Summer 2017 Lab Notes, pp. 231–232), which can provide helpful information on the overall growth conditions and the mollusk species. Recently the New York laboratory had an opportunity to study three freshwater specimens: two blister pearls still attached to their shells, and one loose "wing" pearl that was reportedly

Figure 6. Unnatural veins in manufactured gold-in-quartz. Left: This vein is filled with both polymer, which is not flush with the host quartz, and gold (field of view 4.79 mm). Center: A vein of polymer running alongside a vein of gold with undercutting visible at the boundary of the polymer vein and the host quartz (field of view 3.57 mm). Right: Polymer fills an incomplete gold vein; the rest of the vein is recessed below the host quartz (field of view 7.19 mm).

Figure 7. Three freshwater pearls attached to their host shells. Left to right: A blister pearl measuring approximately 37.45 × 27.48 mm, a loose wing pearl measuring 35.82 × 9.37 × 5.94 mm and weighing 10.60 ct, and a blister pearl measuring approximately 23.60 × 19.49 mm. Specimens courtesy of Mississippi River Pearl Jewelry Co. LLC.

found in the shell with which it was submitted (figure 7).

While approximately 1,000 species of freshwater mussels have been identified worldwide, the United States alone is said to host about 300 species, compared to 96 species in Africa, 60 in China, and 12 in Europe (Virginia Department of Game and Inland Fisheries, 2018, https://www.dgif.virginia.gov/wildlife/freshwater-mussels/). The number of U.S. species shows the spectacular diversity of its freshwater resources. Hence, it proves how difficult it can be to apply correct zoological names to specific shells. However, experienced local fishermen who harvest the mussels are often the source of helpful information (T. Hsu et al., "Freshwater pearling in Tennessee," 2016, https://www.gia.edu/gia-news-research/freshwater-pearling-tennessee). The owner claimed that the loose wing-shaped pearl (figure 7, center) was found in a *Potamilus purpuratus* "Bluefer" mussel in a U.S. river. Bluefer mussels exhibit a pinkish purple to deep purple nacre lining and can produce pearls of a similar color range. Energy-dispersive X-ray fluorescence (EDXRF) spectrometry confirmed that it originated from a freshwater environment, based on its chemistry result of more than 1000 ppmw manganese. Freshwater pearls usually show higher than 100 ppmw manganese content. Real-time X-ray microradiography (RTX) revealed a natural growth structure, while Raman spectroscopy detected aragonite and polyenic peaks, the latter indicating the presence of natural coloring pigments (S. Karampelas et al., "Role of polyenes in the coloration of cultured freshwater pearls," *European Journal of Mineralogy*, Vol. 21, 2009, pp. 85–97). This specimen also displayed the characteristic elongated, flat, and slightly curved shape characteristic of wing pearls that, as the name implies, resembles the shape of a bird's wing. Wing pearls commonly form in the hinge area within shells, and it was interesting to see a similar-sized cavity in the shell submitted with this pearl.

The other two blister pearls were also claimed to have originated from a freshwater environment, and this was confirmed by their optical X-ray fluorescence reactions. Both specimens showed a strong yellowish green luminescence under X-ray excitation, a result that agrees with pearls from a freshwater environment due to their higher manganese content (H.A. Hänni et al., "X-ray luminescence, a valuable test in pearl identification," *The Journal of Gemmology*, Vol 29, No. 5/6, 2005, pp. 325–329). According to the owner, the smaller shell (figure 7, right), possibly a washboard mussel (*Megalonaias nervosa*), was found in a U.S. river, while the larger shell (figure 7, left) is likely a hybrid *Hyriopsis* mussel commonly used by cultured pearl farmers in China. Blister pearls form when a whole pearl within the connective tissue breaks through the mantle due to its size and/or weight, or for some other reason, and presses against the nacreous inner surface of the shell, where subsequent nacre deposition fuses the pearl to the shell (E. Strack, *Pearls*, Ruhle-Diebener-Verlag, Stuttgart, Germany, 2006, p. 124).

The size of these two blister pearls is impressive, and both protrude conspicuously from the shell while still attached to their hosts (figure 8). The RTX results of the smaller blister

Figure 8. Close-up images of the freshwater blister pearls from China (left) and the United States (right) attached to their hosts.

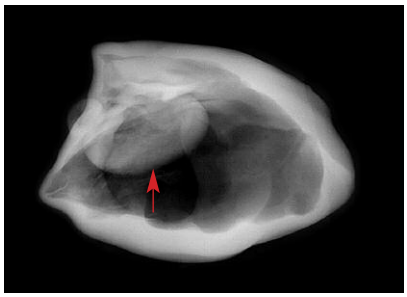

Figure 9. The RTX structure of the large blister pearl (shown on the left in figures 7 and 8) revealed a void-like structure in which a near-oval feature is visible (indicated by the arrow).

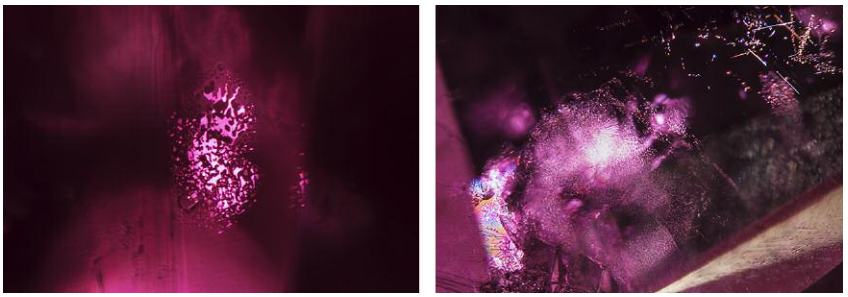

Figure 10. Inclusions in the 1.70 ct ruby from Montana. Left: Close-up of a glassy melt inclusion with an associated thin film showing geometric patterns; field of view 1.76 mm. Right: A melt inclusion with an iridescent thin film, partial hexagonal zone of particles, and short needles; field of view 3.81 mm.

pearl revealed concentric growth arcs proving its natural origin. However, the RTX results of the larger blister pearl revealed a void-like structure that may be found within natural and non-bead-cultured pearls, but a near-oval feature inside the void is uncommon in natural pearls (figure 9). GIA gemologists believe this oval feature was the triggering mechanism that likely resulted in the formation of the blister pearl. Whether this oval feature is a by-product of pearl culturing or a natural formation is hard to prove without examining the blister pearl thoroughly in other orientations, which was precluded by its size and position. While the identification of some freshwater pearls remains challenging, these known freshwater samples together with their host shells serve as useful references for laboratory gemologists.

Joyce Wing Yan Ho

A Rare RUBY from Montana

The Carlsbad laboratory recently received a 1.70 ct purplish red octagonal modified brilliant-cut ruby measuring 6.28 × 6.25 × 4.56 mm for an identification and origin report. Standard gemological testing gave a chromium spectrum indicating ruby and a hydrostatic SG of 4.00. The stone displayed a weak red fluorescence in long-wave UV and no fluorescence under short-wave UV.

Microscopic examination showed an interesting combination of inclusions (figure 10). There were several glassy melt inclusions and small crystals with associated reflective thin films. The thin films often displayed hexagonal geometric patterns conforming to the crystallographic orientation of the host ruby. These resembled the patterns commonly seen in rubies from Thailand and Cambodia and have also been documented in Montana corundum (Fall 2015 *G&G* Micro-World, pp. 329–330). A partial hexagonal zone of particles and more loosely spaced unaltered exsolved rutile needles was also present, a feature that would be very unusual in Thai/Cambodian rubies. A large intact colorless crystal as well as smaller white crystals were located deep within the stone, so we were unable to conclusively identify them with Raman spectroscopy. This inclusion scene is consistent with unheated corundum from Montana.

LA-ICP-MS was used to determine the stone's trace-element chemistry,

Figure 11. The 1.70 ct Montana ruby alongside rough pink to purple corundum samples from the GIA reference collection. These reference samples, collected from Montana's Eldorado Bar along the Missouri River and Wildcat Gulch, part of the Rock Creek deposit, were used to help determine the country of origin.

and the results were compared to corundum samples from GIA's colored stone reference collection. Trace element measurements indicated ranges of 15.1–17.2 ppma Mg, 14.7–16.9 ppma Ti, 3.67–3.87 ppma V, 359–406 ppma Cr, 1500–1580 ppma Fe, and 14.6–14.7 ppma Ga. The chemistry matched well with reference stones GIA has collected from Montana's secondary deposits (figure 11) but not our Thai/Cambodian ruby reference samples. In particular, Thai/Cambodian rubies tend to have higher Mg (often above 100 ppma), while this stone had much lower Mg levels.

Montana's secondary deposits produce sapphires in a wide range of mostly pastel colors. Pink corundum tends to be rarer than blue or green, and those that possess the depth of color to be called ruby are quite rare, particularly without any treatments. The color, combined with the large size, makes the 1.70 ct ruby from Montana an exceptional specimen—this is only the second such report issued by the lab to date. With a combination of microscopic observation, advanced testing methods, and GIA's reference collection, we were able to confirm the country of origin.

Claire Malaquias

Large Pargasite Inclusion in Kashmir SAPPHIRE

Kashmir sapphires are known to have occurred in kaolinized plagioclase feldspar pegmatites, found as pockets between metamorphic stratified beds/cliffs of the Himalayan Zanskar Range. These sapphires captured many cognate mineral inclusions—such as pargasite, plagioclase feldspar, tourmaline, and zircon—which demarcate the pockets against the country rock (E.J. Gübelin and J.I. Koivula, *Photoatlas of Inclusions in Gemstones*, Vol. 3, Opinio Publishers, Basel, Switzerland, 2008, p. 194).

Pargasite mineral inclusions (prismatic or as long, fine needles) in blue sapphire are regarded as a strong indicator of Kashmir origin. (R. Schwieger, "Diagnostic features and heat treatment of Kashmir sapphires," Winter 1990 *G&G*, pp. 267–280).

Recently, a 14.06 ct octagonal-cut blue sapphire (figure 12) submitted to GIA's Carlsbad laboratory for origin determination was of particular interest for its several unusually large, eye-visible pargasite crystal inclusions. Standard gemological properties confirmed the host sapphire's identity, and advanced analytical testing specified its metamorphic geological origin.

Microscopic examination revealed an inclusion scene reminiscent of "new Kashmir," a term referring to Kashmir sapphires that have come into the market since the 2000s. The blue sapphire featured several negative crystals, black graphite inclusions, unidentified rounded and needle-shaped colorless crystal inclusions (probably slender zircon rods or pargasite), reflective thin films, and fluid fingerprints.

Classic Kashmir sapphire features were also observed, such as "milky" turbid whitish broad bands, clouds, a parallel chromium-enriched zone (which glows red under long-wave UV illumination), ladder-like/antenna-like stringers, and snowflake-like inclusions.

Figure 12. This 14.06 ct octagonal blue Kashmir sapphire exhibits large, eye-visible inclusions of prismatic pargasite.

The main inclusion features, the pargasite crystals (figure 13), were transparent with a brownish green bodycolor. Many of them were doubly terminated with a flat, columnar prismatic morphology with striations along their length, surrounded by halo- or rosette-like thin reflective

Figure 13. A large prismatic pargasite mineral inclusion. Field of view 7.19 mm.

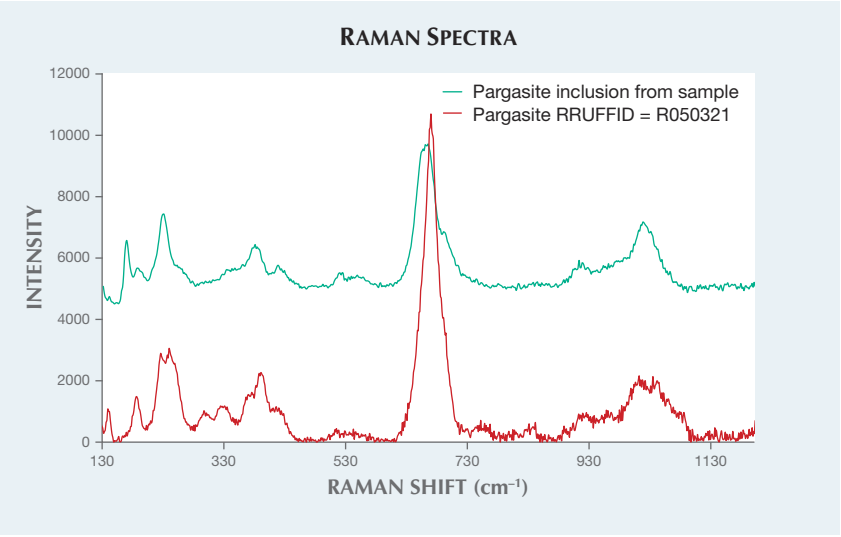

Figure 14. Unoriented Raman spectra with 514 nm excitation confirmed the pargasite mineral inclusion identity (blue spectrum), using the RRUFF database as a reference (red spectrum).

films. The pargasite crystal's surface pits and altered appearance suggested that these pargasite crystals were protogenetic inclusions present in the pegmatitic growth environment before the sapphire began to form. Raman microspectrometry analysis (figure 14) confirmed the identity of several crystal inclusions as pargasite.

The absence of 3309 peak series in IR spectroscopy and the microscopic observation of unaltered internal features supported an unheated call. The classic metamorphic UV-Vis absorption spectra, the metamorphic-type low-Fe chemistry data collected with LA-ICP-MS, and the observed inclusion scene supported a Kashmir origin conclusion. The issued GIA report identified the stone as a natural sapphire from Kashmir with no indications of heating.

Pargasite was once thought to be unique to Kashmir until it was found in sapphires from other countries. Nonetheless, pargasite inclusions are a strong indicator of Kashmir origin. With the support of advanced analytical instrumentation (UV-Vis and LA-ICP-MS) in addition to careful examination of the overall internal features (milky bands, ladder-like stringers, and snowflakes), the presence of pargasite inclusions can conclusively determine a Kashmir origin.

Jonathan Muyal

SYNTHETIC DIAMONDS

An Irradiated CVD Synthetic Melee Diamond Found in Irradiated Natural Melee Diamonds

Mixing of synthetic melee diamonds with natural melee diamonds has been reported several times. Those examples were colorless (Winter 2016 Lab Notes, pp. 416–417; Summer 2017 Lab Notes, pp. 236–237) and yellow (Winter 2014 Lab Notes, pp. 293–294). Recently, GIA's Tokyo lab found a single irradiated green-blue CVD synthetic melee diamond in a parcel of similarly colored irradiated natural melee.

The parcel of 300 uniformly green-blue round melee was submitted for identification (figure 15). Each diamond's color was attributed to strong

Figure 15. This group of 300 green-blue diamonds (1.97 carats total) was screened by GIA's Tokyo laboratory. Among these, 299 were irradiated natural melee diamonds and the one on the right was an irradiated CVD synthetic melee diamond.

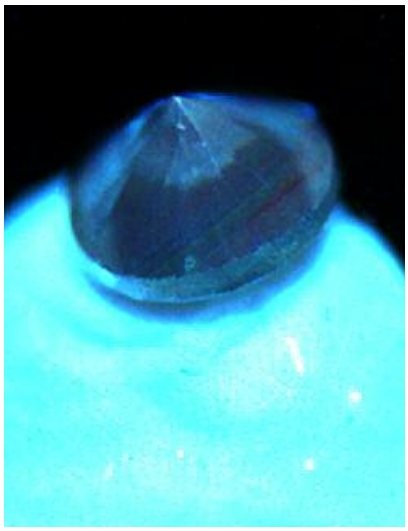

Figure 16. DiamondView imaging revealing weak linear striations in the pavilion of the irradiated CVD synthetic melee diamond.

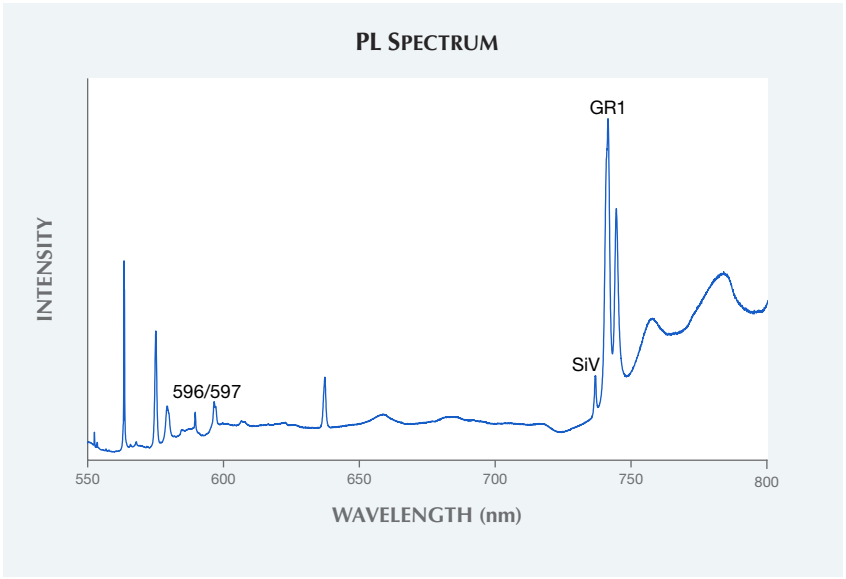

Figure 17. The photoluminescence spectrum of the green-blue CVD synthetic melee diamond at liquid nitrogen temperature shows a strong GR1 peak. The SiV^- center defect can be observed at around 736 nm. The doublet at 596/597 nm indicates that this diamond did not undergo annealing after synthesis.

GR1 by irradiation treatment. Infrared absorption spectroscopy, photoluminescence spectroscopy, and DiamondView analysis confirmed that 299 of them were irradiated natural diamonds and one of them was an irradiated CVD synthetic diamond. The CVD synthetic diamond weighed 0.007 ct, with a diameter of 1.14 mm.

DiamondView images of the synthetic showed very weak linear striations in the pavilion (figure 16). Dark inclusions were observed under the microscope. The infrared spectrum showed a peak at 3123 cm^{-1}, and the photoluminescence spectrum showed doublet peaks at 596/597 nm (figure 17). These peaks are seen in CVD synthetic diamonds without post-annealing. The photoluminescence spectrum also showed a small, broad SiV^- center defect at 737 nm next to a very strong GR1 center at 741 nm (figure 17). From the peak at 3123 cm^{-1} and the 596/597 nm doublet peak, this diamond was concluded to be irradiated without pre-annealing.

Irradiated CVD synthetic diamonds are rarely seen at GIA, which had examined only six of them before this report (Fall 2014 Lab Notes, pp. 240–241; Fall 2015 Lab Notes, pp. 320–321; Summer 2018 Lab Notes, pp. 215–216). Previously reported irradiated CVD synthetic diamonds were relatively large, from 0.43 to 1.34 ct. This is the first melee-sized irradiated CVD synthetic diamond examined by GIA.

Shoko Odake

Gemological Analysis of Lightbox CVD-Grown "White" Diamonds

Lightbox, a De Beers company, has begun selling "white," pink, and blue CVD laboratory-grown diamonds at a flat rate of $800 per carat. Through a third-party vendor, we recently had the opportunity to examine two such samples (0.24 and 0.26 ct) intended for setting in a pair of earrings. Both were near-colorless with color grades equivalent to G color and cut grades of Excellent and Very Good, respectively.

Both lab-grown diamonds had very few clarity characteristics. The 0.24 ct sample had a pinpoint in a bezel facet, and the 0.26 ct round (figure 18, left) had a feather in a star facet, both with VVS clarity. However, the grade-setting feature for both was the Lightbox logo, internally inscribed underneath the table facet (figure 18, center). As a result of the Lightbox mark, the clarity grade for both was reduced to VS. The laser-inscribed internal feature is reportedly made using technology developed by Opsydia (Gem and Jewellery Export Promotion Council, "De Beers to use Opsydia's laser tech to inscribe lab-grown diamonds in Lightbox Jewelry," https://www.gjepc.org/news_detail.php?id=4075). It is composed of dual narrow lines ~2.5 microns wide with a total area of 300 × 300 microns, positioned about 200 microns below the table surface.

Spectroscopic analysis showed both samples had very similar features that were consistent with previously analyzed CVD products from other manufacturers. IR absorption spectroscopy confirmed these samples as type IIa with no detectible single nitrogen at 1344 cm^{-1}. Photoluminescence (PL) spectra showed that both had the 596/597 nm doublet, indicating that they were as-grown and not subjected to post-growth HPHT processing (S. Eaton-Magaña and J.E. Shigley, "Observations on CVD-grown synthetic diamonds: A review," Fall 2016 *G&G*, pp. 222–

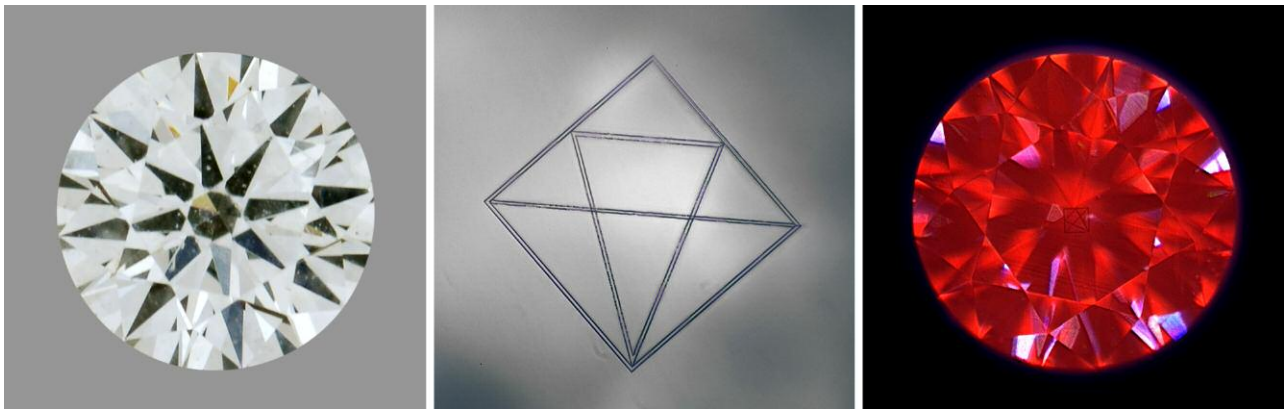

Figure 18. The 0.26 ct near-colorless CVD-grown diamond (left) has an internal inscription showing the Lightbox logo, composed of dual narrow lines. The logo is easily detected with a microscope (center) and clearly visible in the DiamondView image (right), in which the red fluorescence is due to nitrogen-vacancy centers. Also seen in the DiamondView image are subtle striations, additional evidence of the CVD origin. The outer square of the Lightbox logo measures 300 microns on each side.

245). Faceted, as-grown near-colorless CVD samples are less common since most manufacturers grow CVD layers quickly, but with a brown color, knowing that they can be HPHT treated to improve color appearance after growth. Approximately 75% of the CVD material in this color range examined by GIA has been HPHT treated after growth (S. Eaton-Magaña, "Summary of CVD lab-grown diamonds seen at the GIA laboratory," Fall 2018 *G&G*, pp. 269–270).

Through crossed polarizers, we observed very low birefringence compared with the majority of CVD-grown diamonds examined. Additionally, both samples showed very strong emission from nitrogen-vacancy centers by PL spectroscopy (figure 19), as well as visible red fluorescence using DiamondView imaging (figure 18, right), but there was no detectable fluorescence with long-wave UV. With careful DiamondView imaging, subtle CVD striations were visible through the table facet. In the DiamondView images, there were no apparent growth interfaces showing multiple growth events, and no apparent seed crystal remnants were observed. Also, PL spectroscopy of both samples showed very weak but detectable silicon-vacancy centers at 736.6/736.9 nm.

Figure 19. This 514 nm PL spectrum collected on the 0.26 ct sample at liquid nitrogen temperature shows strong nitrogen vacancy centers at 575 and 637 nm and the 596/597 nm doublet, evidence of an as-grown CVD sample.

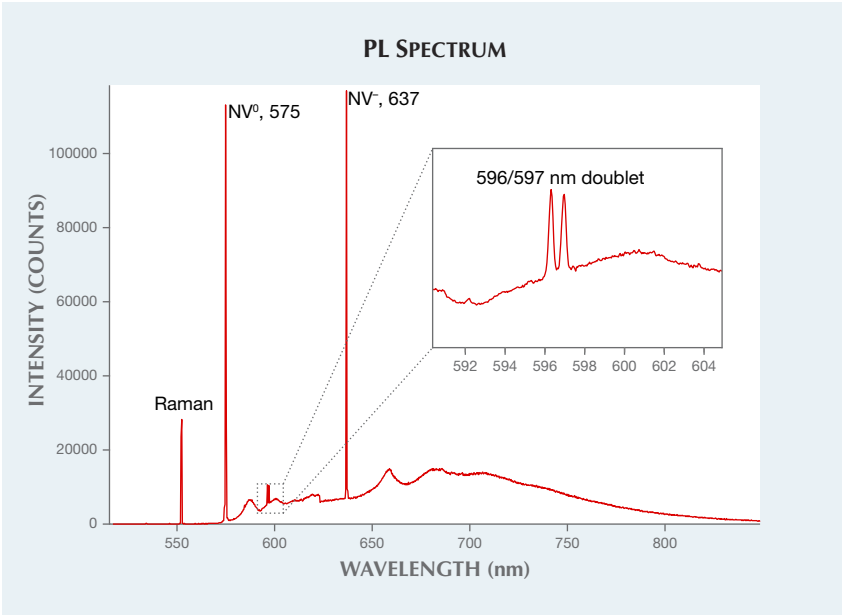

The Lightbox CVD lab-grown diamonds, due to their price point and manufacturer, will likely be highly visible in the trade. The pink and blue samples, as evidenced by De Beers' literature, have an appearance that is unusual among natural-color diamonds and are unlikely to ever be perceived as a natural-color product. However, the colorless Lightbox samples are readily identifiable as CVD-grown diamonds by spectroscopic techniques, DiamondView imaging, and their distinctive internal inscription.

Sally Eaton-Magaña

Cat's-Eye Brazilian Paraíba TOURMALINE

A vivid shade of tourmaline varying

Figure 20. This 0.51 ct Paraíba tourmaline from Brazil displays sharp chatoyancy.

from "neon" blue to greenish blue, caused by copper and manganese, was discovered in Brazil in the 1980s. Recognized as "Paraíba" tourmaline in the gem trade, it is still highly sought after, even though tourmalines exhibiting this "Paraíba" color are now more accessible from localities such as Nigeria and Mozambique.

Recently, GIA's Bangkok laboratory received a vivid blue tourmaline with chatoyancy (figure 20), weighing 0.51 ct and measuring 5.89 × 4.19 × 2.46 mm. Standard gemological testing resulted in a spot refractive index reading of 1.64 and a specific gravity of 3.05. Microscopic examination revealed diagnostic irregular two-phase inclusions, trichites, and acicular (needle-like) features. The sharp cat's-eye effect was caused by an included layer of fine parallel growth tubes positioned just above the base of the cabochon. The phenomenon of chatoyancy enhances its rarity and value.

LA-ICP-MS was used to perform an elemental analysis. The sample showed high Cu ranging from 7289 to 10544 ppmw, as well as 9494–10441 ppmw Mn, 114–133 ppmw Ga, 55–65 ppmw Pb, 39–48 ppmw Fe, 14–20 ppmw Zn, and 0.6–0.5 ppmw Sr. The very high concentration of Cu as well as the results for Ga (<250 ppmw), Pb (<100 ppmw), and Sr (<10 ppmw) supported its Brazilian origin (J.E. Shigley et al., "An update on 'Paraíba' tourmaline from Brazil," Winter 2001 *G&G*, pp. 260–267; A. Abduriyim et al., "Paraíba-type copper-bearing tourmaline from Brazil, Nigeria, and Mozambique: Chemical fingerprinting by LA-ICP-MS," Spring 2006 *G&G*, pp. 4–21; Z. Sun et al., "A simplified species classification for gem-quality tourmaline by LA-ICP-MS," submitted for publication). Copper-bearing tourmaline of this color is typically referred to in the trade as "Paraíba" tourmaline.

Cat's-eye Paraíba tourmaline is not new, though fewer than 10 have been submitted to GIA laboratories. The combination of well-developed chatoyancy, transparency, pleasing vivid blue color, and Brazilian origin make this a rare and noteworthy gemstone.

Vararut Weeramongkhonlert

PHOTO CREDITS

Robison McMurtry—1, 5, 11, 18 (left); Garrett McElhenny—2, 3; Nicole Ahline—4; Hollie McBride—6; Sood Oil (Judy) Chia—7; Joyce Wing Yan Ho—8; Claire Malaquias—10; Towfiq Ahmed—12; Jonathan Muyal—13; Shunsuke Nagai—15; Sally Eaton-Magaña—18 (center and right); Nuttapol Kitdee—20

Karen V. Smit and Steven B. Shirey

How Do Diamonds Form in the Deep Earth?

Carbon is one of the most important elements on our planet, which led the Geological Society of London to name 2019 the Year of Carbon. Diamonds are a main host for carbon in the deep earth and also have a deeper origin than all other gemstones. Whereas ruby, sapphire, and emerald form in the earth's crust, diamonds form many hundreds of kilometers deep in the earth's mantle. Colored gemstones tell scientists about the crust; gem diamonds tell scientists about the mantle. This makes diamonds unique among gemstones: Not only do they have great beauty, but they can also help scientists understand carbon processes deep in the earth. Indeed, diamonds are some of the only direct samples we have of the earth's mantle.

But how do diamonds grow in the mantle? While Hollywood's depiction of Superman squeezing coal captured the public's imagination, in reality this does not work. Coal is a crustal compound and is not found at mantle pressures. Also, we now know that diamond does not prefer to form through direct conversion of solid carbon, even though the pressure and temperature conditions under which diamond forms have traditionally been studied experimentally as the reaction of graphite to diamond.

Generally, two conditions are needed for diamond formation: Carbon must be present in a mantle fluid or melt in sufficient quantity, and the melt or fluid must become reduced enough so that oxygen does not combine with carbon (see below). But do diamonds all grow by the same mechanism? What does their origin reveal about their growth medium and their mantle host rock? Surprisingly, diamonds do not all form in the same way, but rather they form in various environments and through varying mechanisms. Through decades of study, we now understand that diamonds such as the rare blue Hope, the large colorless Cullinan, and the more common yellow "cape" diamonds all have very different origins within the deep earth.

Diamonds Form from Fluids in the Mantle That Migrate Due to Plate Tectonics

Diamond is a metasomatic mineral that forms during migration of carbon-bearing fluids, which means that it forms from fluids and melts that move through the mantle. Diamonds can form in both peridotite and eclogite (box A) in the cratonic lithospheric mantle, as well as their higher-pressure equivalents in the much deeper transition zone and lower mantle (box B). Regardless of a diamond's formation depth, many diamond fluids and melts appear to be related to the recycling of surficial material into the deep earth or to deep melting processes when tectonic plates split apart, or rift, to form new oceans. Both processes occur as part of the geologic cycles that accompany plate tectonics or, in ancient times, some type of pre-plate tectonics.

Since diamonds come from deep and otherwise inaccessible regions, they can be used to study many larger-scale tectonic processes in earth that cannot be studied any other way. Diamonds reveal processes such as early craton development, craton growth and stabilization processes, tectonic processes that can modify and destroy the cratonic lithosphere, and deep subduction (box B) into the lower mantle that may reintroduce volatile elements into the deep earth. This makes the study of diamond source fluids, as well as inclusions in diamond, a powerful way (if not the only way) to study the deep earth cycles of many elements such as carbon, nitrogen, boron, sulfur, and oxygen.

How Do Lithospheric Diamonds Form?

Lithospheric diamonds (box B) often contain detectable nitrogen, implying that they crystallize from carbon- and nitrogen-bearing (C-N-bearing) fluids. Through the study of diamonds from many different localities, we now know that there are subtle differences in the compositions of these C-N-bearing fluids and melts. These differences manifest as changes in the type of carbon and nitrogen compounds contained in these fluids. "Oxidized" hydrous fluids and melts can contain CO_3, CO_2, and N_2, whereas more "reduced" hydrous fluids contain CH_4, NH_3, and minor H_2.

Traditional models for diamond formation from fluids in the mantle invoke either carbonate (CO_3) reduction or methane (CH_4) oxidation to remove the elements bonded to carbon. Both these mechanisms require some oxygen exchange with the surrounding rocks—peridotite or eclogite (box A)—at the site of diamond precipitation so that elemental carbon can be produced to crystallize diamond. Sometimes peridotite has a limited capacity to exchange oxygen, and we now know that cooling of hydrous fluids containing methane (CH_4) and carbon dioxide (CO_2) is an alternative way to precipitate diamonds in these rocks (figure 1; Luth and Stachel, 2014; Smit et al., 2016; Stachel et al., 2017).

Gems & Gemology, Vol. 54, No. 4, pp. 440–445.

BOX A: ROCK TYPES IN THE MANTLE

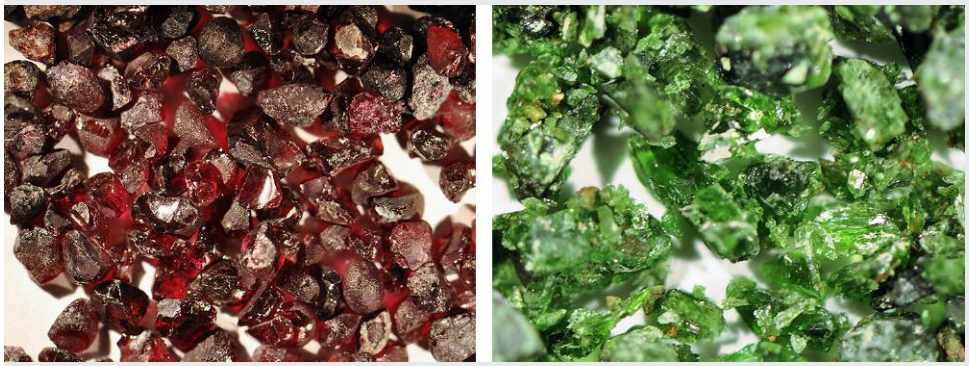

Figure A-1. Red-purple garnet (with Cr-pyrope compositions) and bright green clinopyroxene (with Cr-diopside compositions) separated from a crushed peridotite rock. Photos by Karen Smit/University of Alberta.

Peridotite. Peridotite is the predominant rock type in the mantle. It contains the minerals orthopyroxene, clinopyroxene, and olivine (figure A-1). Peridotite also contains an aluminous phase that can be either spinel or garnet, depending on depth. At the higher pressure conditions in the diamond stability field, the aluminous phase is always garnet (figure A-1). Peridotite melts to form basalt at mid-ocean ridges and ocean islands. This melting removes the basaltic melt from peridotite, leaving the residual peridotite depleted in elements such as Ca, Al, and Fe. This is because the melt moves upward to dikes that eventually feed shallow magma chambers. Lherzolite, the most fertile peridotite, has not undergone significant melt depletion and will contain some combination of the minerals listed above. With high proportions of melt depletion, clinopyroxene is eventually exhausted in the residual peridotite, resulting in the clinopyroxene-free rock known as harzburgite. With around 40–50% melting, orthopyroxene is also exhausted and olivine dominates the peridotitic assemblage. After these high degrees of melting where most of the Ca, Al, and Fe have been lost, the residual peridotite becomes the most depleted dunite. Importantly, both depleted harzburgite and dunite can be re-enriched by passing melts that could reintroduce many of these minerals and convert depleted peridotite back to fertile lherzolite.

Eclogite. Eclogite is another rock type in the lithospheric mantle, a bimineralic rock consisting of a sodium-rich clinopyroxene (known as omphacite) and garnet with pyrope (Mg-rich), grossular (Ca-rich), and almandine (Fe-rich) components (figures 3 and A-2). There are two main models for the origin of eclogites in the lithospheric mantle: as high-pressure mantle melts or as former oceanic crust that has been recycled back into the mantle through subduction (Jacob, 2004). Despite their scarcity in the lithospheric mantle (estimated to be less than 1%), eclogites are often sampled by kimberlites and, due to their frequent recycled origin, can provide important insights into the role of subduction in the assembly of cratonic keels and recycling of surficial components into the deep earth.

Figure A-2. Bimineralic eclogite containing pale green clinopyroxene and orange-red garnet (Victor mine, Canada). This eclogite rock was sawed into a thin section (30 µm thick) and polished so that it could transmit light and be studied under a microscope. Photo by Karen Smit/University of Alberta.

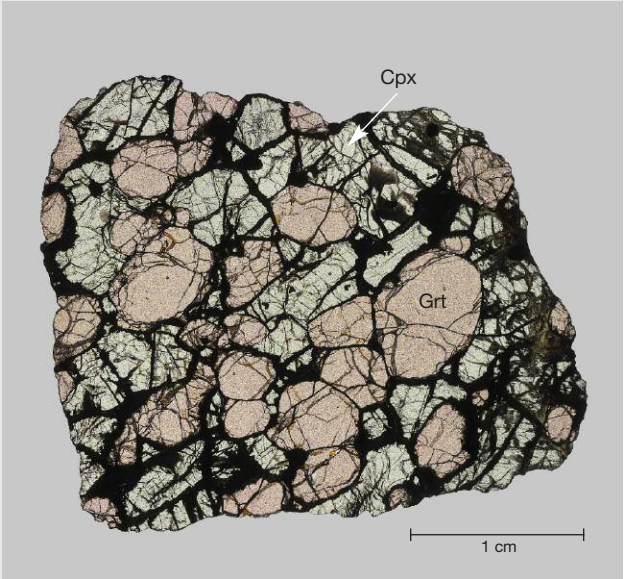

Unfortunately, gem-quality diamonds almost never contain any trapped source fluids that can directly indicate how they formed. However, there are so-called fibrous diamonds (figure 2) that grow much more rapidly than gem-quality diamonds, and even coat earlier gem diamond cores, allowing them to trap abundant fluids. Fibrous diamonds from all over the world, including Canada, West Africa, Siberia, and South Africa, have compositions that

Box B: Where Do Diamonds Form in the Earth?

Natural diamonds typically form 150–200 km below the surface of the earth. Diamond formation does not occur everywhere at these depths, but only below the oldest continents that have been stable for billions of years; these areas are known as *cratons* (see figure 2 in Summer 2018 Diamonds from the Deep). This is because these old cratons all have thick continental roots with cool temperature profiles conducive to diamond formation that geologists term "continental lithospheric mantle." Diamonds that form within these continental roots are known as *lithospheric diamonds* and are carried up to the surface of the earth by rare volcanic eruptions known as *kimberlites.*

Other diamonds form much deeper in the earth, in *sublithospheric* regions of the mantle, below these continental roots. So-called *superdeep diamonds* form at depths much greater than 200 km, in areas of the mantle known as the *transition zone* (410 to 660 km below the earth's surface) and *lower mantle* (> 660 km). After formation they are transported to shallower depths in the mantle, likely through mantle convection cells, and then also brought to the surface by kimberlite eruptions. Earth's mantle convection associated with plate tectonics is responsible for both the availability of fluids necessary to form diamonds and the return of diamonds to the surface. Ocean floor is thrust deep into the mantle by the process known as subduction and carries diamond-forming fluids in its seawater-altered minerals and rocks. Mantle convection return flow also causes hot mantle to rise to shallower levels and melt, generating the kimberlites that deliver diamonds to the surface.

are different mixtures of three end-member fluid compositions: carbonate-like, silica-rich, or salty (e.g., Navon et al., 1988; Izraeli et al., 2001, 2004; Schrauder and Navon, 1994; Smith et al., 2012; Weiss et al., 2013; Timmerman et al., 2018).

The origins of fibrous diamonds and their fluids are still debated. Some researchers argue that fibrous diamonds may be related to the kimberlite magmas that transport diamonds to the surface. If so, fibrous diamonds could form right before the kimberlite eruption to the earth's surface, which would make them much younger than many gem-quality diamonds that may have resided in the mantle for millions to billions of years. One study, however, linked the full range of fluids in some fibrous diamonds from northern Canada to subducting oceanic lithosphere, concluding that the original subducting fluid was related to >200-million-year-old recycled sea water (Weiss et al., 2015). This implies that some fibrous diamonds could have longer mantle residence times and are not necessarily always related to kimberlite eruption.

Figure 1. We now have evidence for a wider range of diamond source fluid compositions in both the lithosphere and sublithosphere that do not include any carbonate components. Both peridotitic and eclogitic diamonds from the lithosphere are now known to also precipitate from non-carbonate-bearing fluids. The Marange cuboctahedral diamonds formed from water-rich fluids that contain both methane and carbon dioxide (Smit et al., 2016), and the Zimmi eclogitic diamonds crystallized from water-rich fluids that are more reduced and contain significant methane (Smit et al., 2019), similar to fluids indicated for peridotitic diamonds from the Cullinan mine (Thomassot et al., 2007). Photos by Joshua Balduf and Karen Smit/GIA.

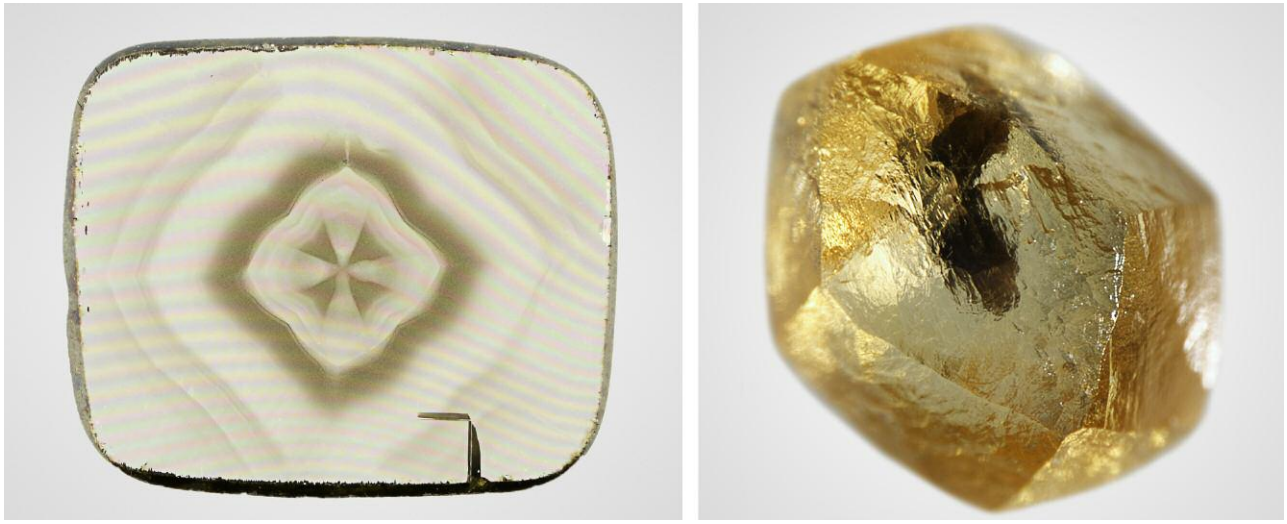

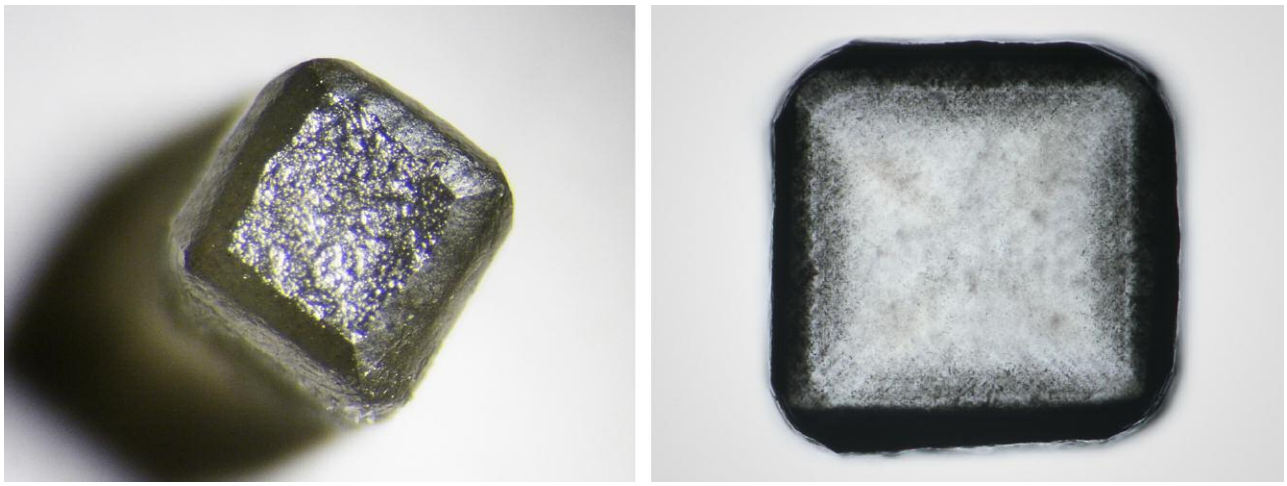

Figure 2. A fibrous cubic diamond (1.3 × 1.3 mm) from Wawa (Superior craton, Canada) that has been cut through the middle and polished into a double-sided plate (right). Fibrous diamonds such as this example typically contain a darker rim of fluid inclusions that have compositions ranging between carbonate-rich, saline-rich, and silica-rich. Fluids similar to those in fibrous diamonds have been found along twin planes in gem-quality diamonds from Voorspoed and Venetia (Jablon and Navon, 2016). Photos by Evan Smith/University of British Columbia.

Fluids similar to those in fibrous diamonds have been found along twin planes in rare gem-quality diamonds from South Africa, indicating that some gem-quality diamonds may have similar formation conditions to fibrous diamonds (Jablon and Navon, 2016). However, fluid inclusions in gem-quality diamonds are actually very rare, and source compositions and the nature of reactants to make diamond must be inferred from the covariation of carbon isotope composition and nitrogen content, either in individual diamonds or diamond suites (Deines, 1980; Stachel et al., 2009). These carbon isotope studies suggest that gem-quality diamonds may form through varying mechanisms, though they typically involve hydrous carbon-bearing fluids that also contain oxygen and hydrogen (either as CO_3, CO_2, or CH_4).

Carbon isotope studies can infer whether a diamond source fluid is "oxidized" or "reduced" (see above) but do not reveal the fluid's full elemental composition. Diamonds are comprised mostly of carbon, and any other elements present in the diamond are normally at incredibly low abundances that are difficult to measure. For this reason, trace element data for gem-quality diamonds are only now being realized with improvements in analytical sensitivity. But the available trace element data for gem-quality diamonds do appear to show many compositional similarities to fluid-rich fibrous diamonds (Krebs et al., 2019), further suggesting that fibrous and gem-quality diamonds crystallize from similar types of mantle fluids.

Sublithospheric Diamonds: The Product of Very Deep Subduction

So-called superdeep diamonds that form in the sublithospheric mantle (box B) contain very little nitrogen and are relatively pure, making them nearly colorless (e.g., CLIPPIR diamonds such as the Cullinan diamond and the Constellation diamond from Karowe mine in Botswana; Smith et al., 2016). Some superdeep diamonds are plastically deformed, making them pink or brown (e.g., diamonds from the Juina area in Brazil). Rarely, they can contain some boron imparting a blue color (e.g., the Hope diamond; Smith et al., 2018). Based on studies of inclusion-bearing superdeep diamonds, we now know that they cannot all form in the same environment and that they must crystallize from a wide variety of source fluids and melts that all relate to different aspects of very deep subduction (box B).

Many superdeep diamonds, such as those from the Juina and Machado River areas in Brazil, preserve inclusion evidence for their crystallization from carbonate-rich fluids (figure 3; Walter et al., 2008; Bulanova et al., 2010; Burnham et al., 2016; Thomson et al., 2016). These CO_3-rich source fluids likely derive from oceanic lithosphere that was deeply subducted into the mantle transition zone (box B). CLIPPIR diamonds (figure 4) are now also known to crystallize from metallic melts in the deep earth that are associated instead with reduced carbon (CH_4) and hydrogen (Smith et al., 2016). These diamonds have carbon isotopic compositions that are unlike those expected for the mantle, but rather indicate an ultimate source for the carbon in the oceanic lithosphere, as do other superdeep diamonds. The third kind of superdeep diamond, boron-containing blue diamonds, are also related to deeply subducted oceanic lithosphere (figure 4; Smith et al., 2018). In this case, however, the source for the boron-containing fluids is likely to be altered peridotite in the deeper portions of the subducted lithosphere.

Our Fluid Understanding of How Diamonds Form: Future Studies of Diamond-Forming Fluids

Our understanding of the fluids from which diamonds form is improving with advances in the sensitivity of analytical

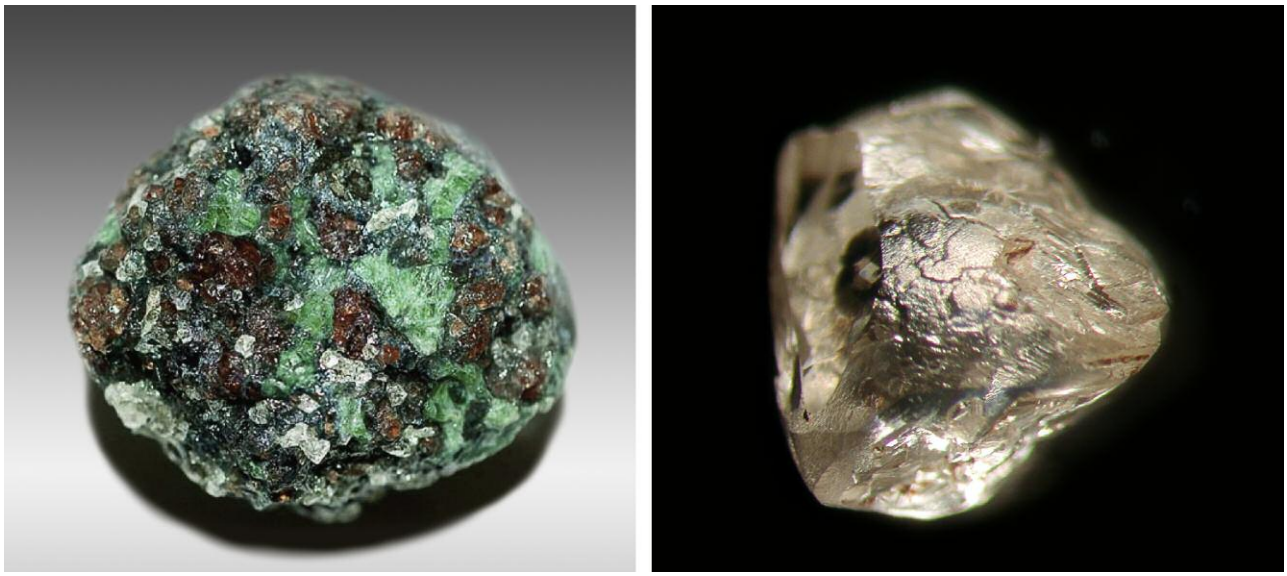

Figure 3. Before 2016, the majority of diamonds were thought to crystallize from fluids and melts that contained carbonate. For example, the diamonds contained in Jericho eclogites (Slave craton, Canada; left) have covariations in carbon isotopic composition and nitrogen content that indicate carbonate-rich source fluids/melts (Smart et al., 2011). Similarly, the trace element compositions of inclusions in Juina superdeep diamonds (right) also indicate their formation from carbonate-rich fluids or melts in the deep mantle (Walter et al., 2008; Bulanova et al., 2010; Thomson et al., 2016). Photos by Katie Smart/University of Alberta and Galina Bulanova/University of Bristol.

techniques. Most diamonds are only comprised of carbon, with less than a few parts per million of nitrogen, boron, and other trace elements. Many elements that scientists are interested in detecting in diamond are currently not able to be measured accurately. With improved analytical techniques that can measure the very low concentrations of trace elements in diamonds, we may be able to better understand the different origins for diamond source fluids.

Future work will also reveal how the different diamond-forming environments relate to each other. Our understanding of the origin of lithospheric diamond source fluids is better developed than it is for sublithospheric diamonds.

Figure 4. Although some superdeep diamonds have been shown to crystallize from carbonate-rich melts (figure 3), there are also some rare superdeep diamonds that crystallize from boron-rich fluids and reduced metallic melts, both variably associated with subducted oceanic lithosphere (Smith et al., 2016, 2018). On the left is a 29.62 ct boron-containing rough blue diamond, and on the right is the 812.77 ct rough Constellation diamond, which contained metallic inclusions. Photos by Jian Xin (Jae) Liao/GIA.

This is because they contain much more nitrogen that can be studied along with carbon, and sometimes they are found still trapped within their peridotite or eclogite host rocks (figure 3). Since superdeep diamonds contain little or no nitrogen, and are never found within their original superdeep mantle host rocks, they provide less information about the geological conditions by which they formed. We do know, however, that the carbonate-rich fluids, metallic melts, and boron-rich fluids in superdeep diamonds all relate in some way to deeply subducted material from the earth's oceanic lithosphere. But the challenge remains for geologists to predict where these domains, all with different oxidation states, occur in the deep earth. Current diamond exploration models have a near-exclusive focus on lithospheric diamonds, so geologists still need to do some work to figure out how to explore for potentially high-value superdeep diamonds.

REFERENCES

Bulanova G.P., Walter M.J., Smith C.B., Kohn S.C., Armstrong L.S., Blundy J., Gobbo L. (2010) Mineral inclusions in sublithospheric diamonds from Collier 4 kimberlite pipe, Juina, Brazil: subducted protoliths, carbonated melts and primary kimberlite magmatism. *Contributions to Mineralogy and Petrology*, Vol. 160, No. 4, pp. 489–510.

Burnham A.D., Bulanova G.P., Smith C.B., Whitehead S.C., Kohn S.C., Gobbo L., Walter M.J. (2016) Diamonds from the Machado River alluvial deposit, Rondonia, Brazil, derived from both lithospheric and sublithospheric mantle. *Lithos*, Vol. 265, pp. 199–213.

Deines P. (1980) The carbon isotopic composition of diamonds: relationship to diamond shape, colour, occurrence and vapour deposition. *Geochimica et Cosmochimica Acta*, Vol. 44, pp. 943–961.

Izraeli E.S., Harris J.W., Navon O. (2001) Brine inclusions in diamonds: a new upper mantle fluid. *Earth and Planetary Science Letters*, Vol. 187, No. 3-4, pp. 323– 332.

Izraeli E.S., Harris J.W., Navon O. (2004) Fluid and mineral inclusions in cloudy diamonds from Koffiefontein, South Africa. *Geochimica et Cosmochimica Acta*, Vol. 68, No. 11, pp. 2561–2575.

Jablon B.M., Navon O. (2016) Most diamonds were created equal. *Earth and Planetary Science Letters*, Vol. 443, pp. 41–47.

Jacob D.E. (2004) Nature and origin of eclogite xenoliths from kimberlites. *Lithos*, Vol. 77, No. 1-4, pp. 295–316.

Krebs M.Y., Pearson D.G., Stachel T., Laiginhas F., Woodland S., Chinn I.L., Kong J. (2019) A common parentage – low abundance trace element data of gem diamonds reveals similar fluids to fibrous diamonds. *Lithos*, Vol. 324-325, pp. 356–370.

Luth R.W., Stachel T. (2014) The buffering capacity of lithospheric mantle: implications for diamond formation. *Contributions to Mineralogy and Petrology*, Vol. 168, No. 5, p. 1083.

Navon O., Hutcheon I.D., Rossman G.R., Wasserburg G.J. (1988) Mantle-derived fluids in diamond micro-inclusions. *Nature*, Vol. 335, No. 6193, pp. 784–789.

Schrauder M., Navon O. (1994) Hydrous and carbonatitic mantle fluids in fibrous diamonds from Jwaneng, Botswana. *Geochimica et Cosmochimica Acta*, Vol. 58, No. 2.

Smart K.A., Heaman L.M., Chacko T., Simonetti A., Kopylova M., Mah D., Daniels D. (2009) The origin of high-MgO diamond eclogites from the Jericho Kimberlite, Canada. *Earth and Planetary Science Letters*, Vol. 284, No. 3-4.

Smart K.A., Chacko T., Stachel T., Muehlenbachs K., Stern R.A., Heaman L.M. (2011) Diamond growth from oxidized carbon sources beneath the Northern Slave Craton, Canada: A δ^{13}C-N study of eclogite-hosted diamonds from the Jericho kimberlite. *Geochimica et Cosmochimica Acta*, Vol. 75, No. 20, pp. 6027–6047.

Smit K.V., Shirey S.B., Stern R.A., Steele A., Wang W. (2016) Diamond growth from C-H-N-O recycled fluids in the lithosphere: evidence from CH_4 micro-inclusions and δ^{13}C-δ^{15}N-N content in Zimbabwe mixed-habit diamonds. *Lithos*, Vol. 265, pp. 68–81.

Smit K.V., Stachel T., Luth R.W., Stern R.A. (2019) Evaluating mechanisms for eclogitic diamond growth from reduced fluids: an example from Neoproterozoic Zimmi diamonds (West African craton). Submitted to *Chemical Geology*.

Smith E.M., Kopylova M.G., Nowell G.M., Pearson D.G., Ryder J. (2012) Archean mantle fluids preserved in fibrous diamonds from Wawa, Superior craton. *Geology*, Vol. 40, No. 12, pp. 1071–1074.

Smith E.M., Shirey S.B., Nestola F., Bullock E.S., Wang J., Richardson S.H., Wang W. (2016) Large gem diamonds from metallic liquid in Earth's deep mantle. *Science*, Vol. 354, No. 6318, pp. 1403–1405.

Smith E.M., Shirey S.B., Richardson S.H., Nestola F., Bullock E.S., Wang J., Wang W. (2018) Blue boron-bearing diamonds from Earth's lower mantle. *Nature*, Vol. 560, pp. 84–87.

Stachel T., Harris J.W., Muehlenbachs K. (2009) Sources of carbon in inclusion-bearing diamonds. *Lithos*, Vol. 112S, pp. 625–637.

Stachel T., Chacko T., Luth R.W. (2017) Carbon isotopic fractionation during diamond growth in depleted peridotite: Counterintuitive insights from modelling water-maximum CHO fluids as multi-component systems. *Earth and Planetary Science Letters*, Vol. 473, pp. 44–51.

Thomassot E., Cartigny P., Harris J.W., Viljoen K.S. (2007) Methane-related diamond crystallisation in the Earth's mantle: Stable isotope evidences from a single diamond-bearing xenolith. *Earth and Planetary Science Letters*, Vol. 257, pp. 362–371.

Thomson A.R., Kohn S.C., Bulanova G.P., Smith C.B., Araujo D., Walter M.J. (2016) Trace element composition of silicate inclusions in sub-lithospheric diamonds from the Juina-5 kimberlite: Evidence for diamond growth from slab melts. *Lithos*, Vol. 265, pp. 108–124.

Timmerman S., Jaques A.L., Weiss Y., Harris J.W. (2018) N-δ^{13}C-inclusion profiles of cloudy diamonds from Koffiefontein: Evidence for formation by continuous Rayleigh fractionation and multiple fluids. *Chemical Geology*, Vol. 483, pp. 31–46.

Walter M.J., Bulanova G.P., Armstrong L.S., Keshav S., Blundy J.D., Gudfinnsson G., Lord O.T., Lennie A.R., Clark S.M., Smith C.B., Gobbo L. (2008) Primary carbonatite melt from deeply subducted oceanic crust. *Nature*, Vol. 454, pp. 622–625.

Weiss Y., Griffin W.L., Navon O. (2013) Diamond-forming fluids in fibrous diamonds: The trace-element perspective. *Earth and Planetary Science Letters*, Vol. 376, pp. 110–125.

Weiss Y., McNeill J., Pearson D.G., Nowell G.M., Ottley C.J. (2015) Highly saline fluids from a subducting slab as the source for fluid-rich diamonds. *Nature*, Vol. 524, p. 339.

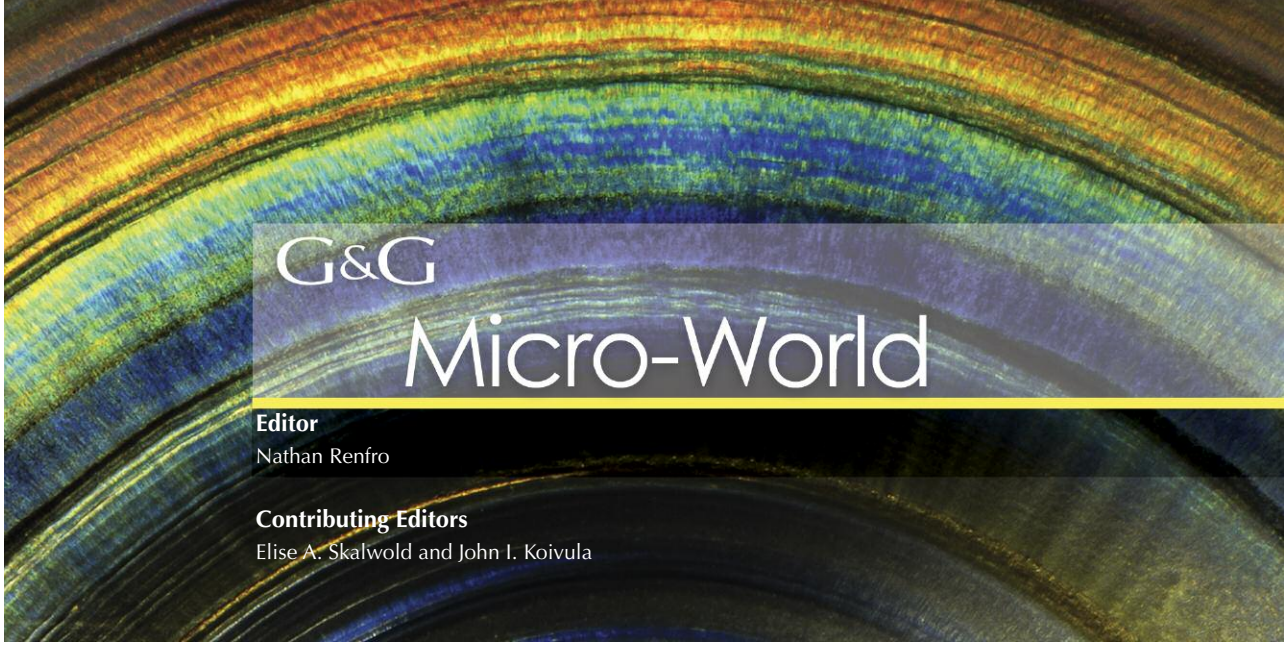

Rose in Demantoid from Madagascar

Garnets have been known since antiquity. However, it was only during the late nineteenth century that the green variety demantoid—named for its "diamond-like" luster—was discovered in the Ural Mountains of Russia. A few decades later, Fabergé and other jewelers helped demantoid gain more exposure and popularity. Today demantoid garnet is found in various deposits around the world, including Russia, Namibia, Italy, Iran, Afghanistan, and Madagascar.

The authors recently examined a 0.33 ct round brilliant demantoid from Antetezambato, Madagascar—a skarn-related deposit—that was of particular interest for a large inclusion resembling a flower (figure 1). Further microscopic examination revealed the inclusion to be a growth blockage followed by a large etch tube.

The observed shape immediately evokes a flower in repose. The subtle oblique illumination also reflects a shadow on the opposite facet, adding more three-dimensionality to this "still-life" image. Finally, the use of Rheinberg illumination (Fall 2015 Micro-World, pp. 328–329) enhances the colors and gives the inclusion a suitable rose red color.

Even though horsetail inclusions are the more heralded internal feature of demantoid, the beautiful flower inclusion in this demantoid specimen from Madagascar proves once more that the exploration of the microscopic world in gemstones will always reserve for us endless surprises.

Jonathan Muyal
GIA, Carlsbad

Pierre-Yves Chatagnier
Tsara International, Paris

Lepidocrocite in Boulder Opal

The term "boulder opal" is used to describe gem-quality opal that fills in the pore spaces and cracks of its ironstone host. When cut, some of that ironstone matrix is included in the finished stone, often to add structural support to delicately thin veins of opal (R.W. Wise, "Queensland boulder

Figure 1. A negative crystal growth blockage followed by an etch tube is observed in a faceted demantoid from Madagascar. The use of Rheinberg illumination gives the inclusion a red color reminiscent of a rose. Photomicrograph by Jonathan Muyal; field of view 1.99 mm.

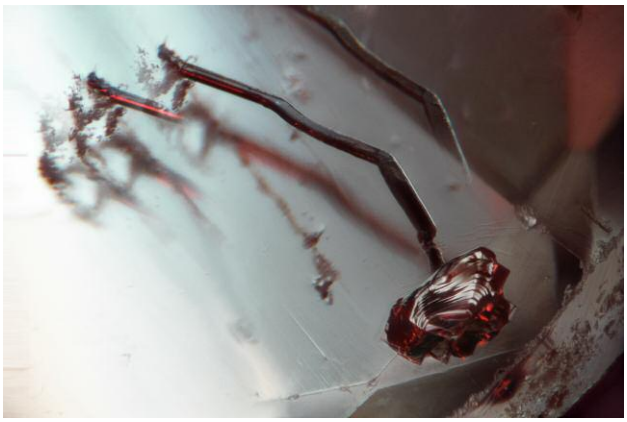

About the banner: An iris agate from Nipomo, California, shows vibrant diffraction colors. Photomicrograph by Nathan Renfro; field of view 11.51 mm. Courtesy of the John Koivula Inclusion Collection.

Editors' note: Interested contributors should contact Nathan Renfro at nrenfro@gia.edu and Jennifer-Lynn Archuleta at jennifer.archuleta@gia.edu for submission information.

Gems & Gemology, Vol. 54, No. 4, pp. 446–451.

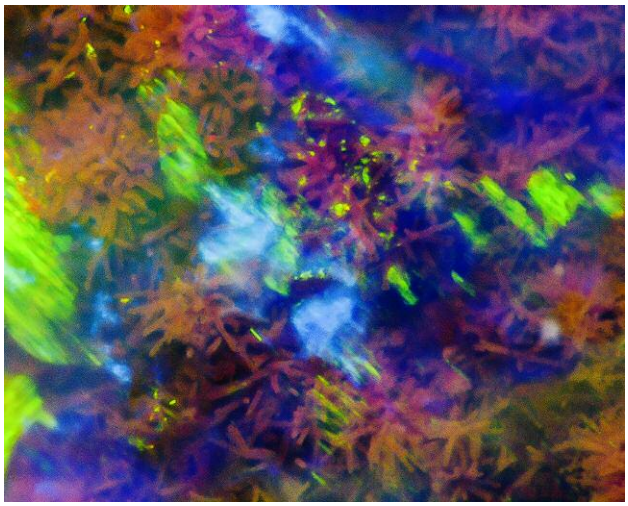

Figure 2. This boulder opal contains a layer of needle-like lepidocrocite inclusions along the interface between the opal and the ironstone matrix. Photomicrograph by Nathan Renfro, field of view 0.96 mm.

opal," Spring 1993 *G&G*, pp. 4–15). The authors recently examined a boulder opal, presumed to be from Australia, that showcased some interesting inclusions along the interface between the opal and ironstone matrix. Microscopic observation revealed a carpet of minute needle-like inclusions radiating outward from the ironstone into the surface opal layer (figure 2). Where some of the inclusions broke the surface, they showed a submetallic luster in reflected light. In order to identify these unusual inclusions, we used Raman spectroscopy to analyze some of the surface-reaching needles. Raman spectroscopy and comparison with the reference spectra from the RRUFF mineral database showed that these inclusions were the iron hydroxide mineral lepidocrocite. Energy-dispersive X-ray fluorescence testing revealed only the presence of iron, which was consistent with the Raman results. This is the first time the authors have encountered a lepidocrocite inclusion in boulder opal.

Nathan Renfro
GIA, Carlsbad

Bona Hiu Yan Chow
GIA, Hong Kong

Prismatic Rutile in Quartz

Rutile, a mineral composed mainly of titanium dioxide (TiO_2), is a common inclusion in quartz in the form of profuse acicular hair-like crystals (E.J. Gübelin and J.I. Koivula, *Photoatlas of Inclusions in Gemstones*, Vol. 1, ABC Edition, Zurich, 1986). These golden needle inclusions are appreciated as a pleasing feature, giving their name to the variety known as rutilated quartz.

However, prismatic single rutile crystal inclusions in quartz remain an underappreciated feature, often synonymous with "flaws." They are rarely showcased by the lapidary. Nevertheless, we observed a 21.27 ct cushion-cut rock crystal quartz that displayed a large, well-formed rutile crystal inclusion (figure 3) under the table.

The protogenetic inclusion showed a black-silver color with adamantine to submetallic luster, a well-formed tetragonal ("stubby"/blocky) prismatic crystal habit with fine striation along its length (parallel to the c-axis), and smooth pyramidal termination faces. Cyclical twinning such as twin knee/sharply angled twins on [011] and parallel twinning crystal growth along the length were also observed (again, see figure 3).

Figure 3. Left: Depending on the viewing angle, these two rutile crystals in rock crystal quartz seem to be touching each other. In the foreground is a black-silver prismatic crystal, and below on the right is a shadowed, fragmented piece, seen in diffuse/fiber-optic illumination. Right: The use of Rheinberg illumination gives warmer colors to the rutile crystals and the background. Photomicrographs by Jonathan Muyal; field of view 14.52 mm.

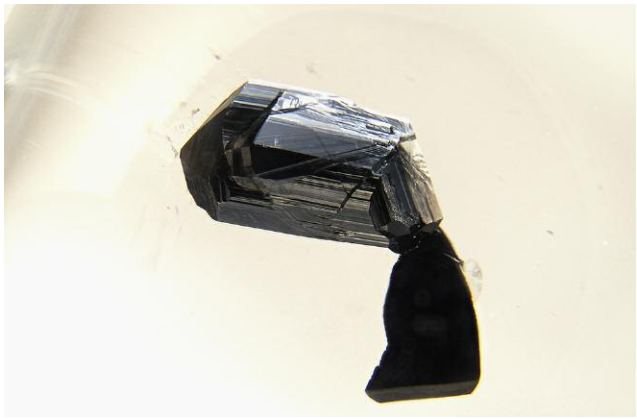

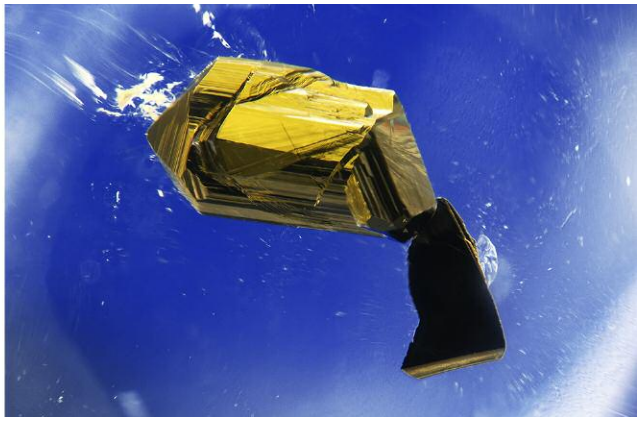

Very close below, in the background, was another rutile crystal inclusion, this one a fragmented piece. At first glance, it could be mistaken for part of the main crystal inclusion described above. Nevertheless, this rutile fragment adds details to the overall visual composition.

Rheinberg illumination (Fall 2015 Micro-World, pp. 328–329) using blue and yellow filters provided additional contrast. Lighting technique is critical in photomicrography. Here it dramatically enhanced the inclusion scene, offering alternative vibrant colors for aesthetic purposes.

This rock crystal quartz had preserved and beautifully highlighted a prismatic rutile crystal inclusion, like a collector mineral specimen in a display window. Such a large inclusion specimen also provides valuable mineralogical information for the gemologist.

Jonathan Muyal and John I. Koivula
GIA, Carlsbad

Drill Hole in Heated Pink Sapphire

While testing a faceted pink sapphire in our laboratory, we looked at its internal features and determined that it was a heat-treated stone from Myanmar. As we examined the surface of the 14.75 × 13.02 × 8.82 mm sapphire, we noticed an unusual feature: a large round drill hole extending from the surface into a crystal or negative crystal within the stone (figure 4). Note that this drill hole did not extend through the sapphire, as one might see in a bead. This stone was faceted, so it is unlikely that the person who drilled into the stone intended to create a bead.

What seems more likely, given the placement of the drill hole, is that it was drilled to minimize the appearance of the crystal that it reached. We suspect that the crystal was originally more opaque and of darker color or filled with a dark substance. It is possible that the drill hole was created so that the crystal could be cleaned out with acid, minimizing its appearance. We can only guess at the intentions of the treater, who might have gotten the idea from the laser drilling of diamonds.

Although the exact process may remain a mystery, this inclusion indicates an unusual treatment in ruby and sapphire.

E. Billie Hughes
Lotus Gemology, Bangkok

Sillimanite in Ruby

Recently, the New York laboratory received for origin determination a ruby whose unusual lathe-like inclusions caught the authors' eyes. The inclusions were long, prismatic, and transparent, often accumulating in small bundles throughout the stone (figure 5). Luckily, a few needles broke the surface, allowing laser Raman spectroscopy to identify the mystery inclusions as sillimanite, an aluminosilicate mineral that forms in high-grade metamorphic rocks, including the amphibolite facies. With a chemical formula of Al_2SiO_5, sillimanite, a polymorph of andalusite and kyanite, is frequently found with ruby.

Laser ablation–inductively coupled plasma–mass spectrometry (LA-ICP-MS) of the host ruby revealed a particularly high iron concentration of 7100–7410 ppmw. The combination of the elemental composition and inclusions indicates the stone is from an amphibolite host rock, a non-classic metamorphic formation (NCL). NCL ruby sources

Figure 4. A drill hole in a heated pink sapphire from Myanmar, seen with diffuse brightfield and fiber-optic illumination. Photomicrograph by E. Billie Hughes; approximate field of view 5 mm.

Figure 5. Bundles of fine sillimanite needles clash within their ruby host. Photomicrograph by Tyler Smith; field of view 1.76 mm.

include East African countries such as Mozambique, Madagascar, and Tanzania, as opposed to classic metamorphic sources such as Burma and Vietnam.

Such a high density of these inclusions is rarely observed in stones submitted to GIA. Sillimanite itself is not a particularly uncommon mineral, especially in amphibolite host rocks, so why has it been missing from previously analyzed East African rubies at GIA? Due to its preferred habit of densely packed needles, sillimanite in ruby likely affects transparency, potentially resulting in non-gem-quality translucent to opaque rubies. Such stones are not frequently submitted to GIA. It is refreshing to see less common mineral inclusions in the lab, as they provide a greater understanding of East African rubies.

Virginia Schneider and Tyler Smith
GIA, New York

Gilson Cat's-Eye Synthetic Emerald

In the early 1960s, French ceramist and engineer Pierre Gilson succeeded in growing and producing flux synthetic emerald of commercially marketable quality. By the mid-1970s, it was reported that Gilson commanded 95% of the world market in synthetic emeralds (J. Sinkankas, *Emerald and Other Beryls*, Chilton Book Company, Radnor, Pennsylvania, 1981, p. 308). While the Gilson factory is no longer active, the material is still occasionally encountered in the trade and in gemological laboratories. The authors recently examined one example, a 2.73 ct cabochon that was of particular interest for its chatoyancy (figure 6).

Gilson synthetics are often grown from seed plates of slices of natural beryl positioned parallel to the c-axis. Microscopic examination of the specimen revealed veils and wispy secondary flux fingerprint inclusions, as well as strain bands like graining aligned parallel to the c-axis, all common features of Gilson synthetic emerald. The numerous growth striae resulted from inner strain, caused by periodic growth interruptions or slight changes in chemical composition when the growth tank was recharged (Sinkankas, 1981; R. Diehl, "Neues zum Thema 'Synthetischer Smaragd': Besuch bei Pierre Gilson," *Zeitschrift der Deutschen Gemmologischen Gesellschaft*, Vol. 26, No. 2, 1977, pp. 61–75).

Figure 6. This 2.73 ct Gilson synthetic emerald cabochon displays a sharp "cat's-eye" phenomenon. Photo by Kevin Schumacher.

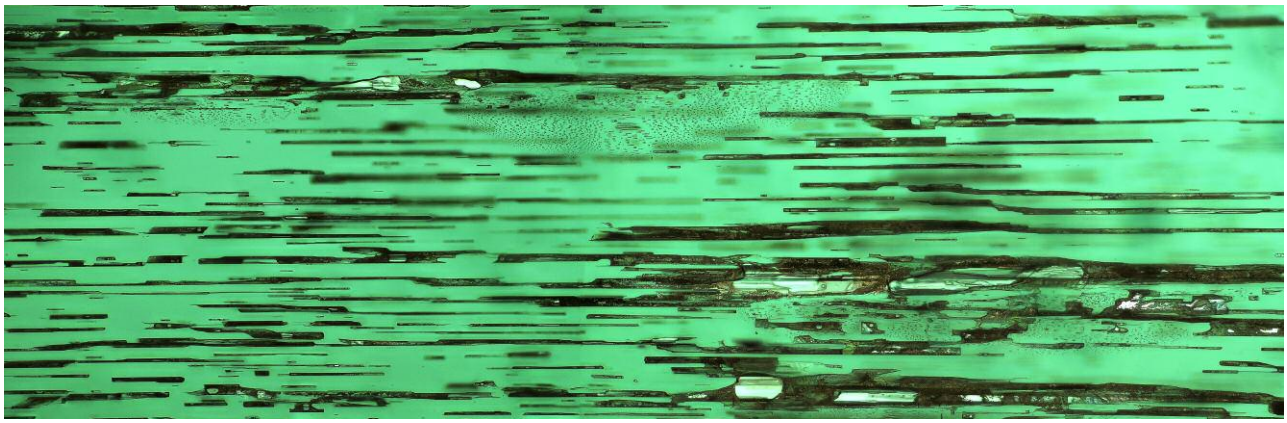

Figure 7. The parallel arrangement of a network of primary flux inclusions is responsible for the cat's-eye effect. Photomicrograph by Jonathan Muyal; field of view 2.77 mm.

Also parallel to the c-axis (the basal pinacoid of the original crystal), we observed a plane of tubes (figure 7) that was responsible for the chatoyant effect. This plane of numerous elongated bubbles/cavities containing the primary flux—and possibly minute phenakite crystals—was located near the base of the cabochon. This oriented plane of primary flux tubes also appears to result from the variation of conditions during growth.

The micro-world of flux-grown Gilson emerald has already been captured extensively (E.J. Gübelin and J.I. Koivula, *Photoatlas of Inclusions in Gemstones*, Vol. 3, Opinio Publishers, Basel, Switzerland, 2008). But the interest of this specimen is its clever fashioning, with the plane of the coarse primary flux residue—which a lapidary would normally want to remove—oriented close to the base and parallel to it, turning this into a chatoyant specimen. In fact, this is the first time a Gilson flux-grown cat's-eye emerald has been encountered by the authors.

Jonathan Muyal and Pierre-Yves Chatagnier

Zircon Cluster in Ethiopian Sapphire

Ethiopia is a known producer of opal, emerald, and commercial-grade sapphire. In March 2018, a GIA team collected a 1.911 ct blue sapphire from the Ch'ila mining area in the Tigray region. The inclusion scene shows a cluster of small transparent euhedral crystals with high relief. Raman spectroscopy identified the smaller crystals as zircon, but the clusters also contain some larger rounded monazite crystals (figure 8). Zircon is a common inclusion

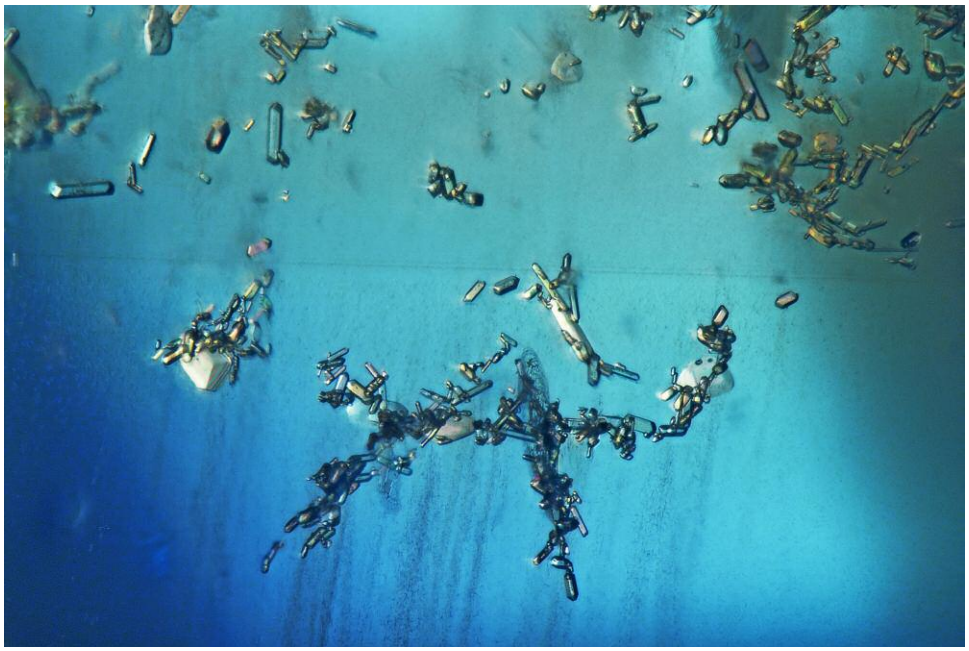

Figure 8. A very dense cluster of euhedral zircon associated with a larger rounded crystal of monazite, viewed under brightfield illumination. Photomicrograph by Charuwan Khowpong; field of view 1.75 mm.

in blue sapphire, usually associated with metamorphic sources such as Myanmar, Sri Lanka, or Madagascar. Zircon inclusions from those deposits typically have more rounded shapes (E.J. Gübelin and J.I. Koivula, *Photoatlas of Inclusions in Gemstones*, Vol. 3, Opinio Publishers, Basel, Switzerland, 2008, pp. 188–308). The sapphire deposit in northern Ethiopia is related to alkali basalt, similar to the deposits in Australia, Nigeria, or Thailand. These sources rarely show clusters of euhedral zircon crystals. The presence of these zircon clusters might help to separate Ethiopian sapphire from other basalt-related sapphire sources.

Charuwan Khowpong
GIA Bangkok

Quarterly Crystal: Bubble in Fluorite

The very lightly etched green fluorite crystals that come from the Rogerley mine, located in Rogerley Quarry, Weardale, County Durham, England, are well known for the beautiful bright fluorescence they display. Rogerley mine fluorite is highly fluorescent, turning bright bluish white on exposure to long-wave ultraviolet radiation.

The fluorescent fluorite from this locality will also take on a purplish color in sunlight. This effect, known as "daylight fluorescence," appears to be unique to fluorite from the Weardale area. Research has shown that this intense fluorescence is due to an elevated rare-earth element (REE) content, including the elements cerium, lanthanum, neodymium, samarium, and yttrium.

The Rogerley fluorite specimen shown in figure 9 measures 17.68 × 17.38 × 13.50 mm and weighs 41.98 ct. What makes this specimen the subject of this issue's "Quarterly Crystal" is the presence of an eye-visible primary fluid inclusion with a moving gas phase. Along the interface, where the two growing crystals came together, negative space was created. This form of primary fluid inclusion hosts fluid remnants that were present when the fluorite was growing. When comparing the two photomicrographs in figure 10, the movement of the gas phase can be clearly seen. Fluid inclusions like this are not at all common in fluorite.

Figure 9. This 41.98 ct cluster of transparent green fluorite cubes contains a large primary two-phase fluid inclusion that was trapped between the cubes as they developed. Photo by Diego Sanchez.

John I. Koivula
GIA, Carlsbad

Figure 10. In this registered pair of images, the movement of the gas phase in the fluorite cluster can be easily seen. Photomicrographs by Nathan Renfro; horizontal field of view 6.54 mm.

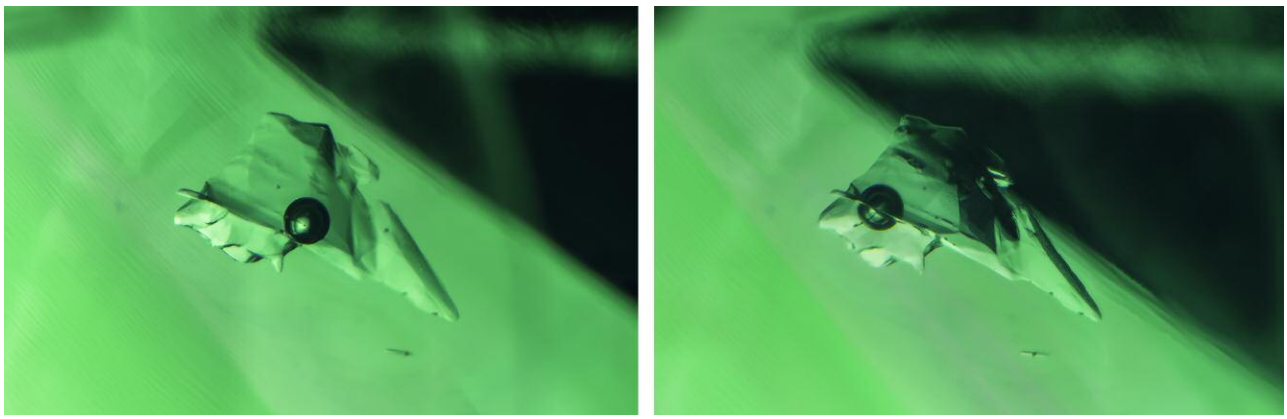

G&G

Gem News International

Contributing Editors
Emmanuel Fritsch, *University of Nantes, CNRS, Team 6502, Institut des Matériaux Jean Rouxel (IMN), Nantes, France* (fritsch@cnrs-imn.fr)
Gagan Choudhary, *Gem Testing Laboratory, Jaipur, India* (gagan@gjepcindia.com)
Christopher M. Breeding, *GIA, Carlsbad* (christopher.breeding@gia.edu)

COLORED STONES AND ORGANIC MATERIALS

Natural emerald with inclusions along three directions. Recently, Guild Gem Laboratories received a 10.48 ct sugarloaf emerald (figure 1) for identification and origin determination. The refractive index (approximately 1.58) and specific gravity (approximately 2.80) fell within the range for beryl, and Fourier-transform infrared (FTIR) testing confirmed it as natural emerald. Additionally, energy-dispersive X-ray fluorescence (EDXRF) analysis revealed Fe, V, and Cr contents consistent with those in Zambian material.

The stone showed interference colors when placed under a polariscope with the bottom facing up. With a conoscope, the optic axis of this emerald was determined to be perpendicular to the bottom. Using the microscope, we found thin platy inclusions arranged in three directions intersected with each other at 60/120 degree angles (figure 2). Those inclusions were mainly dark brownish and transparent with well-formed rectangular shapes, some of which exhibited a light bodycolor resembling an unhealed fracture. Evenly distributed reflective light could be seen at certain angles. We deduced that those inclusions had relatively smooth surfaces, which means that their original crystal faces were not corroded during the emerald's formation. Further observation revealed hexagonal inclusions in the basal plane. Owing to uneven development during their crystalline formation, several of them were nearly triangular in shape. Their sides were parallel to the direction of the platy inclusions (figure 3, top). We also found distinct growth lines near the bottom of the sugarloaf perpendicular to the c-axis. These platy inclusions appeared to be concentrated sparsely in a thin layer with a thickness around 1.5–2.0 mm, as shown figure 3 (bottom). The sparseness of

Figure 1. This 10.48 ct sugarloaf emerald from Zambia shows a vivid and highly saturated green color. Photo by Yizhi Zhao.

Figure 2. Platy inclusions in the emerald in three directions, intersecting at 60/120 degree angles viewed along the c-axis. Photo by Yujie Gao; field of view 2.8 mm.

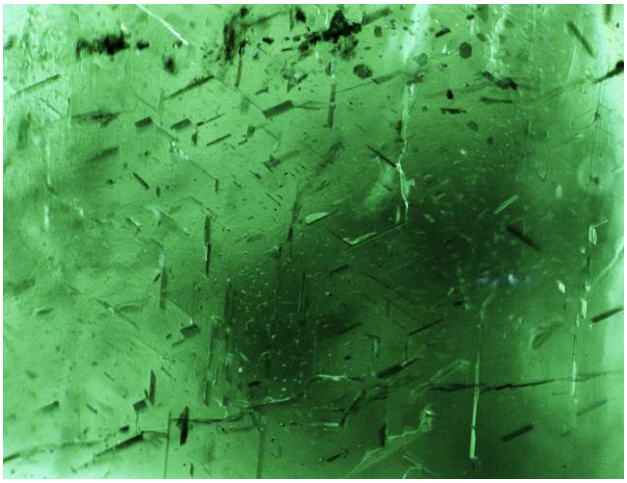

Editors' note: Interested contributors should send information and illustrations to Stuart Overlin at soverlin@gia.edu or GIA, The Robert Mouawad Campus, 5345 Armada Drive, Carlsbad, CA 92008.

Gems & Gemology, Vol. 54, No. 4, pp. 452–469.

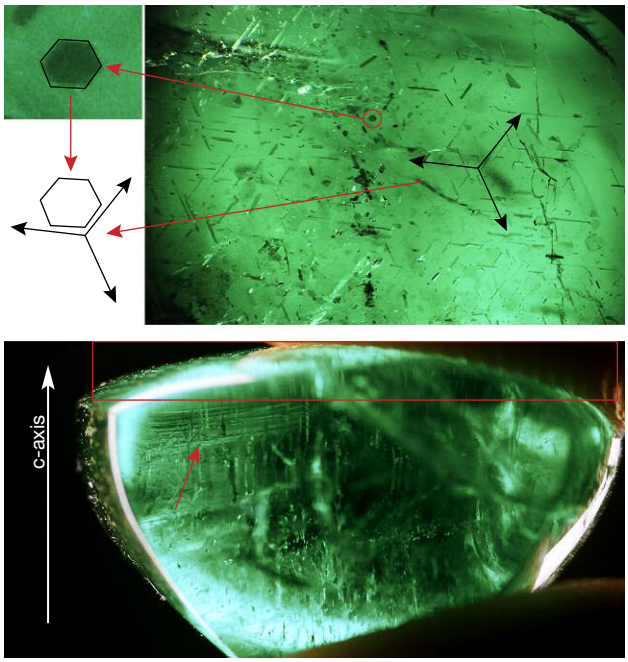

Figure 3. Top: The hexagonal inclusions in the basal plane are parallel to the orientation of the platy inclusion described in figure 2. Field of view 3.1 mm. Bottom: A thin layer exhibiting growth lines is perpendicular to the emerald's c-axis. Photos by Yujie Gao.

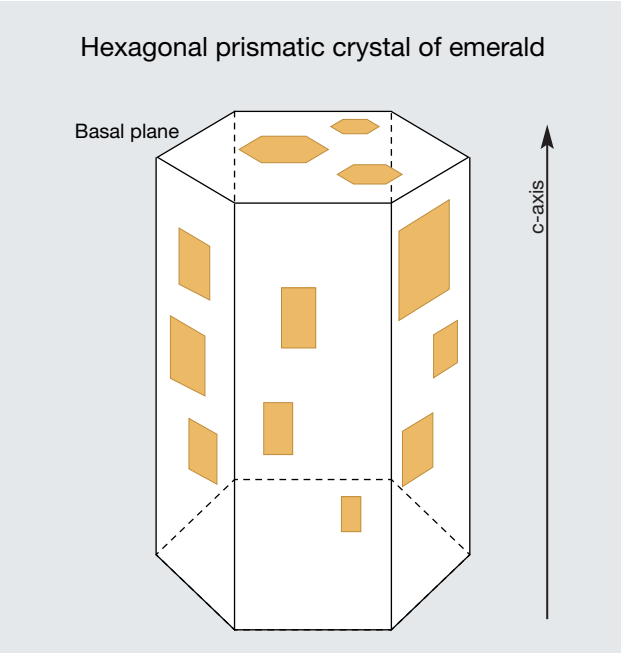

Figure 4. Proposed illustration of hexagonal inclusions in the basal plane and platy inclusions along the prismatic faces. Illustration by Yujie Gao.

the oriented inclusions resulted in the absence of asterism or cat's-eye phenomena.

Considering the optic axis, we concluded that the platy inclusions grew along the hexagonal prismatic emerald faces, with the hexagonal platy inclusion parallel to the basal plane, as illustrated in figure 4. However, it is still unclear whether they were syngenetic or exsolution, since their well-preserved shapes showed little evidence of corrosion and there was insufficient evidence of exsolution.

Yujie Gao (peter.gao@guildgemlab.com) and Kai Li
Guild Gem Laboratories, Shenzhen
Darwin Fortaleché
Guild Gem Laboratories, Hong Kong

DIAMONDS

Nominal type IaB diamond with detectable uncompensated boron. In recent years, nominal type IaAB and IIa diamonds with transient 2800 cm^{-1} FTIR absorption peaks arising from uncompensated boron produced under UV radiation have been reported (J. Li et al., "A diamond with a transient 2804 cm^{-1} absorption peak," *Journal of Gemmology*, Vol. 35, 2016, pp. 248–252; Winter 2016 Lab Notes, pp. 412–413). The National Center of Supervision and Inspection on Quality of Gold and Silver Products recently examined a type IaB diamond that exhibited instantaneous 2803 cm^{-1} FTIR absorption shortly after exposure to an ultra-short-wave (< 230 nm) UV source.

Under ultra-short-wave UV excitation, the 0.30 ct K-L diamond with faint brown color, mounted in an 18K gold prong setting (figure 5), showed strong blue fluorescence and strong greenish blue phosphorescence that lasted for approximately eight seconds (figure 6). Infrared absorption spectroscopy showed low concentrations of the hydrogen-related peak (3107 cm^{-1}) and nitrogen impurities in the B aggregates at 1174 cm^{-1} (figure 7), indicating a type IaB diamond (C.M. Breeding and J.E. Shigley, "The 'type' classi-

Figure 5. This 0.30 ct K-L diamond with faint brown color, mounted in an 18K gold prong setting, is a nominal type IaB diamond with detectable uncompensated boron. Photo by Wenqing Huang.

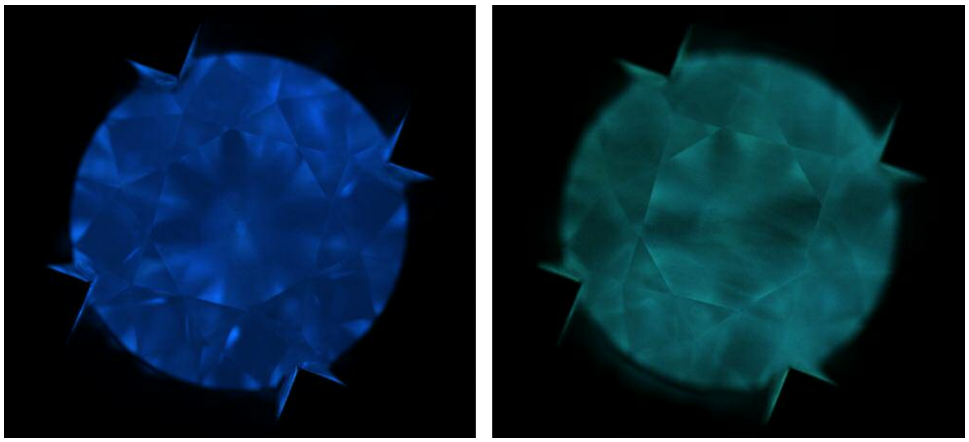

Figure 6. DiamondView imaging shows blue fluorescence (left) and greenish blue phosphorescence (right) in the natural type IaB diamond. Images by Wenqing Huang.

fication system of diamonds and its importance in gemology," Summer 2009 *G&G*, pp. 96–111); prior to ultra-short-wave UV excitation, we were unable to detect the presence of the B center. No boron-related absorption was detected before UV radiation exposure, due to uncompensated B concentrations below the detection level of the FTIR spectrometer. But shortly after ultra-short-wave UV exposure, the transient boron-related absorption peak was recorded at 2803 cm^{-1} (again, see figure 7). Nitrogen-related peaks were detected at 415.7, 428.5, 439.0, and 452.4 nm using photoluminescence (PL) spectroscopy (figure 8); the peak at 415.7 nm belongs to the zero-phonon line (ZPL), while the others belong to its associated phonon replicas (A.M. Zaitsev, *Optical Properties of Diamond: A Data Handbook*, Springer-Verlag, Berlin, 2000). PL and FTIR spectra confirmed the diamond's natural origin.

The generally accepted mechanism for interpreting the phosphorescence in type IIb diamonds is donor-acceptor pair recombination processes involving boron and other defects (P.J. Dean, "Bound excitons and donor-acceptor pairs in natural and synthetic diamond," *Physical Review*, Vol. 139, 1965, pp. A588–A602). Boron is deemed as the acceptor in the model, where the donor is believed to be nitrogen related, either as isolated nitrogen, aggregated nitrogen, or a plastic deformation–related defect (S. Eaton-Magaña and R. Lu, "Phosphorescence of type IIb diamonds," *Diamond and Related Materials*, Vol. 20, 2011, pp. 983–989; E. Gaillou et al., "Boron in natural type IIb blue diamonds: Chemical and spectroscopic measurements," *American Mineralogist*, Vol. 97, 2012, pp. 1–18).

Figure 7. The FTIR spectra reveal low concentrations of the hydrogen peak (3107 cm^{-1}) and nitrogen impurities in the B aggregates (1174 cm^{-1}) (blue line). Shortly after ultra-short-wave (< 230 nm) UV exposure, the transient boron-related absorption was recorded at 2803 cm^{-1} (red line). Spectra have been offset vertically for clarity.

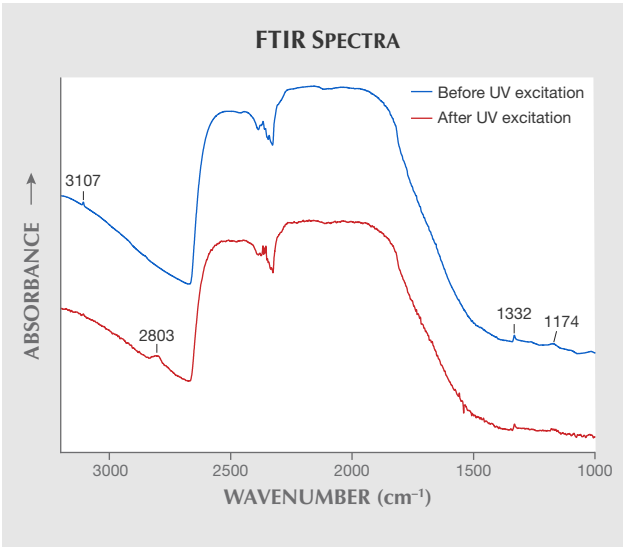

Figure 8. The photoluminescence spectrum of the sample excited at room temperature with a 405 nm laser reveals an N3 center with its zero-phonon line (ZPL) at 415.7 nm and its associated phonon replicas with peaks at 428.5, 439.0, and 452.4 nm.

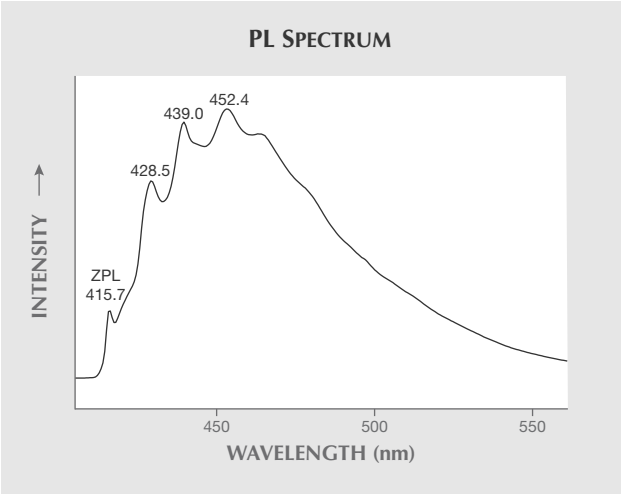

When almost all of the boron impurities received electrons from donors, almost no uncompensated boron (B_0) was left behind, and therefore no boron-related absorption peaks were recorded. When the diamond was exposed to ultra-short-wave UV excitation, some of the compensated boron converted to an uncompensated state due to a charge transfer process between compensated boron and ionized donors, which could be recorded before the phosphorescence decayed. This mechanism is also suitable for interpreting the observed phenomenon of this specimen.

Natural diamonds with long-lasting phosphorescence under UV excitation are typically type IIb or chameleon diamonds (J.M. King et al., "Characterizing natural-color type IIb blue diamonds," Winter 1998 *G&G*, pp. 246–268; T. Hainschwang et al., "A gemological study of a collection of chameleon diamonds," Spring 2005 *G&G*, pp. 20–35). It is rare to find diamonds of other types, especially type IaB diamonds, showing this phenomenon. Finding a detectable, if temporary, B_0 defect in a type IaB diamond is also unusual.

Wenqing Huang, Yijing Liu, and Shujia Dong
National Center of Supervision and Inspection on Quality of Gold and Silver Products
Nanjing, China

Dongjuan Chao
Jiangsu Daocun Industrial Development Co. Ltd.
Nanjing, China

Guizhou Jade from Qinglong, China. A green-blue quartzite produced in the Qinglong antimony deposit, in southwestern Guizhou Province, is called Guizhou Jade in the trade. The source area is located in the middle of the Yunnan-Guizhou Plateau at 25°N latitude, rising 1,600 meters (5,250 ft) above sea level (figure 9). This material was discovered in the 1950s, when the antimony deposit was economically more important to the area. The accompanying blue quartzite was only commercially mined as a decorative material. Later, it was used as a gem material, and it has been popular in Chinese jade markets since about 2011 (figure 10).

In June 2018, the authors went to the source to inspect the antimony deposit and conduct exploration and collection for Guizhou Jade in the mine. The host rocks are mainly pyroclastic (breccia) rocks, breccia clay rocks of the Dachang layer, and bio-limestones of the Maokou Formation. The Dachang layer is the main ore-bearing layer of the antimony deposit, which is a set of pyroclastic and chemical deposits, and subjected to alteration to siliceous and clay rocks (J.C. Cao, "The dyeing mechanism and cause of Guicui," *Acta Mineralogica Sinica*, No. 3, 1983, pp. 183–192).

The authors observed that in the mine, this material has a close relationship with stibnite. It is mostly developed in the interlayer fissures, fracture zones, and areas where brecciation has taken place. The material occurs as blocks and/or veins (figure 11). In the ores, there are calcite- and gypsum-filled cracks and voids. Green or white

Figure 9. Qinglong, the site of the Guizhou Jade deposit, is located in southwestern China.

clay minerals are often found in the micro-cracks or small holes in the gem material.

Guizhou Jade is translucent to opaque, with a refractive index of about 1.54 (spot reading), a specific gravity of 2.62, and a Mohs hardness of 6.5–7. According to the infrared

Figure 10. This Guizhou Jade ornament, typical in the Chinese jade markets, stands about 11 cm high. Photo by Yushan Dai.

Figure 11. Left: In the mine, Guizhou Jade is mostly developed in the interlaminar fissures and closely related to stibnite. Right: Guizhou Jade, which develops between layers of stibnite, is massive and can be seen in some small holes in the surface. Photos by Yushan Dai.

spectrum, the main constituent mineral is quartz, and its infrared spectrum matches the α-quartz standard infrared spectrum, including several obvious absorption peaks at 1172, 1124, 1085, 798, 781, 540, and 478 cm^{-1} (figure 12). Quartzite is generally cryptocrystalline. Its colors range from light green-blue to dark green-blue. The most sought-after color is ocean blue, as shown in figure 10.

UV-Vis-NIR absorption spectra (figure 13) of both samples show an obvious 415 nm absorption band and a strong absorption band at 590–620 nm, located in the blue-green range of visible light. The absorption intensity of the light-colored sample is significantly lower than that of the deep-colored sample. The 415 nm absorption band is caused by $^4A_{2g} \rightarrow {}^4T_{1g}$ transition and $^4A_{2g} \rightarrow {}^4T_{2g}$ transition of Cr^{3+}. The strong absorption band at 590 to 620 nm is caused by charge transfer between $Fe^{2+} \rightarrow Ti^{4+}$ and $^4A_{2g} \rightarrow {}^4T_{2g}$ transition of Cr^{3+} (J. Liu, "The color formation of common green quartz jade," *Ming Ri Feng Shang*, No. 3, 2017, pp. 368–371).

High-quality Guizhou Jade is rich in color and loved by collectors. It has been widely used in necklaces, bracelets, earrings, and other items.

Yushan Dai and Xuemei He
School of Gemmology, China University of Geosciences Beijing

SYNTHETICS AND SIMULANTS

Single HPHT synthetic diamond mixed in natural diamond ring. Recently, a ring with 195 mounted colorless and near-colorless stones (figure 14) was submitted to Dubai Central Laboratory for identification. The ring con-

Figure 12. The infrared spectrum of a Guizhou Jade sample.

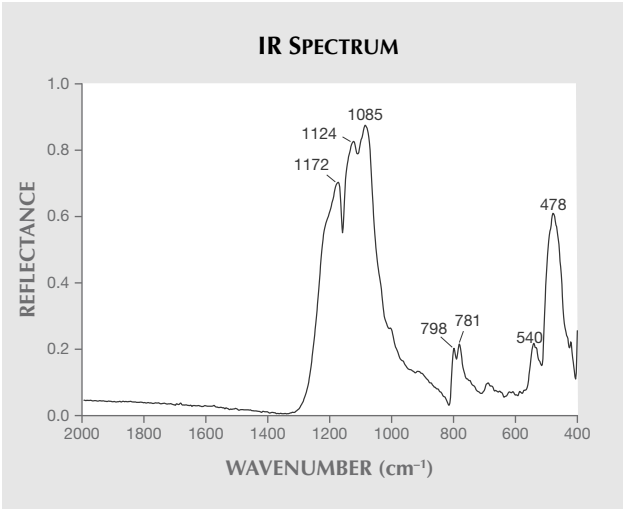

Figure 13. The UV-Vis-NIR spectra of both Guizhou Jades show a 415 nm absorption band and a strong absorption band at 590–620 nm.

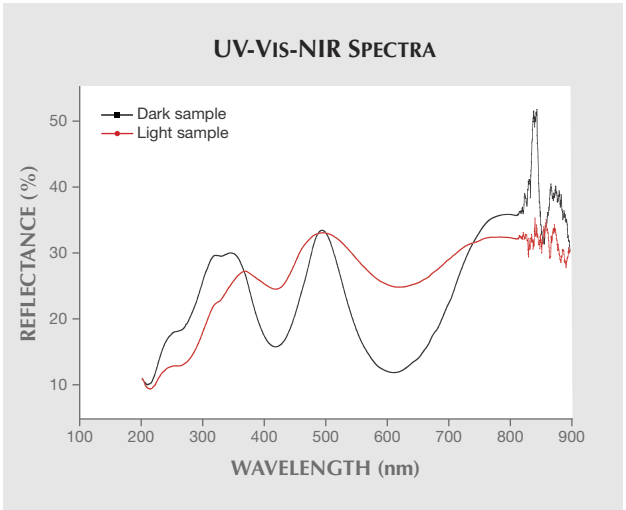

Figure 14. The ring with 194 natural diamonds and one HPHT-grown specimen. Photo by Nazar Ahmed Ambalathveettil.

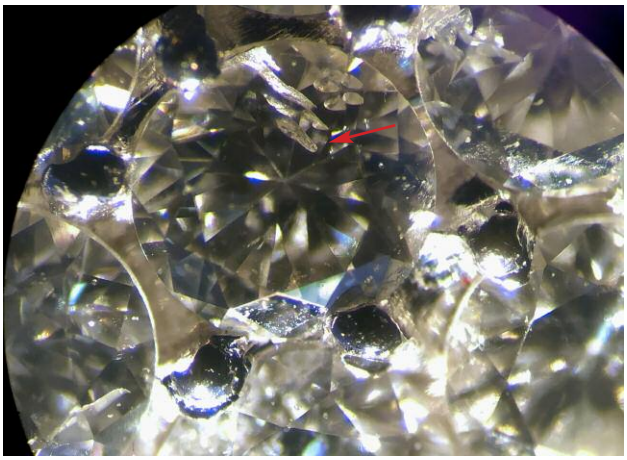

Figure 15. These metallic flux inclusions that are associated with feathers show high reflection in oblique light. Photo by Nazar Ahmed Ambalathveettil.

tained round-brilliant-cut diamond melee arranged in rows. Testing with the DiamondSure instrument identified 194 of them as natural diamond, and the remaining melee was referred for further testing.

The sample's setting in the ring restricted us to FTIR spectroscopy in reflection mode to determine its identity. Solid metallic inclusions were revealed under the microscope (figure 15). The specimen displayed strong yellow and moderate greenish yellow fluorescence under long-wave UV and short-wave UV, respectively (figure 16). The inclusions and fluorescence suggested HPHT-grown diamond, which generally shows a stronger fluorescence reaction to short-wave UV than to long-wave UV. The vast majority of HPHT synthetics in the "colorless" range exhibit no detectable fluorescence to long-wave UV (S. Eaton-Magaña et al., "Observations on HPHT-grown synthetic diamonds: A review," Fall 2017 *G&G*, pp. 262–284), but this one showed strong fluorescence under long-wave UV.

The stone was further examined with DiamondView imaging and photoluminescence (PL) spectroscopy. Strong yellowish green fluorescence and blue phosphorescence were observed with the DiamondView, but the growth sector pattern typical of HPHT-grown diamond was not visible because of the stone's size. PL spectroscopy showed nickel-related peaks at 882/884 nm. Based on these results, we concluded that this was an HPHT laboratory-grown diamond.

We later learned that the customer had given the ring to a jewelry repair shop to replace a broken diamond, which may account for the single lab-grown specimen. This is a good example of the need for vigilance in every stage of diamond jewelry making.

Nazar Ahmed Ambalathveettil (nanezar@dm.gov.ae), Nahla Al Muhari, and Sutas Singbamroong
Gemstone Unit, Dubai Central Laboratory
United Arab Emirates

Figure 16. The laboratory-grown diamond fluoresced yellow under long-wave UV (left) and greenish yellow under short-wave UV light (right). Photos by Nazar Ahmed Ambalathveettil.

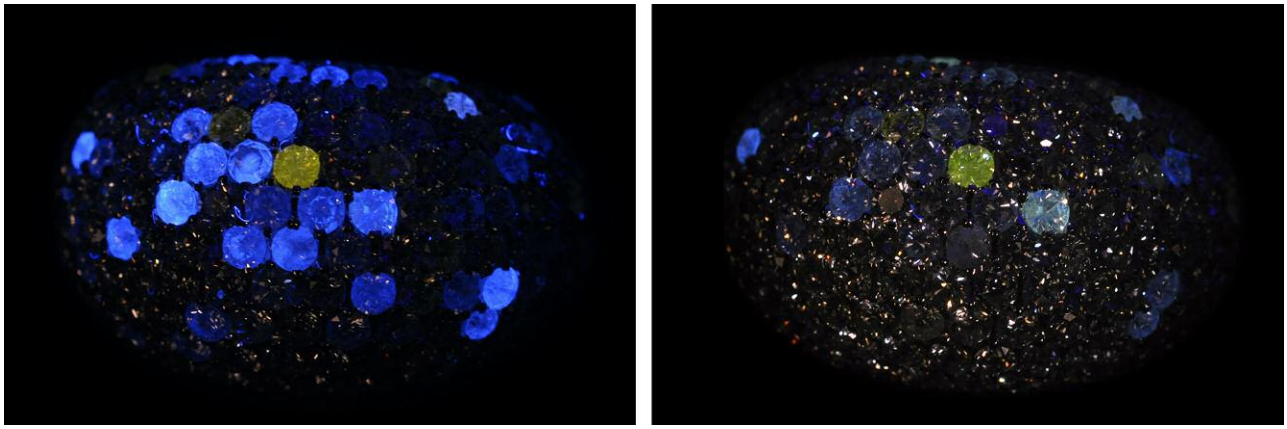

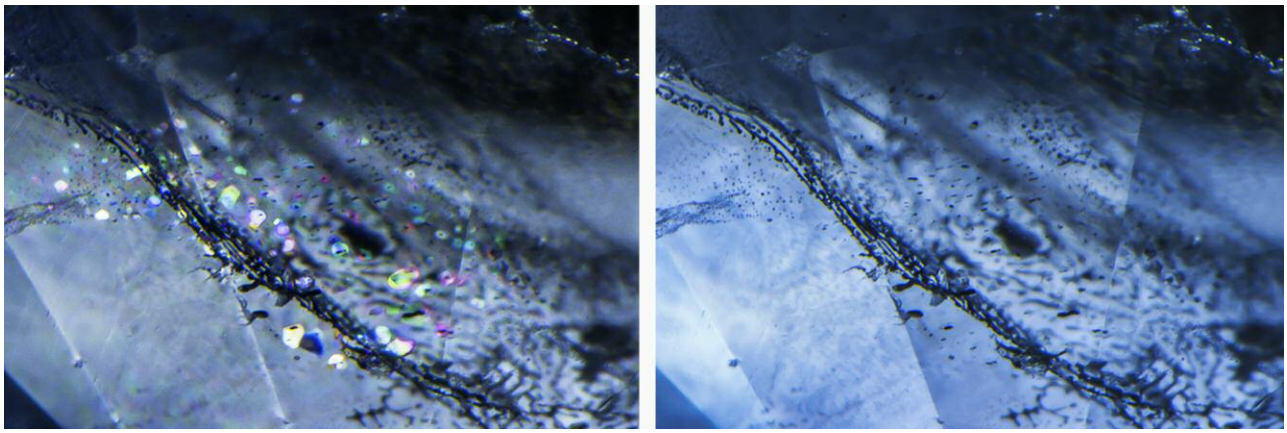

Figure 17. This sapphire that was treated with heat and pressure contained small birefringent crystals (left) that were nearly invisible with unpolarized light, as seen in the brightfield image (right). Photomicrographs by Nathan Renfro; field of view 1.81 mm.

TREATMENTS

Microscopic observations of blue sapphires treated with heat and pressure. In recent months, sapphires treated under heat and pressure have been documented in the trade. This material is reported to be treated under pressure of 1 kbar at temperatures between 1200 and 1800°C by HB Laboratory Co. Ltd. of Korea (H. Choi et al., "Sri Lankan sapphire enhanced by heat with pressure," *The Journal of the Gemmological Association of Hong Kong*, Vol. 39, 2018, pp. 16–25). This process is used to improve blue coloration and potentially heal any fractures within the stones.

GIA acquired from Sri Lankan gem dealer Imam Faris of Imam Gems (Pvt) Ltd. six samples that were said to have been treated under the conditions mentioned above. The samples were examined using a standard gemological microscope to look for any unusual features resulting from this type of treatment. Five of the six sapphires showed a feature that to our knowledge has not been reported before. Viewed in polarized light (figure 17, left), planes of small crystallites were observed as bright spots against a dark background when the host corundum was in the extinct position. But under unpolarized light (figure 17, right), the crystallites were either invisible or nearly so, and only visible from a low-relief interface between the crystallite and the host corundum. Due to the extremely low relief of these inclusions, the author speculates that these inclusions are corundum crystals that originated from fractures and were healed by recrystallization of the corundum. While it is certainly possible to have birefringent crystals of corundum in untreated corundum, the consistent observation of the planes of birefringent crystals by the author suggests that this feature could be a useful indicator for corundum treated with heat and pressure. These preliminary observations offer some interesting clues, but further research will be needed to fully characterize corundum treated with this technique.

Nathan Renfro
GIA, Carlsbad

Emeralds filled with epoxy resin: DiamondView observations. Emeralds from all sources routinely contain surface-reaching fissures, and as a result are subjected to clarity enhancement processes (oiling or resin filling) to improve their appearance. The quantity and variety of emerald-filling substances undoubtedly affects the final market value (M.L. Johnson et al., "On the identification of various emerald filling substances," Summer 1999 *G&G*, pp. 82–107). Recently, the Lai Tai-An Gem Lab received a stone—reported as an emerald by the client—for identification services, with a request to focus on the degree of clarity enhancement. DiamondView imaging allowed us to visually explain the degree of filling in a way the client was quickly able to understand.

The transparent emerald-cut stone weighed 16.15 ct and measured 16.80 × 14.07 × 9.48 mm. It exhibited a light to medium green saturation and contained white hazy inclusions that were visible to the eye (figure 18). Standard

Figure 18. This 16.15 ct emerald was filled with epoxy resin. Photo by Lai Tai-An Gem Lab.

gemological testing revealed an RI of 1.570–1.575, an SG of approximately 2.66, and a weak yellowish green reaction under long-wave ultraviolet radiation. Magnification with a gemological microscope revealed fluid and three-phase inclusions typical of natural emeralds. When turning the specimen, "blue flashes" characteristic of resin-filled material were seen within many of the fissures (figure 19). These results confirmed that the stone was a natural, clarity-enhanced emerald. Infrared spectrometry was subsequently performed to analyze the filling in more detail. Epoxy resin peaks at 3061, 3040, 2965, 2930, and 2870 cm^{-1} (figure 20) confirmed the epoxy resin treatment of the stone, as indicated by the initial microscopy.

Although it may not be difficult for experienced gemologists to identify various emerald-filling substances using high-end equipment like Fourier-transform infrared (FTIR) or Raman spectroscopy, we wanted to check on the suitability of another tool to assist in identifying fillers and to help see the extent and degree of filling applied. We turned to the DiamondView and obtained some interesting images for this clarity-enhanced emerald.

The stone's surface was first observed in different directions under the DiamondView's visible light source until obvious surface-reaching fissures appeared. Subsequent exposure to the unit's ultra-short energy UV light clearly revealed the epoxy resin filler within the fissures as a series of blue lines extending over the entire surface against the beryl's orange-fluorescing bodycolor. The more severe (quantity in relation to width and depth) the treated fissures were, the stronger the blue reaction (figure 21). The results of this simple test show how the DiamondView may be applied. Although the DiamondView cannot precisely identify the fillers, it does provide a means of detection that can be applied to a variety of gems. The option of ultra-short-wave radiation should be considered, as there may be concerns about the color and structural durability of host and fillers that have not been fully taken into account.

Figure 19. When viewed through a gemological microscope, "blue flashes" characteristic of resin-filled emeralds are clearly visible. Photo by Lai Tai-An Gem Lab; field of view 8.8 mm.

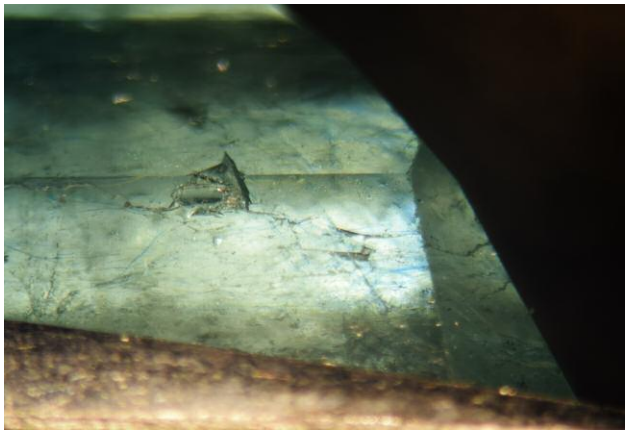

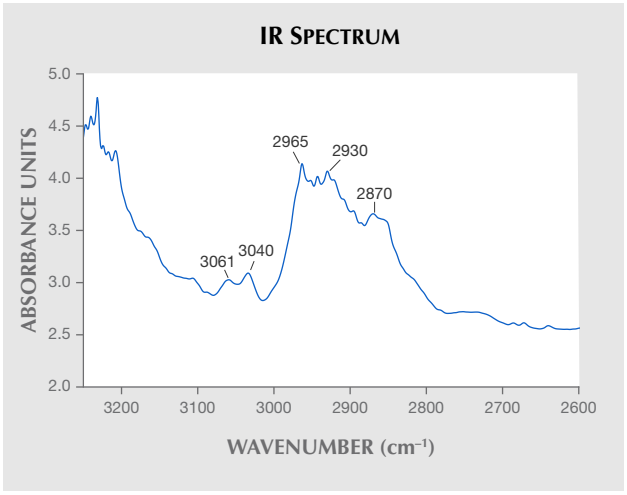

Figure 20. Characteristic epoxy resin peaks were detected at 3061, 3040, 2965, 2930, and 2870 cm^{-1} with FTIR spectrometry.

Larry Tai-An Lai (service@laitaian.com.tw)
Lai Tai-An Gem Laboratory, Taipei

Coated pink synthetic moissanite. The French Gemmological Laboratory (LFG) recently received a 0.41 ct pink stone resembling a pink diamond (figure 22) for identification. The surface of the stone showed numerous patches (figure 23), casting doubts about the natural origin of its color.

Figure 21. Surface-reaching fissures with greater concentrations reveal a stronger blue reaction when observed in different directions under the DiamondView's visible light (left) and when exposed to the unit's ultra-short-wave UV energy (right).

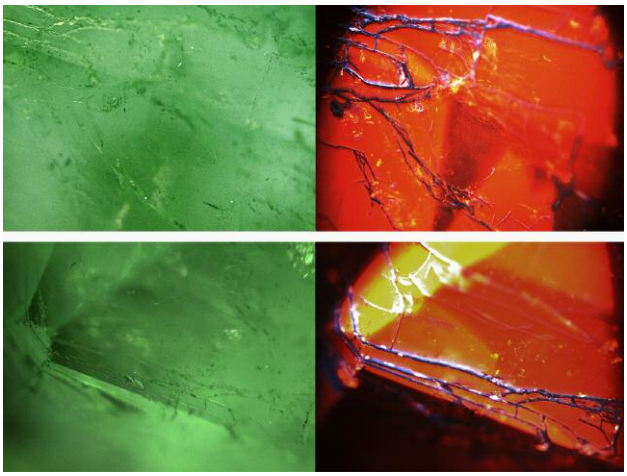

Figure 22. This 0.41 ct pink stone was revealed to be a coated synthetic moissanite. Photo by Aurélien Delaunay.

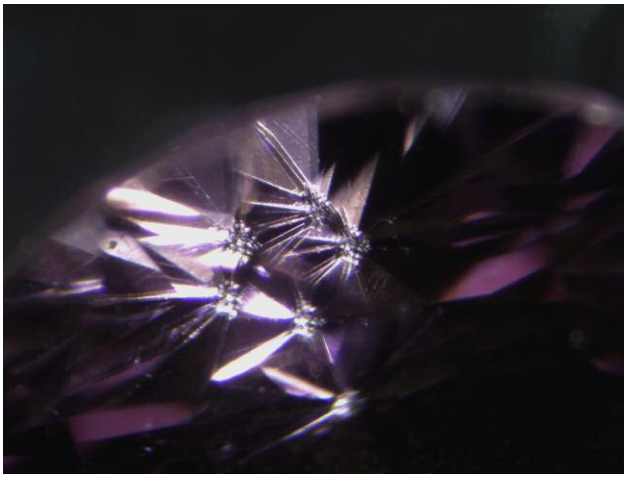

Figure 24. Doubling of the edges, observed near the crown in this synthetic moissanite. Photomicrograph by Aurélien Delaunay; field of view approximately 3.4 mm.

Under the microscope, these flakes showed metallic luster. Furthermore, the pink color appeared concentrated at the surface. Some unevenness in the color was observed due to scratches of this film. When observed through the crown, the gem showed a clear doubling of its edges, indicating an anisotropic material. These observations confirmed the client's doubts that the gem was a pink diamond (figure 24).

The sample was analyzed using infrared, UV-visible, and Raman spectrometers. All the spectra collected indicated a synthetic moissanite coated with a colored film. Chemical study of this film acquired with an EDXRF spectrometer revealed that iron and titanium were responsible for the color of the calcium-rich film.

This is the first example the LFG has seen of synthetic moissanite coated with a thin colored film. This type of treatment is not rare with topaz, quartz, diamond, or tanzanite. Gemologists must remain vigilant because this treatment can be performed on all gems, natural or synthetic.

Aurélien Delaunay
Laboratoire Français de Gemmologie (LFG)
Paris

Figure 23. Metallic flakes on the surface raised questions about the origin of the pink color. Photomicrograph by Aurélien Delaunay; field of view approximately 1.8 mm.

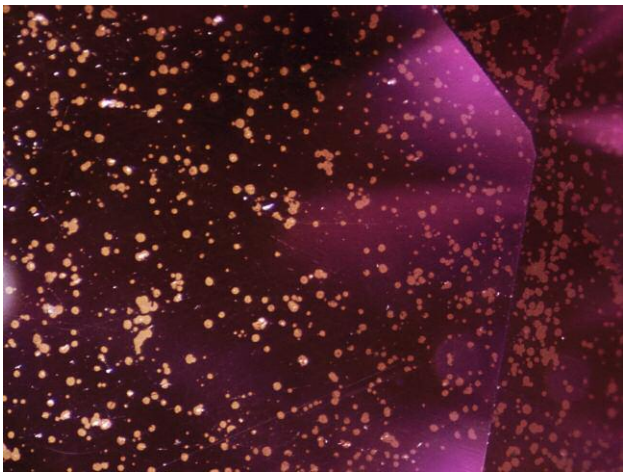

Synthetic moissanite coated with diamond film imitating rough diamond. A transparent yellowish octahedral (sawable) crystal (figure 25) weighing 5.35 ct was submitted as a rough diamond to the Far East Geological Institute (FEGI) for examination.

The faces of the octahedron showed a stepped appearance, and the edges had parallel grooves and combinational surfaces. The faces and edges were smooth except for one face where mechanical damage was noticeable. Initially, the specimen was examined using conventional gemological instruments. It was inert to long-wave UV (365 nm) and anisotropic. Thermal conductivity testing indicated diamond. Tests for electrical conductivity were not convincing, however: Some areas (mostly on the edges) corresponded to diamond, but others (on smooth faces and dimples) indicated synthetic moissanite. There were no inclusions associated with natural diamond. Only small parallel needle-like inclusions, typical for synthetic moissanite, were found using a gemological microscope (figure 26).

Figure 25. This 5.35 ct sample, submitted as a rough diamond, was identified as synthetic moissanite coated with a diamond film. Photo by V. Pakhomova.

Figure 26. Needle-like inclusions in the rough synthetic moissanite sample. Photo by V. Pakhomova.

X-ray tomography showed that the inner part of the sample was distinguished by its X-ray density from the outer shell, which had a variable thickness from 19 to 115 microns (figure 27). Microprobe analysis with a JEOL JXA-8100 four-channel microanalyzer revealed the presence of up to 61 wt.% silicon on some polished faces of the crystal, along with titanium in the composition of the surface layer (figure 28 and table 1). Some polished faces showed a diamond chemical signature.

Figure 27. Three-dimensional X-ray tomography rendering of the reconstructed sample. The coloring of the image corresponds to the degree of X-ray permeability. The green color represents the SiC crystal, and the blue color represents the film.

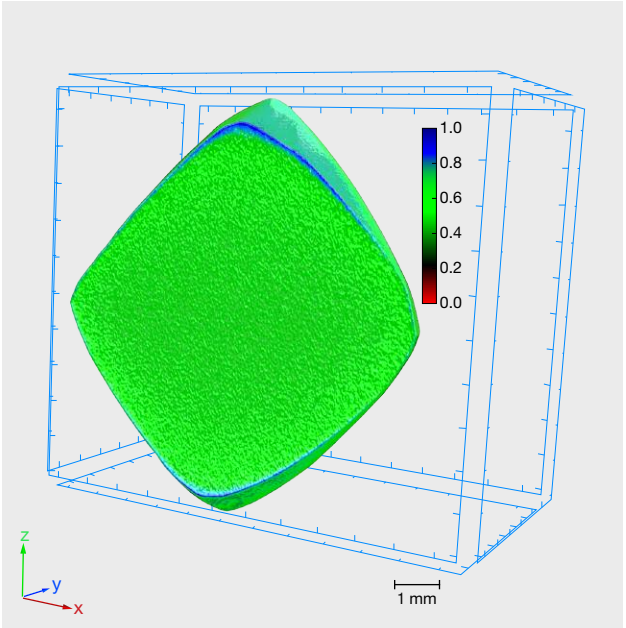

Based on these results, we identified the sample as synthetic moissanite that had been covered with a thin diamond film. Based on the study by T. Teraji et al. ("Chemical vapor deposition of ^{12}C isotopically enriched polycrystalline diamond," *Japanese Journal of Applied Physics*, No. 51, 090104, 2012, pp. 1–7), the diamond coating was likely applied using polycrystalline diamonds. The top layer was made of a composite material consisting of metal matrix and nano-diamond particles.

A diamond imitation such as synthetic moissanite coated with a thin diamond film is challenging to identify, since its luster and thermal properties correspond to diamond. Even with a very thin coating that did not exceed 0.001 mm, the sample tested positive for diamond. This

TABLE 1. Electron microprobe analysis of some parts of the surface of the "diamond" crystal.

Spectrum	C	O	Al	Si	Ti	Total
1	37.52	1.61	0.12	60.76	0	100
2	46.93	4.96	0.13	47.82	0.16	100
3	37.88	0.59	0.10	61.28	0.15	100
4	8.84	0	0.47	11.90	78.79	100
5	40.74	0	0.07	59.18	0	100
6	41.18	1.25	0.08	57.46	0.04	100

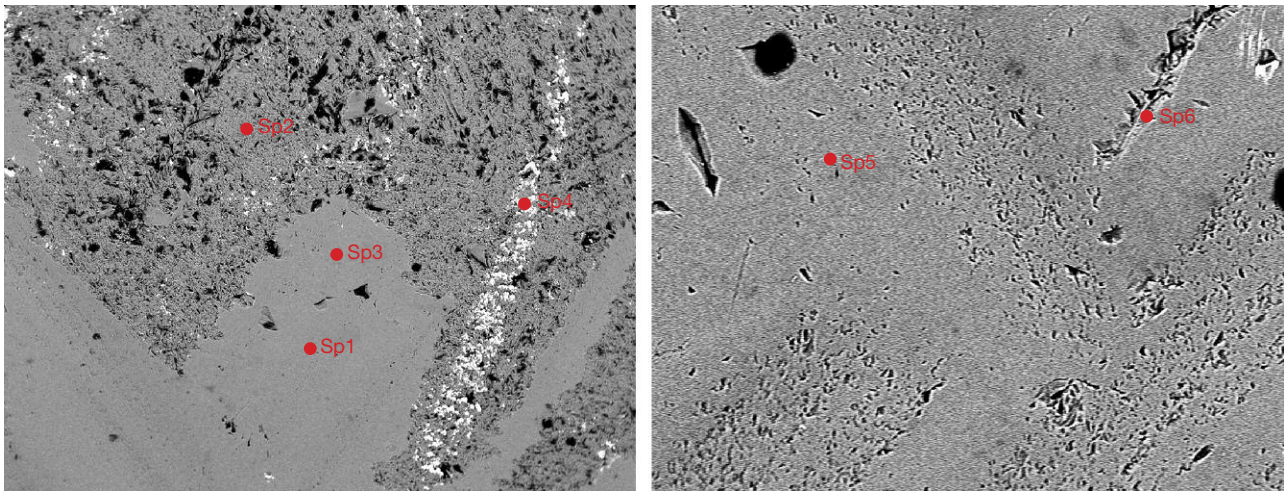

Figure 28. A fragment of the synthetic moissanite crystal, viewed with the electron probe microanalyzer. The crystal was analyzed on the surface. Spectrum numbers correspond to the analysis numbers in table 1.

application of thin diamond films onto non-diamond material could be an issue for gemologists in the future.

This work was supported by the Russian Foundation for Basic Research (grant N 16-05-00283) and the Far Eastern Branch of the Russian Academy of Sciences (N 15-1-2-003).

Vera A. Pakhomova, Dmitrii G. Fedoseev, Svetlana Y. Kultenko, Alexander A. Karabtsov, Vitaliia B. Tishkina, and Valentina A. Solyanik
Far East Geological Institute (FEGI FEB RAS), Vladivostok

Vladimir A. Kamynin
Gokhran of Russia, Moscow

CONFERENCE REPORTS

GSA 2018 report. The Geological Society of America (GSA) annual meeting took place in Indianapolis November 4–7. GIA participated as both exhibitor and technical session holder. In total, 21 presenters reported new findings on a broad range of research topics. The GIA booth and the two technical sessions attracted a large audience with an interest in gemology (figure 29).

The "Gemological Research in the 21st Century" technical program included both poster and speaker sessions. Seven posters were presented on the second day of the conference (figure 30). **Kyle Tollefson** (Louisiana State University) and **Phillip Ihinger** (University of Wisconsin-Eau Claire) reported their characterization study on watermelon tourmaline. Their spectroscopic measurements showed that the chromophores Fe and Mn correlate to green and pink colorations, as expected. The infrared spectroscopy and microprobe analyses showed similar trends of hydroxyl occupancy on the V site in this type of tourmaline. **Nikita Kepezhinskas** (University of Florida) presented the results of petrographic, geochemical, and isotopic analyses of moissanite and diamond from the shoshonite dike in eastern Finnmark, Norway. The shoshonite host of these minerals is a type of Mg- and K-rich basaltic rock, which is indicative of a subduction-modified mantle source. This study proved that carbonate recycling into the lower mantle through subduction, followed by the formation of superdeep diamonds, moissanite, and other carbides, plays an important role in the global carbon cycle. **Paul Johnson** and **Kyaw Soe Moe** (GIA, New York) showed an unusual find of a natural diamond with a cuboctahedral growth habit. This diamond should alert gem labs to the fact that cuboctahedral growth does not occur just in HPHT synthetic diamonds. This special diamond also indicated a potentially very interesting and uncommon growth history before it was lifted to the surface of the earth. **Richard Berg** (Montana Bureau of Mines and Geology) described significant magmatic splitting of sapphire xenocrysts in basaltic trachyandesite sill. Through extremely careful examination of *in situ* sapphires in their host rock and advanced instrument analyses such as SEM, XRD, and EDS, he was able to assemble a sequence of what happened to the sapphires before emplacement into their current location. **Ying Song** (China University of Petroleum) introduced a newly designed and developed computer-vision based intelligent RI measuring system. This system aimed to enhance the clarity and efficiency of RI and other optical measurements. Classroom demonstration, rapid crystal identification, optic axis characterization, and crystal orientation determination are the four modes currently implemented in this instrument. **Ziyin Sun** and coauthors (GIA, Carlsbad) displayed their study on chromophore strength in pyralspite garnet. Since multiple color-causing elements work singularly or together to color garnets, the authors isolated each of them and performed quantitative study by experimenting with various combinations of these chromophores' UV-Vis-NIR

Figure 29. Each year, the GIA booth at the GSA exhibition hall attracts participants from all over the world. Here, Paula Rucinski (left) and Dona Dirlam (right) speak with a visitor to the booth. Photo by Cathy Jonathan.

spectra under different lighting conditions. **Aaron Palke** and coauthors (GIA, Carlsbad) reported on a Montana sapphire study aiming to unravel its gemological mysteries. Based on their inclusion and geochemical study, the authors proposed a new model of sapphire formation through peritectic melting reactions during partial melting of an Al-rich protolith.

This year's speaker session attracted 14 presenters from multiple research institutes and universities (figure 31). **Mike Breeding** (GIA, Carlsbad) kicked off the session with an overview of colored diamonds formed at different depths within the earth. He elaborated on the defects that cause diamond's blue, pink, yellow, brown, and green colors. The audience was given a grand tour of colored diamond formation, from the transition zone all the way to the surface of the earth. Next, **Sally Eaton-Magaña** (GIA, Carlsbad) presented her photoluminescence study on pink diamonds based on GIA's uniquely large database. She explained the cause of pink color as a 550 nm absorption band and explored the difference of pink coloration in various diamond types. She also showed some visual clues that can help to separate pink diamonds from different sources. **Tyler Sundell** (Missouri State University) talked about the feasibility of using time-of-flight secondary ion mass spectrometry (ToF-SIMS) to image diamonds, especially on their trace-element composition and isotope analyses. Evaluation of this method focuses on its spatial resolution and analytical precision. Results show that this method lacks the precision to quantify carbon isotope values. **Karen Smit** (GIA, New York) presented her research on natural black diamonds found in the billion-year-old Marange conglomerate (Zimbabwe). Diamonds from this source are full of fractures and can be easily treated to achieve a more valuable fancy black color grade, which makes identification challenging with-

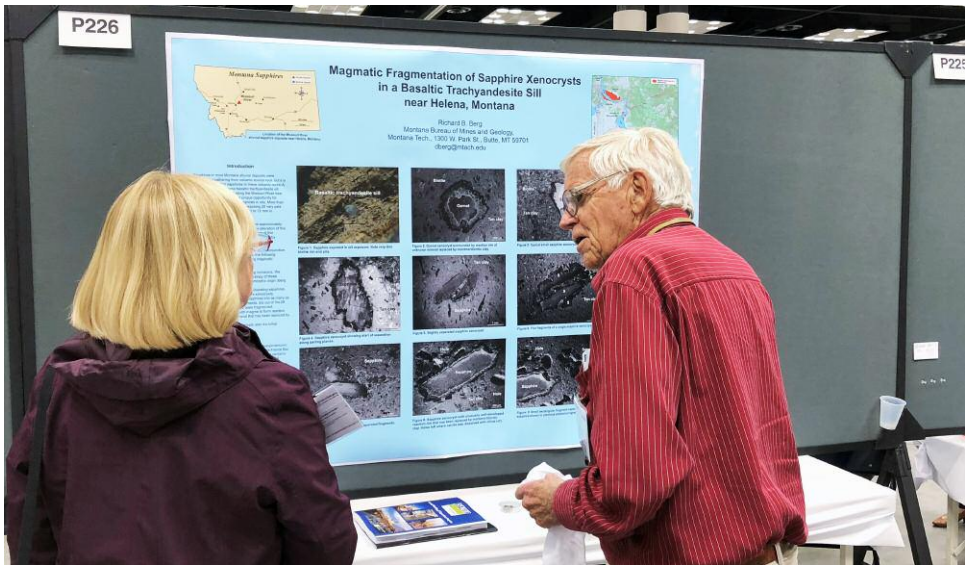

Figure 30. Richard Berg from the Montana Bureau of Mines and Geology presented his poster on Montana sapphires at the GSA annual meeting. Photo by Tao Hsu.

out characterization of the natural stones. Visual observation of graphite grain size and the detection of methane associated with the micro-inclusions are necessary to distinguish between natural and treated Marange diamonds. **Evan Smith** (GIA, New York) delivered his research on carbonatitic melt inclusions he discovered in partially healed cracks within a CLIPPIR diamond (for more on these diamonds, see Winter 2017 *G&G*, pp. 388–403). The characterization of these inclusions is consistent with carbonatitic melt, providing direct evidence of this melt's existence at mantle depths. **Russell Harmon** (North Carolina State University) evaluated the potential of handheld laser-induced breakdown spectroscopy (LIBS) to identify garnets associated with kimberlites, the host rock of most diamond deposits. This study aims to test whether this instrument will help diamond exploration in the field. Initial results showed that it works very well on garnets from the South Africa kimberlite field but not as well on some other samples, especially those from extensive solid solution. **Rod Smith** (Geological Survey of Canada) presented field and lab research on the Banks Island region in the western Canadian Arctic, aiming to find promising diamond-bearing kimberlite. Based on newly found stream sediments and till samples, geothermometry data, and Lu-Hf geochronology results, the research group demonstrated the need to continue the search for potential diamond-bearing kimberlite in this region and presented a potentially unknown kimberlite glacial dispersal model. **Tingting Gu** (GIA, New York) talked about inclusion studies on type IaB diamonds. This study offered the first piece of evidence that hydrous phosphate can subduct to the depth of the transition zone. It also showed the first ringwoodite found in diamond, which proved that this diamond formed in the deep mantle.

The second half of the speaker session started with **Mandy Krebs** (GIA, New York), who showed the application of Sr-Pb isotope data to colored gemstones' country-of-origin determination. The analyses were done by thermal ionization mass spectrometry (TIMS) to precisely measure the Sr-Pb isotope compositions in gem corundum for the first time. The separation is promising for certain sources but less so for others. **Rachelle Turnier** (University of Wisconsin-Madison) used Raman spectroscopy to evaluate the depth of zircon inclusion formation. These zircons are inclusions in corundum sourced from different deposits. Her study is based on an ideal linear upshift of Raman band of zircon with increasing pressure. However, many other factors can influence this ideal situation, such as radiation damage, stress, and internal heterogeneity. With careful consideration of these influencing factors, using Raman as a zircon barometer can help to distinguish corundum from various sources. **William Nachlas** (Syracuse University) presented the three different formation mechanisms for rutilated quartz. These include the overgrowth/entrapment mechanism, the precipitation mechanism, and the grain boundary migration mechanism, each with different relative timing of quartz and rutile growth. All three mechanisms were reproduced with well-designed experiments. **Peter Heaney** (Penn State University) explored the reason behind the striking iridescence displayed by some ochre-colored botryoidal goethite. Dr. Heaney applied focused ion beam (FIB) milling and scanning electron microscopy (SEM) to zoom in on the internal structure of this gem. With these powerful tools, some subsurface void layers were revealed to be responsible for the angle-independent iridescence. The origin of these voids remains a mystery. **Barbara Dutrow** (Louisiana State University) reported a geochemistry study on some uncommon tourmaline + corundum–bearing rocks from Afghanistan's Badakhshan Province with randomly oriented phlogopites as the matrix. Major, minor, and trace elements were measured with electron microprobe and laser ablation–inductively coupled plasma–mass spectrometry (LA-ICP-MS). The results indicate the involvement of boron-bearing fluids at the beginning of tourmaline growth and continuous infiltration of this fluid. The bulk composition of this rock is consistent with metasomatism of a clay-containing metacarbonate rock with a metamorphic overprint. **Chunhui Zhou** (GIA, New York) gave the first-ever pearl presentation in this technical session. Three American freshwater cultured pearls were sliced open and their oxygen isotopes were analyzed using SIMS, aiming to reconstruct the ambient water temperature when the nacre formed. This method is very useful in terms of growth cycle determination and can potentially shine a light on pearl origin determination.

Tao Hsu
GIA, Carlsbad

Meeting of the International Mineralogical Association. The 22nd meeting of the International Mineralogical Association (IMA), the first held in Australia and only the second in the Southern Hemisphere, took place in the Melbourne Convention and Exhibition Centre August 13–17, 2018. The meeting was hosted by the Geological Society of Australia.

Two technical sessions on gems were presented to about 100 attendees. The August 13 session, "Sciences Behind Gemstone Treatments," was chaired by **Andy Shen** (China University of Geosciences, Wuhan) and **Pornsawat Wathanakul** (Gem and Jewelry Institute of Thailand). The second day's session, titled "Recent Advances in Our Understanding of Gem Minerals" and led by **Ian Graham** (University of New South Wales, Australia), **Lee Groat** (University of British Columbia, Canada), and **Gaston Giuliani** (University of Lorraine, France), is detailed below.

The session consisted of 18 oral presentations covering several gem topics. **Frederick Sutherland** (Australian Museum, Sydney) opened with a keynote talk on the diversity in the geochemistry and inclusions of ruby from Myanmar and eastern Australia. He also discussed the ages of ruby formation through zircon ages and the *P-T* conditions through inclusion assemblages.

The other talks concerned different types of gems from supergene minerals up to corundum and spinel, including mining discoveries and activities from ancient and modern

Figure 31. Presenters, guests, and advocates from the GSA poster and speaker sessions. Left to right: Peter Heaney, Dona Dirlam, Mandy Krebs, Richard Berg, Mike Breeding, Jim Shigley, Tingting Gu, Tyler Sundell, Rachelle Turnier, Nancy McMillan, Evan Smith, Chunhui Zhou, Barbara Dutrow, and Sally Eaton-Magaña. Photo by Tao Hsu.

ages. **Ruslan Kostov** (Sofia University of Mining and Geology, Bulgaria) presented the archeological mineralogy of the Balkans through prehistoric (7 to 5 million BCE) gem minerals (nephrite, jadeite, talc, gabbros, jasper, and turquoise) and gold. **Lee Groat** revealed recent advances in colored gemstones in Canada, focusing on emerald from Yukon and blue spinel, sapphire, and scapolite from Baffin Island, as well as the use of different techniques such as drones for exploration. **Peter Lyckberg** (Luxembourg) offered a detailed state-of-the art presentation on the mining of gem pegmatites in Afghanistan and Pakistan, with amazing photos of aquamarine, kunzite, indicolite, and spessartine crystals from deposits in the High Karakoram range. **Wim Vertriest** (GIA, Bangkok) discussed the dynamics of gemstone discoveries and the challenges for research on the basis of timing the life of a deposit and the market perception of the gems' quality.

Different techniques for source determination of gems were also presented. **Hao Wang** (SSEF, Basel, Switzerland) related the advances in origin determination for gems using inductively coupled plasma time-of-flight (ICP-TOF) spectroscopy, with applications for blue sapphires and emeralds. **Zhiqing Zhang** (China University of Geosciences, Wuhan) used Fourier-transform infrared (FTIR) characteristics of amber from different areas of the world for origin determination. **Allan Pring** (Flinders University, Adelaide, Australia) related the use of multiple techniques on 200 opal samples of various origins, showing their similarities and differences. **Kemela Wijayanti** (Padjadjaran University, Indonesia) combined petrographic analysis with scanning electron microscopy (SEM) and X-ray fluorescence (XRF) techniques to characterize green jasper from southern Java. **Peter Downes** (Western Australian Museum, Perth) applied multiple techniques on variscite and associated phosphate minerals from the Mt. Deverell deposits in the Gascoyne region of Western Australia. **Isabella Pignatelli** (University of Lorraine) reported on the use of electron microprobe analysis, SEM, and X-ray tomographic images for characterizing trapiche ruby from Luc Yen in northern Vietnam.

New studies combining fieldwork with mineralogy and geochemistry were presented for several types of gems. **Philippe Belley** (University of British Columbia) discussed advances in trace-element fingerprinting for blue spinel and new insights into the origin of cobalt-blue spinel from Baffin Island in Canada. **This author** gave an update on gem demantoid garnet from Madagascar's Antetezambato deposit, based on new field data, and geochemical analysis of the most important demantoid deposits worldwide. **Simon Pecover** (Pan Gem Resources) coupled tectonic, hydrodynamic, rheologic, and shear-induced crystallization processes in the formation of opal veins in Australia, showing that the genetic model for the formation of Australian opal is more complex than previously known. **Ahmadjan**

Abduriyim (Tokyo Gem Science) used the U/Pb method on zircon inclusions for determining the formation ages of sapphires from the New England fields in New South Wales. **Kandy Wang** (University of New South Wales) presented data obtained on ruby from Paranesti, Greece, specifying the geographic typing of ruby via oxygen isotopes and trace elements. **Nick Raffan**, also of the University of New South Wales, combined fieldwork with remote sensing, petrographic analysis, and SEM to decipher the source of sapphires near tertiary volcanic plugs and Devonian conglomerates from Tomahawk Creek in central Queensland. **Ian Graham** related the presence of unusual alluvial sapphires from Orosmayo in Argentina using a multi-analytical approach to uncover their origin.

This session was followed by an evening meeting at the Gemmological Association of Australia (GAA) House in Melbourne, under the direction of **Margaret Blood**, president of the GAA's Victorian Division, and organized by **Andy Shen** and **Pornsawat Wathanakul**. The meeting was open to all researchers who participated in the two gem sessions of IMA and to Australian gemologists. The meeting consisted of three hour-long talks by **this author** on Colombian emeralds, **Lee Groat** on spinel and sapphire from Baffin Island, and **Brendan Laurs** (*Journal of Gemmology*) on pegmatites of Namibia.

Gaston Giuliani
University of Lorraine, France

Chicago Responsible Jewelry Conference. Held October 21 and 22 at Cinema Row, the Chicago Responsible Jewelry Conference drew 200 attendees who heard industry experts discuss safe, sustainable, ethical gem production and jewelry design.

Friday's session opened with a keynote address by **Mark Hanna** (Richline Group). "Our vision is the creation and maintenance of a *responsible*, worldwide supply chain that promotes trust in the global fine jewelry industry," Hanna announced. He discussed the ways blockchain technology is allowing for greater mine-to-market transparency. While there are communication and efficiency issues, as the various blockchains do not yet interact, open-source tracking does seem to be the wave of the future. Following Hanna's presentation, **Rolberto Alvarez** of Colombia's Mina Gualconda reported on the gold mine's transformation from a manual operation with mercury extraction (1974–2001) to an environmentally conscious, Fairmined-branded enterprise, supporting 12 families and using zero mercury.

Eric Braunwart (Columbia Gem House) moderated the first of several panels held during the conference. A group of gem cutters, representing four continents, discussed locale-based challenges that included the costs of replacing broken equipment, a lack of cutting knowledge and experience among locals, and recent restrictions on exporting rough from countries such as Tanzania. Panelists observed that clients also want corporate social responsibility (CSR) efforts to extend to cutters and reiterated what has been said at similar gatherings: The art of cutting involves more than just faceting a stone. Often cutters say the stones "speak" to them, telling them where to begin and end. The storytelling that has become part of the jewelry industry's outreach to customers should include tales of the cut as well.

Day one ended with the work of sustainability consultants The Dragonfly Initiative (TDI), which has developed the Coloured Gemstone Working Group (CGWG) to support the communities impacted by the colored gems sector. TDI's **Sarah Caven** posed the question: "Things are not perfect, and we can maybe never get perfection, but what can we do to improve transparency and do a better job in the supply chains?" She explained that the CGWG has created due diligence systems that are adaptable for everything from micro-businesses to large corporations, with commitments from 12 major luxury jewelry brands. With corporate partnerships, TDI has also launched artisanal and small-scale mining projects in Tanzania, Uganda, Kenya, and Brazil. **Brian Cook** (Nature's Geometry) spoke of his work as a consultant for TDI, investigating the financial records and environmental reclamation efforts of alluvial mining sites in Brazil. He also provided updates on the rutilated golden quartz community he established in Brazil's Bahia State.

The first day also featured the premiere of *River of Gold*, a documentary on illegal gold mining in the Amazon rainforest. The film shows the environmental devastation and human corruption that results from this form of gold exploitation. After the screening, sustainable jewelry consultant **Christina Miller** moderated a Q&A session with producer **Sarah DuPont**, joined by **Susan Egan Keane** (Natural Resources Defense Council) and **Nigel Pitman** (The Field Museum).

Day two opened with a panel in which jewelry designers described how they began working ethically sourced material. Moderated by jewelry designer and metalsmith **Alexandra Hart**, panelists told of humble beginnings in the responsible sourcing sphere; **Helene Grassin** (Paulette à Bicyclette) recalled sharing casting trees with other like-minded Parisian designers in order to afford the cost of ethically mined gold. The designers noted that their clientele know how to find them and were adamant about balancing bad news with transparency: If the customer cannot be told honestly that their materials are ethically sourced, they will often select a different metal or gemstone. They shared a desire to reach out to independent ethical, environmentally responsible gem suppliers so that designers and suppliers could join together to create a remarkable story for clientele. As one panelist stated, "We are the pioneers of creating these relationships."

Joanne Lebert (Impact) used a case study from the Democratic Republic of the Congo to explain how Impact believes ASM activity should operate. Borrowing the

Reagan-era dictum "Trust, but verify" allows the gemstone or jewelry piece's story to be told honestly and ethically. The Clinton campaign mantra "It's the economy, stupid!" reminds us that producers along the supply chain should be seen as economic actors who have a stake—and a final impact—on the material. Finally, Lebert's assertion that Obama focused on the good of the community as a whole reminds us that men and women in the mining and cutting sectors benefit differently from CSR efforts, a point examined further by the next speaker. **Glenn Lehrer** (Colourful Life Foundation) discussed the importance of giving back to communities that produce and work in the gem and jewelry industry. While the foundation is working in gem communities around the world, Lehrer focused on the schools it has opened for low-income children in Jaipur, India. Mothers of the children attending Colourful Life schools were provided with faceting training to prepare them for Jaipur's workforce. He was surprised to learn that the women rejected at-home training and workshop equipment. Going to school and work was a form of dignity for them, whereas Western workers often prefer the convenience of working remotely.

The last panel of the conference, moderated by **Monica Stephenson** (Anza Gems and iDazzle) focused on artisanal mining. Panelists recounted their personal experiences, challenges, and triumphs in the mining sector. Among the speakers was **Salma Kundi**, a tourmaline miner from Tanga, Tanzania, and secretary general of Tanzanian Women's Mining Association (TAWOMA); her group was involved in the Pact/GIA guidebook project (see below). Where Kundi comes from, a miner pays for a concession and a license and exploits the deposit with assistance. A mining license costs about US$400, a high price for a woman, and that does not cover mining and food expenses. Membership in TAWOMA allows for collective mining, enabling women to pay for licenses. Other challenges include a need to reach buyers beyond their local markets.

Robert Weldon spoke about GIA's collaboration with Washington, DC–based NGO Pact to create and distribute a rough gem guidebook among Tanzanian miners (Summer 2018 GNI, pp. 245–246). Since early 2017, GIA and Pact have provided training with the Swahili-language guidebook, which is accompanied by a tray for sorting gemstones using reflected and transmitted light. Follow-up surveys revealed a $12 social return on investment for every $1 invested in the program. As of October 2018, the guidebook has reached approximately 1,000 Tanzanian miners. The final speaker of the day, **Yianni Melas** (The Gem Explorer), recounted his experiences as a human rights advocate for gem and jewelry laborers, including a recent 31-day hunger strike that made international headlines.

Both days also featured a gem boutique, with information on ventures and gemstones available for sale. There were also optional lunch sessions that elaborated on topics that will affect the industry's future, such as the Jewelry Development Index, the flagship project of the University of Delaware's "Mines, Minerals and Society" program; the Mercury-Free Mining Challenge; and TrustChain, a collaboration between industry leaders and IBM to create a blockchain solution. As Mark Hanna said in opening the conference, "The challenge of our unknown future is so much more exciting than the stories of our accomplished past."

The 2019 Chicago Responsible Jewelry Conference is slated for Friday, October 25 and Saturday, October 26.

Jennifer-Lynn Archuleta
GIA, Carlsbad

Second World Emerald Symposium. Hosted by Fedesmeraldas (the Colombian Emerald Federation), Acodes (the Emerald Exporter Association), Aprecol (the Emerald Producers Association), Asocoemeral (the Emerald Dealers Association), and Minminas (the Ministry of Mines), the second World Emerald Symposium was held in Bogotá October 12–14, 2018.

The inaugural event in 2015 was themed "Be part of the change." Three years later, the emphasis was on sustainability, blockchain, nanotechnology, and traceability. Does the community share the benefit from the companies? The future of the emerald industry should develop with the local communities through education, improving health care and working conditions. These questions/keywords were among the important topics expressed during this second edition of the symposium.

More than 60 Colombian and international speakers and panelists presented a wide variety of topics such as gemology, ethics, government, stakeholders, and marketing before a large audience from around the world and representing all levels in the emerald industry.

Day one began with opening talks by Colombian officials, symposium organizers, and presidents of gem and jewelry associations (ICA, CIBJO, and AGTA). This was followed by geology and mining sessions. **Gaston Giuliani** (IRD, CRPG, Nancy, France) again offered an exciting talk on world emerald deposits in the 21st century, assessing current knowledge, types of deposit, and exploration. **Lee Groat** (University of British Columbia, Vancouver) spoke on emerald occurrences in Canada's Yukon Territory and the challenges for exploration and exploitation. **Gian Carlo Parodi** (National Museum of Natural History, Paris) reviewed the species and varieties of the beryl group and shared photos of various rare collector specimens such as stoppaniite and bazzite.

In the afternoon session on gemology, **Gabriel Angarita** (CDTEC Gemlab, Bogotá) introduced a new treatment for emeralds coming onto the market called "Naturalys." He compared it to traditional oil treatment or resin and described its identification. **Taijin Lu** (NGTC, Beijing) discussed the recently formed Chinese national standard on emerald grading. **Vincent Pardieu** (DANAT, Bahrain) spoke on emerald from Madagascar and presented a well-made

video from his most recent field expedition to Madagascar. **Olivier Segura** (L'École des Arts Joailliers, Paris) presented the school, which is supported by Van Cleef & Arpels, and its rich variety of classes such as jewelry history, gouache techniques, setting, gemology, and more.

Andy Lucas (Guild Gemlab, Shenzhen) talked about educating Chinese consumers on colored gemstones and China's potential as a luxury jewelry market. He concluded by introducing the new education programs offered by the Guild Institute of Gemology. **Alan Hart** (Gem-A, London) reviewed the association's heritage and long history. He also presented Gem-A resources such as its library, the *Journal of Gemmology*, and traditional education and alumni activities across the world.

This first day ended with two panel discussions, with **Ronald Ringsrud** and **Shane McClure** moderating the first. **Laurent Cartier** (SSEF, Basel), **Gagan Choudhary** (GTL, Jaipur), **Rodrigo Giraldo** (RGLAB, Bogotá), and **Aurélien Delaunay** (LFG, Paris) discussed laboratory reports on emerald treatments and the difficulties in determining the degree of enhancement. Is it a subjective call? Is a finding of minor, moderate, or significant enhancement sufficient, or would the addition of more degrees of enhancement on the reports be more accurate and benefit the industry? These were among the questions exchanged.

A second panel on gemology and origin (figure 32) was led by Shane McClure with panelists **Kenneth Scarratt** (DANAT), **Taijin Lu** (NGTC), and **Claudio Milisenda** (DSEF German Gem Lab). The group offered a frank discussion of many critical issues on country of origin determination. They also shared the difficulties gem labs encounter in building a reliable dataset to support country of origin determination. Potential solutions were also proposed.

The second day emphasized stakeholders' social responsibility, ethics, and marketing. The day began with speakers from mining companies. **Assheton Carter** (The Dragonfly Initiative), **Rosie Perkins** (FURA Gems), **German Forero** (Santa Rosa), and **Elena Basaglia** (Gemfields) talked about their respective projects on sustainability and development of social programs to support local communities. Projects included modernizing the mines, developing schools, and implementing health care systems. Independent consultant **Gerardo Vargas** concluded the session by discussing the importance of appellation of origin for Colombian emeralds and how it would benefit and protect the market, increase value, develop the industry, and give recognition to Colombian emeralds.

After the lunch break, the session continued with **Prida Tiasuwan** (Pranda Group) who offered insight on Thailand's gem and jewelry industry and its potential as a global gem and jewelry hub. Pointing at the duty-free, tax-free, and non-VAT trading system for gemstones, he talked about Thailand as a major center for colored stone education, cutting, manufacturing, and treatment.

Zhao Xin Hua presented information on the Gemstone Association of China and shared data and statistics on the Chinese colored gem market. **Liu Yi** (GAGCC) talked about the gem and jewelry investment hub opportunities

Figure 32. GIA's Shane McClure led the discussion panel on country of origin. Joining him, from left to right, were Kenneth Scarratt, Taijin Lu, and Claudio Milisenda. Photo by Tao Hsu.

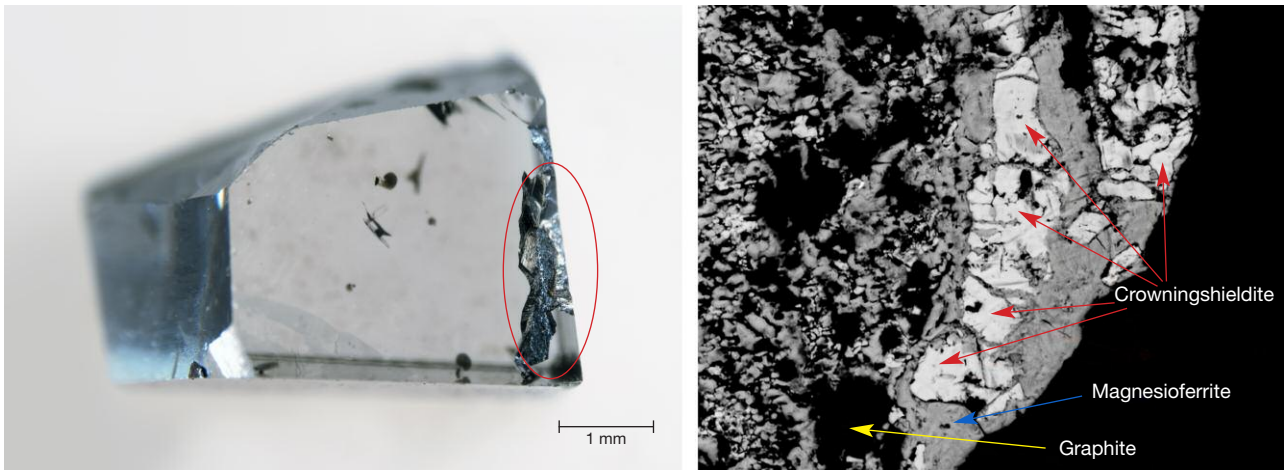

Figure 33. Left: A diamond sample from the Letšeng mine in Lesotho that contains the newly recognized mineral crowningshieldite, in the area circled in red. Right: Electron microscopy reveals individual grains of crowningshieldite in a fine-grained mixture with other minerals. Photos by Evan M. Smith (left) and Fabrizio Nestola (right).

with China. Next, **Laurent Cartier** (Gemstones and Sustainable Development Knowledge Hub) explained the organization's work and discussed the challenges regarding artisanal mining, short-life deposits, stock management, and consideration of quality over origin.

The last session was devoted to ethics and corporate social responsibility. **Cathlijne Klomp** (LVMH) spoke about responsible sourcing of colored gemstones as well as the challenges and opportunities for creating sustainable value. Next, **Charles Chaussepied** (Responsible Jewellery Council) explained the RJC's history, role, and mission. This last session was by a panel discussion regarding certifications with **Edwin Molina** (APRECOL) and **Charles Burgess** (Muzo MTC).

Day three was a half-day exploration of history. Independent jewelry specialist **Joanna Hardy** spoke on the Colombian emerald pocket watch from the Cheapside Hoard, the emerald and diamond parure of Empress Marie-Louise of France, and many other important antique emerald jewels. **Ronald Ringsrud** followed with more storytelling about people, miners, and emerald adventures. **Ioannis Alexandris** (Gemolithos) covered the magnificent Old Mine emeralds, historical jewelry featuring Colombian emeralds, and record-breaking auction sales. **Gerard Martayan** (Schlumberger) reviewed the rediscovery of the fascinating Chivor emerald mine.

Closing keynote addresses by **Shri Pramon Agrawal** (GJEPC), **Carlos Amaya** (governor of Boyacá), and **Oscar Baquero** (Fedesmeraldas) concluded the 2nd World Emerald Symposium.

Jonathan Muyal and Tao Hsu
GIA, Carlsbad

ANNOUNCEMENT

Crowningshieldite: A new mineral. GIA, in collaboration with researchers at the University of Padova, recently discovered crowningshieldite (figure 33), a new mineral named in honor of G. Robert Crowningshield (1919–2006), a pioneering researcher at GIA for more than 50 years. His many landmark contributions included the detection of irradiated diamonds, the initial report on General Electric's facet-quality synthetic diamonds, and the description of "padparadscha" sapphire's orangy pink to pinkish orange color. Crowningshieldite is a nickel sulfide mineral with a hexagonal crystal structure and can be regarded as the high-temperature polymorph of the mineral millerite. Discovered as an altered inclusion in two diamonds from the Letšeng mine in Lesotho, it was accepted as a mineral on September 18, 2018, by the International Mineralogical Association.

GEMS & GEMOLOGY

2018

CONGRATULATIONS

This year, hundreds of readers participated in the 2018 *Gems & Gemology* Challenge. Entries arrived from around the world as readers tested their gemological knowledge by answering questions listed in the Spring 2018 issue. Those who earned a score of 75% or better received a GIA Certificate of Completion recognizing their achievement. The participants who scored a perfect 100% are listed below.

G&G Challenge Winners

Australia
Michael Merritt
Barbara Wodecki

Belarus
Dmitry Stepanenko

France
Sylvie Jacquot

United States
Robert Campbell
Kenneth Fogelberg
Lois A. Henning
Douglas Kennedy
Paul Mattlin
Lisa Neely
Geraldine M. Vest
Ryan Waddell
Colleen Walsh
Kate Waterman
Jana White
Alvin Zimmer

Answers

See pages 54–55 of the Spring 2018 issue for the questions.

1 (d), 2 (a), 3 (a), 4 (b), 5 (c), 6 (a), 7 (d), 8 (a), 9 (b), 10 (c), 11 (d), 12 (a), 13 (b), 14 (b), 15 (a), 16 (a), 17 (d), 18 (a), 19 (b), 20 (c), 21 (a), 22 (d), 23 (b), 24 (d), 25 (a)

Micro-Features of Diamond

Treated

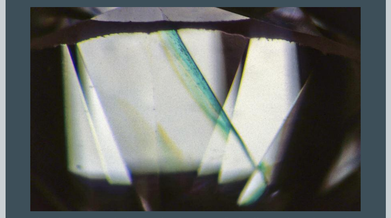

This cleavage crack shows a bright green "flash effect" when observed subparallel to the plane of the break against a bright background. This is diagnostic of clarity enhancement in diamonds. Field of view 3.20 mm.

The pavilion of this diamond was covered with an ultra-thin coating that is responsible for the stone's pink color. The coating is heavily abraded along facet junctions. Field of view 1.92 mm.

Due to the difficulty of detecting some treatments, such as HPHT processing, some gemological labs inscribe an indication of treatment on the stone's girdle. Field of view 2.01 mm.

The "umbrella effect" seen here results from cyclotron treatment along the culet area of a diamond and is diagnostic of artificial irradiation-induced color. Field of view 3.50 mm.

Internal laser drilling is a technique used to open a cleavage crack near dark inclusions to allow bleaching solutions to enter. Instead of a typical drill hole, this treatment is characterized by irregular, wormhole-like channels. Field of view 1.91 mm.

Natural

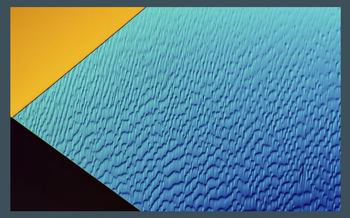

"Lizard skin" results from polishing a facet that lies nearly parallel to the octahedral face, which is the hardest crystal direction in diamond. Field of view 0.72 mm.

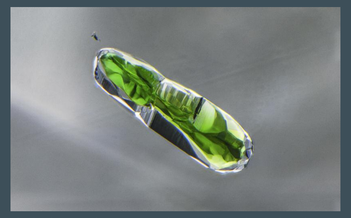

This bright green chromian diopside crystal proves that the host diamond is of peridotitic origin. Field of view 1.33 mm.

Interlocking grains with different crystallographic orientations show undercutting in this polycrystalline diamond. Field of view 2.88 mm.

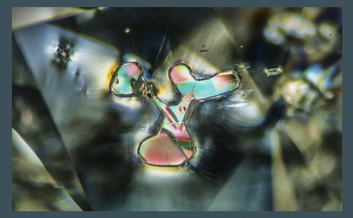

An olivine crystal inclusion in diamond shows high-order birefringent colors in cross-polarized light. Field of view 2.00 mm.

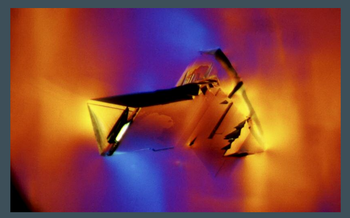

A diamond crystal inclusion in a diamond host is often nearly invisible, but cross-polarized light reveals significant strain between the inclusion and host. Field of view 1.36 mm.

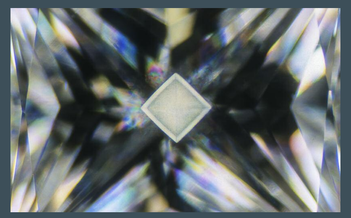

This diamond has an octahedral hydrogen cloud in its core. The cloud shows strong yellow fluorescence under long-wave ultraviolet light. Field of view 5.00 mm.

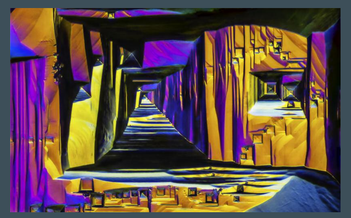

This differential interference contrast image shows square-shaped stepped etching along the cube faces of a rough diamond crystal. Field of view 2.88 mm.

This negative crystal resulted from partial dissolution and contains a loose diamond that rattles around in the cavity. It was stained green by radioactive fluids that were present in the host rock. Field of view 4.36 mm.

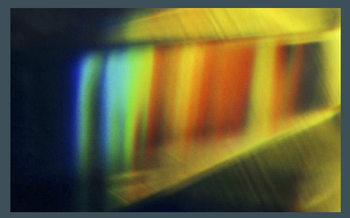

Rainbow graining, rarely seen in diamonds, results from planar structural defects that lead to the vibrant colors seen here. Field of view 1.90 mm.

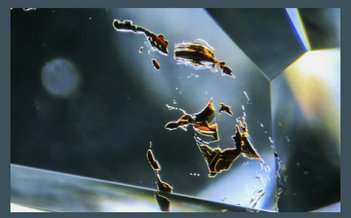

Sometimes thought to be "carbon spots," these chromite crystals reveal their identity by showing orangy brown coloration on thin edges. Field of view 2.10 mm.

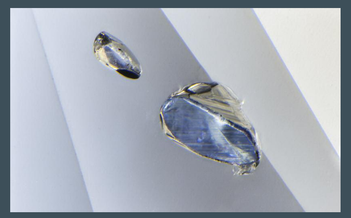

Sapphires, one of the rarest inclusions encountered in diamond, suggest an eclogitic origin. Field of view 0.99 mm.

The dense light-scattering accumulations of particles known as hydrogen clouds, which lie along phantom planes in this diamond, produce a "Maltese cross" pattern. Field of view 6.39 mm.

Bright purplish pink chromian garnets are a relatively common type of colored inclusion in gem diamonds and indicate peridotitic origin. Field of view 1.99 mm.

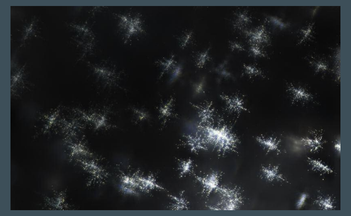

This unique diamond is host to numerous stellate clouds, which are rarely seen in such high density in a single stone. Field of view 0.72 mm.

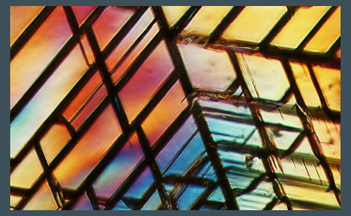

This network of cleavage cracks, seen in a pink diamond with polarized light, reveals weakness along octahedral planes. Field of view 0.61 mm.

Some of the most recognizable features on the surface of rough diamond crystals are the triangular etch features, known as trigons, that lie on the octahedral faces. Field of view 1.20 mm.

This rare bimineralic inclusion consists of a grayish green omphacite crystal and a pyrope-almandine garnet. The presence of these minerals indicates an eclogitic origin. Field of view 1.22 mm.

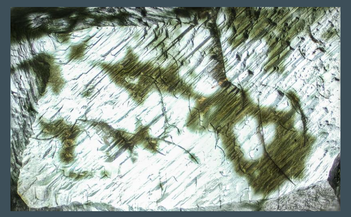

Deep green radiation staining on the surface of this diamond likely resulted from radioactive materials deposited by groundwater along the interface of the diamond crystal and host rock. Field of view 2.40 mm.

This bright blue kyanite crystal is a rare sight in a faceted diamond. The presence of kyanite suggests that this diamond is from an eclogitic environment. Field of view 2.18 mm.

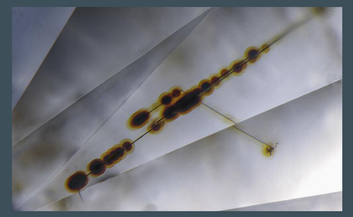

Thin etch tubes allowed radioactive material to enter the host diamond, causing localized brown radiation halos. Field of view 1.03 mm.

Synthetic

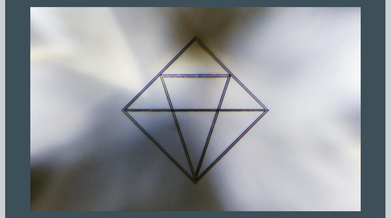

De Beers' line of CVD laboratory-grown diamonds can be easily recognized by the 300 × 300 micron logo inscribed about 200 microns below the surface of the table facet.

This HPHT-grown yellow diamond contains large iron-nickel flux inclusions. Graining and colorless zones are also present. Field of view 2.30 mm.

The girdle may contain information showing that a diamond is man-made, as seen here using differential interference contrast. Field of view 1.44 mm.

This flux-grown laboratory-grown diamond contains a large flux-filled negative crystal. Field of view 1.44 mm.

Black carbon inclusions that stand out in high relief are occasionally seen in CVD-grown diamonds. Field of view 1.42 mm.

This chart contains a selection of photomicrographs of natural, synthetic, and treated diamonds. It is by no means comprehensive. The images show the appearance of numerous features a gemologist might observe when viewing diamonds with a microscope.

Published in conjunction with Nathan D. Renfro, John I. Koivula, Jonathan Muyal, Shane F. McClure, Kevin Schumacher, and James E. Shigley (2018), "Inclusions in Natural, Synthetic, and Treated Diamond," *Gems & Gemology*, Vol. 54, No. 4, pp. 428–429. Photomicrographs by Nathan D. Renfro, John I. Koivula, Jonathan Muyal, and Shane F. McClure.

GIA®